POLITECNICO DI MILANO

Scuola di Ingegneria Industriale e dell'Informazione

Dipartimento di Chimica, Materiali e Ingegneria Chimica "Giulio Natta"

Optimal operating conditions for Dual Reflux Pressure Swing Adsorption process

Relatore: Prof. Renato Rota

Correlatore: Ing. Ester Rossi

Tesi di laurea di:

Cesare Borsa Matr. 905466

Anno accademico 2020/2021

Summary

Figures Index

Tables Index

Nomenclature

Symbols

A	Heavy component	N_{cycles}	Number of cycles simulated
a_i	Langmuir's parameter a	n_i^{feed}	Moles of the component i fed
B	Light component	n_i^{prod}	Moles of the component i produced
b_i	Langmuir's parameter b	n_{tot}^{prod}	Total moles produced
c_0	concentration	P	Pressure
C	Bed capacity ratio	P_{EQ}	Equalization pressure
C_{max}	Maximum bed capacity ratio	P_H	High pressure
D_{column}	Diameter of the adsorption bed	P_L	Light pressure
$d_{particles}$	Diameter of the solid particles	Pr	Productivity
G	Light recycle ratio	$purity_{i,j}$	Purity of component j in stream i
IP_1	Langmuir's parameter a	Q_{HP}	Heavy product molar flowrate
IP_2	Temperature	q_i	Amount of component i adsorbed on the solid
IP_3	Langmuir's parameter b	q_i^*	Amount of component i adsorbed on the solid at equilibrium
IP_4	Temperature	Q_L	Light reflux molar flowrate
k_{bk}	Blake-Kozeny constant	Q_{LP}	Light product molar flowrate
$k_{LDF,i}$	Mass transfer coefficient of component i	Q_{Press}	Pressurization molar flowrate
L_{column}	Length of the column	R	Ideal gas constant

$recovery_i$	Recovery of the component i
R_p	Macroparticle radius
$S_{F,\phi j}$	Sensitivity of parameter ϕ
$s_{F,\phi j}$	Incremental ratio of sensitivity
T	Temperature
$t_{Blowdown}$	Blowdown phase time
$t_{Equalization}$	Equalization phase time
t_{Feed}	Feed phase time
t_{Press}	Pressurization phase time
t_{Purge}	Purge phase time
u	Superficial velocity
V_{bed}	Volume of the bed
W	Work
y_F	Feed molar fraction
$y_{i,j}$	Molar fraction of the component j in stream i
z	Coordinate along the column
z_{Feed}	Feed position
$z_{F,max}$	Maximum feed position of the TOZ
$z_{F,min}$	Minimum feed position of the TOZ
$z_{F,opt}$	Optimum feed position of TOZ

Greek symbols

β	Separation factor
β_i	Adsorbent selectivity for species i
$\Delta_{\phi min}$	Minimum increment/decrement for parameter ϕ in sensitivity analysis
ε_b	Bed void fraction
ε_θ	Allowable fractional error in
ε_p	Particle void fraction
ε_s	Allowable fractional error in incremental ratio of sensitivity
ε_{rel}	Relative error
ε_T	Total void fraction
γ	Specific heat ratio of the gas
π	Pressure ratio
ρ_b	Density of the bed
ρ_s	Density of the adsorbent

Acronyms

BD	Blowdown phase

BM	Material balance	LDF	Linear driving force
CI	Initial conditions	LR	Light reflux
CSS	Cyclic steady state	MOO	Multi-objective optimization
DRPSA	Dual reflux pressure swing adsorption	PSA	Pressure swing adsorption
DRPHA	Dual-reflux pressure swing adsorption process with feed at high pressure and pressurization step performed with heavy component	PDE	Partial differential equation
DRPHB	Dual-reflux pressure swing adsorption process with feed at high pressure and pressurization step performed with light component	PR	Pressurization step
DRPLA	dual-reflux pressure swing adsorption process with feed at low pressure and pressurization step performed with heavy component	RS	Rectifying section
DRPLB	dual-reflux pressure swing adsorption process with feed at low pressure and pressurization step performed with light component	SS	Stripping section
EQ	Equalization step	TOZ	Triangular operative zone
FDM	Finite difference method		
FE	Feed step		
FVM	Finite volume method		
GA	Genetic algorithm		
HR	Heavy reflux		

Chapter 1

Introduction and literature analysis

1. Introduction

The separation process of a chemical mixture in its pure components is an important phase for the chemical industry (Sholl and Lively, 2016). Since it covers about 10 - 15% of the energy consumption of the industry, thus having a high impact on costs, studies have been carried out to develop economic and energy-efficient processes. In particular, research efforts have been directed towards those potentially cost-reducing and less energy-intensive (Rossi et al. 2019).

Among the possible separation processes including: adsorption, distillation and membrane separation, the Pressure Swing Adsorption (PSA) is particularly suitable in the case of separation of gaseous streams. It is characterized by a wide range of industrial applications like air separation, CO_2 capture from flue gas, hydrocarbons separation, natural gas and hydrogen purification. PSA wide use is due to its characteristics such as autonomy, reliability and quick process stabilization (Ruthven et al., 1993).

The adsorption-based processes exploit the different affinity of the components of the mixture for a solid adsorbent to selectively adsorb them onto the particles, thus obtaining separation. There are two types of selectivity: equilibrium selectivity, where the difference is in the affinity of the gases with solid surface or kinetic selectivity, where gases have different rates of adsorption.

The contact between the fluid phase and the solid adsorbent occurs inside a column where the particles are packed in a bed. The process continues until the adsorbent is saturated by the adsorbed specie, then regeneration of the bed is required.

The regeneration of the solid makes the process inherently discontinuous, characterized by a cyclic behaviour. For each bed the adsorption phase is followed by the regeneration one, in which the heavy component, that is the one preferentially adsorbed, is collected.

The regeneration of the bed can be performed with different methods, in this thesis we are particularly interested in the Pressure Swing Adsorption where the pressure in the beds is switched from a high value during the feed (FE) or adsorption step to a lower value during the purge (PU) or regeneration step to allow the adsorbed specie to be released.

The cycle for a standard two-bed PSA process is based on four steps during which the beds are operated simultaneously and cyclically as represented in Figure 1:

1. The first stage is PRESSURIZATION (PR): bed 1 reaches the set pressure value P_H through the injection of a gaseous stream at a constant flowrate Q_{Press} and with duration t_{Press}.
2. The second stage is ADSORPTION or FEED (FE): the adsorption of the heavy component A occurs. This step is performed at constant pressure P_H and flowrate Q_{Feed} with duration t_{Feed}. A raffinate stream, rich in the light component B (less adsorbable) is in part produced, in part it is used to purge bed 2.
3. The third stage is BLOWDOWN (BD): an extract stream of the component present in the column is discharged and recycled in the first step to reduce the pressure from P_H to a lower pressure value P_L.
4. The fourth and last stage is the PURGE (PU): a part of the raffinate stream rich in light component B from bed 2 adsorption phase is fed to bed 1 to recover the component A adsorbed.

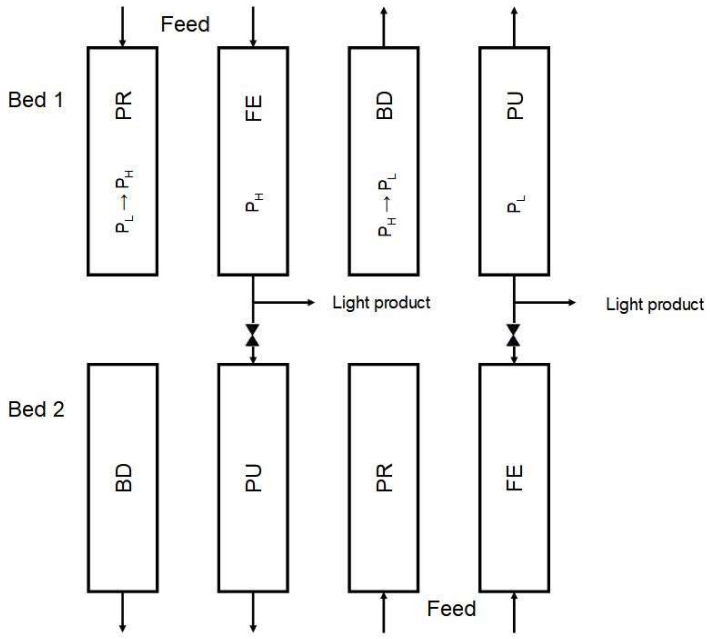

Figure 1: Standard two-bed PSA process scheme

There are two main PSA configurations in industrial processes: stripping type and rectifying type.

The first one is based on Skarstrom cycle (1959) represented in Figure 2. From a binary gas mixture fed at high pressure, it is capable of producing only the light product B at high purity, because the purity of the strongly adsorbed specie A is restricted by the so-called thermodynamic limit (Subramanian and Ritter, 1997). To obtain the heavy product at high purity, larger P_H/P_L and/or adsorbents with higher selectivity are required, which lead to an increase in both capital and operating costs (Kearns and Webley, 2006).

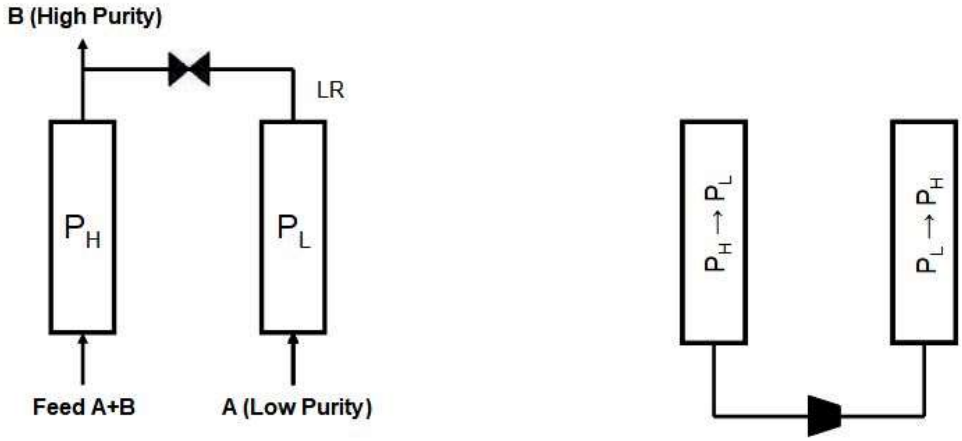

Figure 2: Skarstrom cycle

In the rectifying type (Diagne et al., 1994; Ebner and Ritter, 2002), also referred to as enriching reflux PSA (Yoshida et al., 2003), shown in Figure 3, the feed and the purge step pressure values are switched with respect to the stripping type, so that the gaseous mixture is fed at the adsorbent bed at P_L, while the purge phase occurs at P_H, thus allowing to obtain the heavy product with high purity. In the Diagne cycle it happens the opposite situation with respect to the Skarstrom cycle: heavy product A can be produced at high purity, while light product is subjected to the thermodynamic constraint on the purity.

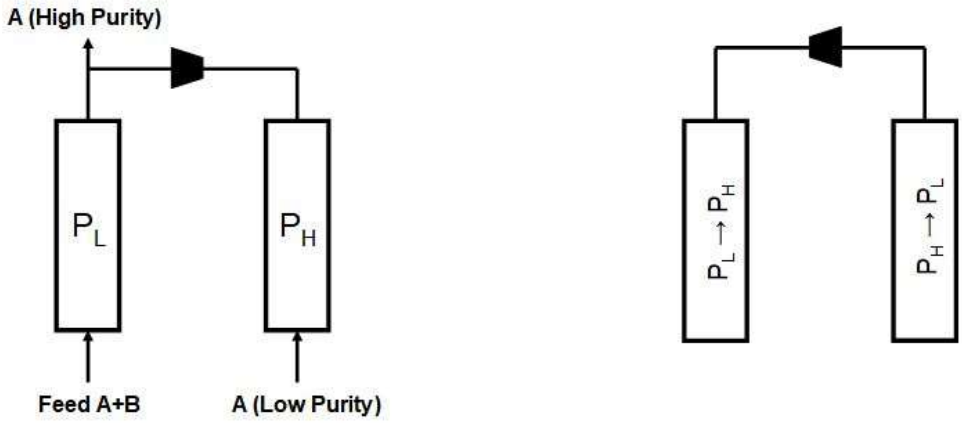

Figure 3: Diagne cycle

Therefore, PSA processes based on the conventional cycles (Skarstrom or Diagne) are not able to produce both high and light products at high purity (Yoshida et al., 2003), this happens, in particular, when the selectivity between the two species is low (May et al., 2017).

To overcome this limit, a new configuration based on the PSA process, called Dual Reflux PSA (DRPSA), has been proposed (Leavitt 1992), which allows to produce from binary gaseous mixture, under defined conditions, complete separation with both pure product

streams (Kearns and Webley part I (2006); Bhatt et al., (2013); May et al., (2017)) and which is going to be the subject of this work.

DRPSA separation process have been analysed experimentally in literature and several applications have been studied:

- CO_2 separation (Wawrzynczak et al. 2019; Shen 2017; Li et al. 2016; Kim et al. 2016; Sivakumar et al. 2011a, b; Takamura et al. 2001; Diagne et al. 1995, 1994;)
- N_2/O_2 separation (Wang et al. 2019; Tian et al. 2017)
- N_2/CH_4 separation (Weh et al. 2020; Xiao et al. 2019; Zhang et al. 2016; Salemann et al. 2015)
- N_2/C_2H_6 separation (Mc Intyre 2002, 2010)

In the DRPSA configuration, stripping and rectifying cycles are combined into a single two bed system. Moreover, the feed inlet position of the gaseous mixture is located laterally along the column axial coordinate, as it happens for the distillation, and two streams guarantee the reflux that gives the process its name.

Although the presence of the two simultaneous recycles requires further work, it increases the partial pressure of A in the high pressure column, therefore the purity obtainable is no longer limited by the PH / PL ratio, but only the constraints on the BM determines the theoretical limits of the products purities (Diagne et al. 1994, Yoshida et al. 2003). With the DRPSA process, under defined conditions, it is theoretically possible to achieve complete separation of a binary gaseous mixture.

The column is divided by the lateral feed injection into stripping and rectifying section. Its dimensionless position z_{Feed} is defined as the normalized axial coordinate by the ratio between the axial coordinate z and the column length L, such that $z_{Feed} = z/L$.

- $z < z_{Feed}$ – stripping section (SS)
- $z > z_{Feed}$ – rectifying section (RS)

For a two-bed process, schematically represented in Figure 4, four process configurations can be applied, which lead to two operating choices for the pressure of the FE step (P_H or P_L) and for the stream which is used for the reflux, A-rich or B-rich (Kearns and Webley 2006b).

The four possible configurations are:

1. DR PL – A: Feed injected in the low pressure column P_L and A-rich stream used for the PR/BD steps at variable pressure
2. DR PH – A: Feed injected in the high pressure column P_H and A-rich stream used for the PR/BD steps at variable pressure
3. DR PL – B: Feed injected in the low pressure column P_L and B-rich stream used for the PR/BD steps at variable pressure

4. DR PH – B: Feed injected in the high pressure column P_H and B-rich stream used for the PR/BD steps at variable pressure

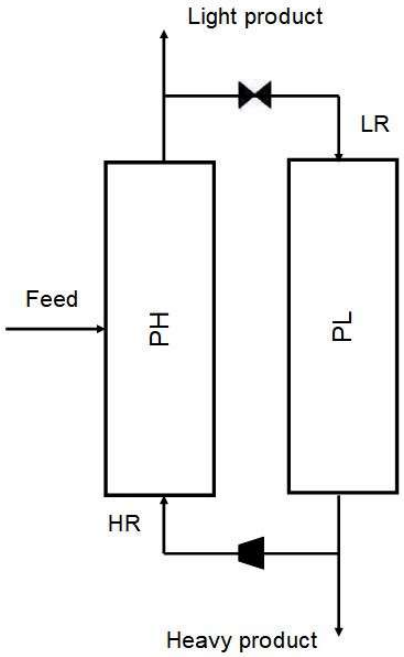

Figure 4: Two-bed standard DRPSA

2. Literature overview and aim of this work

The DRPSA process has been widely studied and analysed due to its suitable characteristics and good perspective in the separation of gaseous mixtures. Several models have been reported in literature for the design and the optimization of the process, from simplified models to more complex.

Three main approaches have been studied on the DR – PSA process:

- Experimental
- Simplified modelling
- Detailed modelling

The first studies on the DR – PSA (Diagne et al. 1995) had the purpose to determine empirically the influence on the concentration of CO_2 in the light and heavy products of some parameters such as feed composition (y_F), feed position (z_{Feed}), pressure ratio (π) and recycle to feed ratio (R/F).

Mc Intyre et al. (2002) experimentally studied the recovery and enrichment of ethane diluted in a nitrogen stream with a DRPLA unit. The results again showed that DRPSA is not limited by thermodynamics, as it was possible to produce ethane at 50 to 90 times the initial concentration, despite modest pressure ratios.

Among the simplified models, particular importance is given to the *Equilibrium Model* (or *Equilibirum Theory*) by Shendalman and Mitchell (1972), that had found application in the PSA studies, which is based on the assumptions of instantaneous linear equilibrium throughout the columns, isothermal operations, negligible transport phenomena and pressure drop, ideal gas behaviour and it exclusively considers mass conservation.

Ebner and Ritter, (2004) firstly applied successfully the Equilibrium Theory model for binary gas mixtures on a DRPLA configuration. They analysed the effect of changes in z_{Feed} between a minimum and a maximum value. This was the first model which clearly proved that it was possible to obtain complete separation of binary gas mixture using DRPSA (Bhatt et al., 2013).

Kearns and Webley, (2006a) developed the first mathematical model for the DR – PSA process based on the *Equilibrium Theory*, for each of the four configurations. In that study they also ensured a more efficient use of the adsorbent, respect to the Ebner and Ritter approach.

A further study (Kearns and Webley, 2006b) focused on the energy consumption and productivity trade off for the DR – PSA configurations analysed during the first part concerning the mathematical model based on the *Equilibrium Theory*. The performances of the four different configurations were compared varying some parameters like feed composition (y_F), pressure ratio (π) and separation factor (β). The results showed that DR – PHA obtains the best separation, also in terms of energy required, for low feed concentration of the heavy component and, on the contrary, DR – PLB showed the best behaviour for high concentration of the heavy component in the feed, thus demonstrating that y_F was the variable which mostly influences the choice between the configurations.

Bhatt et al. (2013) proposed a study based on the *Equilibrium Theory* for a DR – PHA unit, in which are investigated the design parameters to obtain complete separation of a binary gaseous mixture on the hypothesis of linear isotherms. The key parameters have been identified as the dimensionless feed injection position (z_{Feed}), the capacity ratio (C), proportional to the number of moles fed during the adsorption phase and the amount of adsorbent and the light recycle ratio (G), proportional to the light reflux flowrate. As results an expression for the optimal z_{Feed} position and a region inside the plane z_{Feed} vs. C have been developed in which, at Cyclic Steady State (CSS) conditions, any operating point ensures complete separations, with the value of G fixed; this region is called *Triangular Operating Zone* (TOZ).

This approach represents an important step towards the study of the optimal operating conditions, but the assumptions on which the Equilibrium Theory is based significantly limit its validity, in particular the requirement of complete separation (Rossi et al. 2020).

Later (Bhatt et al. 2017, Bhatt et al. 2019), with the same approach used for the 2013 work, discuss the impact of process variables on the design parameters and developed optimal design for the DR – PSA configurations left. They made a comparison between the four configurations and they proposed a criterion for choosing the most suitable configuration on a case-by-case basis.

With regards to the detailed model, we can find, among the others, Thakur et al. (2011) where non-linear adsorption isotherms are considered and pressure drops and transport phenomena are no more negligible.

Zhang et al. (2016) developed and implemented in Aspen Adsorption a dynamic numerical model with a complete pressure-flow network for a DRPSA cycle. It consisted of material, momentum and energy balances.

May et al. (2017), using an extended version of the model developed by Zhang in 2016, studied the effect of key parameters such as heavy product to feed ratio (Q_{HP}/Q_{Feed}), heavy reflux to feed ratio (HR/F) and bed capacity ratio (C) on the separation of a gaseous mixture composed of N_2 and CH_4.

Lastly Rossi et al. (2019) using Langmuir adsorption isotherms and on the base of several assumptions like isothermal process, ideal gas behaviour, mass transfer between solid and gas phase represented by Linear Driving Force (LDF) (Farooq et al. 1989), pressure drops along the columns estimated through Blake – Kozeny equation (Thakur et al. 2011) and axial dispersion negligible due to large values of the axial Peclet number (Liao and Shiau, 2000) proposed a design procedure which allows to select the pressure ratio when a sharp separation is required.

However, no one of this studies was able to develop clear design rules for this complex process.

Therefore, the aim of this study is to develop a general procedure to identify optimal operative conditions, from the point of view of productivity and work required, for an almost complete separation by means of a DRPHA process. This was done through an optimization procedure for which strategies were developed and implemented to make it more efficient. This is crucial given the large computational times and the numerical complexity related to the simulation of the DRPHA process (Rossi et al., 2019).

Starting from an operating condition identified through a trial and error procedure based on the information provided by the Equilibrium Theory (Chapter 3), the performance of the process was studied with the variation of some key parameters, complemented with a sensitivity analysis of the optimum operating conditions found. Moreover, as a preliminary investigation, a 6-step DRPSA process was also studied and a code for its simulation was validated (Chapter 4).

Chapter 2

Mathematical model for the DR – PHA process

1. DR – PSA configurations

As previously mentioned, the DR – PSA process represents the evolution of the conventional PSA cycle for the separation of binary gaseous mixtures, combining in a single unit the two PSA process configurations, the stripping and rectifying sections, divided by the lateral feed injection as shown in Figure 5. In order to achieve sharp or even complete separation, the thermodynamic limitations that affect the PSA cycle have been overcome by means of two reflux streams and the lateral feed injection, thus allowing to collect both heavy and light products at high purity.

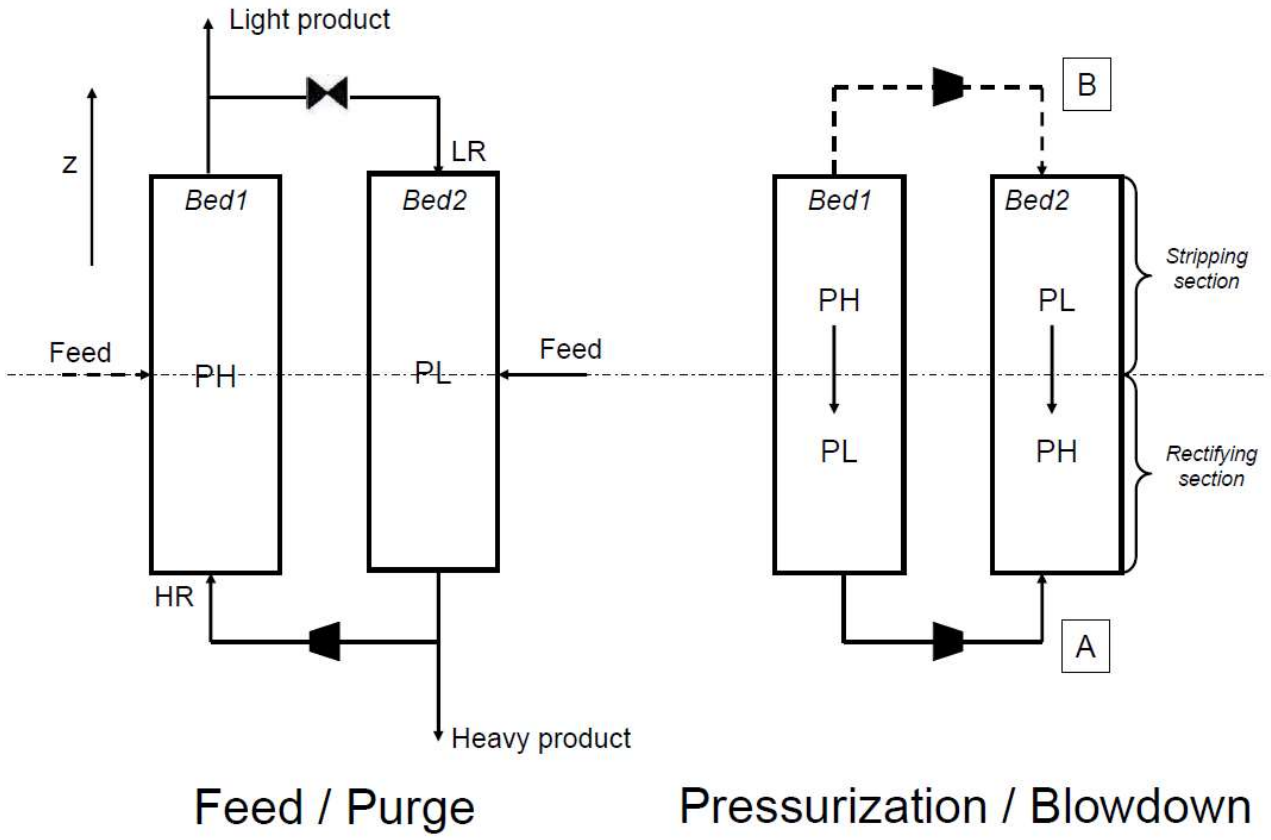

Figure 5: DRPSA possible configurations

The four available configurations differ in the choice of the bed at which the feed is injected, wether high pressure P_H or low pressure P_L, and if the recycle during the PR/BD step occurs

in the stripping section (B) or in the rectifying section (A), thus leading to the four different configurations called:

- DR – PHA
- DR – PHB
- DR – PLA
- DR – PLB

2. DR – PHA process

Among these, in our work we focus on the DR – PHA, shown in Figure 6, and its pressure profile represented in Figure 7.

Each of the two columns, is subjected to a four steps cyclical steps, where two of them occur at constant pressure, while the other two at variable pressure.

From now on we are going to refer to the heavy component (most adsorbable) as A and to the light component (less adsorbable) as B.

The feed binary gas mixture (A + B) is injected at axial coordinate z_{Feed} to Bed 1, with high pressure P_H, in the Feed step (FE), during which the heavy component adsorbs on the solid. At the same time, in Bed 2 occurs the Purge step (PU) at pressure P_L, where the heavy component is desorbed.

During FE, from the stripping section of Bed 1 we obtain pure B, in part recycled at Bed 2 during PU as Light Reflux (LR), in part collect as product; on the other end pure A exits from the rectifying section of Bed 2; in part it is collected as product stream and in part compressed and reinjected in Bed 1 as Heavy Reflux (HR).

In order to regenerate the solid adsorbent the pressure of the columns must be exchanged. At the end of the FE/PU steps, the upper parts of the columns are closed. Pure A is sent from the rectifying section of Bed 1 to the one of Bed 2 respectively in Blowdown step (BD) and Pressurization step (PR). The first part of this phase, called Equalization, occurs spontaneously until the columns have the same pressure (this strategy is adopted to have an energy saving). The pressure exchange is then completed with the help of a compressor. In this way it is possible to simultaneously obtain a change in pressure from P_H to P_L in Bed 1 and from P_L to P_H in Bed 2.

The columns are then switched so that Bed 1 undergoes PU at P_L while in Bed 2, where there is the regenerated adsorbent, starts FE at P_H.

This is repeated cyclically and since FE and PU occur at the same time as BD and PR, they are characterized by the same duration so that:

$t_{Feed} = t_{Purge}$

$t_{Blowdown} = t_{Press}$

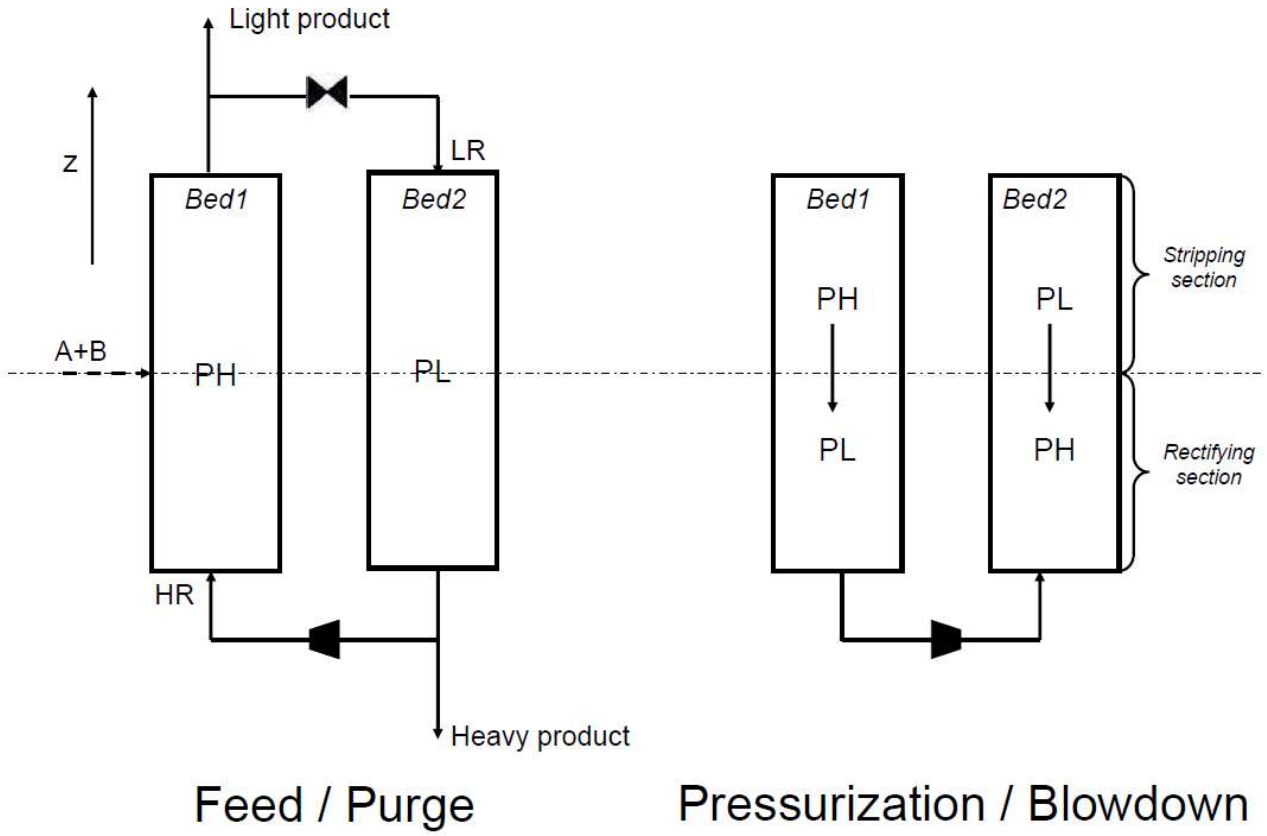

Figure 6: DRPHA configuration

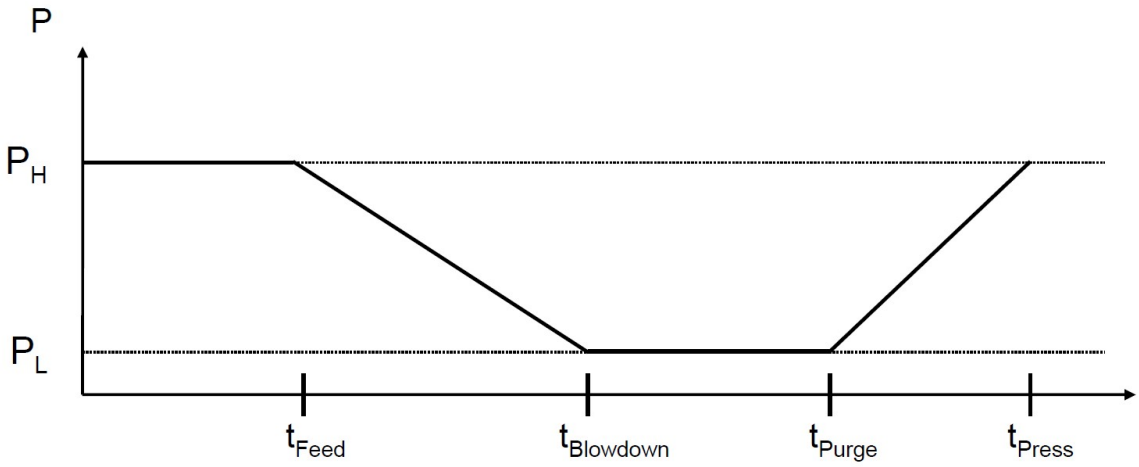

Figure 7: DRPHA Pressure profile for a single column

3. Model equations

Different models have been developed in order to simulate the dynamic of the DR – PSA processes, many of these are based on the Equilibrium Theory by Shendalman and Mitchell (1972), firstly applied on the DR – PSA by Ebner and Ritter (2004), that relies on the assumptions reported in Bhatt et al. (2013):

- Linear adsorption isotherms
- Instantaneous adsorption equilibrium throughout the columns (no mass transport limitations)
- Ideal gas behaviour
- No axial dispersion, radial velocities, dead volumes and pressure drop throughout the adsorption columns
- Isothermal operations
- Complete separation of binary feed gas

Some of these hypothesis have a significant influence on the field of application of this model. Later, detailed models try to reduce the stress of the assumptions, like the model presented in (Rossi et al. in 2019) adopted in this study, which is based on:

- Ideal gas behaviour
- Isothermal process, that means negligible energy balance
- Linear Driving Force model represents the mass transfer between gas and solid phases
- Pressure drops along the bed are described by the Blake – Kozeny equation
- Axial dispersion is negligible due to a very high Peclet number, which means ideal plug – flow
- The concentration of the adsorbed species, at equilibrium condition with gas phase, is described by a generic adsorption isotherm $q_i^* = f(P, y_i)$
- Homogeneous bed property along the column

Following these assumptions, the dynamics of each adsorption bed is simulated by a system of Partial Differential Equations (PDEs):

$$\varepsilon_T \frac{\partial P}{\partial t} + \frac{\partial (uP)}{\partial z} + \rho_B RT \sum_{i=1}^{2} \frac{\partial q_i}{\partial t} = 0 \qquad \rightarrow \text{Global Material Balance (BM)} \qquad (2.1)$$

$$\varepsilon_T \frac{\partial (Py_i)}{\partial t} + \frac{\partial (uPy_i)}{\partial z} + \rho_B RT \frac{\partial q_i}{\partial t} = 0 \qquad \rightarrow \text{Component i Mass Balance (BMi)} \qquad (2.2)$$

$$\frac{\partial q_i}{\partial t} = k_{LDF,i}(q_i^* - q_i) \qquad \rightarrow \text{Solid phase Material Balance} \qquad (2.3)$$

$$\frac{\partial P}{\partial z} = -\frac{u}{k_{bk}} \quad \rightarrow \text{Blake – Kozeny equation} \qquad (2.4)$$

$$q_i^* = f(P, y_i) \quad \rightarrow \text{Adsorption isotherm} \qquad (2.5)$$

The unknown variables of this PDEs system are P, y_i, q_i and u.

The last equation, (5), describes the relationship between the amount of component *i* adsorbed and its partial pressure in the fluid phase. Among the possible alternatives, we use the Langmuir isotherm which is derived under the assumptions of: possibility only of monomolecular layer, all sites are equal and no interaction between adsorbed molecules.

The equation that describes Langmuir Isotherm is:

$$q_i^* = \frac{a_i P y_i}{1 + b_i P y_i} \qquad (2.6)$$

where q_i^* is the concentration of the adsorbed species *i* at equilibrium conditions and a_i and b_i are the Langmuir coefficients for species *i*, respectively in $\frac{mol}{kg * Pa}$ and Pa.

4. Finite Volume Method and numerical solution

In order to describe the DR – PSA system, the PDEs must be solved numerically with a suitable method like the Finite Volume Method (FVM) used in this work.

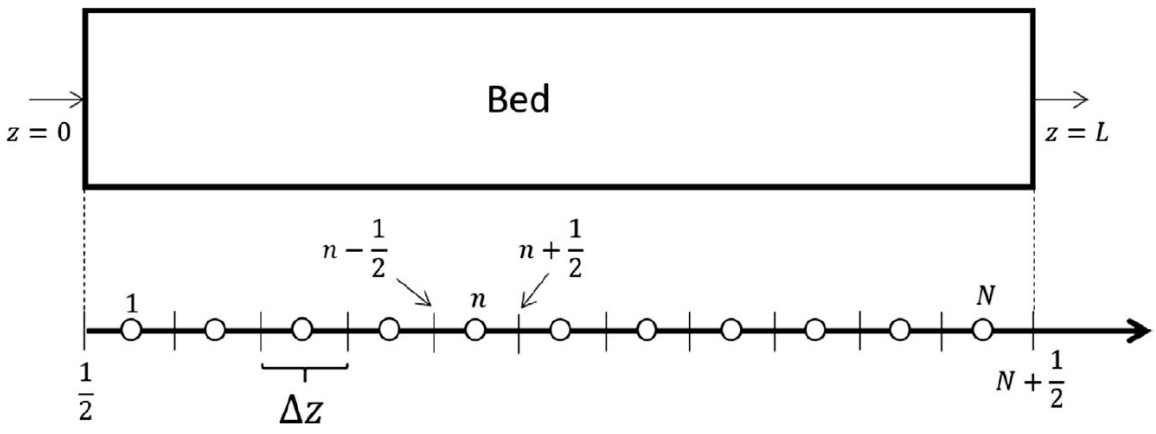

Figure 8: FVM discretization

In the FVM, the spatial domain is discretized into a set of finite volumes (Figure 8) while the resulting set of Ordinary Differential Equations (ODEs) is solved numerically in time inside each discrete volume (Rossi et al., 2019). Each state variable *s(z)* is assumed constant in the interval Δz with its average value s_n lumped at the centre of the interval:

$$\int_{n-\frac{1}{2}}^{n+\frac{1}{2}} s(z)dz = s_n \Delta z \tag{2.7}$$

This way, each PDE is discretized into N ordinary differential equations.

To simulate the DR – PSA cycle, have been established three different situations during the cyclical adsorption process:

- open – open step: the stream enters from one side of the bed and exits through the other one (FE and PU steps)
- open – closed step: one end of the bed is closed while the other is opened to perform the pressurization (PR step)
- closed – open step: it is the same as the open – closed step but with the stream leaving the bed without any inlet flow (BD step)

The system of ordinary differential equations, obtained by the discretization of the set of PDE by the FVM and representing the model of the DR – PHA process, can be solved by the routine ode15s present in Matlab.

Arbitrary values can be taken as initial conditions for the BD step, since the achievement of CSS does not depend on them, but proper initial conditions lead to a decrease in the time requested for the computational simulation of the cycle. Moreover, the final conditions of each step represent the initial conditions of the following one, for instance the final conditions of the PU become the initial conditions of the BD.

After each simulation, the Matlab code provides the following outputs:

1. global mass balance error:

$$\varepsilon_{rel} = \frac{Q_{Feed} - Q_{HP} - Q_{LP}}{Q_{Feed}} \tag{2.8}$$

2. heavy product mass balance error:

$$\varepsilon_{rel,A} = \frac{Q_{Feed} y_{F,A} - Q_{HP} y_{H,A} - Q_{LP} y_{L,A}}{Q_{Feed} y_{F,A}} \tag{2.9}$$

3. light product mass balance error:

$$\varepsilon_{rel,B} = \frac{Q_{Feed} y_{F,B} - Q_{HP} y_{H,B} - Q_{LP} y_{L,B}}{Q_{Feed} y_{L,B}} \tag{2.10}$$

4. purity of the heavy component:

$$purity_{HP,A} = \overline{y_{H,A}} \tag{2.11}$$

5. purity of the light component:

$$purity_{LP,B} = \overline{y_{L,B}} \tag{2.12}$$

6. composition profiles of the heavy component for each simulated cycle and for each of the four steps at the beginning and at the end of the step

7. heavy product purities approaching the CSS conditions:

$$\varepsilon_{purity,LP,A} = purity_{LP,A}(N_{cycles} - 1) - purity_{LP,A}(N_{cycles}) \tag{2.13}$$

$$\varepsilon_{purity,LP,B} = purity_{LP,B}(N_{cycles} - 1) - purity_{LP,B}(N_{cycles}) \tag{2.14}$$

8. light product purities approaching the CSS conditions:

$$\varepsilon_{purity,HP,A} = purity_{HP,A}(N_{cycles} - 1) - purity_{HP,A}(N_{cycles}) \tag{2.15}$$

$$\varepsilon_{purity,HP,B} = purity_{HP,B}(N_{cycles} - 1) - purity_{HP,B}(N_{cycles}) \tag{2.16}$$

5. Multi-objective optimization

A large part of this study deals with the multiobjective optimization, a problem where there are more than one objective function, which are to be optimized simultaneously. In this study they are *purity* and *recovery*:

$$purity_i = \frac{n_i^{prod}}{n_{tot}^{prod}} \tag{2.17}$$

$$recovery_i = \frac{n_i^{prod}}{n_i^{feed}} \tag{2.18}$$

which can be related to the light or heavy component.

The optimization is called multivariate because the objective functions depend on multiple parameters which are left free to vary in a physically consistent range of values. These key parameters that govern the process are identified as manipulated variables:

- *pressure ratio*

$$\pi = \frac{P_H}{P_L} \tag{2.19}$$

- light recycle flowrate and thus *light recycle ratio G*

$$G = \frac{Q_L}{Q_{Feed}} \tag{2.20}$$

- duration of the FE/PU phase t_{Feed} and thus *capacity ratio C*

$$C = \frac{\beta_i RTG}{P_L \varepsilon} \frac{Q_{Feed} t_{Feed}}{V_{bed}} \tag{2.21}$$

- flowrate of heavy product extracted, that in our case was set equal to the stoichiometric one:

$$Q_{HP} = Q_{Feed} y_{F,A} \tag{2.22}$$

π, G and C parameters are defined as reported in (Bhatt et al., 2013) for the *Equilibrium Theory*.

The process involves the solution of the PDEs system, for the search of the optimum operating conditions, identified by maximum purity and recovery.

In general, the purpose of the optimization, is to develop a Pareto front on the plane, defined by two competing goals, which is the best trade-off between the two objectives. To each point of the front corresponds a vector of values of the manipulated variables, which constitutes a combination that represents an optimum operating condition. The region above the front is considered implausible, while that below represents sub-optimal operating conditions.

In the case of the optimizations carried in this study, having fixed the flowrate of heavy product extracted equal to that allowing the complete separation of the mixture, the optimum search will not build a Pareto curve on the recovery vs. purity plane, because in this case purity is equal to recovery, as shown in Figure 9.

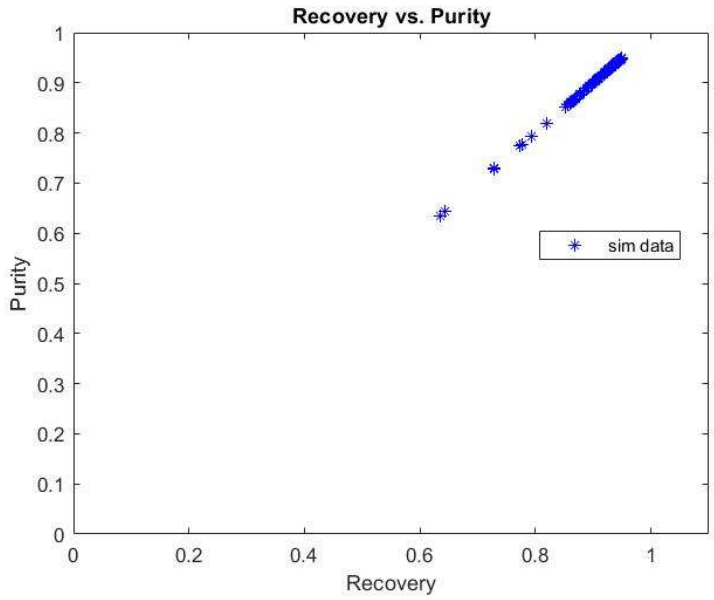

Figure 9: Recovery vs. Purity

The optimization process has been carried out using the gamultiobj Matlab function, which is based on the *genetic algorithm*.

6. Genetic Algorithms

The extensive use of Genetic Algorithms in chemical engineering literature is found in the optimization of several processes such as catalytic reactions, simulated moving bed and pressure swing adsorption (Krishnamurthy et al., 2014). The validity of their use in recovery and purity optimizations for gaseous mixture separation processes has been validated in literature by comparison with experimental results showing a very good match in works such as Perez et al., (2019). In this field, several other studies exploit genetic algorithms in the multi-objective optimization process like Fiandaca et al., (2009), Krishanmurthy et al., (2014), Capra et al., (2018) and Subraveti et al., (2019) often with the aim of reducing energy consumption and increasing productivity, always maximizing recovery and purity.

The Genetic Algorithms (GAs) belongs to the larger class of evolutionary algorithms, which borrow their working principle from the process of natural selection through operators such as mutation, crossover and selection. Genetic algorithms are particularly suitable in the case of problems for which no other efficient algorithms of linear or polynomial complexity are known.

Genetic Algorithms were first introduced by John Holland in 1975. They have been extensively used for their broad applicability and ease of use as search and optimization tools in several problem domains such as sciences, commerce, and engineering (Deb 1999).

The flexibility of use of the GAs comes from its probabilistically guided search and from initial random population, no major decision is made at first so that the search may proceed in any direction, while most of the traditional methods use fixed transition rules to move from one solution to another.

The algorithm begins with a random set of solutions, which are then evaluated once a population of solutions is created. A termination criterion is then checked, if it is not satisfied, before proceeding to the next iteration the population of solutions is modified by three operators that create a new population.

The three operators are:

- *Reproduction operator*
  It enhances the good solutions and eliminates bad ones of a population, while keeping its size constant, through:
  - Identification of good solutions
  - Reproduction of multiple copies of good solutions
  - Elimination of bad solutions to make room for the good ones
- *Crossover operator*
  Since reproduction operator can only copy and eliminate solutions without create new solutions, it is necessary the crossover operator, which, together with the mutation operator, performs this task by picking randomly two good strings from the mating pool in order to take some portions of the strings to exchange between them
- *Mutation operator*
  The crossover operator performs the search task, the mutation operator changes 1 to 0 and vice versa with a small mutation probability, a fundamental process to keep diversity in the population

The bad solutions created will be eliminated by the reproduction operator in the next iteration, while the good strings will be enhanced.

The optimization process starts with an initial population that consists of a collection of unique set of decision variables, whose fitness with respect to the objective functions is evaluated by the DR – PSA model. The fitness of the individuals of a generation is used as a criteria to select the next one, in this phase the reproduction, crossover and mutation operators guarantee the diversity of the population and the development of the solutions. Until further improvements are possible in the fitness of individuals, the process is repeated for other generations.

7. Multi-objective optimization specifications

The Multi-Objective Optimization problems were solved using *gamultiobj* Genetic Algorithms in Matlab Global Optimization Toolbox. The computations were performed on a desktop workstation with Intel – Core i5-8250U CPU @ 1.60 1.80 GHz processors and 8 GB RAM or on computational facilities characterized by 8 core (Intel Xeon CPU E5540 2.53 GHz), 24 GB RAM and 12 core (Intel Xeon CPU X5670 2.93 GHzz), 32 GB RAM.

As a rule of thumb, the number of simulations required to achieve a stationary behaviour during the optimization process was about 300 to 400 simulations, characterized by an average duration of each simulation between 5 and 10 minutes, which increased to 30 and 100 minutes for higher π values. Once the stationarity of the results has been achieved, the optimization process continued up to about 600 or 800 simulated points in order to make the Pareto front more dense, in our case the diagonal on the Purity versus Recovery plane, since the heavy product flowrate has been set equal to the stoichiometric one.

These long simulation times would be even much longer if standard accuracy of each simulation would be required. To keep computational time as low as possible (and therefore to make the optimization procedure feasible) relatively low number of computational points was used, which is translated into a lower accuracy of the results and a significant reduction of the time required for the calculation.

Typically, a number of 50 computational points for the optimization was used, while for a single control simulation, 300 computational points were set. Sample operating conditions from that, obtained during the optimization, have been simulated with greater accuracy to ensure consistency and reliability of the results obtained. As shown in Figure 10, where the heavy component purity is reported for two simulations performed using 50 and 300 grid points, while the final result may differ slightly, the trend that characterizes the profile is comparable:

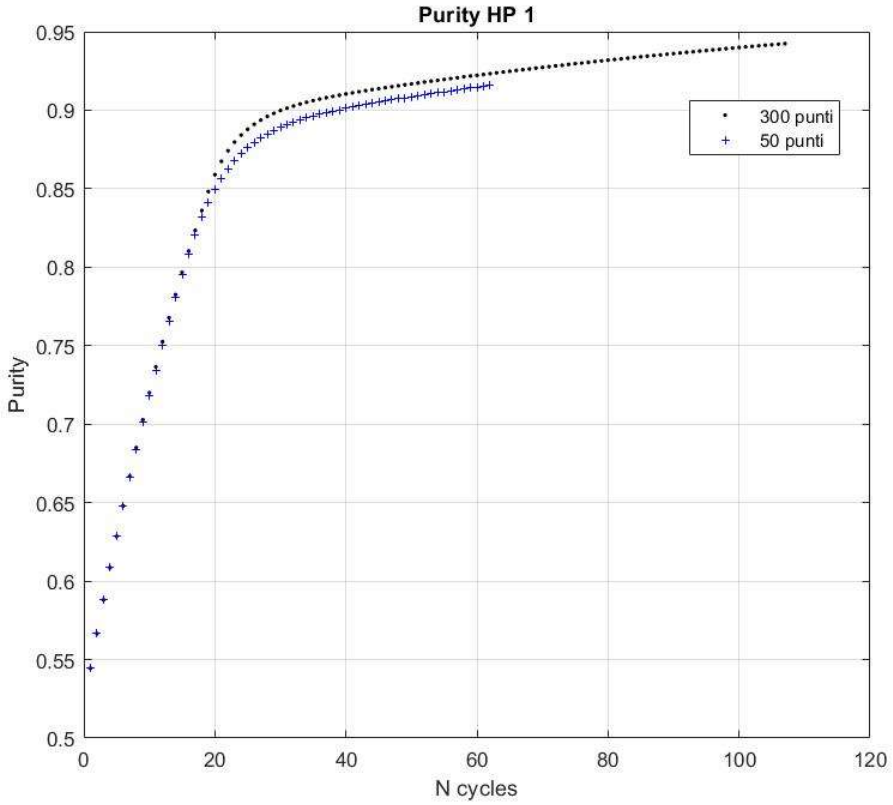

Figure 10: Comparison of the profile at different number of computational points

This confirms the possibility to perform the optimizations with fewer computational points, in order to reduce the computational time, without losing the reliability of the results. Simulations of some of the operating conditions identified by the optimization procedure were repeated with greater accuracy to ensure the reliability of the results.

8. Productivity and Work

A part of this study investigated the economic performances of the process as represented by productivity and work required. High productivity and low energy requirements consumption are by far preferable given the same recovery and purity values.

The following equation was used to calculate Productivity:

$$\mathrm{Pr} = \frac{Q_{feed} * t_{feed}}{V_{bed} * (t_{feed} + t_{Blowdown})} \tag{2.23}$$

with unit of measure $\frac{mol}{m^3 * cycle}$.

The Work computation has been carried out using the following relation (May et al., 2017).

$$W = \frac{\gamma}{\gamma-1} * (RT_{in}) * \left[\left(\left(\frac{Pout}{Pin}\right)^{\frac{\gamma}{\gamma-1}} - 1\right)\right] \quad (2.24)$$

with unit of measure $\frac{J}{mol}$ and:

- $Pout = P_H$
- $Pin = \frac{P_H + P_L}{2}$
- γ = 1,4 specific heat ratio of the gas

Chapter 3

Optimization of the separation process of a gas stream

1. Definition of the system

In this section the optimization process, carried out to enhance the performance of the system in terms of purity, recovery, productivity and work required. The separation has been carried out on the DR – PHA configuration for a binary gas mixture characterized by weakly non-linear Langmuir isotherms (Rossi et al. 2019), as shown in Figure 11.

The optimization code has been implemented on Matlab using the Finite Volume Method (FVM) and the numerical model discussed in Chapter 2, for the part concerning the simulation of the separation process, and the genetic algorithms for the optimization task. Firstly, the objective functions have been set as the Purity and Recovery of the light component defined by the equations Equations 2.17 and 2.18.

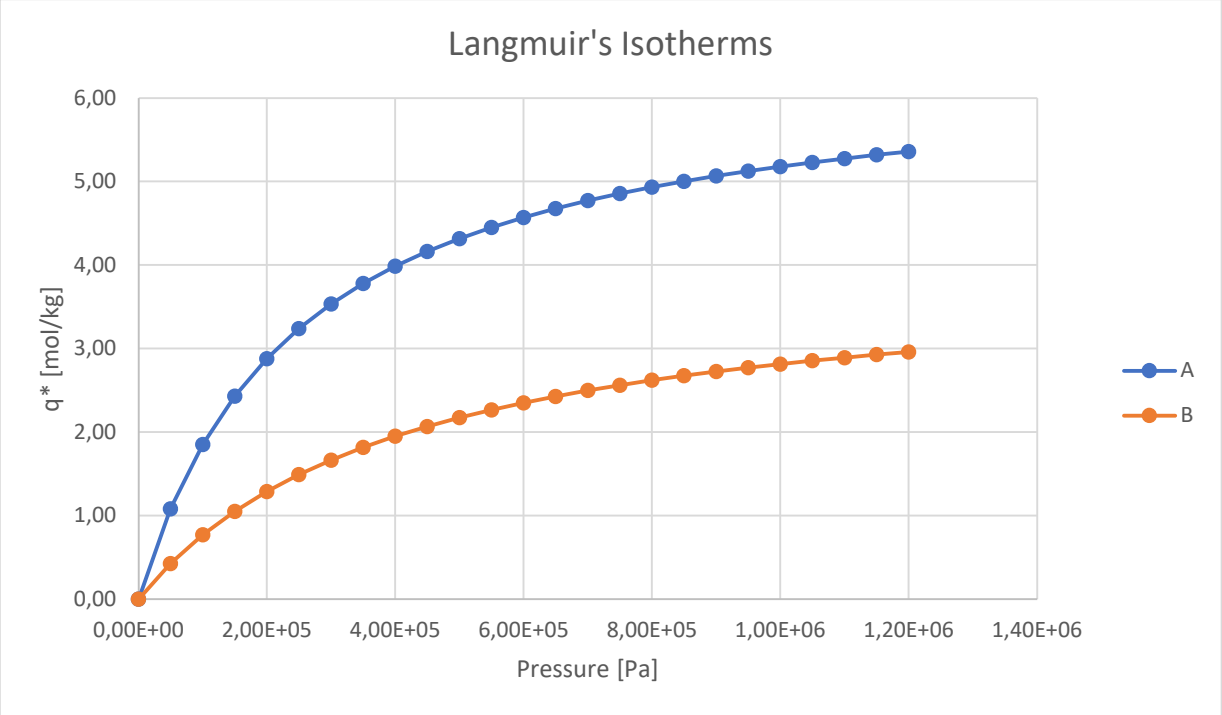

Figure 11: Langmuir's isotherms of component A and B

For the implementation of the code it had to be taken into account that the process layout for a generic DR – PHA system in Figure 6 is just conceptual. In a real process, to ensure proper operation, two additional tanks are required. Since the process never reaches steady state conditions, before reaching cyclic stationary conditions, to comply with the material balances, some additional amount can be required with respect to that recovered by the columns. Moreover, due to the non-linear shape of the adsorption isotherms, the amount of gas adsorbed in the BD step can be different from that required in the PR step. Therefore, the tanks were placed at the top and at the bottom of the columns, as shown in Figure 12:

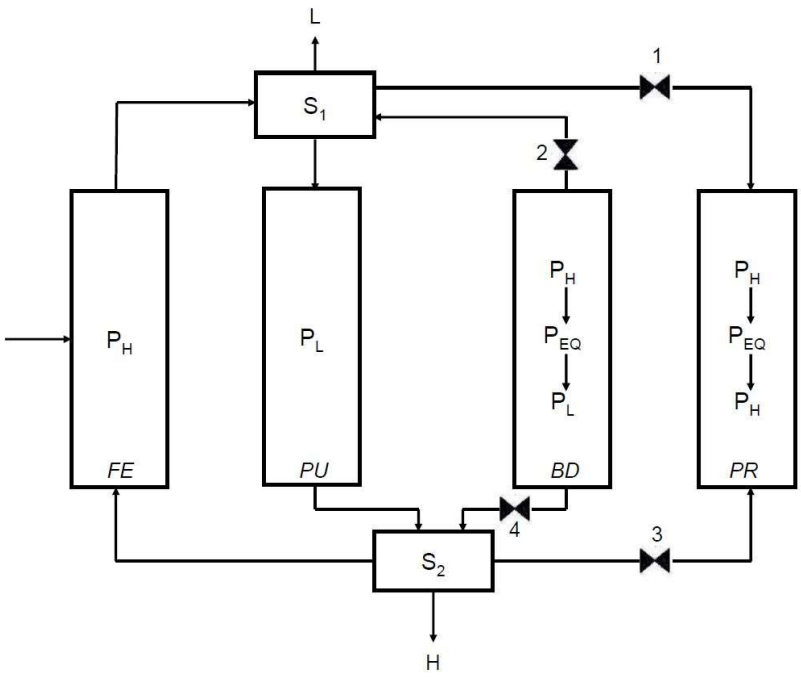

Figure 12: DRPSA configuration with tanks for the simulation and optimization work

During the optimization process and more widely in this study, there were some variables of particular importance for the performance of the system, which are:

- pressures: P_H and P_L
- dimensionless feed coordinate z_{Feed}
- feed molar fraction y_F
- feed flowrate Q_{Feed}
- light recycle flowrate Q_L
- heavy product flowrate Q_{HP}
- duration of the feed step t_{Feed}

Some of them have been fixed, some have been manually changed (in order to reduce the computational time requested by the optimization procedure) and some have been left free to change during the optimization process.

Since the heavy product flowrate Q_{HP} has been set equal to:

$$Q_{HP} = Q_{Feed} y_{F,A} \tag{3.1}$$

in order to guarantee complete separation, this results in equal values of purity and recovery

For this reason, from now on, we will refer to their both numerical results indistinctly.

2. Simulation of the starting operating conditions

The beginning of this work is represented by a set of operating parameters, which resulted from a trial and error procedure starting from the values provided by the Equilibrium Theory and for which it was possible to obtain complete separation with values of purity and recovery of both components higher than 99%.

In chapter 1 the Equilibrium Theory has already been mentioned along with the study reported in Bhatt et al., (2013) for the DR – PHA configuration with linear isotherms. In that work, the key parameters for the design of the separation have been identified as:

- Feed inlet position z_{Feed}
- Bed capacity ratio C
- Light recycle ratio G

It has been shown that it is possible to achieve complete separation for specific values of z_{Feed} and C at constant G. The z_{Feed} values were between $z_{Feed,min}$ and $z_{Feed,max}$ which included an optimal value called $z_{Feed,opt}$.

Moreover, it has been found a region in the plane z_{Feed} vs. C characterized by complete separation, which was named Triangular Operating Zone (TOZ), since it has a triangular shape as shown in Figure 13:

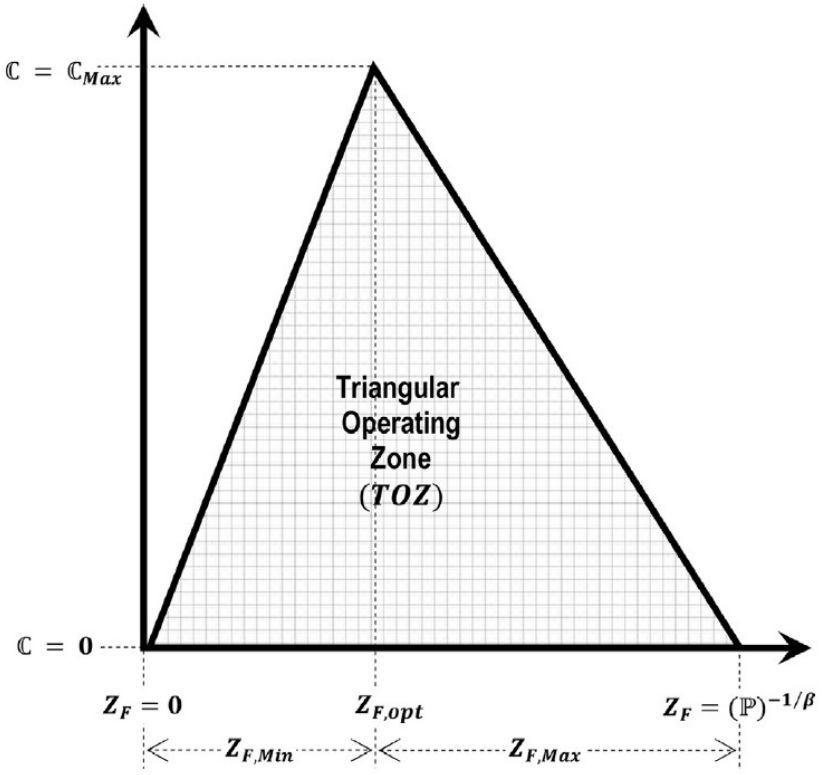

Figure 13: TOZ from Bhatt et al., 2013

The optimal conditions correspond to the upper vertex of the TOZ, with the feed coordinate $z_{Feed,opt}$ and the maximum capacity ratio Cmax, which represents the maximum productivity, since the C expression on Bhatt et al., (2013) is the one of a productivity, that means best use of the adsorbent and shortest possible column. However, the conditions just described are unfeasible in practical applications because of their sensitivity, since any perturbation of the operating parameters would lead outside the TOZ and to a non-complete separation. For this reason, it is preferred to work inside the TOZ in order to improve the robustness of the process even if this would result into a higher adsorbent demand.

For the starting point of this work, the following key operational parameter values were found after simulations performed with trial and error procedure:

1. $Q_L = 6.5 * 10^{-4}\ mol/s$
2. $t_{Feed} = 214\ s$
3. $P_H = 12 * 10^5\ Pa$
4. $P_L = 4.5 * 10^5\ Pa$
5. $Q_{HP} = 8.85 * 10^{-5}\ mol/s$
6. $z_{Feed} = 0.8$

The complete input data entered in the simulation code are reported in Table 1.

Table 24: Input data for the starting point simulation

Variable	Values	Units	Meaning
ε_p	0.65	-	particle void fraction
ε_b	0.31	-	bed void fraction
P_H	$12*10^5$	Pa	high pressure
P_L	$4.5*10^5$	Pa	low pressure
y_F	0.5	-	feed composition
T	298	K	temperature
ρ_s	3310	kg/m3	solid density
$d_{particles}$	$2.6*10^{-3}$	m	particle diameter of the solid adsorbent
μ_{mix}	$1.85*10^{-5}$	Pa*s	mixture viscosity
L_{column}	1	m	length of the column
D_{column}	0.03	m	diameter of the column
$k_{LDF,1}$	1000	1/s	mass transfer constant of the heavy component
$k_{LDF,2}$	1000	1/s	mass transfer constant of the light component
$Langmuir_{1,a}$	$2.59*10^{-5}$	mol/kg/Pa	Langmuir parameter a of the heavy component
$Langmuir_{2,a}$	$9.51*10^{-6}$	1/Pa	Langmuir parameter a of the light component
$Langmuir_{1,b}$	$4*10^{-6}$	mol/kg/Pa	Langmuir parameter b of the heavy component
$Langmuir_{2,b}$	$2.38*10^{-6}$	1/Pa	Langmuir parameter b of the light component
t_{Feed}	214	s	feed/purge time
$t_{Blowdown}$	1500	s	blowdown/pressurization time
Q_{Feed}	$1.77*10^{-4}$	mol/s	feed molar flowrate
Q_L	$6.5*10^{-4}$	mol/s	light recycle molar flowrate
Q_{HP}	$8.85*10^{-5}$	mol/s	heavy product molar flowrate
z_{Feed}	0.8	-	dimensionless feed injection coordinate

The duration of the BD/PR phase was set at 1500 s, a rather long time, in order to favor the numerical integration. Has already been proved that the numerical results are not affected by the duration of the equalization and pressurization steps since they are processes of pure matter transport and the only governing parameter is the set pressure. Moreover, the integrator is favored by longer duration of the blowdown and pressurization steps, because in this way it is possible to better describe the pressure profiles that are formed in the columns and thus avoiding the failure of the simulation.

Also, the mass transfer coefficients of both components were set at an imposed value arbitrarily high, that is 1000 1/s, to guarantee no mass transfer limitations.

For this case a high accuracy simulation was performed with 300 computational points and 1500 cycles, at which Cyclic Steady State (CSS) conditions are achieved, as can be seen from the relative errors on the material balances of the heavy and light components.

The results, reported in Table 2, show complete separation, since light product purity is equal to 100% (Figure 15) and heavy product purity reaches 99,9% (Figure 14). The CSS conditions are established after 1500 cycles, which means an overall duration of the process of about 115 hours.

Table 25: Purity and Mass Balance Error results of the starting operating conditions simulation

	Heavy product	Light product
Purity [%]	99.9	100
Mass Balance relative error [%]	0.1	0.16

As can be noticed, for both components the relative error on the Mass Balance is far below 1%, which is considered as threshold value to ensure enough accuracy of the model.

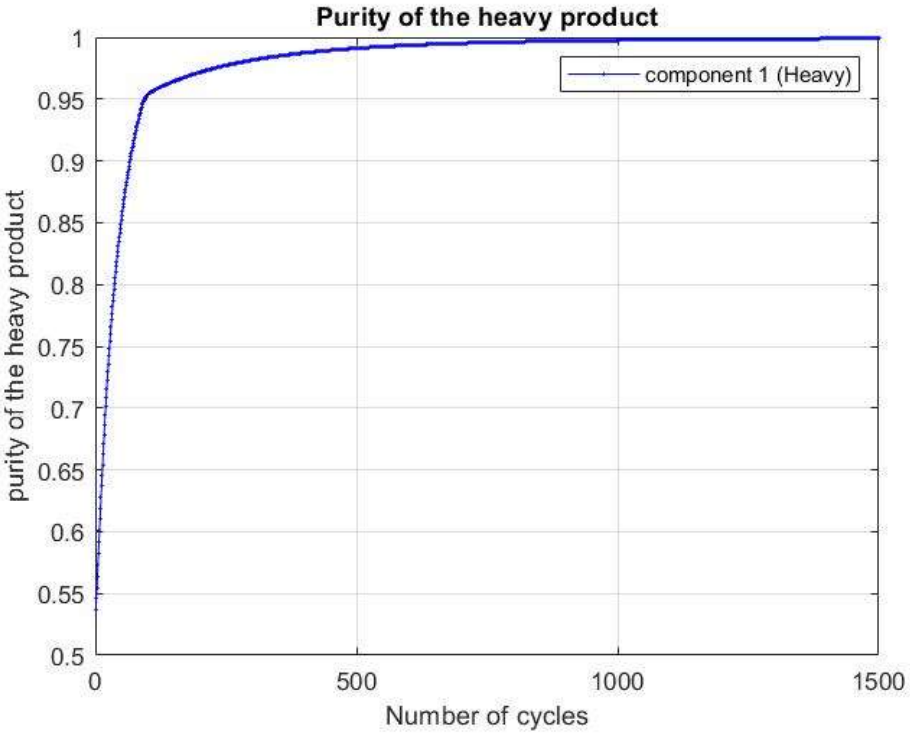

Figure 14: Heavy product purity profile of the starting operating conditions

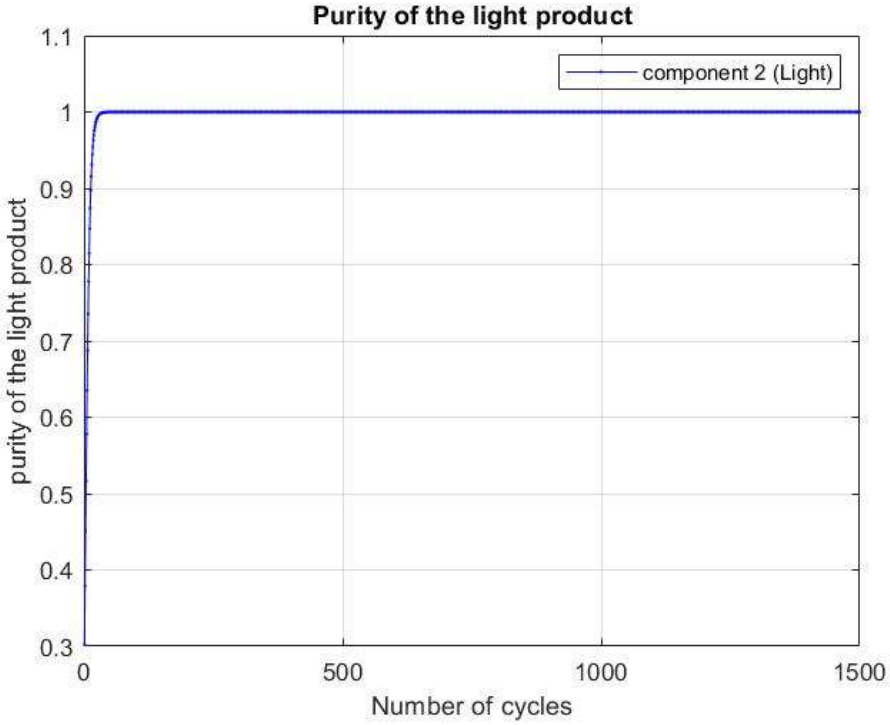

Figure 15: Light product purity profile of the starting operating conditions

The relative errors of heavy and light components are calculated from Eq. 2.9 and Eq. 2.10 and their results are shown in Figure 16 and Figure 17.

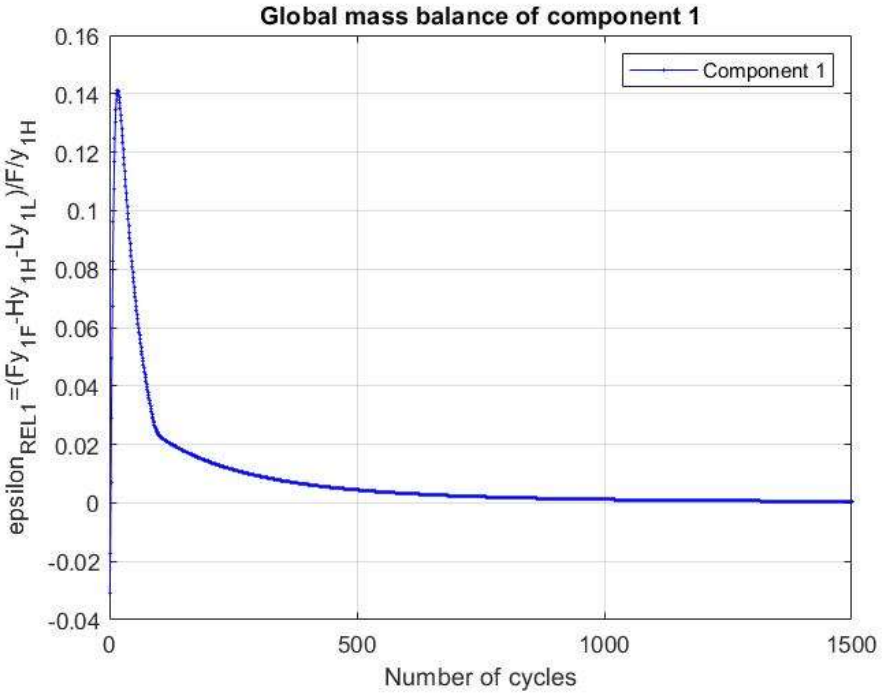

Figure 16: Heavy product mass balance error of the starting operating conditions

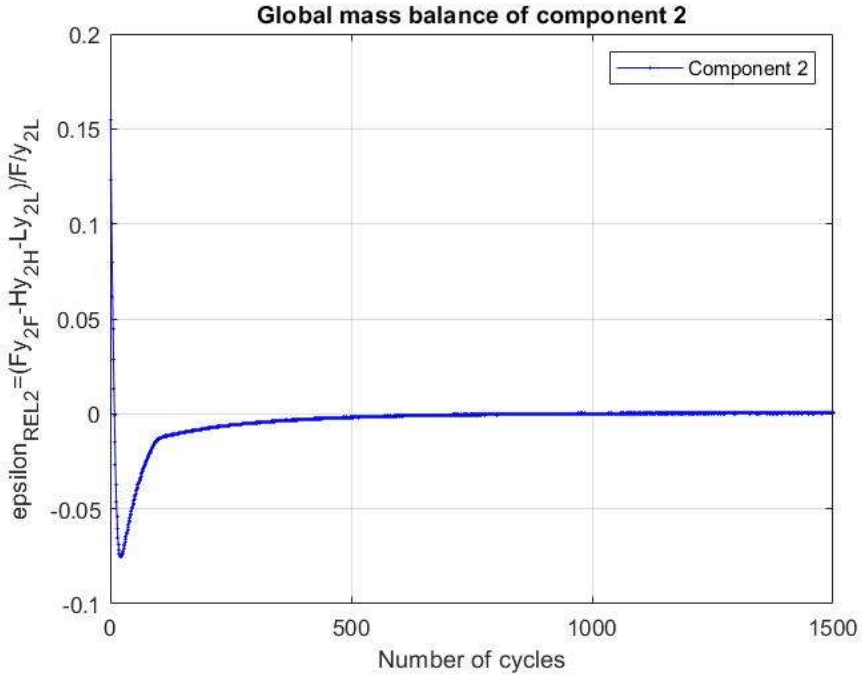

Figure 17: Light product mass balance error of the starting operating conditions

In Figure 18 the concentration profiles of the heavy component inside the column at the beginning and at the end of all the four steps of the process cycle are shown.

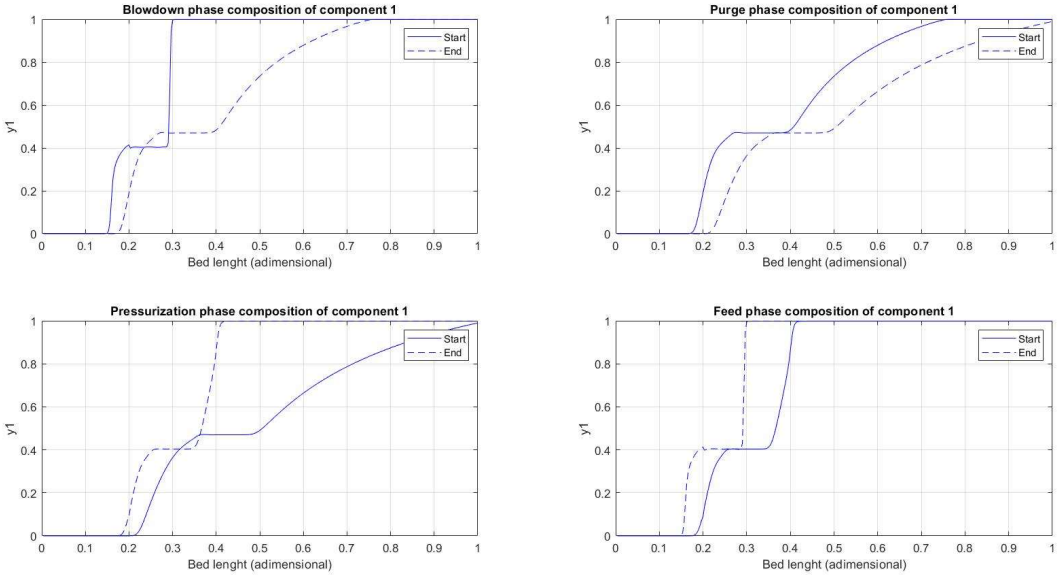

Figure 18: FVM start to end of the starting point

We can see that very sharp profiles are developed, leading to the huge computational time required to reach CSS.

3. Preliminary studies: Optimization of purity and recovery of the light component

The optimization work started with purity and recovery of the light component as objective functions with one or more parameters left free to vary. The starting operating conditions previously discussed was used as base case for the analysis, therefore its input data are the same of the first optimization, except for the variables used in the optimization process.

It was chosen to work with a Multi-Objective Optimization to set the job in a general way, to ensure validity even in the case of multiple functions to be optimized simultaneously, for which MOO is usually used. In this case, since the Q_{HP} flowrate has been fixed, we are in the situation of optimizing only one variable because the purity and recovery values are identical.

3.1. t_{Feed} variable, z_{Feed} imposed

Starting from the initial operating conditions found, for which the high accuracy simulation showed complete separation, a preliminary analysis was carried out in a wide range of z_{Feed} and t_{Feed} to investigate the performance in terms of purity and recovery of the light component when changing these parameters.

As explained earlier in Chapter 2, the aim of the optimization code is to maximize the value of the objective functions by varying one or more parameters in a physically consistent and feasible range of values. In this case, the two objective functions are set as Purity and Recovery of the light component, while the manipulated variable is t_{Feed}; z_{Feed} was set for each optimization and varied manually.

The choice of varying t_{Feed}, through the optimizer, and z_{Feed}, manually, was taken as these are the representative parameters of the TOZ obtained through the Equilibrium Theory, which is obtained in the case of linear adsorption isotherms, while our system is characterized by weakly non-linear isotherms, as described at the beginning of this chapter.

For this reason, together with the study of the performance, it was of interest to be able to compare the behavior of the process by abandoning linear conditions.

The optimization process was carried out using 50 computational points and 90 cycles for each operating conditions identified. As previously mentioned, this was necessary in order to reduce the required computation time to affordable values.

The range for the variation of t_{Feed}, with respect to the original value of 214 s, was set as:

- lower limit: t_{Feed} = 100 s
- upper limit: t_{Feed} = 1000 s

Instead for z_{Feed}, starting from the value of the initial point equal to 0.8, a delta equal to 0.1 was used, plus two further cases at 0.85 and 0.825, in a range between 0.9 and 0.1.

The points with purity and recovery of the light component greater than 99% were sought.

It is worth noting that the π parameter is fixed equal to 2.67 and the value of the heavy product flowrate is set equal to the stoichiometric one, so that purity and recovery are equal and results on the diagonal of their graph, as shown in the example at z_{Feed} = 0.6 (Figure 19) and z_{Feed} = 0.3 (Figure 20).

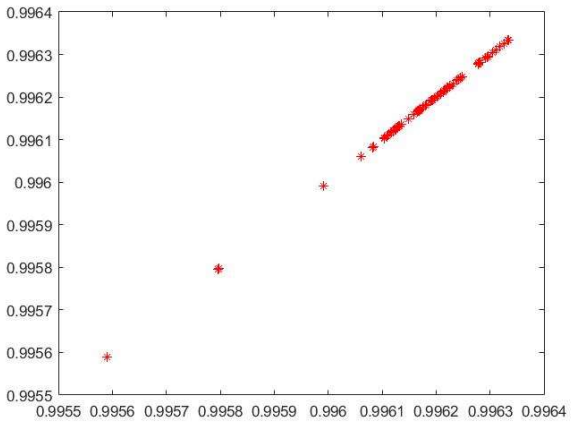

Figure 19: Purity vs. Recovery for the optimization with zFeed = 0.6

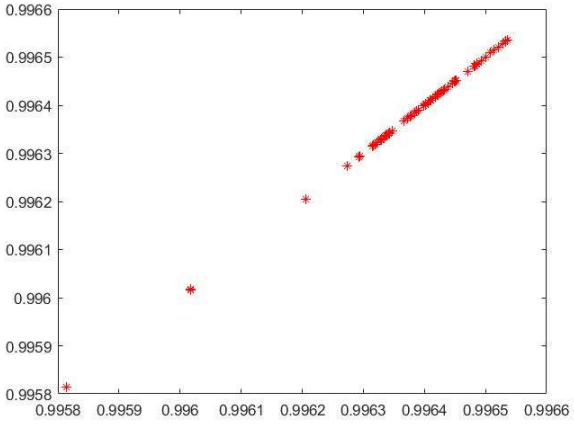

Figure 20: Purity vs. Recovery for the optimization with zFeed = 0.3

Figure from 21 to 24 show the points obtained by optimization at different z_{Feed} values on the Recovery vs. t_{Feed}. The results are grouped together in a rather small range of t_{Feed} values as high recovery values are immediately detected by the optimizer starting from the lower limit 100 s.

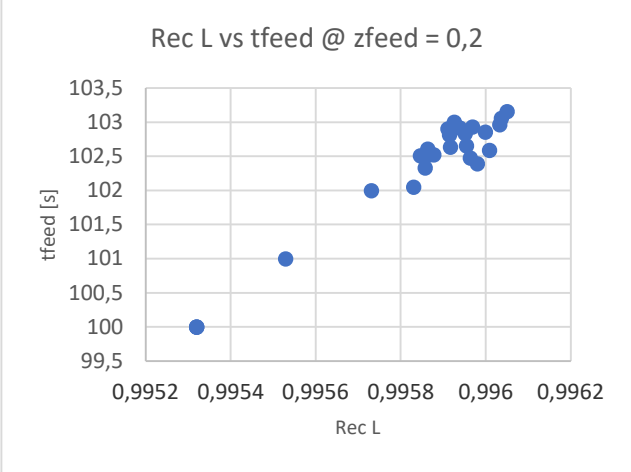

Figure 21: Results for the optimization with zfeed = 0.2

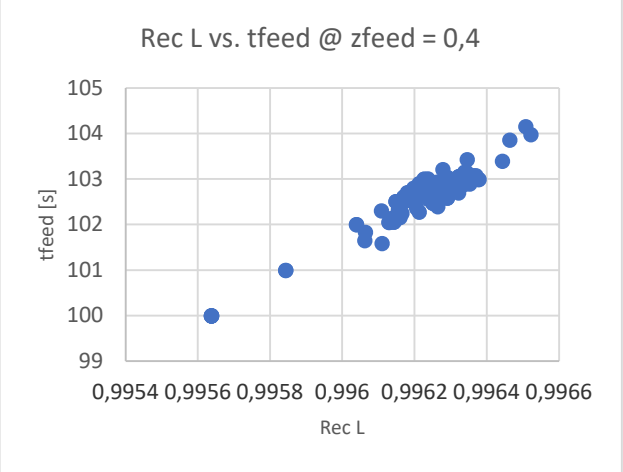

Figure 22: Results for the optimization with zfeed = 0.4

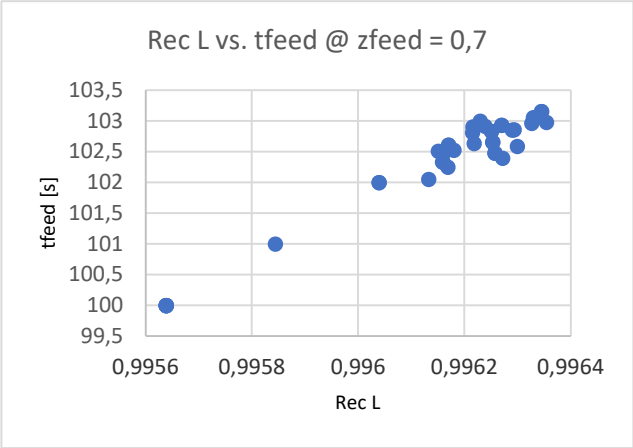

Figure 23: Results for the optimization with zfeed = 0.7

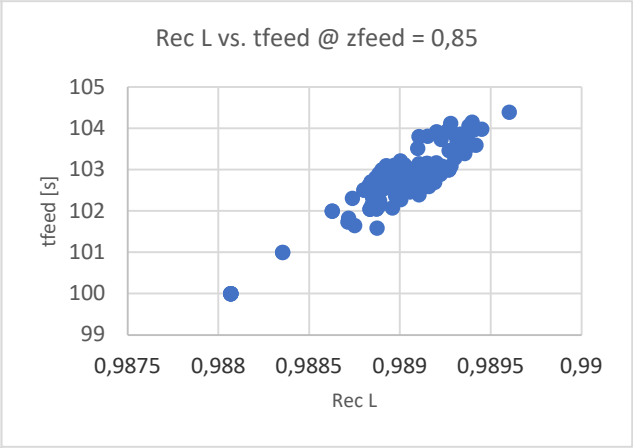

Figure 24: Results for the optimization with zfeed = 0.85

The Figure 25 and Figure 26 show the results of Purity/Recovery of the light component with respect to z_{Feed} and t_{Feed}.

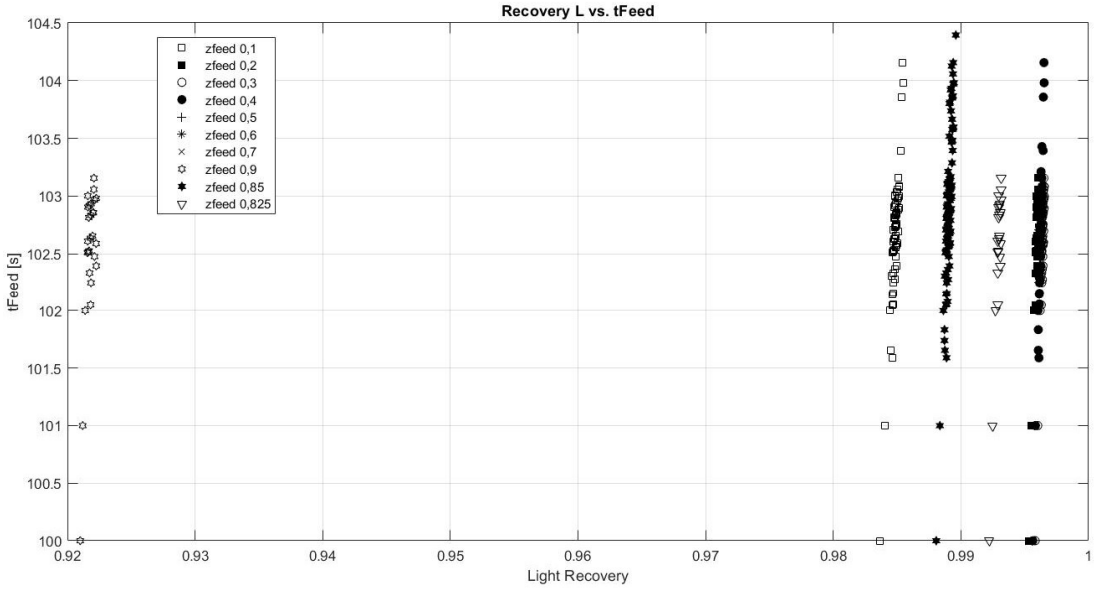

Figure 25: Results of the optimization of the light component purity and recovery at variable tFeed and zFeed on the Recovery of the light product vs. tFeed plane

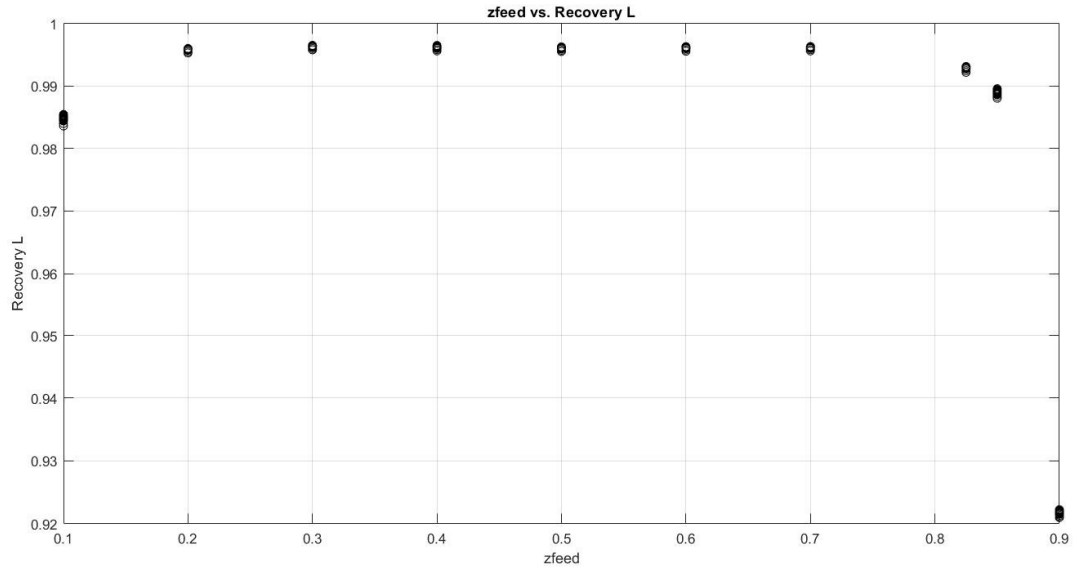

Figure 26: Results of the optimization of the light component purity and recovery at variable tFeed and zFeed on the light product recovery vs. zFeed plane

The results of the check simulation performed with greater accuracy on some of the points are reported in Table 5.

Table 26: Check simulations results for the optimization of the light product purity and recovery with different number of computational points

	$Purity_{HP,A}$	$Purity_{LP,B}$	$\varepsilon_{rel,A}$	$\varepsilon_{rel,B}$
zfeed = 0,6 @ 150 punti tfeed = 102,93	99,34	100	$4*10^{-3}$	$3*10^{-3}$
zfeed = 0,6 @ 300 punti tfeed = 102,93	97,63	100	$2,4*10^{-2}$	$7,6*10^{-3}$
zfeed = 0,825 @ 300 punti tfeed = 103,15	98,9	100	$1,1*10^{-2}$	$8,2*10^{-4}$

It can be easily seen that the purity of the heavy component is below 99%, but with the tendency to increase approaching the starting point at z_{Feed} = 0.8. However, the results are stable to the grid changes, as shown by the simulations carried out for the case at z_{Feed} = 0,6 with 150 and 300 computational points, which profiles are shown in Figure from 27 to 34.

For the case at z_{Feed} = 0,6 with 150 computational points:

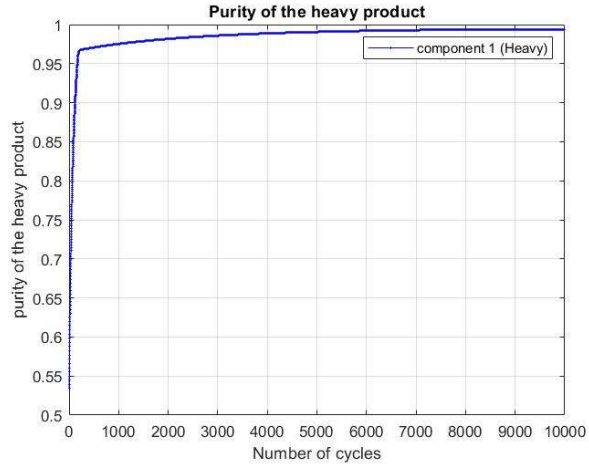

Figure 27: Heavy product purity for the check simulation with 150 points of the case at zFeed = 0.6

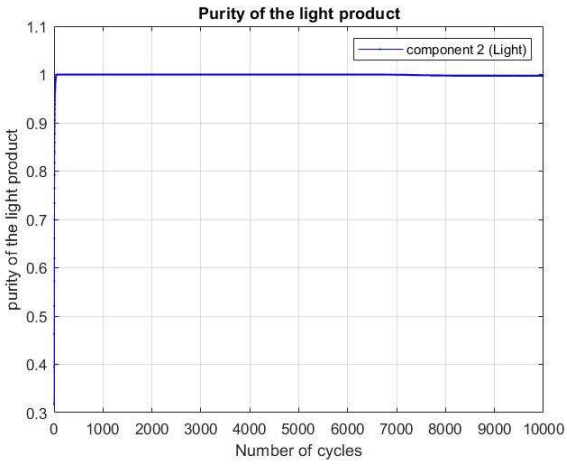

Figure 28: Light product purity for the check simulation with 150 points of the case at zFeed = 0.6

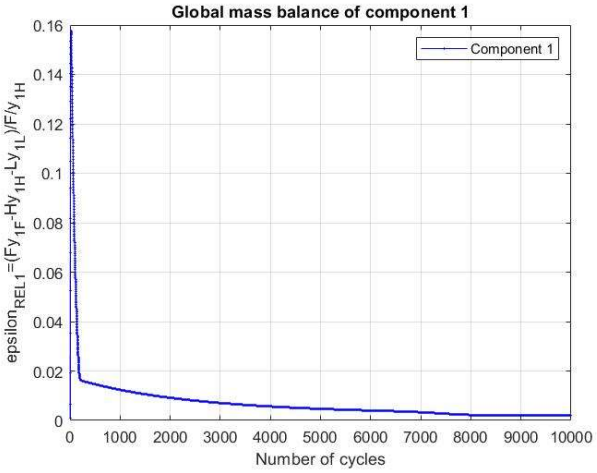

Figure 29: Mass Balance of the heavy component for the check simulation with 150 points of the case at zFeed = 0.6

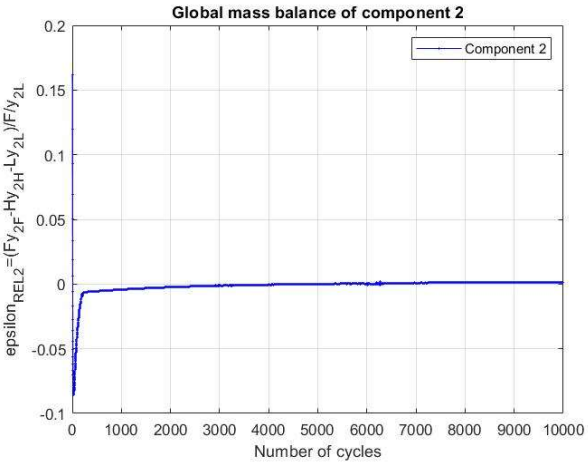

Figure 30: Mass Balance of the light component for the check simulation with 150 points of the case at zFeed = 0.6

For the case at z_{Feed} = 0,6 with 300 computational points:

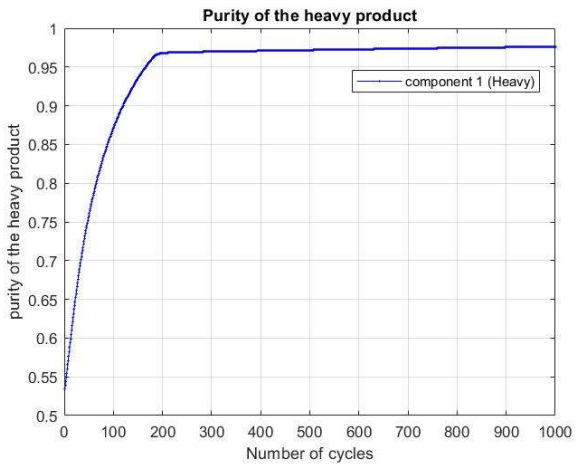

Figure 31: Heavy product purity for the check simulation with 300 points for the case at zFeed = 0.6

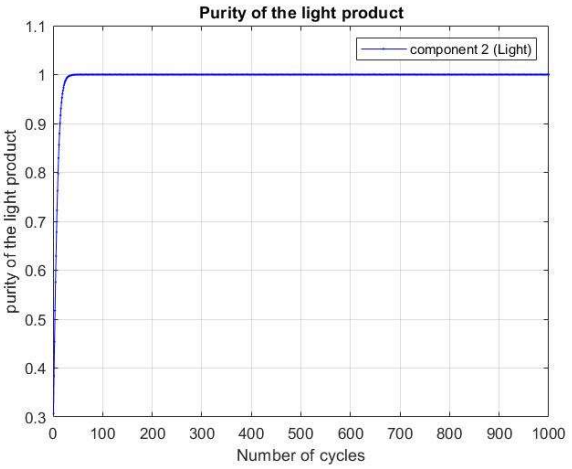

Figure 32: Light product purity for the check simulation with 300 points for the case at zFeed = 0.6

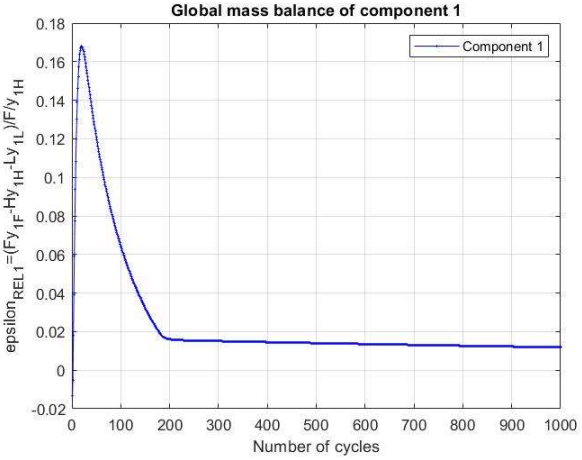

Figure 33: Mass Balance of the heavy component for the check simulation with 300 points of the case at zFeed = 0.6

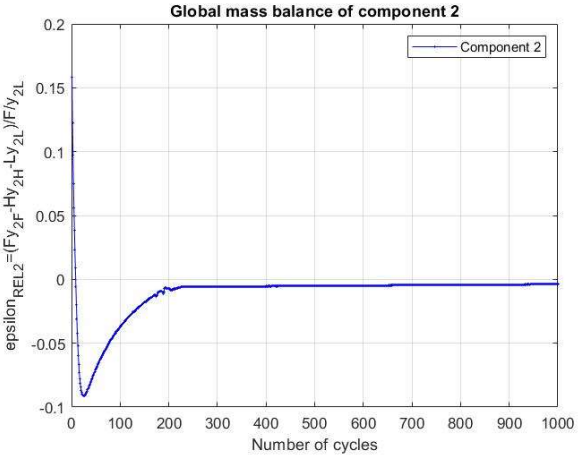

Figure 34: Mass Balance of the light component for the check simulation with 300 points of the case at zFeed = 0.6

It is possible to obtain very high Purity and Recovery of the light component in a wide range of z_{Feed} and for a specific t_{Feed} interval, going towards the ends of the column, purity drops. Moreover, the starting point shows very good performances, since the purity of its high accuracy simulation reached greater values.

The results of the check simulation, both numerically and graphically, show that 1000 cycles are not enough to reach CSS conditions. There is still a deviation between heavy and light product purities that will meet at an intermediate value between 100% and 97%, demonstrated by the fact that purity profiles are still rising in Figures 27 and 31, while errors are decreasing. However, this does not compromise the credibility of the results obtained.

3.2. t_{Feed} and Q_L variable

Following the results obtained from the optimization at variable t_{Feed} and different values of z_{Feed}, it was decided to add Q_L as a manipulated variable in the optimization code, and, instead, keep z_{Feed} fixed at 0.8 due to the excellent separation results shown during the simulation of the starting point.

The reasons why Q_L was chosen, among all the previously identified key parameters, are:

1. Economic considerations:

   The *Bed capacity ratio* C, directly dependent on t_{Feed} which is its only variable parameter, represents the fixed costs of the plant since it is a clue of the size of the column. The *Light recycle ratio* G, directly dependent on Q_L, which is the only variable parameter in the equation, represents the part related to the operating costs through the compressor work.

   Moreover, in the case under study, t_{Feed} is the only variable parameter in the productivity expression, while Q_L strongly affects the energy requirement of the process.

2. Comparison with Equilibrium Theory:

   It was previously described, at the beginning of this chapter, that the TOZ, resulting from the Equilibrium Theory, is characterized by a single constant value of G.

From an economic point of view, it was of interest to study the trade-off between operating and plant costs and between productivity and work required by the separation process, therefore QL was chosen as an additional manipulated variable.

It was possible to study the behavior of the objective functions purity and recovery of the light component as G varies, in order to verify if there was a single value to characterize a region with complete separation as in the linear case of the Equilibrium Theory, or if moving away from linearity, a range of *Light recycle ratio* values would be found, for which it was possible to obtain sharp separation.

The optimization process was carried out using 50 computational points and 90 cycles for each point identified, the objective functions purity and recovery of the light component are the same as the previous case. The upper and lower limits for the two manipulated variables are reported in Table 6.

Table 27: tFeed and QL boundaries for the optimization of the light product purity and recovery

	min	max
t_{Feed} [s]	100	600
Q_L [mol/s]	$0.8*Q_{Feed} = 1.42*10^{-4}$	$8*Q_{Feed} = 14{,}16*10^{-4}$

As in the previous optimization, the points with purity and recovery of the light component greater than 99% were sought.

The system is still characterized by a value of the parameter π fixed and equal to 2.67. The value of the heavy product flowrate is set equal to the stoichiometric one, so that purity and recovery are equal and results on the diagonal of their graph.

All the points obtained by means of the two parameters optimization are reported in Figure 35, Figure 36 and Figure 37 where the graphs of light component recovery versus t_{Feed} and Q_L and t_{Feed} versus Q_L show the trend of the results.

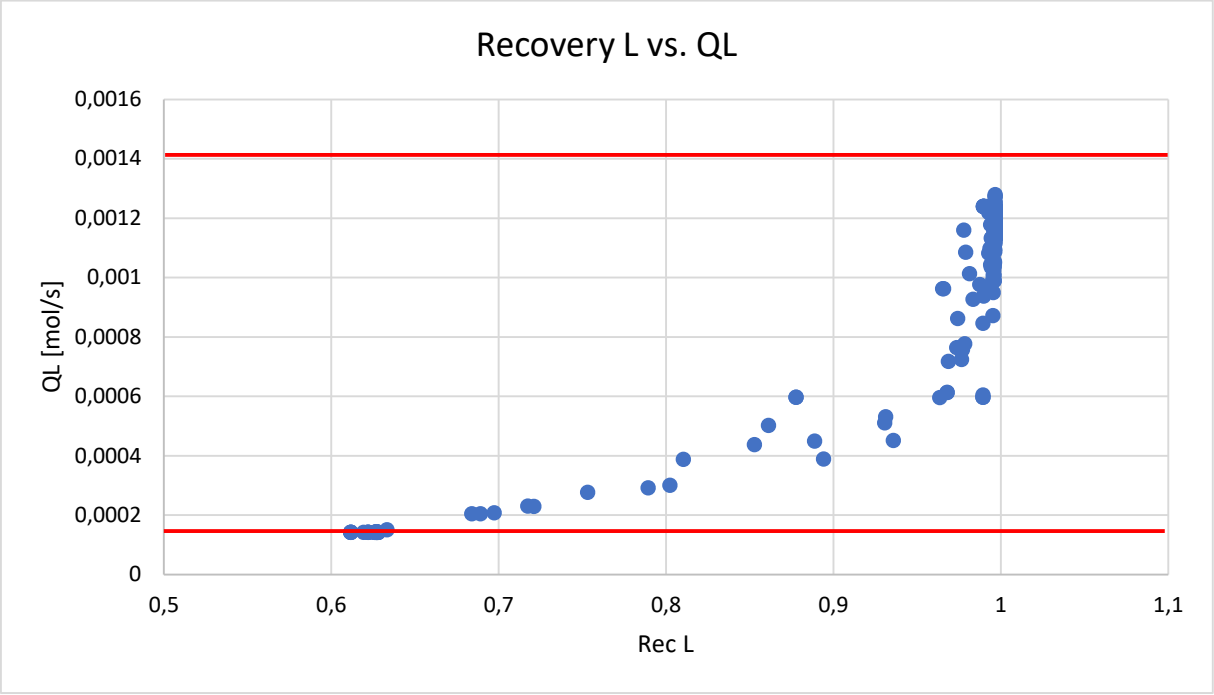

Figure 35: Results of the light product purity and recovery optimization at variable QL and tFeed on the light product Recovery vs. QL plane

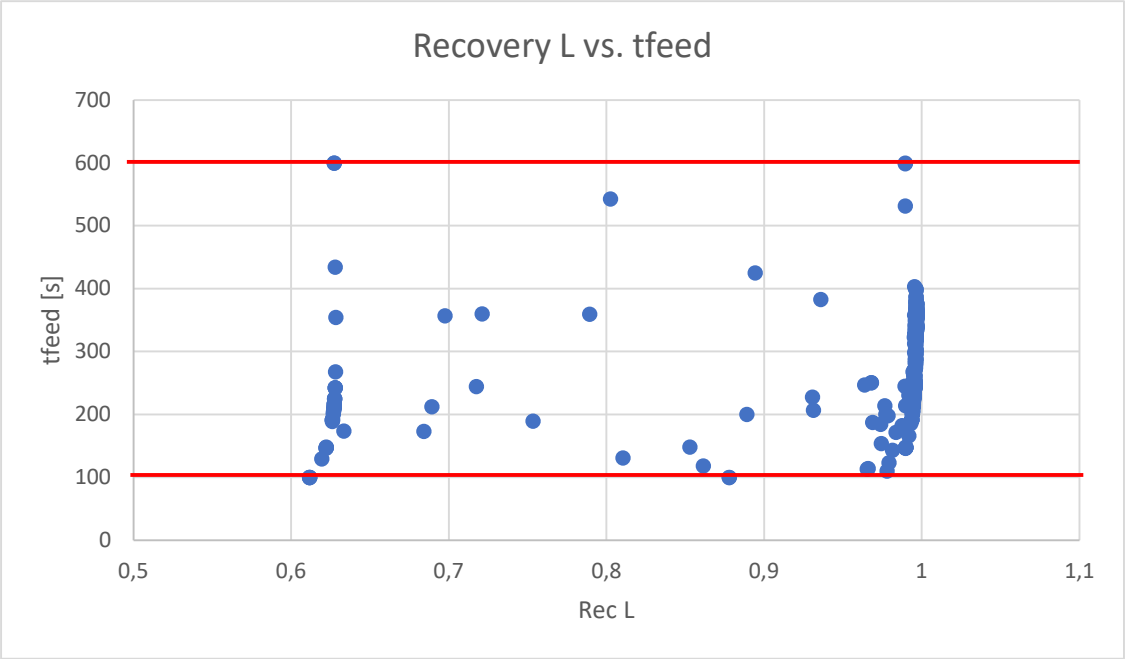

Figure 36: Results of the light product purity and recovery optimization at variable QL and tFeed on the light product Recovery vs. tFeed plane

The lines represent the boundaries of the domains.

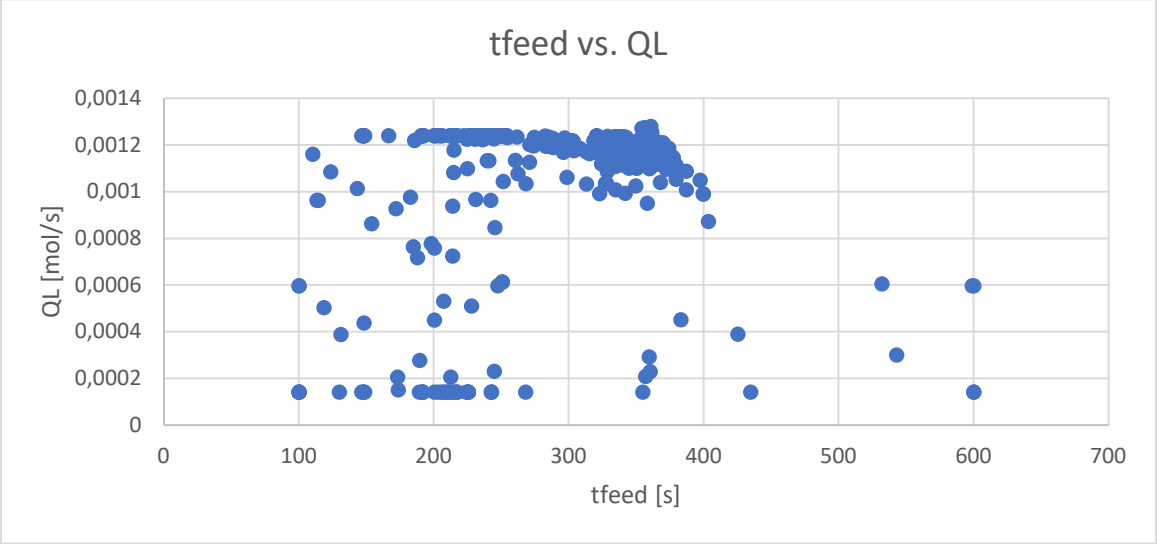

Figure 37: Results of the light product purity and recovery optimization at variable QL and tFeed on the tFeed vs. QL plane

Of greatest interest is the graph in Figure 38, which shows the results, in terms of duration of the feed phase with respect to the flowrate of the light compound recycled, obtained with purity and recovery of the light component greater than 99%.

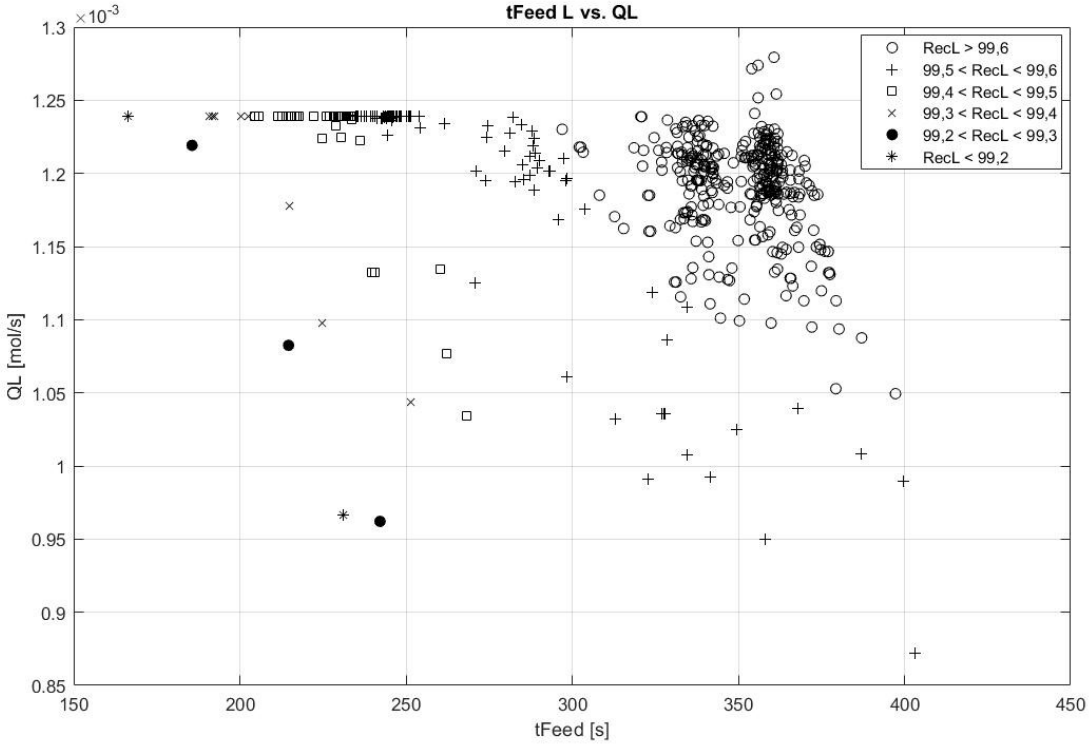

Figure 38: Results > 99% of the light product purity and recovery optimization at variable QL and tFeed on tFeed vs. QL plane

For a wide range of t_{Feed} and Q_L a high value of the light component recovery can be obtained, which it can be noticed that increases with both manipulated variables.

Two check simulation for a sample case at high purity were performed with 50 and 300 computational points at:

- t_{Feed} = 377 s
- Q_L = 12,39*10^{-4} mol/s

For which the optimization had obtained a purity value of the light component equal to 99.64%.

Figure 39 and 40 show the trend of the light product purity, which after 63 and 107 cycles reaches 100% and stationary conditions, while for the heavy product we obtain:

- purity heavy product @ 300 points = 94,24
- purity heavy product @ 50 points = 91,59

represented in Figure 41 and 42.

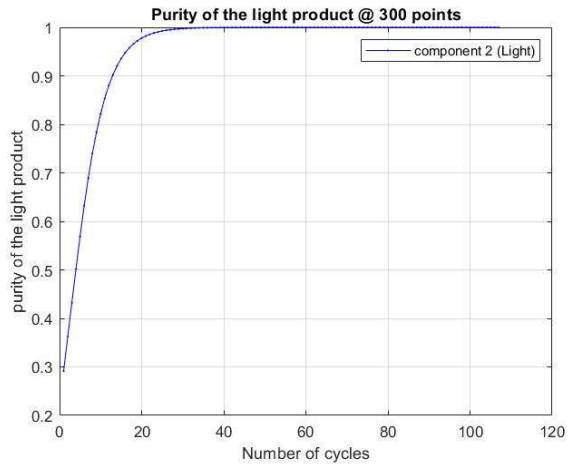

Figure 39: Purity of the light product from the check simulation with 300 points

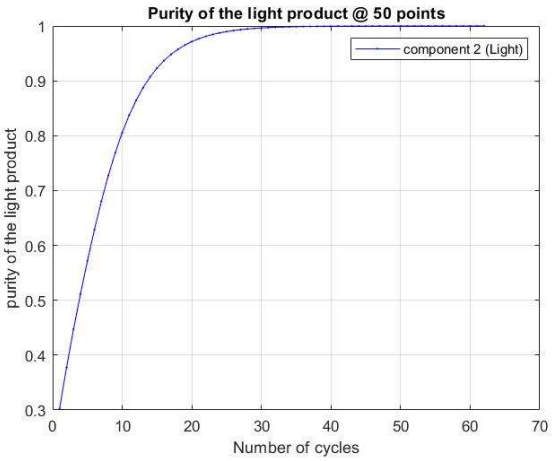

Figure 40: Puirty of the light component from the check simulation with 50 points

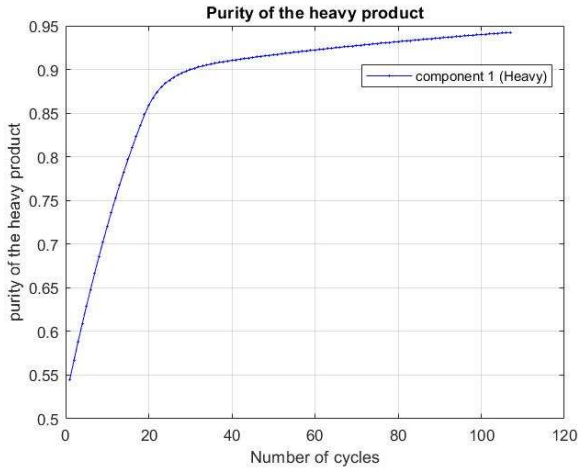

Figure 41: Purity of the heavy product from the check simulation with 300 points

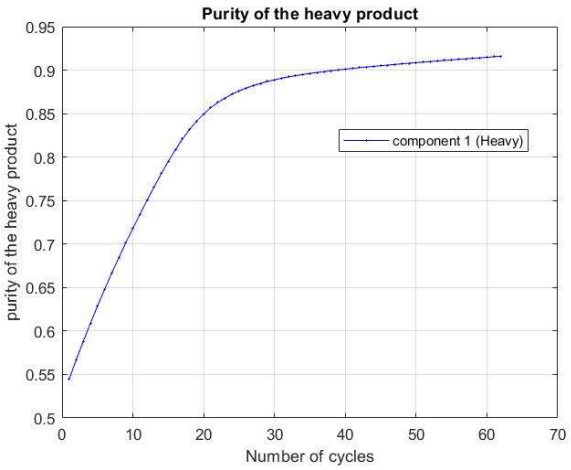

Figure 42: Purity of the heavy product from the check simulation with 50 points

It can be seen that after about 90 cycles, those set for optimization, the purity of the heavy compound is still growing, this is also underlined by Figure 43 and 44 that represent the heavy compound relative error on the material balance, which after few cycles is still quite large:

- relative error on heavy product BM = 2,9% @ 300 points
- relative error on heavy product BM = 4,2% @ 50 points

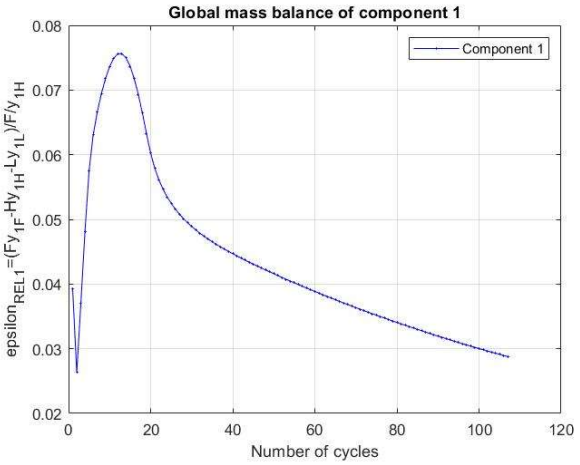

Figure 43: Relative error on the heavy product BM for the check simulation with 300 computational points

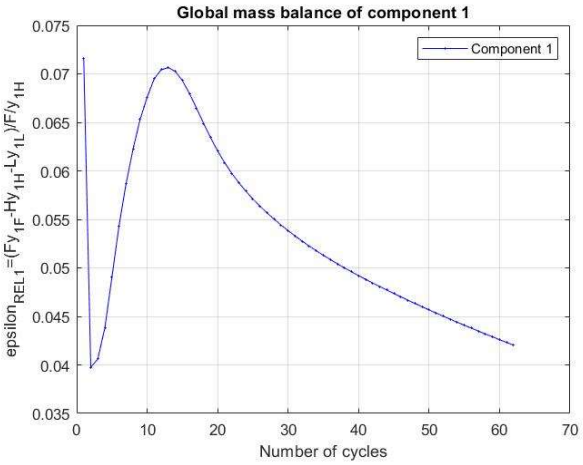

Figure 44: Relative error on the heavy product BM for the check simulation with 50 computational points

What had been noted for the previous case in Figures 27 to 34 was confirmed by the present optimization and important conclusions can be drawn. The trends are consistent, but as shown in Figure 41 and by the relative error values on the BM of the heavy product, the results obtained do not reach CSS conditions after 90 cycles. Therefore, it is impossible to obtain precise results with such a low number of cycles, but on the other hand using a very high number of cycles would increase the computational time up to a duration that would make the optimization process unfeasible.

For this reasons, 3 strategies have been implemented in the optimizer:

1. Objective functions

In the configuration we are investigating, the light product purity profile reaches quickly the 100% and settles at this value. After a variable number of cycles, the breakthrough of the profile occurs, so that a step is formed in which the purity of the light compound approaches that of the heavy compound, to which it is linked by the material balance on species.

The profile of the heavy component, on the other hand, shows greater reliability as it is characterized by a monotonic trend. Therefore, the objective functions to be optimized were modified involving purity and recovery of the heavy product.

2. Material balance criterion

It has been noticed that 90 cycles, previously imposed for each simulation of the optimizer, are not sufficient to reach the CSS conditions. Since reaching CSS requires a number of cycles that can vary over an extremely wide range, increasing the number of cycles is not a suitable option. Instead, it was chosen to impose a criterion on the relative error on the material

balance of the heavy component (Equation 2.9) to stop the simulations, in order to guarantee the achievement of CSS conditions.

Following a trial and error procedure, the value chosen was 10^{-2}, considered the limit value for the reliability of the results, since an excessively small value would have led to a very high numbers of cycles, a considerable lengthening of the calculation times and in some cases the failure of the optimization.

To prevent excessively expensive simulations of the points, a limit number of cycles was also imposed, after which the simulation was eliminated to proceed with the next one. The value that has been chosen is 700 cycles.

3. Criterion on the Initial Conditions (IC)

In the previous optimizations, the initial conditions were first set and then used for each simulation performed. Following the criterion on the BM, since the number of cycles is no longer fixed at 90, the simulations can considerably increase their duration. Therefore, to decrease computational times by accelerating convergence, the initial conditions for a given simulation "N", carried out by the optimizer, are set equal to the profile obtained at a fixed cycle of the simulation "N – 1". The number of the cycle at which the profile of the column is saved to be uploaded as ICs for the next simulation must be such that it is:

- not too small → because it would be still influenced by the previous ICs
- not too high → when the optimization reaches the stationary, the number of cycles per simulation decreases, therefore it would not be reached

3.3. Tuning of the strategies implemented

Following the changes described in the previous paragraph implemented in the optimization code, it was necessary to carry out some test to fine-tune the procedure.

An important step was the choice of the value imposed on the error of the material balance of the heavy product, smaller values allow to approach closely the CSS, but they would require much longer computational time. Some attempts have been made up to the final value 10^{-2} which represents a percentage error equal to 1%, which represents a reasonable compromise between accuracy and computational time.

After having identified the right error value on the BM it was possible to carry out the first optimizations.

As in the case of the optimizations of purity and recovery of the light component, 50 computational points were used and initially the same values of the t_{Feed} and Q_L limits (Table 8) were maintained, to be modified later if they would proved inadequate.

Table 28: tFeed and QL boundaries for the heavy product purity and recovery tuning optimization

	min	max
t_feed [s]	100	600
Q_L [mol/s]	0.8*Q_feed = 0.000142	8*Q_feed = 0.001416

With the first optimizations we also wanted to study how the calculation times varied with different values of the criterion for updating the initial conditions described in the previous paragraph. For this purpose, in the first two optimizations carried out, the same input data have been entered, but the criterion on CI was imposed at 10 and 100 cycles.

The input data are the same used in the previous simulations.

In particular, the value of $\pi = P_H/P_L$ is always equal to 2.67 and the flow rate of the heavy product extracted is set equal to the stoichiometric one, thus providing equal values of purity and recovery.

The results of the optimizations are reported from Figure 45 to 48 as the criterion on the updating of the initial conditions changes, respectively equal to 10 and 100 cycles.

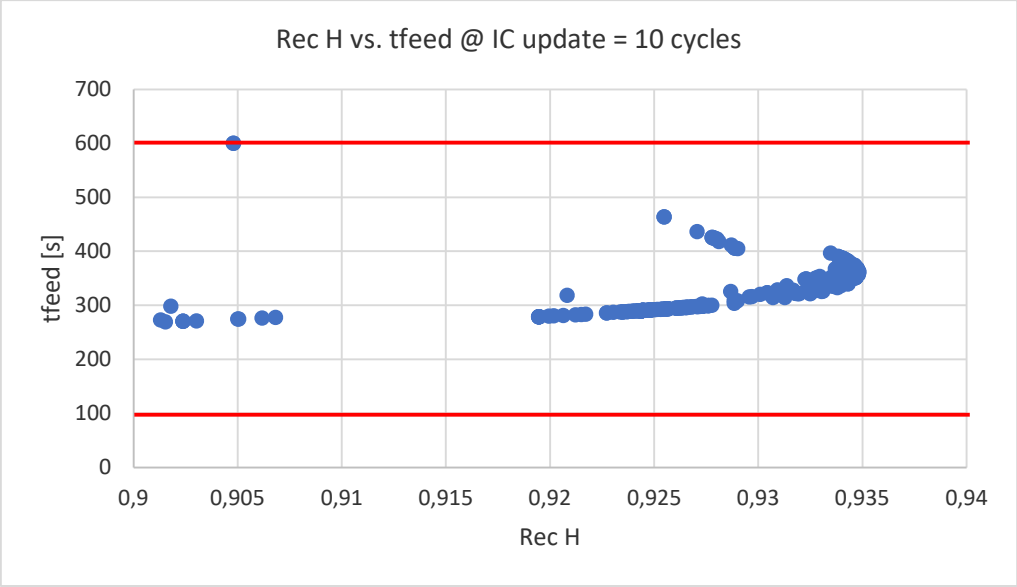

Figure 45: Results of the tuning optimization of the heavy product purity and recovery with the upload of the IC at 10 cycles on the plane Recovery vs. tFeed

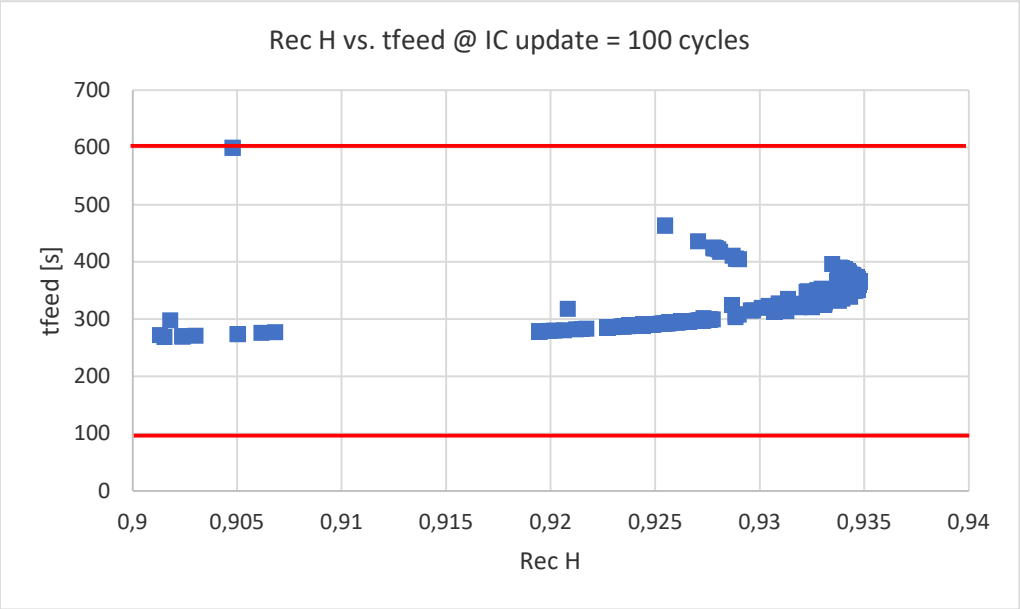

Figure 46: Results of the tuning optimization of the heavy product purity and recovery with upload of the IC at 100 cycles on the plane Recovery vs. tFeed

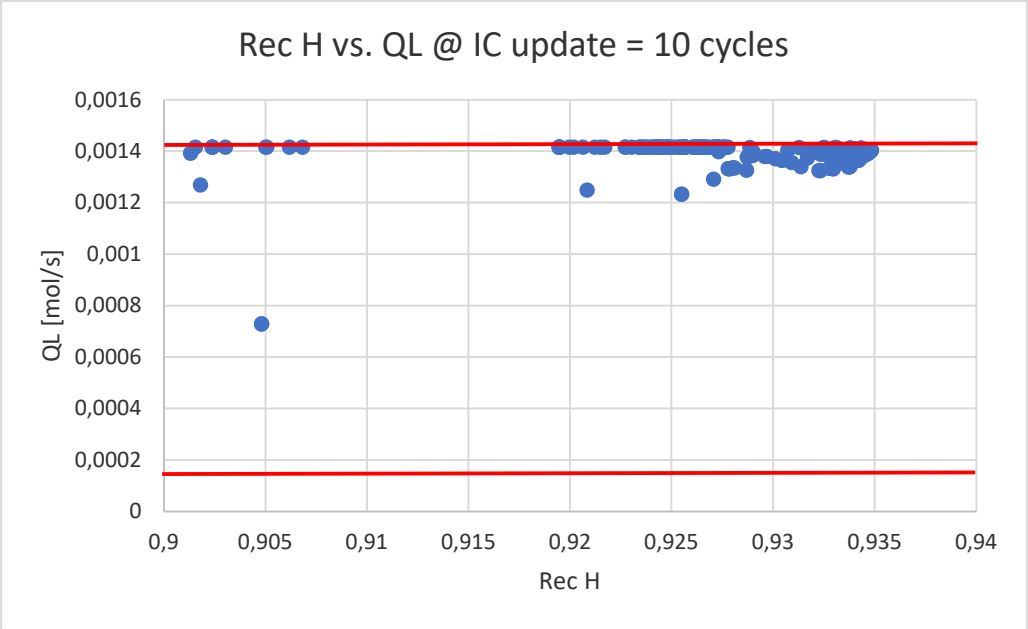

Figure 47: Results of the tuning optimization of the heavy product purity and recovery with IC upload at 10 cycles on the plane Recovery vs. QL

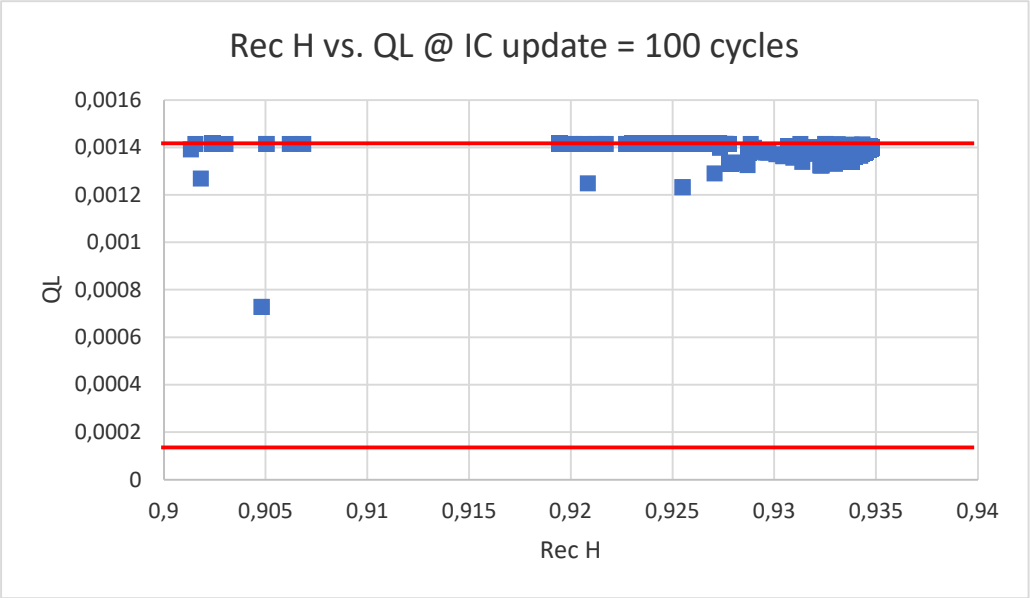

Figure 48: Results of the tuning optimization of the heavy product purity and recovery with IC upload at 100 cycles on the plane Recovery vs. QL

The lines represent the upper and lower limits of the manipulated variables.

It can be easily seen that there are no substantial differences regarding the numerical results, as also summarized in Table 10.

Table 29: Optimization results at different IC upload criterion

	IC upload @ 10 cycles	IC upload @ 100 cycles
Number of points simulated	469	364
Average number of cycles per point	29	32
Average error on the BM	0.52%	0.56%
Average duration for simulation	5.35	5.98 min
Recovery and Purity @ CSS conditions	93.5	93.5

Although the numerical results in Table 10 show that by updating the ICs to cycle 10 the program is slightly more efficient, however it should be noted that as the number of

simulated points increases, the number of cycles required and therefore the average duration for each simulation reduces to an asymptotic value much lower than the initial ones. For this reason, the results are comparable and it can be said that there are no significant differences between the two cases.

However, from Figure 47 and 48, it can be noted that the upper limit for Q_L is too low, since most of the results crushes against it. It is therefore necessary to raise it.

4. Optimization of purity and recovery of the heavy component

4.1. π = 2.67

An optimization of the objective functions purity and recovery of the heavy compound was carried out with t_{Feed} and Q_L left free to vary, like the one performed previously for the objective functions relating to the light compound (paragraph 3.2) in the case of π = 2.67.

Since in the previous paragraph it was shown that the upper limit of Q_L was too low, it was increased from $8*Q_{feed}$ to $20*Q_{feed}$, as reported in the Table 11:

Table 30: tFeed and QL boundaries for the optimization of the heavy component purity and recovery for the case at π = 2.67

	min	max
t_feed [s]	100	600
Q_L [mol/s]	0.8*Q_feed = 0.000142	20*Q_feed = 0.00354

The criterion on the upload of the ICs was set at 17 cycles because in the previous test optimizations it was the cycle around which the number of cycles per simulation settled once stationary conditions were reached.

The input data are the ones reported previously in Table 1.

It should be noted that the Q_{HP} value, flowrate of the heavy product extracted, is set equal to the stoichiometric value for which purity and recovery are equal to each other.

As in the previous cases 50 computational points have been set, as they represent a good compromise between computation time and accuracy.

In Figure 49 are reported the heavy product purity and recovery results. As usual, because of the heavy product flowrate set equal to the stoichiometric one, the points are disposed on the diagonal, instead of forming a Pareto front.

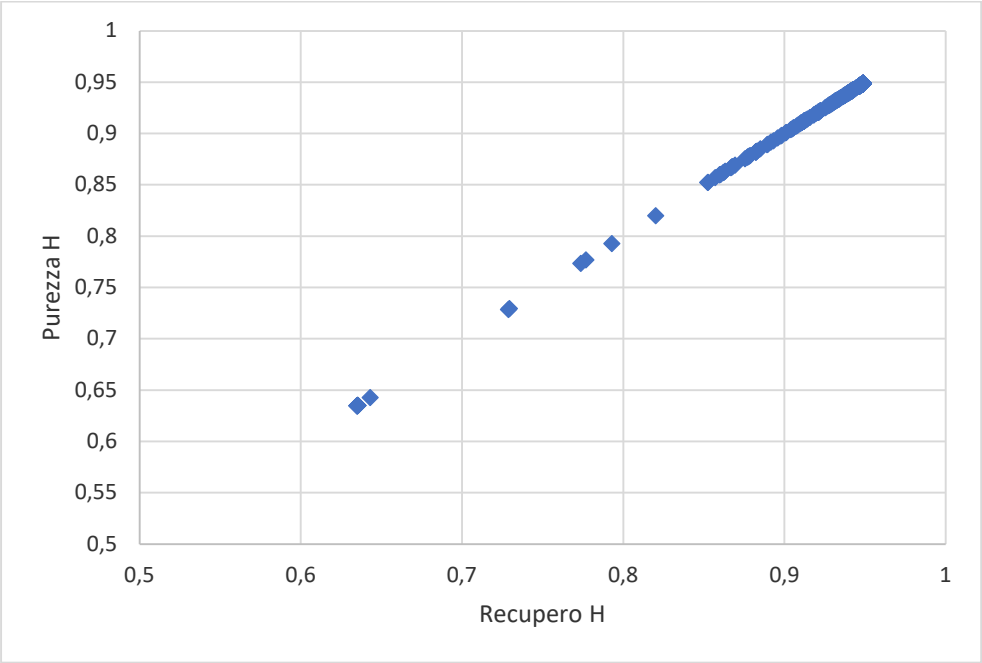

Figure 49: Results on Recovery vs. Purity plane of the heavy component optimization

The results obtained, once CSS conditions are reached, tend to settle at purity and recovery values around 95%.

In Figure 50, 51 and 52 all the results obtained by the optimizer are graphically represented, with the recovery as a function of the two manipulated variables t_{Feed} and Q_L and a graph with the duration of the feed phase versus the recycling flowrate of the light component.

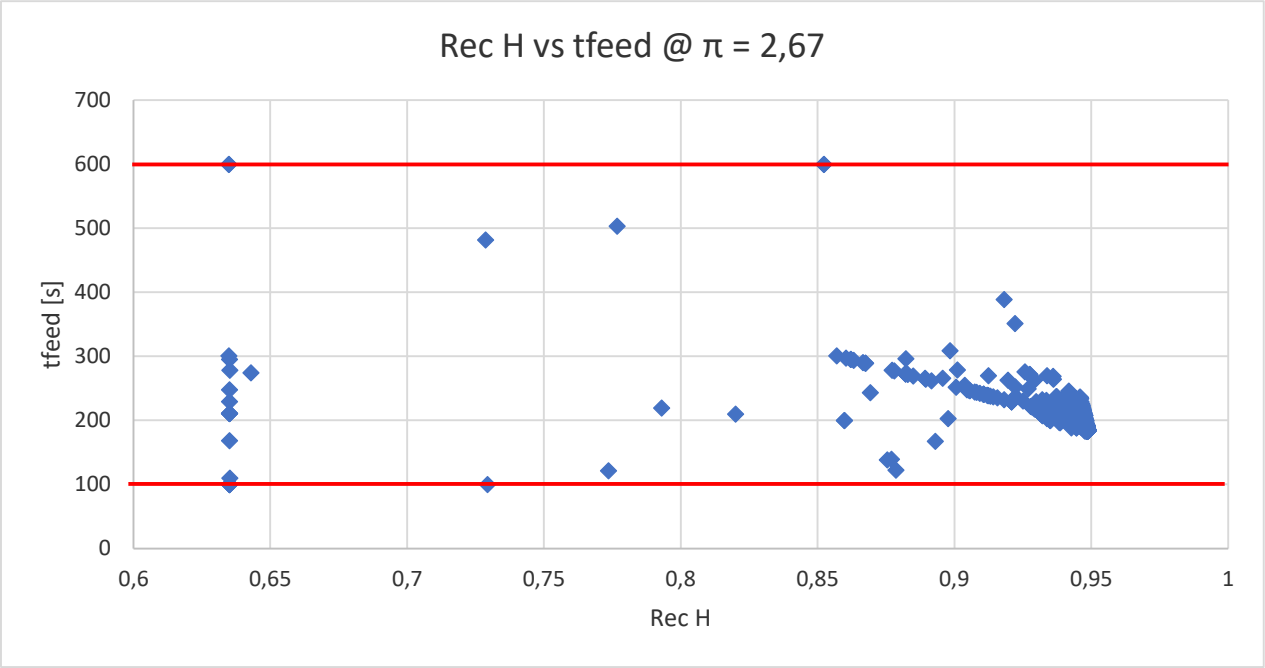

Figure 50: Results on the plane heavy product recovery vs. tFeed for the optimization at π = 2.67

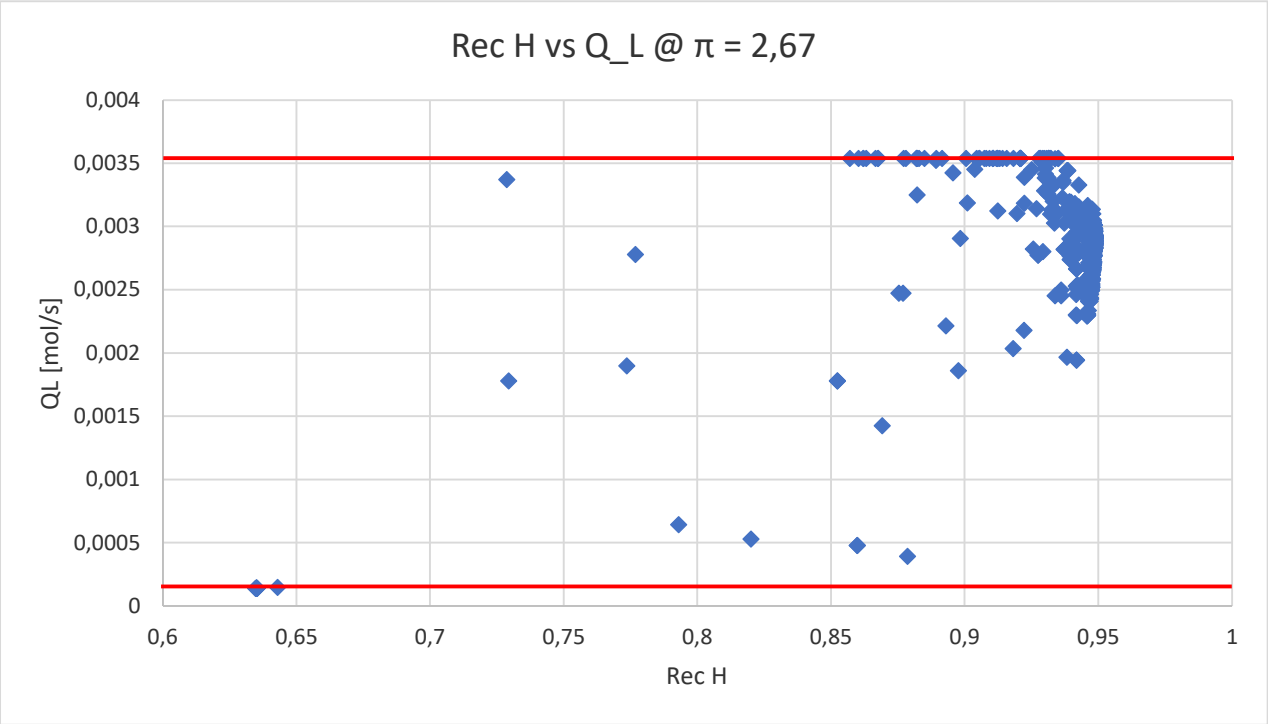

Figure 51: Results on the plane heavy product recovery vs. QL for the optimization at π = 2.67

The lines represent the boundaries of the domains.

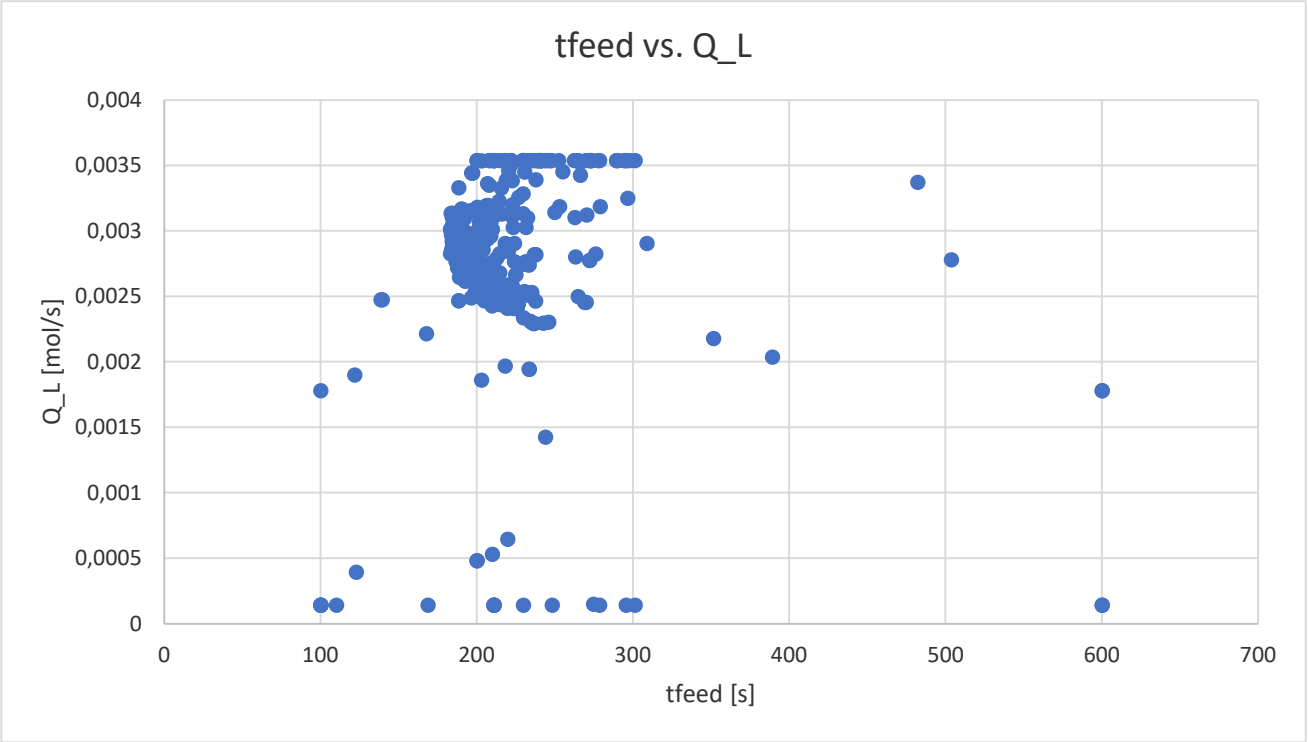

Figure 52: Results on the plane tFeed vs. QL for the optimization at π = 2.67

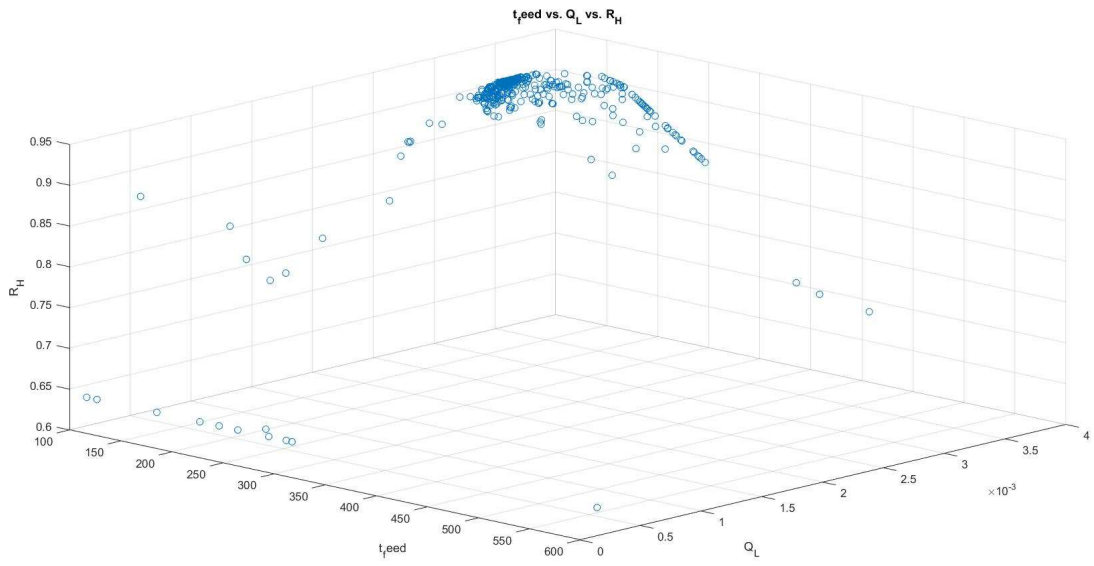

Figure 53: Results of the optimization at π = 2.67 on the 3D plane Recovery of the heavy product vs. tFeed vs. QL

In the Figure 53 the results previously shown are reported in a single 3D graph t_{Feed} vs. Q_L vs. Recovery of the heavy component.

It can be seen from Figure 51 that although some points are positioned on the upper limit, as the recovery increases, the Q_L values are in a range below it and for this reason they are

considered acceptable results. For the t_{Feed} limits, as shown in the previous paragraph, they are correct since the results are positioned within them.

Of particular interest is the graph in Figure 54 to, as it graphically reports the results obtained with purity and recovery above 94%, and the subsequent ones (Figure 55 to 58), where the recovery range between 94 and 95% has been divided into four intervals.

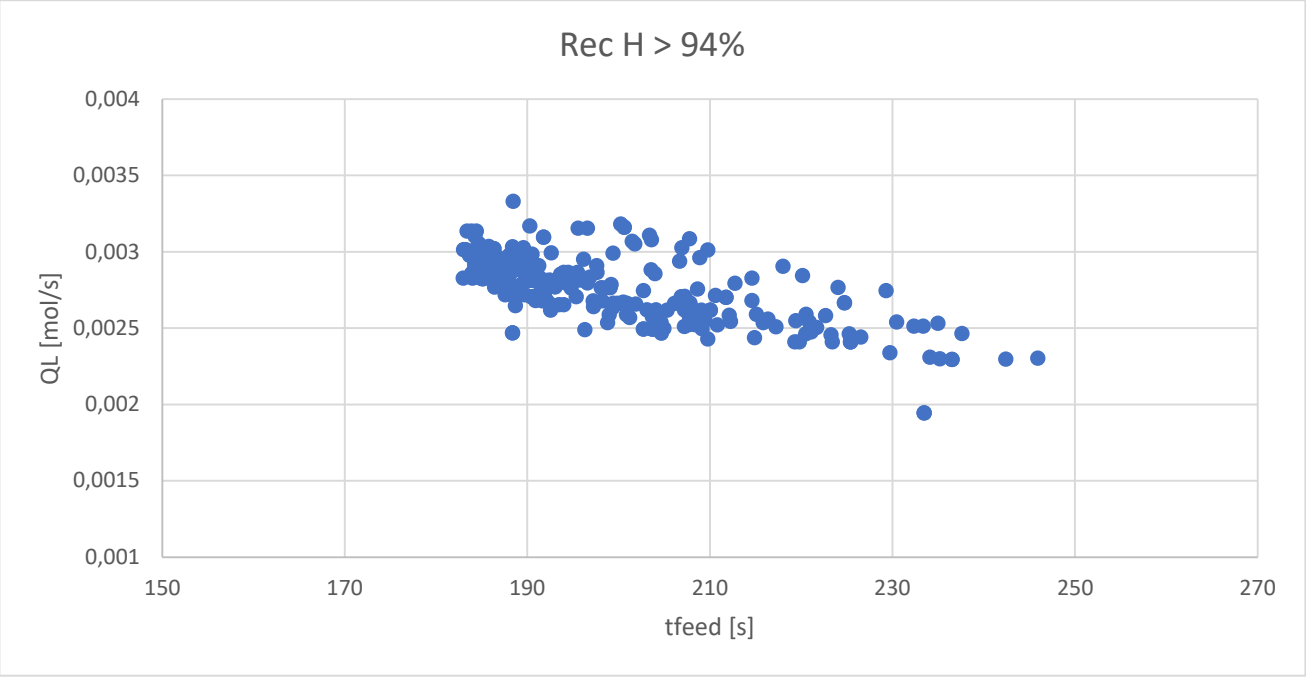

Figure 54: Results with purity > 94% of the heavy product optimization at π = 2.67

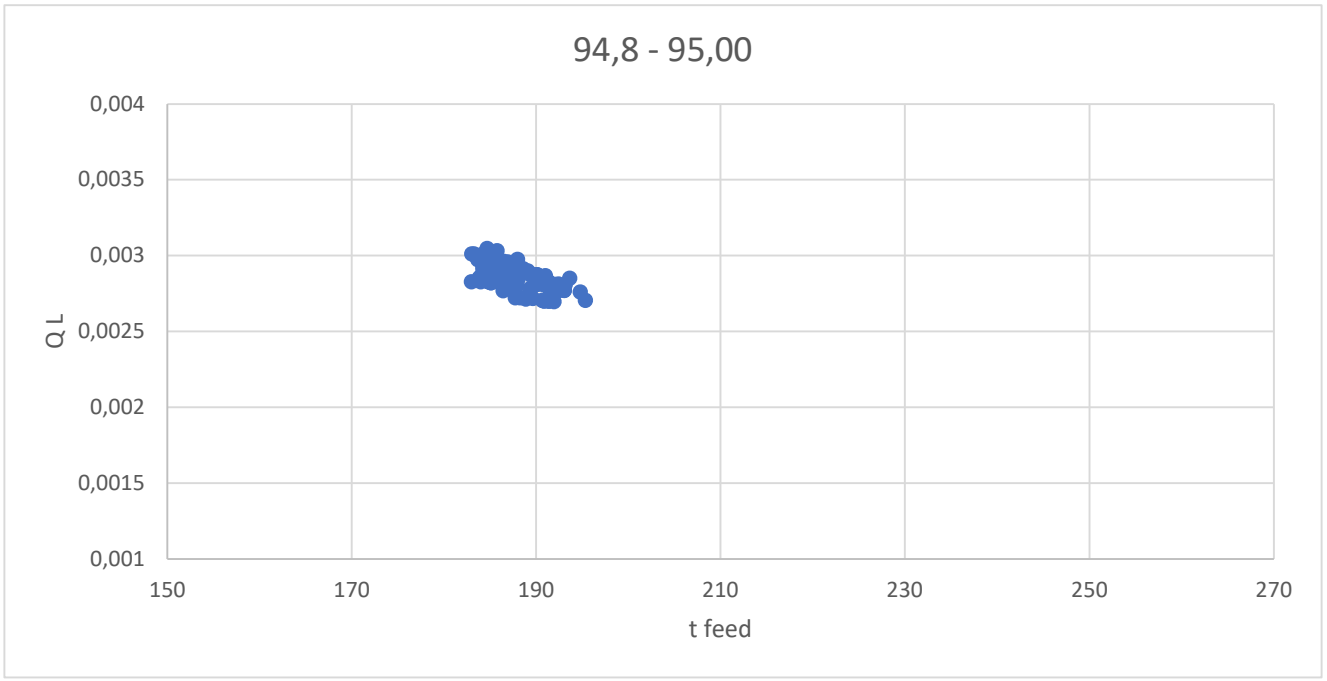

Figure 55: Results with purity between 94,8 and 95% of the heavy product optimization at π = 2.67

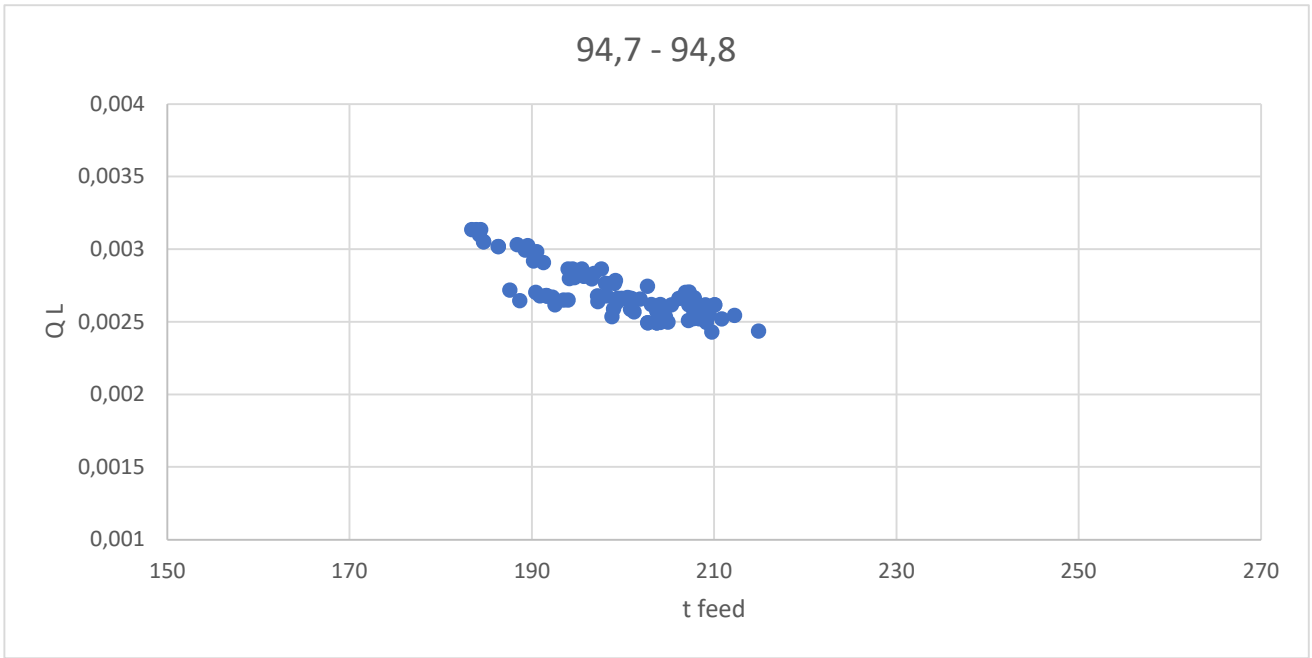

Figure 56: Results with purity between 94,7 and 94,8% of the heavy product optimization at π = 2.67

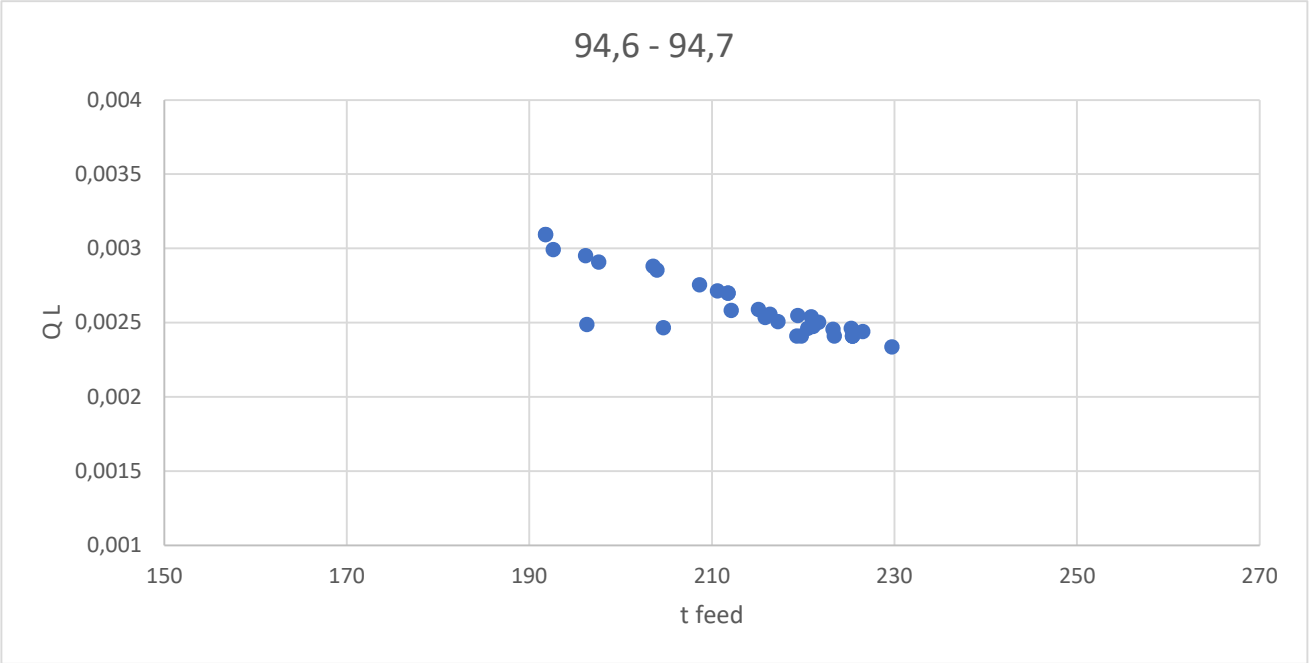

Figure 57: Results with purity between 94,6 and 94,7% of the heavy product optimization at π = 2.67

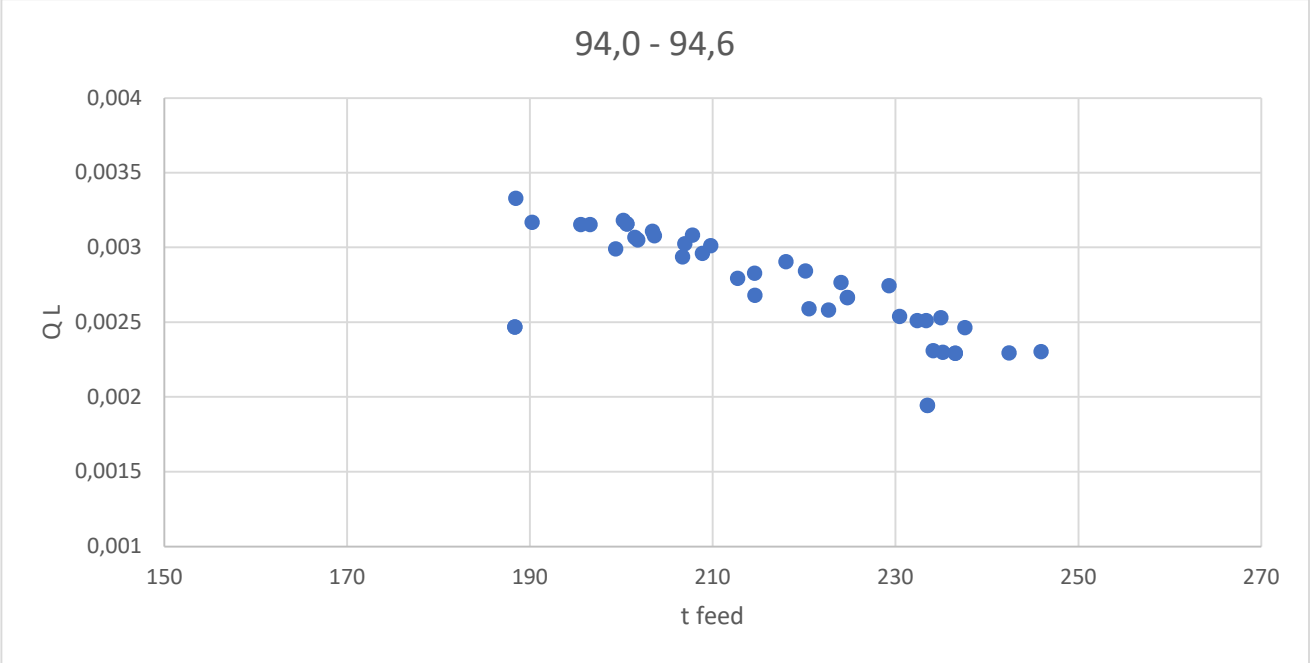

Figure 58: Results with purity between 94 and 94,6% of the heavy product optimization at π = 2.67

It can be seen that high purity and recovery values can be obtained for rather narrow ranges of t_{Feed} and Q_L.

The characteristics of the optimization are shown in Table 12, it is possible to see that increasing the upper limit of Q_L it was possible to reach higher purity and recovery values.

Table 31: Results for the heavy product purity and recovery optimization with variable tFeed and QL for the case at π = 2.67

	π = 2,67
Number of points simulated	630
Average number of cycles per point	33
Average error on the BM	0.66%
Average duration for simulation	10.04 min
Recovery and Purity @ CSS conditions	> 94.5

Despite the increase in the number of points simulated, there is a slightly higher average number of cycles per point and average error on BM respect the previous cases of the test optimizations with a lower upper limit of Q_L. On the other hand, the average duration per simulated point nearly doubled.

Some check simulations with higher accuracy were carried out on 6 of the points found with purity higher than 94%, in order to verify the results obtained with the optimization. The points were chosen in different regions of the t_{Feed} vs. Q_L plane and are highlighted with triangular indicators in Figure 59.

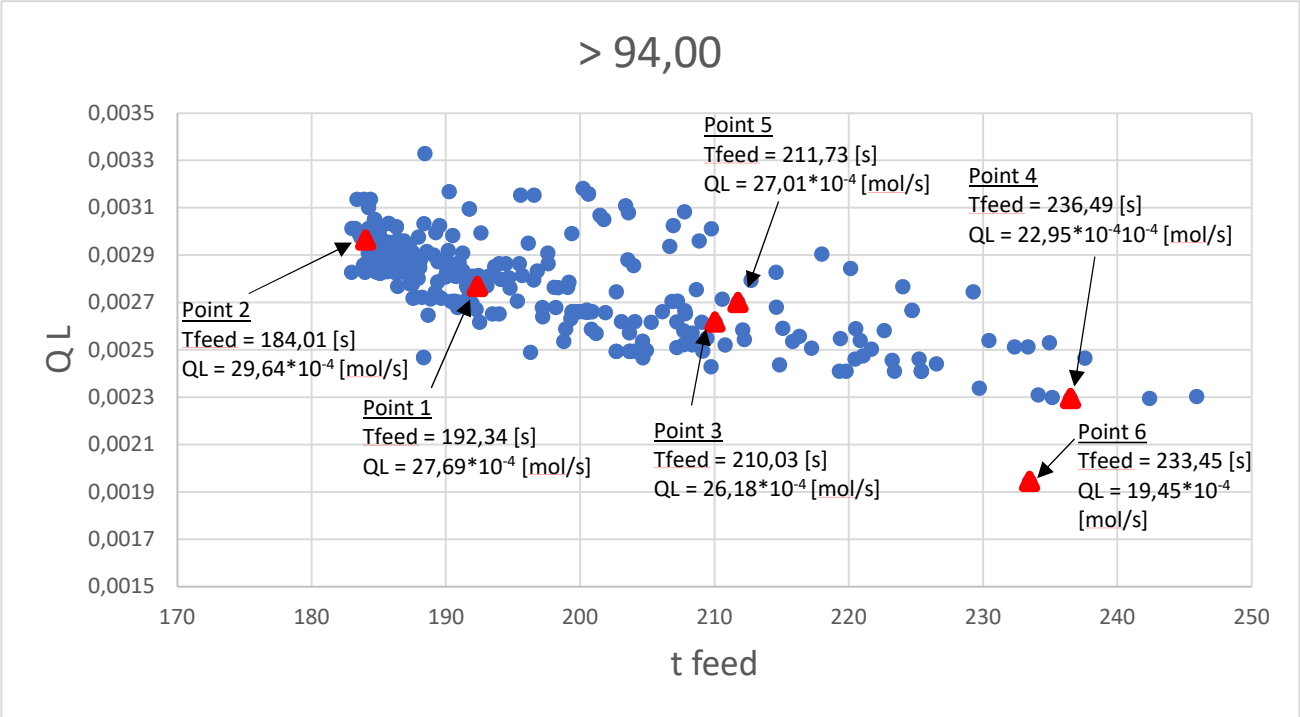

Figure 59: Check simulation points on the tFeed vs. QL plane for the case at π = 2.67

In Figure 60 and 61 are reported the points object of the check simulations in the Recovery vs. Q_L and Recovery vs. t_{Feed} plane respectively.

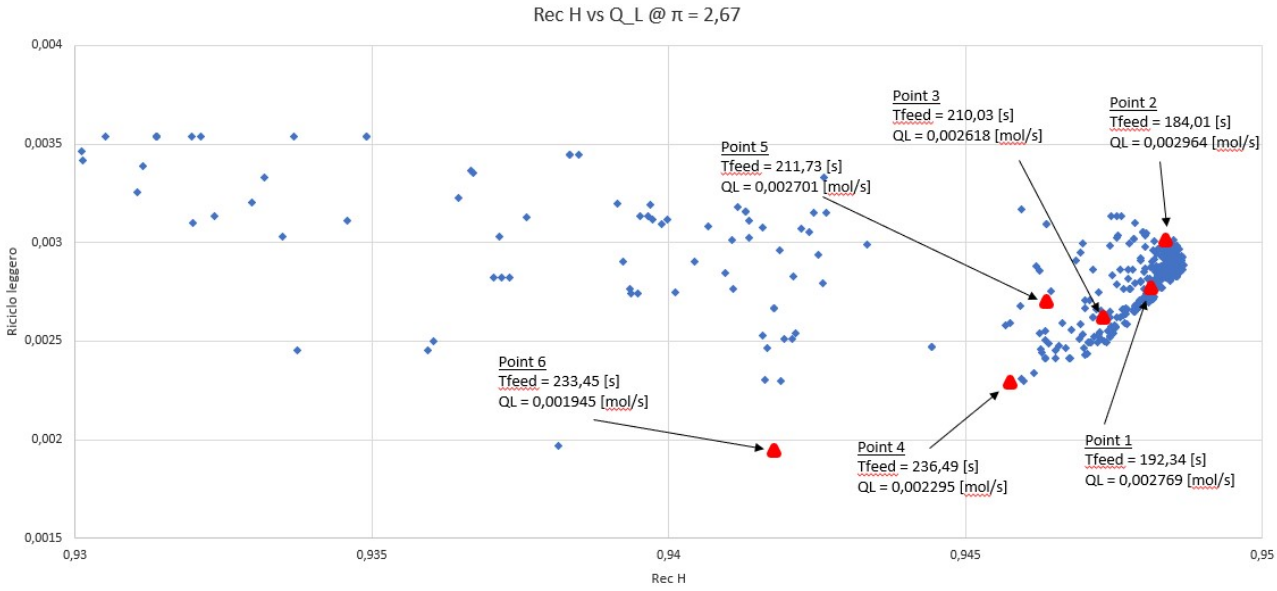

Figure 60: Check simulation points on the Rec H vs. QL plane for the case at π = 2.67

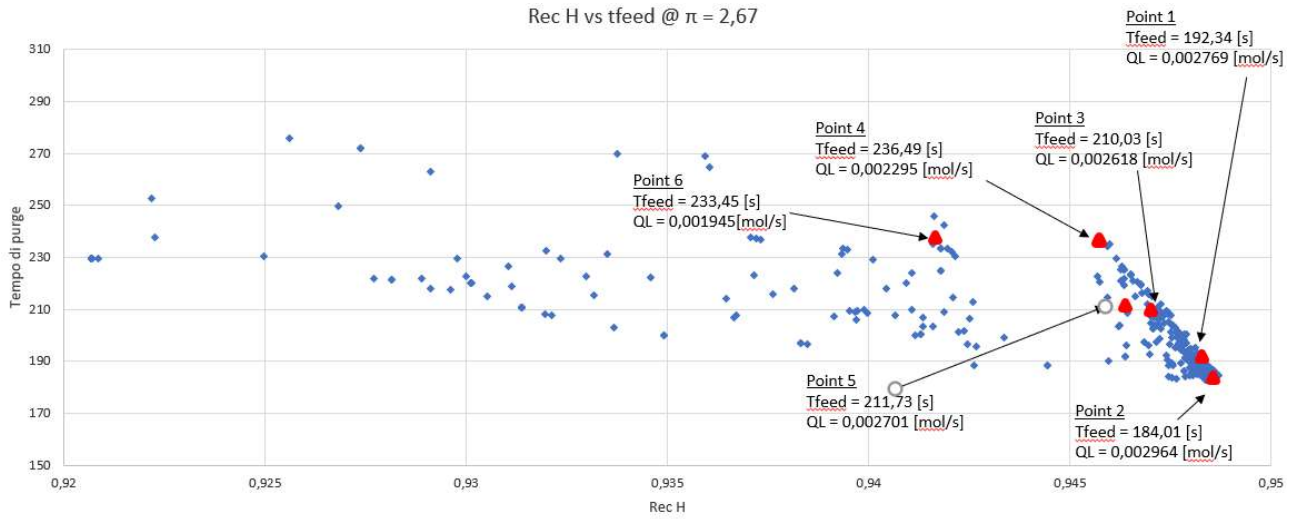

Figure 61: Check simulation points on the Rec H vs. tFeed plane for the case at π = 2.67

By using 300 computational points and the input data previously reported in Table 9 for the optimization, the results in Table 13 are obtained:

Table 32: Check simulations results for the points obtained with the optimization at π = 2.67

	Point 1	Point 2	Point 3	Point 4	Point 5	Point 6
$Purity_{HP,A}$ ott	94,82	94,86	94,72	94,57	94,63	94,17
$Purity_{HP,A}$ sim	98,55	98,53	98,34	98,10	98,08	98,49
$Purity_{LP,B}$ sim	99,67	98,97	99,00	100	98,84	100
tfeed [s]	192,34	184,01	210,03	236,49	211,73	233,45
Q_L [mol/s]	$27,69*10^{-4}$	$29,64*10^{-4}$	$26,18*10^{-4}$	$22,95*10^{-4}$	$27,01*10^{-4}$	$19,45*10^{-4}$
$\varepsilon_{rel,A}$	$1,12*10^{-2}$	$4,56*10^{-3}$	$6,6*10^{-3}$	$1,9*10^{-2}$	$7,6*10^{-3}$	$1,52*10^{-2}$
Ncycles	1962	1500	2000	2000	1500	1500

The heavy product can be obtained with high purity and recovery, higher than 98%.

In Figures from 62 to 67 are reported the profiles resulting for some of the check simulations performed for Point 2 and Point 6.

- Point 2

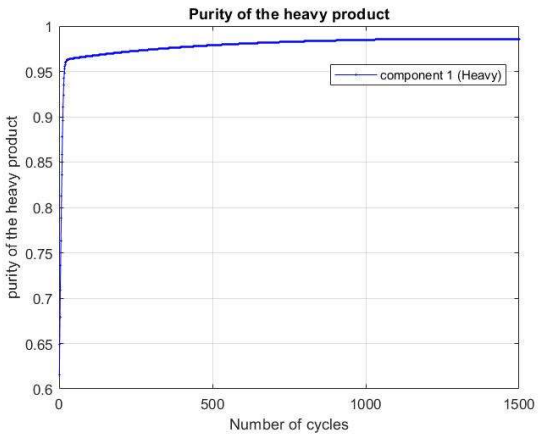

Figure 62: Heavy product purity for the Point 2 check simulation at π = 2.67

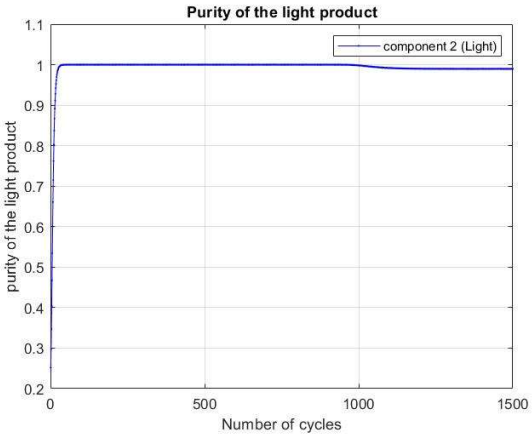

Figure 63: Light product purity for the Point 2 check simulation at π = 2.67

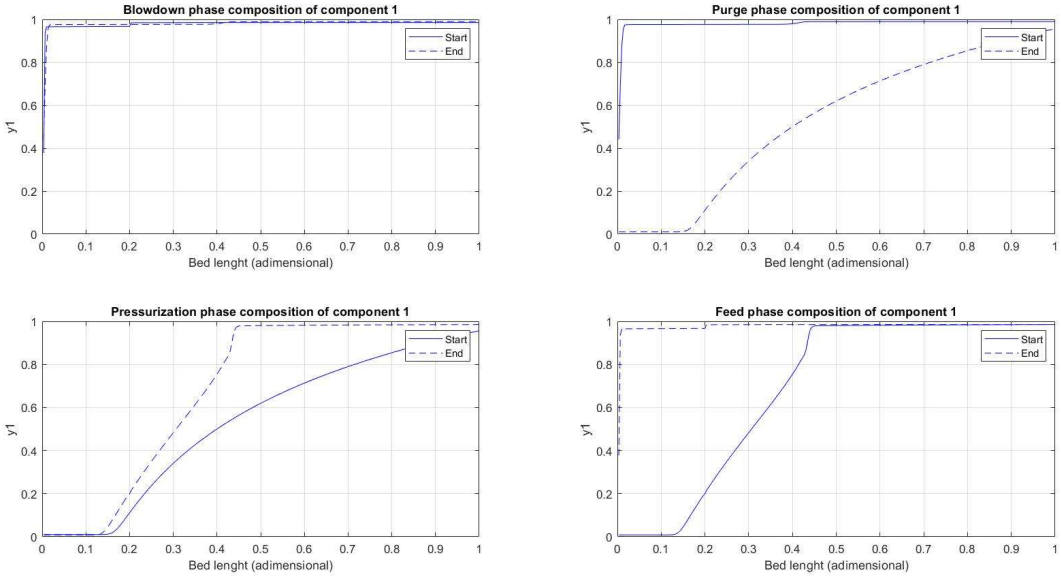

Figure 64: FVM start to end profiles for the check simulation of Point 2 of the case at π = 2.67

- Point 6

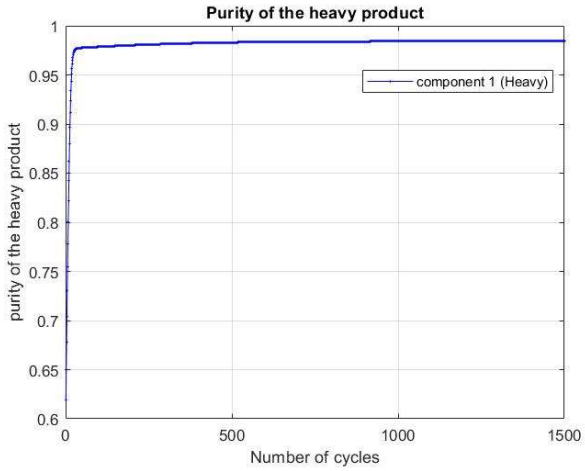

Figure 65: Heavy product purity for the Point 6 check simulation at π = 2.67

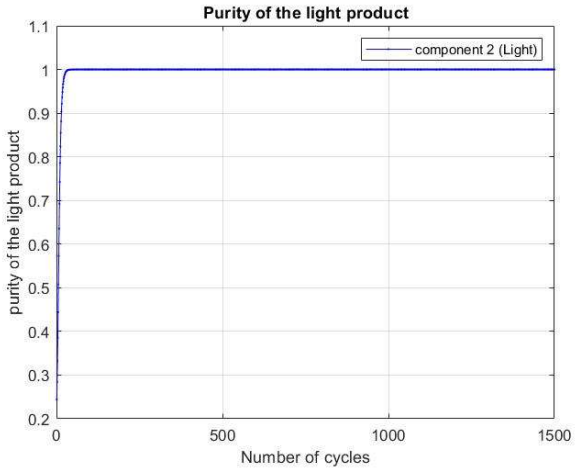

Figure 66: Light product purity for the Point 6 check simulation at π = 2.67

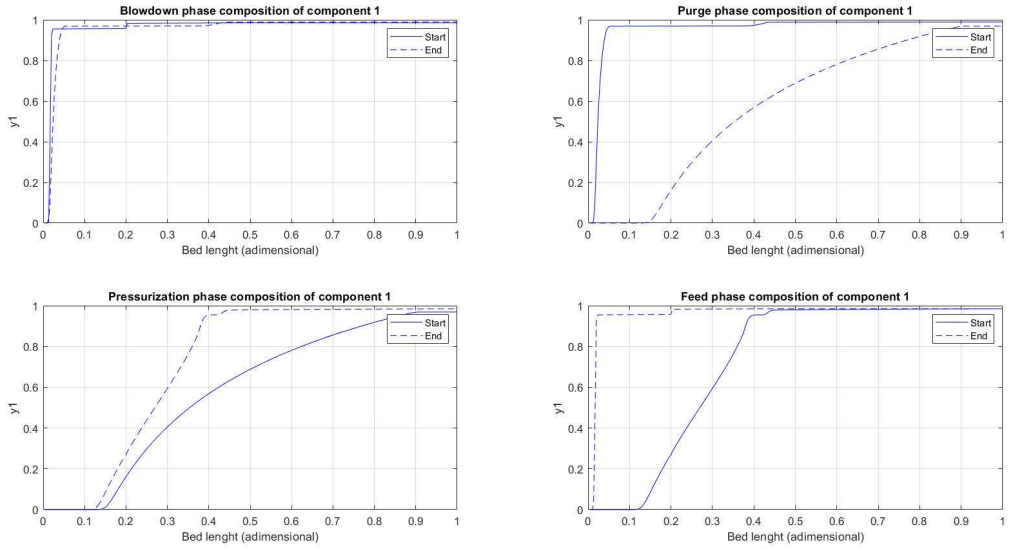

Figure 67: FVM start to end profiles for the check simulation of Point 6 of the case at π = 2.67

The point 6 represents an interesting case, because it combines excellent performance in terms of recovery and purity of the heavy compound with relatively high t_{Feed} and low Q_L values compared to the other points found, which translates into high productivity and low work required.

In Table 14 are reported the results of Productivity and Work calculated with Eq. 2.23 and 2.24 present in paragraph 8 of chapter 2.

Table 33: Productivity and Work results for the simulated points for the π = 2.67 case

	Point 1	Point 2	Point 3	Point 4	Point 5	Point 6
W [J/mol]	84020	89520	78735	69150	80700	59980
Pr [mol/m^3/cycle]	0,041223	0,039632	0,044548	0,049396	0,044864	0,048847

In Figure 72 and 73 are shown the results in the table above, where it can be noticed that the trend on the plane t_{Feed} vs. Q_L is almost the same as in the plane Productivity vs. Work since they are linearly dependent only on t_{Feed} and Q_L, having set the other parameters.

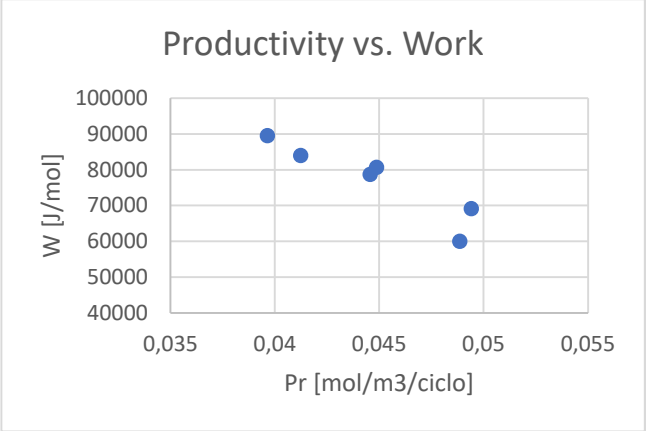

Figure 68: Check simulations Productivity vs. Work for the case at π = 2.67

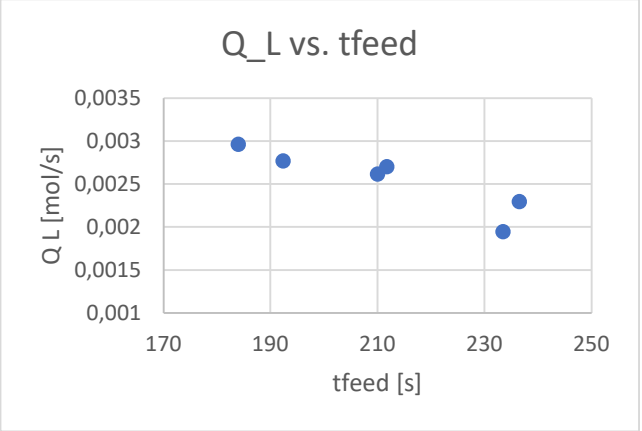

Figure 69: Check simulations tFeed vs. QL for the case at π = 2.67

Further simulations were carried out around point 6 towards higher t_{Feed} and lower Q_L, at high accuracy with 300 computational points, with the aim of analyzing the recovery and purity trend of the heavy compound, heading to a region characterized by higher productivity and lower energy consumption.

The points simulated are represented in Figure 70 with the starting point (Point 6), the results of the simulations performed are reported in Table 15.

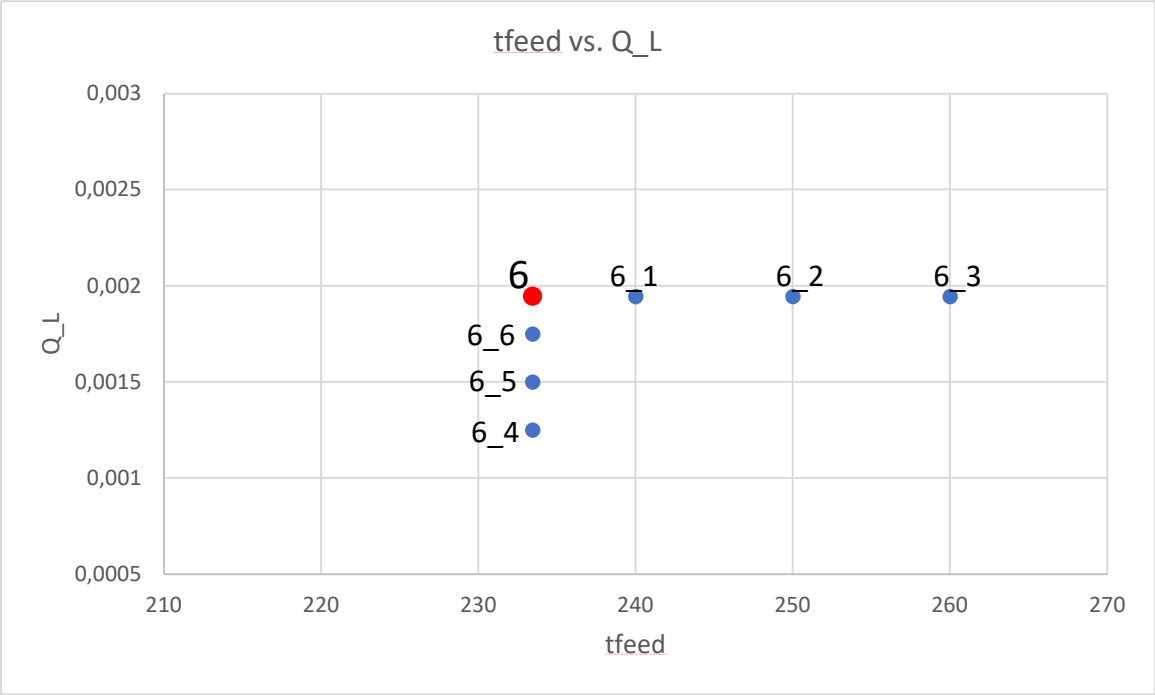

Figure 70: Further simulations from Point 6 towards higher Productivity and lower Work

A Δt_{Feed} equal to 10 s and a ΔQ_L equal to $12{,}5*10^{-4}$ have been chosen.

Table 34: Results of the simulations performed for points at increased productivity and deacreased work for the case at $\pi = 2.67$

	Point 6	6_1	6_2	6_3	6_4	6_5	6_6
$Purity_{HP,A}$	98,49	98,45	98,33	98,21	99,36	98,91	98,60
$Purity_{LP,B}$	100	98,50	98,37	98,26	100	100	100
tfeed [s]	233,45	240	250	260	233,45	233,45	233,45
$QL*10^{-4}$ [mol/s]	19,45	19,45	19,45	19,45	12,5	15	17,5
$\varepsilon_{rel,A}$	$1{,}52*10^{-2}$	$5{,}2*10^{-4}$	$5{,}4*10^{-4}$	$5{,}4*10^{-4}$	$6{,}4*10^{-3}$	$1{,}99*10^{-2}$	$1{,}38*10^{-2}$
Work [J/mol]	59980	59325	58915	58535	42032,5	48379,5	54885
Productivity [mol/m^3/ciclo]	0,048847	0,050028	0,051815	0,053581	0,048847	0,048847	0,048847

Excellent results (Table 15) are obtained also for the points simulated around point 6 with purity and recovery of the heavy component higher than 98%, furthermore it is noted that when moving to lower recycling flow rates of the light component the values increase up to over 99% with point 6_4.

The profiles for point 6_4 are reported in Figure 71 to 73 as an example.

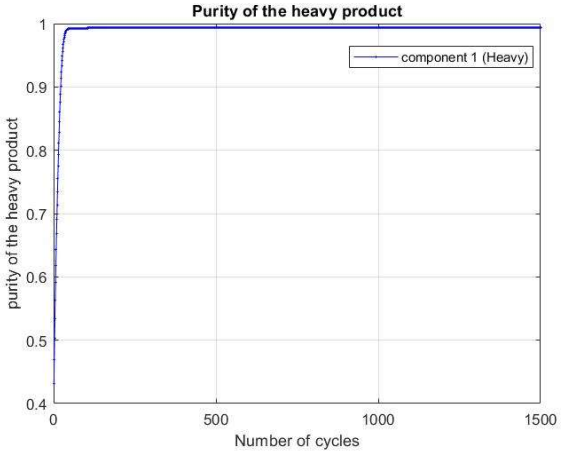

Figure 71: Heavy product purity for the Point 6_4 simulation

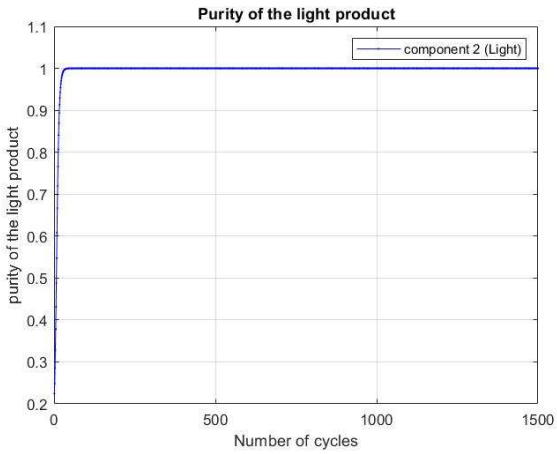

Figure 72: Light product purity for the Point 6_4 simulation

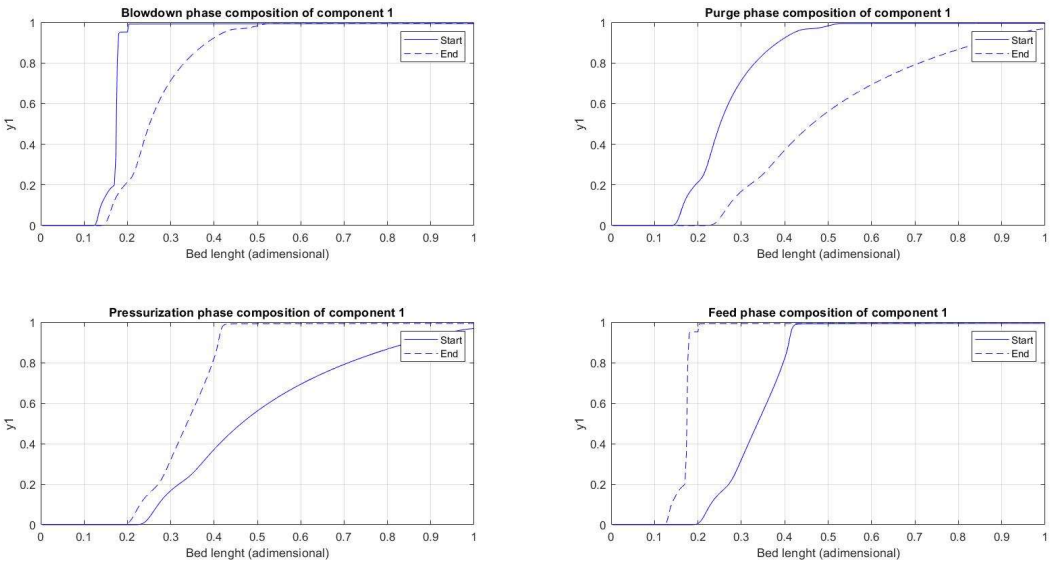

Figure 73: FVM start to end profiles for the simulation of Point 6_4

Following these results, it was decided to analyze the performance of the process in a region between point 6 and the upper limits of t_{Feed} and lower limits of Q_L, included in the lines in Figure 74.

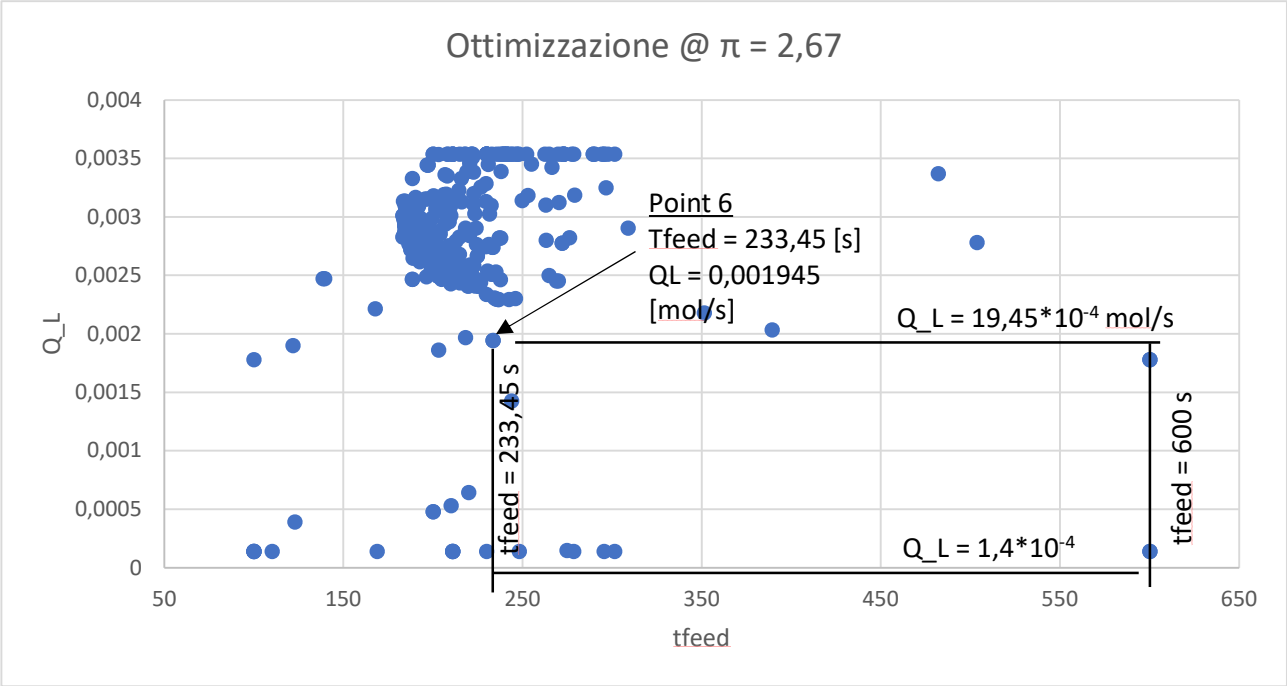

Figure 74: Starting area for the search of the region at high separation for the case at π = 2.67

The goal was to analyze an area with high productivity and low work required, through a hand optimization, to search for a region characterized at the same time by high purity and recovery of the heavy component (> 98%) and optimal plant and economic features.

The manual optimization was carried out by means of the bisection method. Several simulations were performed at high accuracy (300 computational points), starting from the boundaries of the domains towards point 6. The method consists of repeatedly bisecting the interval between two points which values are known. If purity greater than 98% was found, a new point was simulated towards the boundary of the domain in the middle of the interval, if purity lower than 98% was found, the new point to be simulated was the one in the middle of the interval towards the starting point 6.

Table 35: ΔtFeed and ΔQL criteria for the manual optimization with the bisection method for the case at π = 2.67

	tFeed	QL
Δ	20 s	$2*10^{-4}$ [mol/s]
Δ%	5,4 %	7,8 %

Suitable Δt_{Feed} and ΔQ_L were identified, reached which the manual optimization work could be considered concluded, whose value and ratio to the investigated domain are reported in Table 16.

The region found is represented in Figure 75 where the points crossed did not reach purity and recovery equal or greater than 98% which can be obtained in the region between the blue lines.

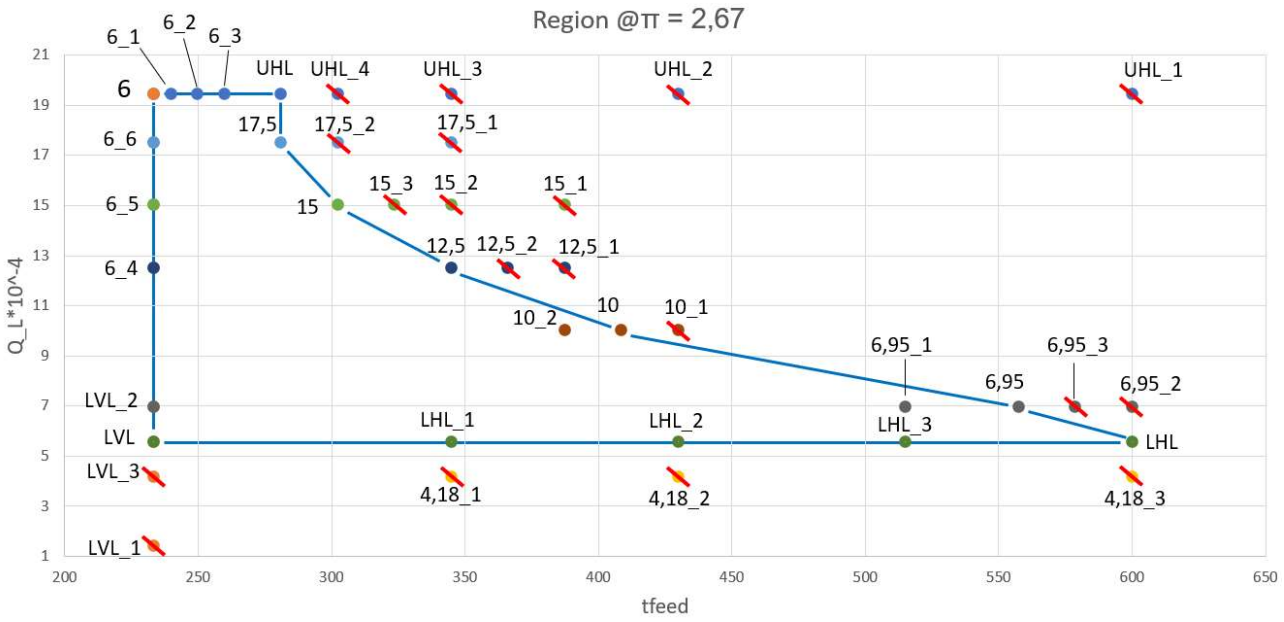

Figure 75: High separation region for the case at π = 2.67

Simulations were performed with 300 computational points with a variable number of cycles, with the aim of keeping the error on the BM of the heavy component below 10^{-2}, as for the optimization.

The results of all the simulation carried out are reported from Table 17 to Table 25.

For the left vertical limit @ t_{Feed} = 233,45 s:

Table 36: Results of the simulations carried out for the vertical limit of the high separation region for the case at π = 2.67

	6	6_6	6_5	6_4	LVL_2	LVL	LVL_3	LVL_1
Q_L*10^{-4}	19,45	17,5	15	12,5	6,95	5,565	4,18	1,4
$Purity_{HP,A}$	98,49	98,60	98,91	99,36	98,17	99,36	93,16	62,42
$Purity_{LP,B}$	100	100	100	100	100	100	93,63	62,43
Ncycles	1500	1500	1500	1500	336	600	401	929
$\varepsilon_{rel,A}$	$1,52*10^{-2}$	$1,38*10^{-2}$	$1,98*10^{-2}$	$6,4*10^{-3}$	$1,84*10^{-2}$	$6,4*10^{-3}$	$5,0*10^{-3}$	$6,6*10^{-4}$

For the upper horizontal limit @ $Q_L = 19{,}45*10^{-4}$ mol/s:

Table 37: Results of the simulations carried out for the upper limit of the high separation region for the case at π = 2.67

	6	6_1	6_2	6_3	UHL	UHL_4	UHL_3	UHL_2	UHL_1
tfeed	233,45	240	250	260	281,25	302,5	345	430	600
$Purity_{HP,A}$	98,49	98,45	98,33	98,21	97,96	97,47	95,89	91,87	83,45
$Purity_{LP,B}$	100	98,50	98,37	98,26	98,63	97,52	95,91	91,95	83,43
Ncycles	1500	1500	1500	1500	982	428	257	228	215
$\varepsilon_{rel,A}$	$1{,}52*10^{-2}$	$5{,}2*10^{-4}$	$5{,}4*10^{-4}$	$5{,}4*10^{-4}$	$6{,}8*10^{-3}$	$5{,}6*10^{-4}$	$3{,}2*10^{-4}$	$9{,}8*10^{-4}$	$1{,}26*10^{-4}$

For the lower horizontal limit @ $Q_L = 5{,}565*10^{-4}$ mol/s:

Table 38: Results of the simulations carried out for the lower horizontal limit of the high separation region for the case at π = 2.67

	LVL	LHL_1	LHL_2	LHL_3	LHL
tfeed [s]	233,45	345	430	515	600
$Purity_{HP,A}$	99,36	99,24	99,50	99,21	99,24
$Purity_{LP,B}$	100	100	100	100	99,25
Ncycles	600	371	401	295	2000
$\varepsilon_{rel,A}$	$6{,}4*10^{-3}$	$7{,}6*10^{-3}$	$5{,}0*10^{-3}$	$7{,}8*10^{-3}$	$7{,}2*10^{-5}$

Check on the lower horizontal limit @ QL = 4,18*10^{-4} mol/s:

*Table 39: Results of the simulations carried out for the limit at QL = 4,18*10^{-4} mol/s of the high separation region for the case at π = 2.67*

	LVL_3	4,18_1	4,18_2	4,18_3
tfeed [s]	233,45	345	430	600
$Purity_{HP,A}$	93,16	93,40	93,43	93,44
$Purity_{LP,B}$	93,63	93,46	93,44	93,44
Ncycles	401	411	447	492
$\varepsilon_{rel,A}$	5,0*10^{-3}	6,4*10^{-4}	1,44*10^{-4}	2*10^{-5}

Limit at Q_L = 17,5*10^{-4} mol/s:

*Table 40: Results of the simulations carried out for the limit at QL = 17,5*10^{-4} mol/s of the high separation region for the case at π = 2.67*

	6_6	17,5	17,5_2	17,5_1
tfeed [s]	23,45	281,25	302,5	345
$Purity_{HP,A}$	98,60	98,12	97,89	97,07
$Purity_{LP,B}$	100	98,72	97,93	97,17
Ncycles	1500	1022	747	306
$\varepsilon_{rel,A}$	5,2*10^{-4}	6,0*10^{-4}	4,8*10^{-3}	1,08*10^{-3}

Limit at $Q_L = 15*10^{-4}$ mol/s:

*Table 41: Results of the simulations carried out for the limit at QL = 15*10^{-4} mol/s of the high separation region for the case at π = 2.67*

	6_5	15	15_3	15_2	15_1
tfeed [s]	233,45	302,5	323,75	345	387,5
$Purity_{HP,A}$	98,91	98,18	97,91	97,67	97,15
$Purity_{LP,B}$	100	98,27	98,36	97,95	97,16
Ncycles	1500	702	771	400	396
$\varepsilon_{rel,A}$	$5,4*10^{-4}$	$8,8*10^{-4}$	$4,6*10^{-3}$	$2,8*10^{-3}$	$2,4*10^{-4}$

Limit at $Q_L = 12,5*10^{-4}$ mol/s:

*Table 42: Results of the simulations carried out for the limit at QL = 12,5*10^{-4} mol/s of the high separation region for the case at π = 2.67*

	6_4	12,5	12,5_2	12,5_1
tfeed [s]	233,45	345	366,25	387,5
$Purity_{HP,A}$	99,36	98,14	97,86	97,59
$Purity_{LP,B}$	100	98,50	98,18	97,92
Ncycles	1500	600	675	389
$\varepsilon_{rel,A}$	$6,4*10^{-3}$	$3,6*10^{-3}$	$3,4*10^{-3}$	$3,2*10^{-3}$

Limit at $Q_L = 10*10^{-4}$ mol/s:

Table 43: Results of the simulations carried out for the limit at QL = $10*10^{-4}$ mol/s of the high separation region for the case at π = 2.67

	10_2	10	10_1
tfeed [s]	387,5	408,75	430
$Purity_{HP,A}$	98,42	98,15	97,85
$Purity_{LP,B}$	99,95	98,38	97,87
Ncycles	584	620	461
$\varepsilon_{rel,A}$	$1,52*10^{-2}$	$2,4*10^{-3}$	$2,2*10^{-4}$

Limit at $Q_L = 6,95*10^{-4}$ mol/s:

Table 44: Results of the simulations carried out for the limit at QL = $6,95*10^{-4}$ mol/s of the high separation region for the case at π = 2.67

	LVL_2	6,95_1	6,95	6,95_3	6,95_2
tfeed [s]	233,45	515	557,5	578,75	600
$Purity_{HP,A}$	98,17	98,78	98,15	97,84	97,55
$Purity_{LP,B}$	100	99,26	98,32	97,97	97,56
Ncycles	336	613	412	390	346
$\varepsilon_{rel,A}$	$1,84*10^{-2}$	$4,8*10^{-3}$	$1,72*10^{-3}$	$1,32*10^{-3}$	$1,06*10^{-4}$

From Figure 76 to 80 are reported the profile of the case LHL.

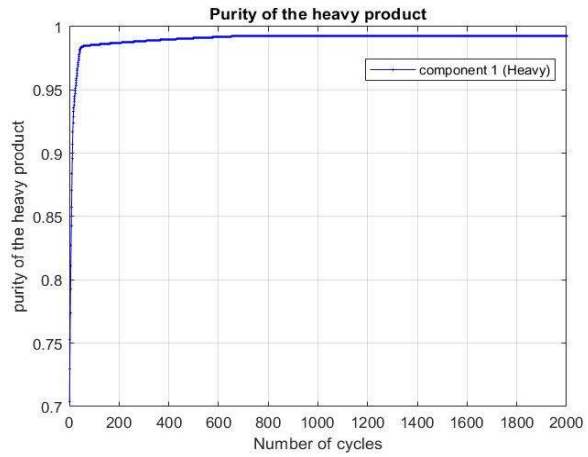

Figure 76: Heavy product purity for the simulation of LHL at π = 2.67

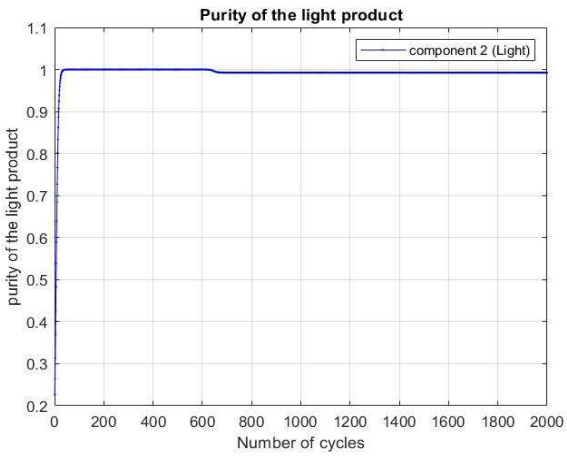

Figure 77: Light product purity for the simulation of LHL at π = 2.67

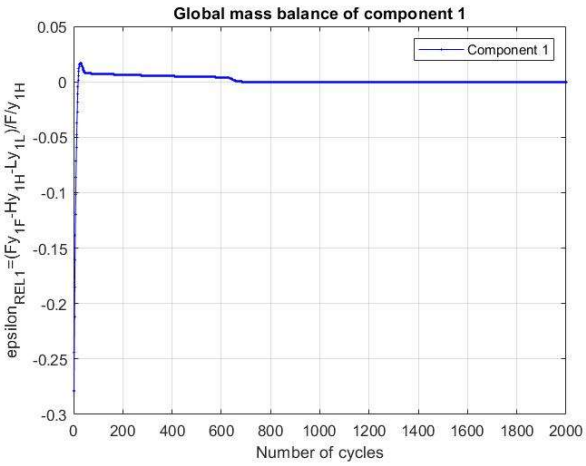

Figure 78: Error on the heavy product BM for the simulation of LHL at π = 2.67

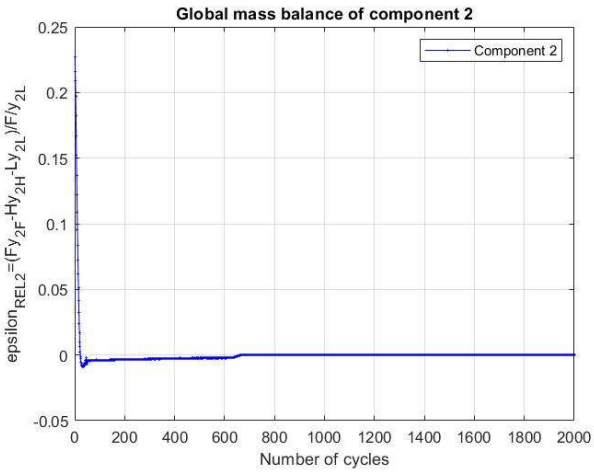

Figure 79: Error on the light product BM for the simulation of LHL at π = 2.67

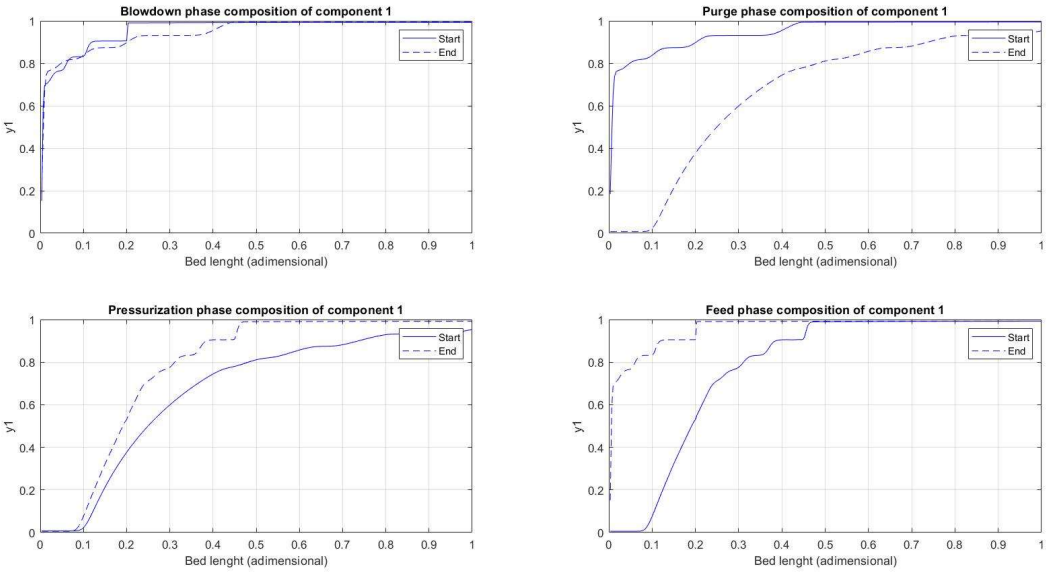

Figure 80: FVM start to end profiles for the simulation of LHL at π = 2.67

The results in terms of productivity and work for the points constituting the boundaries of the region are reported in Table 26 and Figure 81.

Table 45: Productivity and Work results for the boundaries of the high separation region at π = 2.67

	tfeed	QL	Pr	W
6	233,45	0,001945	0,048847	59980
6_6	233,45	0,00175	0,048847	54885
6_5	233,45	0,0015	0,048847	48379,5
6_4	233,45	0,00125	0,048847	42032,5
LVL_2	233,45	0,000695	0,048847	27033,5
LVL	233,45	0,0005565	0,048847	23415
6_1	240	0,001945	0,050028	59325
6_2	250	0,001945	0,051815	58915
6_3	260	0,001945	0,053581	58535
UHL	281,25	0,001945	0,057269	57940
LHL_1	345	0,0005565	0,067823	20191
LHL_2	430	0,0005565	0,08081	18882,5
LHL_3	515	0,0005565	0,092701	17970,5
LHL	600	0,0005565	0,10363	17179,5
17,5	281,25	0,00175	0,057269	52785
15	302,5	0,0015	0,06087	45503,5
12,5	345	0,00125	0,067823	38004,5
10	408,75	0,001	0,077672	30370
6,95	557,5	0,000695	0,098278	20873,5

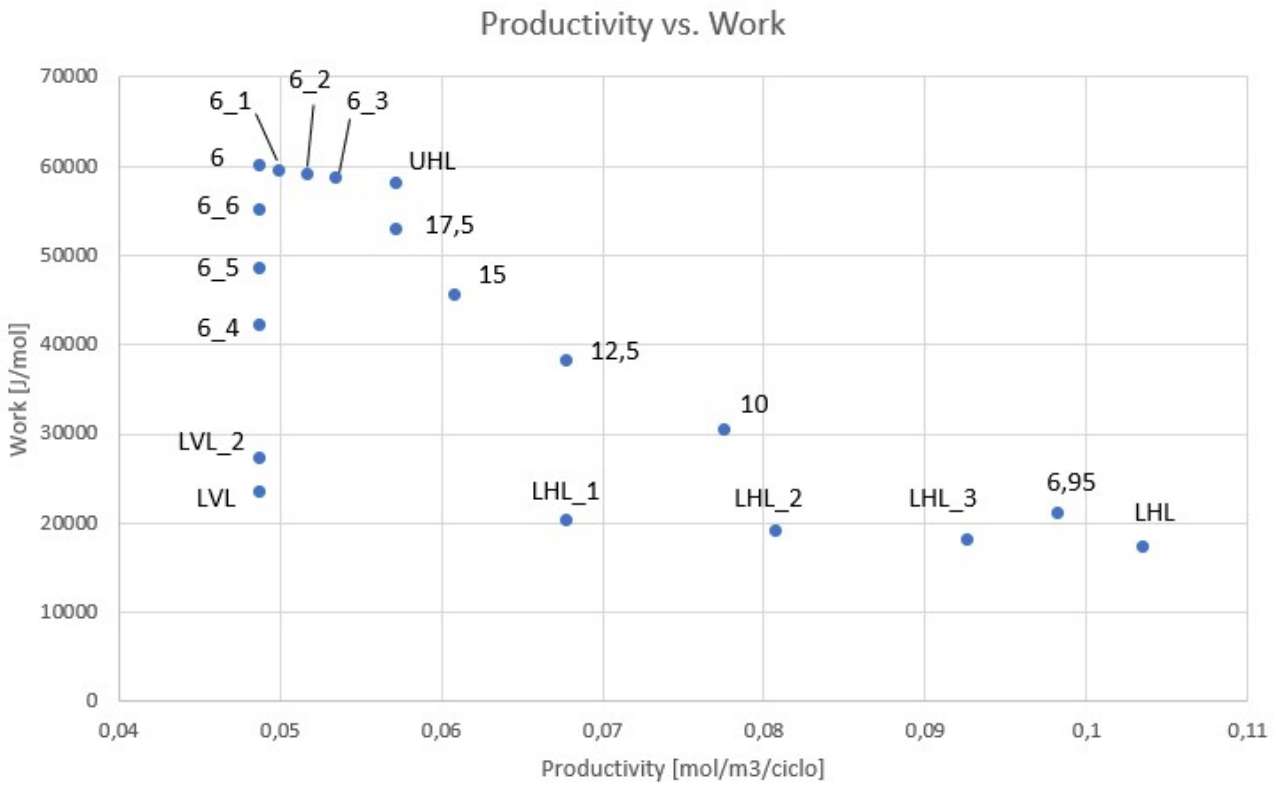

Figure 81: Productivity vs. Work for the high separation region at π = 2.67

A further analysis has been carried out towards t_{Feed} values beyond the upper boundary and Q_L values up to the upper limit to verify the width of the high separation region.

As previously done, several simulations were carried out with 300 computational points, applying the bisection method to find the boundaries of thie region with purity and recovery of the heavy product greater than or equal to 98%. Δt_{Feed} and ΔQ_L of the previous cases were maintained.

The new region found is reported in Figure 82.

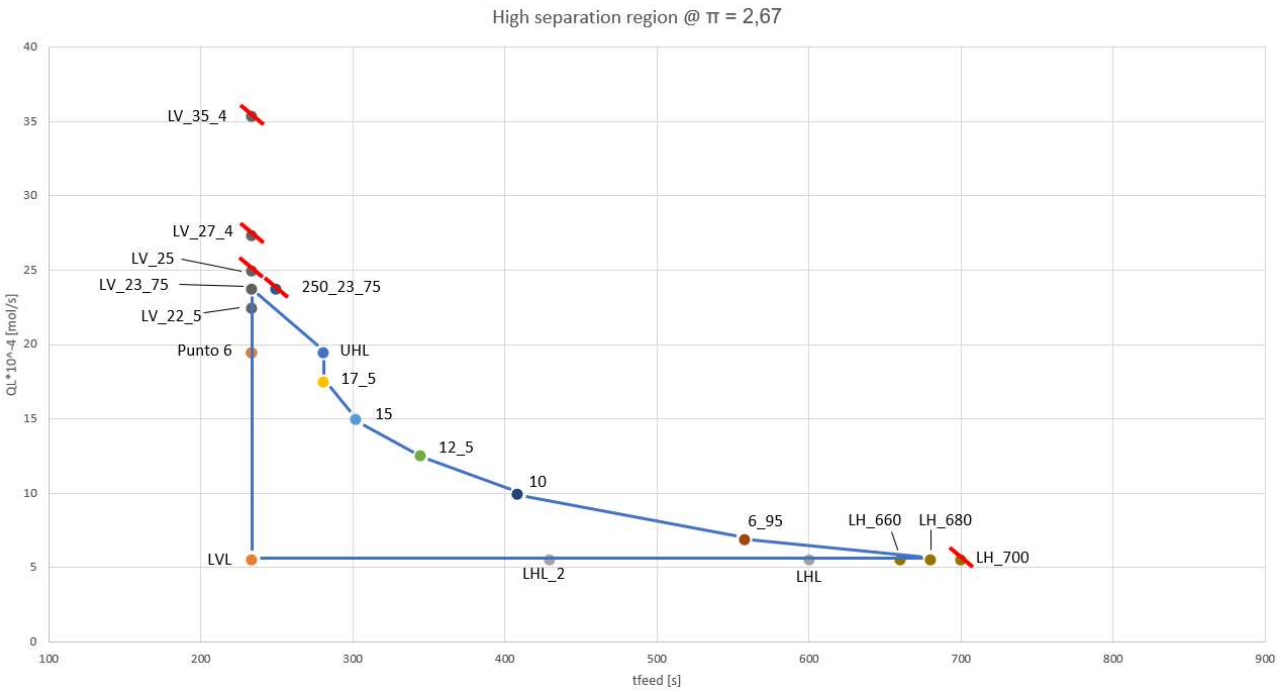

Figure 82: Extended high separation region at π = 2.67

The numerical results for the π = 2.67 case are reported from Table 27 to 29.

Horizontal limit at Q_L = 5,565*10^{-4} mol/s:

Table 27: Results of the further simulations performed for the lower limit of the high separation region at π = 2,67

	LHL_700	LHL_660	LHL_680	LHL
tfeed	700	660	680	600
$Purity_{HP,A}$	97,93	98,48	98,21	99,24
$Purity_{LP,B}$	97,94	98,49	98,21	99,25
$\varepsilon_{rel,A}$	4,8*10^{-5}	5,6*10^{-5}	5,4*10^{-5}	7,2*10^{-5}
W [J/mol]	16377	16653	16512	17179,5
Ncycles	586	516	790	2000

Vertical limit at t_{Feed} = 233,45 s:

Table 28: Results of the further simulations performed for the vertical limit of the high separation region at π = 2,67

	LV_35_4	LV_27_4	LV_25	LV_22_5	LV_23_75	Punto 6
$QL*10^{-4}$	35,4	27,4	25	22,5	23,75	19,45
$Purity_{HP,A}$	92,41	96,82	97,81	98,33	98,16	98,49
$Purity_{LP,B}$	93,57	97,86	98,81	99,27	99,15	100
$\varepsilon_{rel,A}$	$1,3*10^{-2}$	$1,08*10^{-2}$	$1,02*10^{-2}$	$9,6*10^{-3}$	10^{-2}	$1,5*10^{-2}$
W [J/mol]	96525	79885	74275	67920	71180	59980
N cycles	616	742	1500	1771	1538	1500

Limit at Q_L = $23,75*10^{-4}$ mol/s:

Table 29: Results of the further simulations performed for the limit at QL = $23,75*10^{-4}$ mol/s of the high separation region at π = 2,67

	LV_23_75	250_23_75
tfeed	233,45	250
$Purity_{HP,A}$	98,16	97,63
$Purity_{LP,B}$	99,15	97,66
$\varepsilon_{rel,A}$	10^{-2}	$3,4*10^{-4}$
W [J/mol]	71180	69950
Ncycles	1538	678

The profiles of case LH_680 are reported as example in Figure 83 to 87.

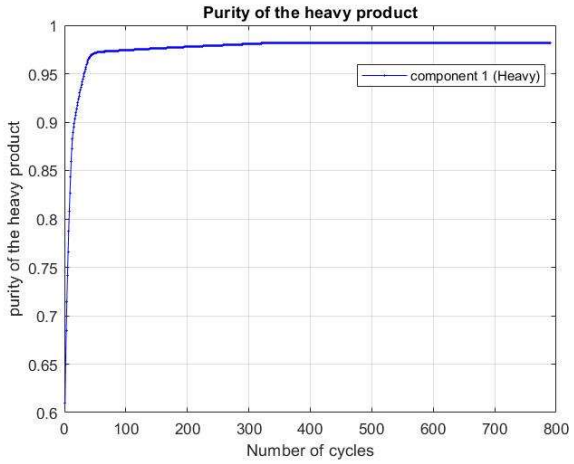

Figure 83: Heavy product purity for the simulation of LH_680 at π = 2,67

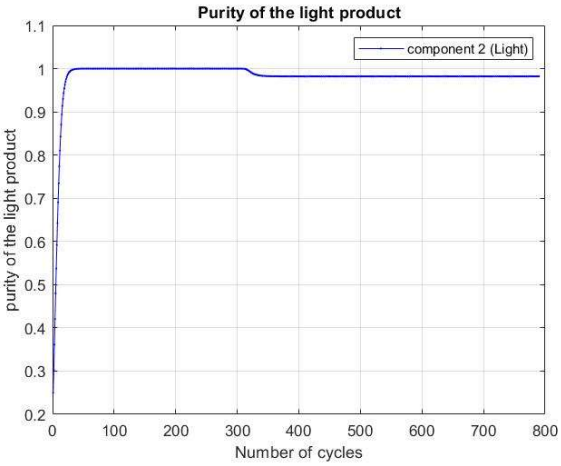

Figure 84: Light product purity for the simulation of LH_680 at π = 2,67

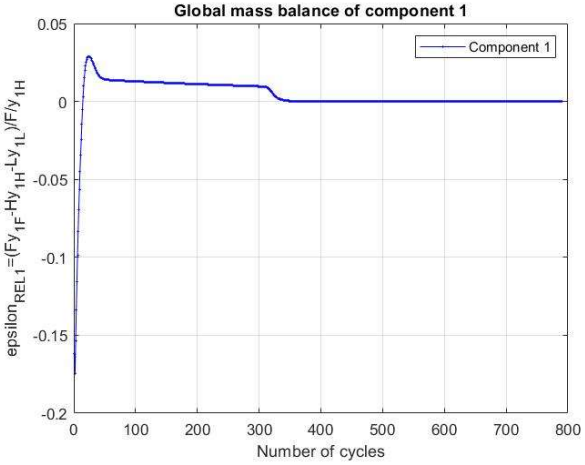

Figure 85: Error on the heavy product BM for the simulation of LH_680 at π = 2,67

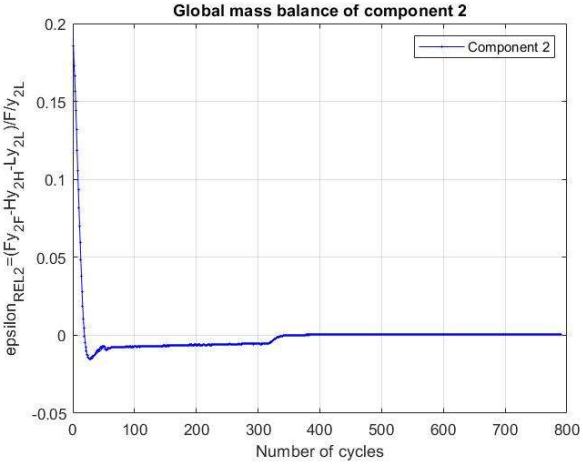

Figure 86: Error on the light product BM for the simulation of LH_680 at π = 2,67

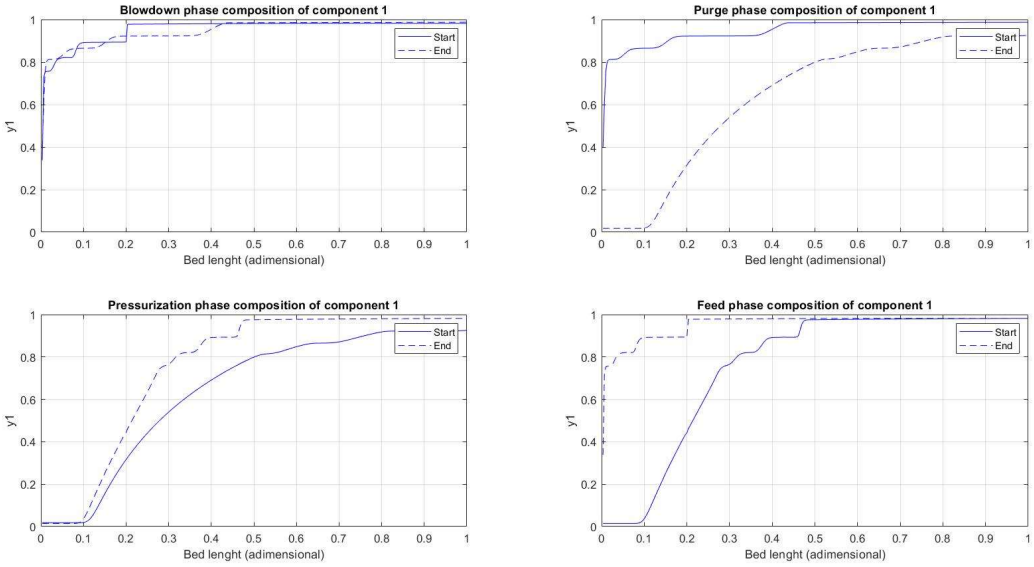

Figure 87: FVM start to end profiles for the simulation of LH_680 at π = 2,67

The results in terms of productivity and work for the points constituting the boundaries of the region are reported in Table 30 and Figure 88.

Table 30: Productivity and Work results for the boundaries of the extended high separation region at π = 2.67

π = 2,67	tfeed	QL	Pr	W
6	233,45	0,001945	0,048847	59980
6_6	233,45	0,00175	0,048847	54885
LVL	233,45	0,000557	0,048847	23415
UHL	281,25	0,001945	0,057269	57940
LHL_2	430	0,000557	0,08081	18882,5
LHL	600	0,000557	0,10363	17179,5
17,5	281,25	0,00175	0,057269	52785
15	302,5	0,0015	0,06087	45503,5
12,5	345	0,00125	0,067823	38004,5
10	408,75	0,001	0,077672	30370
6,95	557,5	0,000695	0,098278	20873,5
LH_660	660	0,000557	0,110827	16653
LH_680	680	0,000557	0,113137	16512
LV_23_75	233,45	0,002375	0,048847	71180
LV_22_5	233,45	0,00225	0,048847	67920

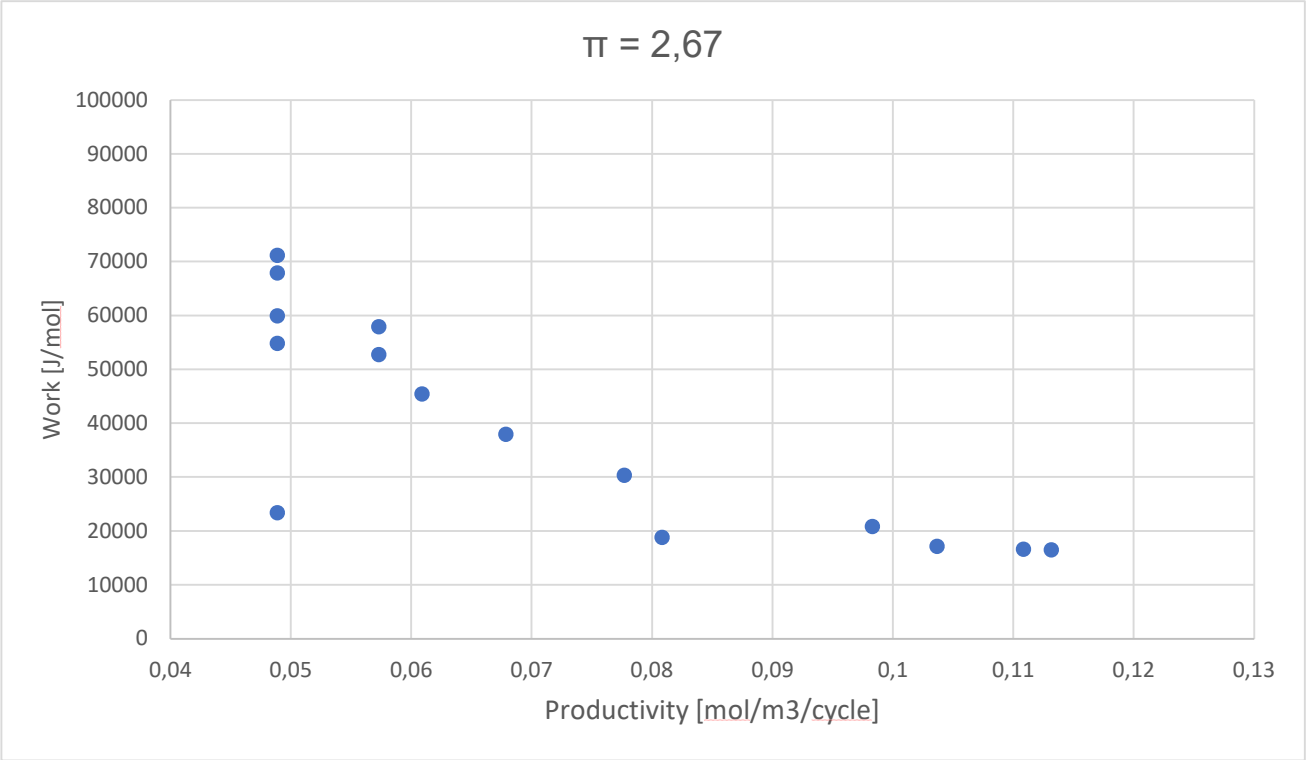

Figure 88: Productivity vs. Work for the extended high separation region at π = 2,67

It can be seen that it is possible to obtain sharp separation with purity and recovery of the heavy component higher than 98% and in some cases than 99% at low work required and high productivity. The point LHL_680 shows both these characteristics and could be identified as an optimum point for the DR – PHA process under the assumptions and conditions previously described, although it is characterized by not very robust conditions of Q_L and t_{Feed} being at the lower right vertex of the region.

This is evident from the profiles in Figure 87, where very sharp profiles develop close to the left end of the column. Small perturbation can easily lead to the profile breakthrough.

Following these results, it was decided to investigate the behavior of the process by working with larger π. Since the heavy product flowrate has been set equal to the stoichiometric one, in order to reach theoretically complete separation, and z_F = 0,8 showed good performances for the system studied, it was of interest to analyze the Productivity and Work trend, toghether with purity and recovery, at different values of the pressure ratio, which influences the energy requirements with Q_L.

4.2. π = 4

The first case we analyzed is π = 4 where the value of P_L was decreased from $4.5*10^5$ Pa to $3*10^5$ Pa, keeping fixed $P_H = 12*10^5$ Pa.

The work performed was the same as that done for the case at π = 2.67, starting from the optimization with variable t_{Feed} and Q_L.

The otpimization was carried out with 50 computational points as the one at π = 2.67 with the same input data, excecpt for the low pressure P_L, reported in Table 27.

A first optimization at π = 4 was performed with the boundaries used in the previous case, but from Figure 88 it is possible to see that the upper limit of Q_L is too low since the points tend to concentrate against it at high value of purity and recovery of the heavy component.

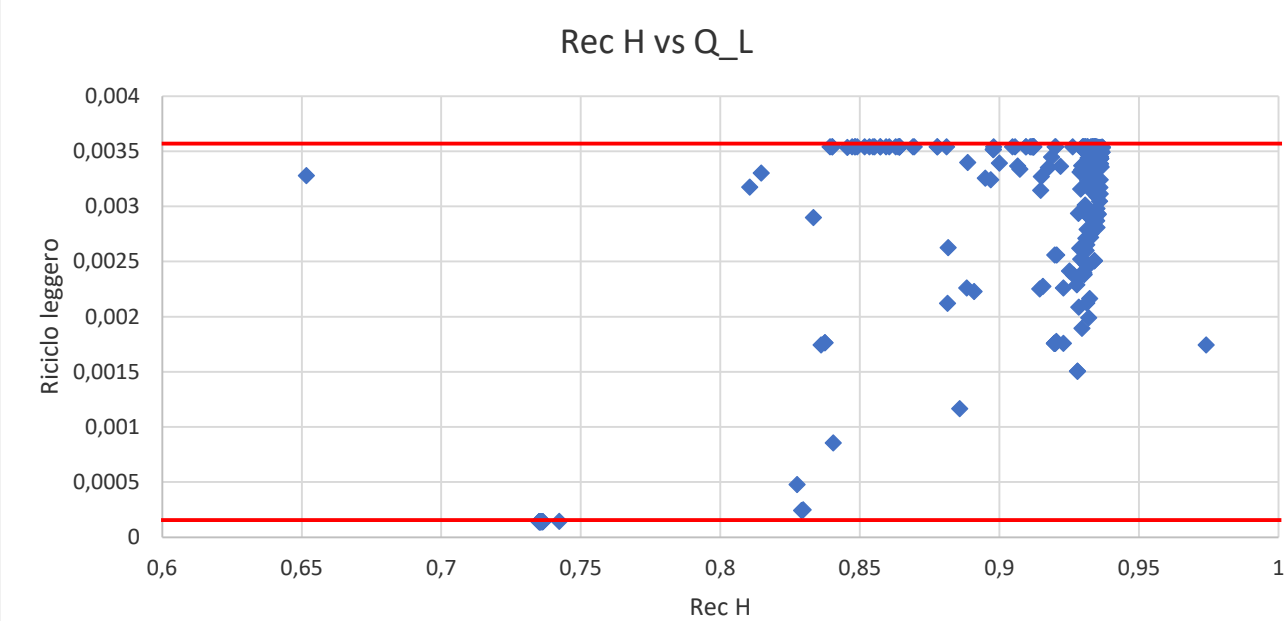

Figure 89: QL upper limit is too low for the optimization of the heavy product purity and recovery at π = 4

Therefore, the Q_L upper limite was increased from $20*Q_{feed}$ to $25*Q_{feed}$, while the t_{Feed} boundaries were found to be correct, as reported in Table 31.

Table 31: tFeed and QL boundaries for the heavy product purity and recovery optimization for the case at π = 4

	min	max
t_feed [s]	100	600
Q_L [mol/s]	0.8*Q_feed = 0.000142	25*Q_feed = 0.004425

The IC upload criterion was set at 9 cycles because in the first optimization at π = 4 when the CSS condition were reached the points simulations settle around 10 cycles.

In Figure 90 is represented the purity vs. recovery graph where the points are on the diagonal because of the heavy product flowrate set equal to the stoichiometric value.

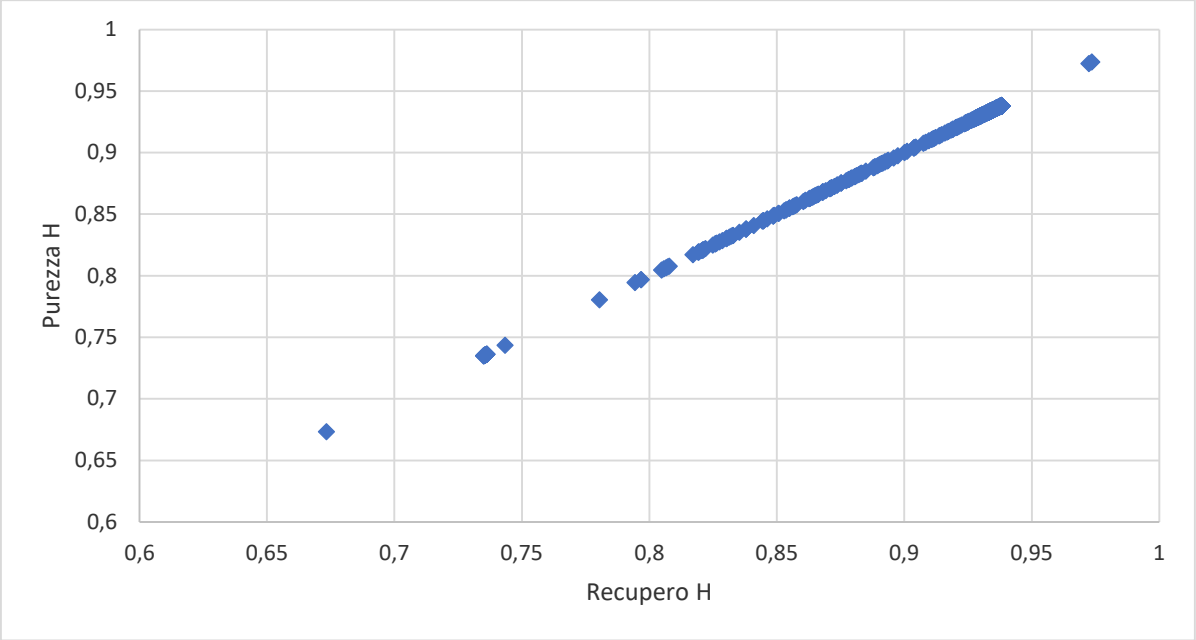

Figure 90: Purity vs. Recovery for the heavy product optimization at π = 4

The purity and recovery of the heavy product tended to settle at values just below 94% when stationary conditions were reached, there were also some points for which it was possible to obtain high purity and recovery of the order of 97%.

In Figure 91, 92 and 93 all the results obtained by the optimizer are graphically represented, with the recovery as a function of the two manipulated variables t_{Feed} and Q_L and a graph with the duration of the feed phase versus the recycling flowrate of the heavy component.

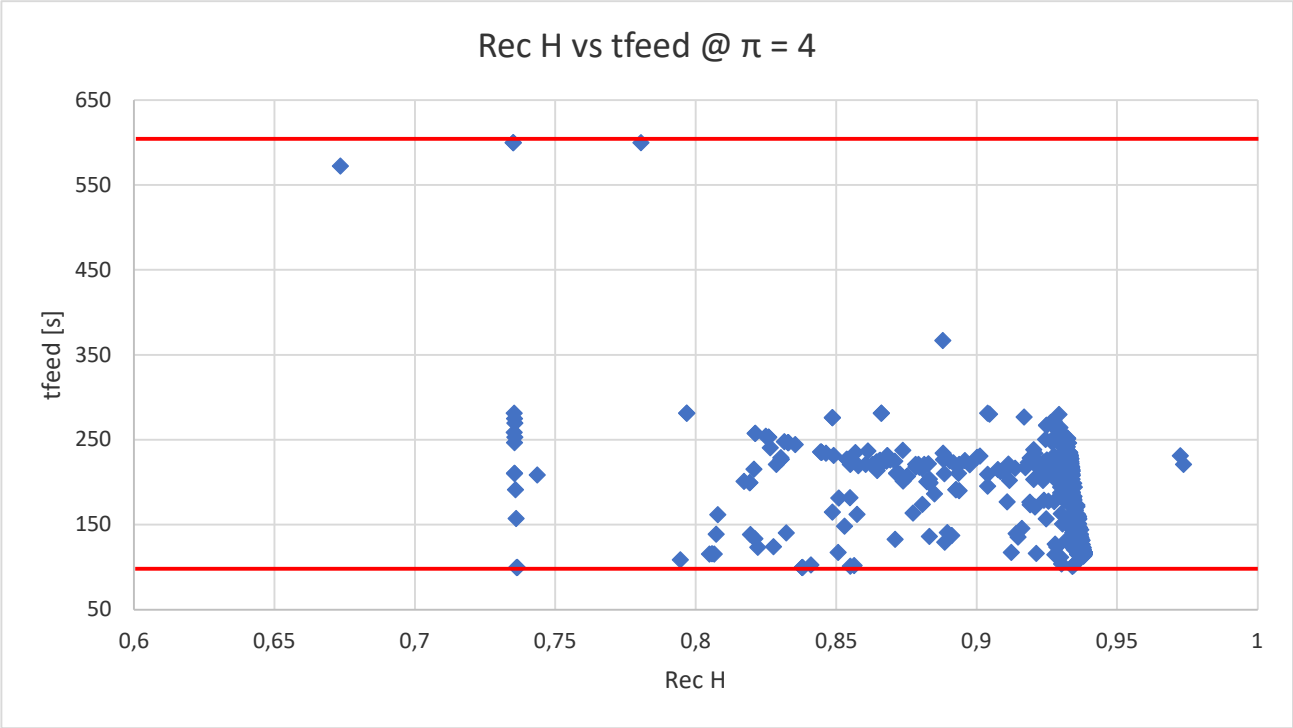

Figure 91: Results on the plane heavy product recovery vs. tFeed for the optimization at π = 4

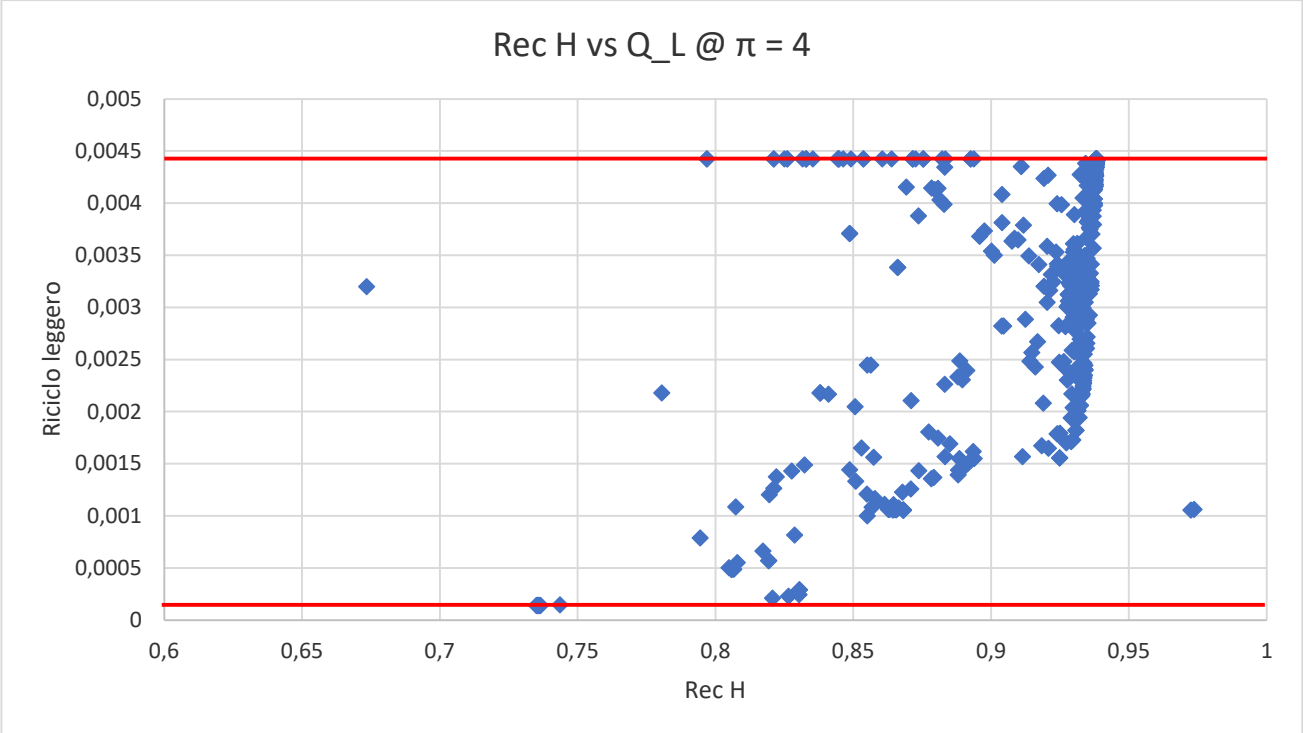

Figure 92: Results on the plane heavy product recovery vs. QL for the optimization at π = 4

Although some points are still against the upper limit, the high recovery front is widely distributed along the domain, so we considered the results acceptable without the need for a new optimization with a further increased upper limit of Q_L.

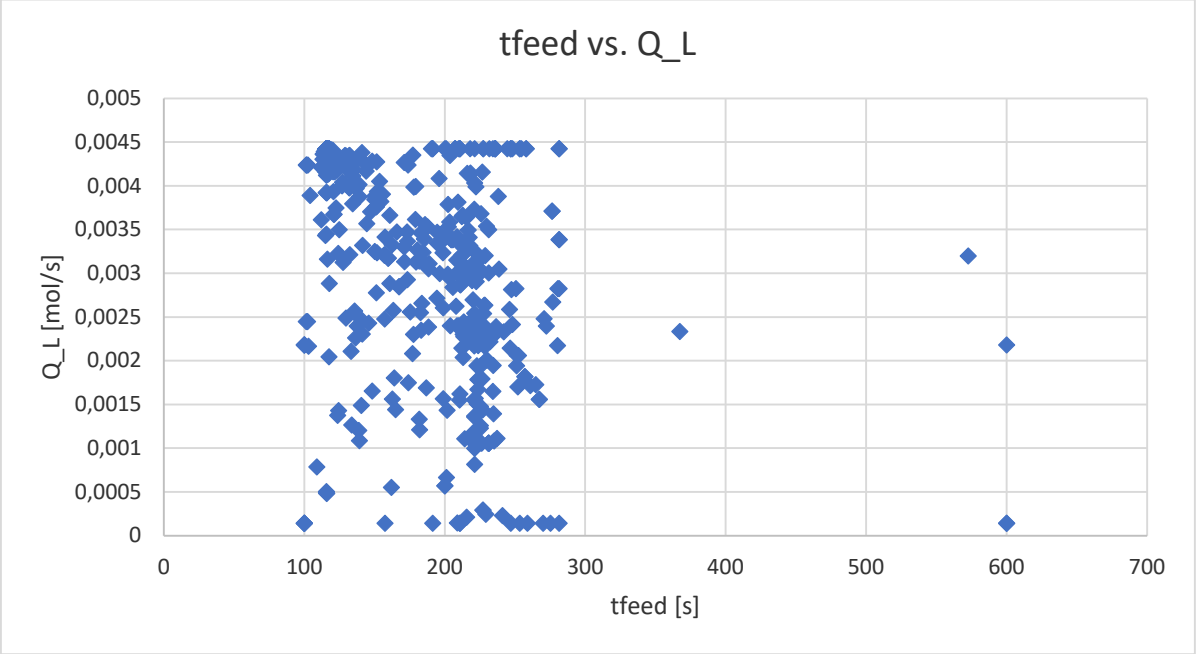

Figure 93: Results on the plane tFeed vs. QL for the optimization at π = 4

From the comparison with the results obtained for the optimization at π = 2.67, it can be seen that slightly lower purity and recovery are obtained at lower t_{Feed} values and for Q_L values covering a wider range, reaching both lower and higher values than those that characterized the previous case.

The Figure 94 to 98 show the results for purity and recovery higher than 90% and for the interval between 94% and 90%.

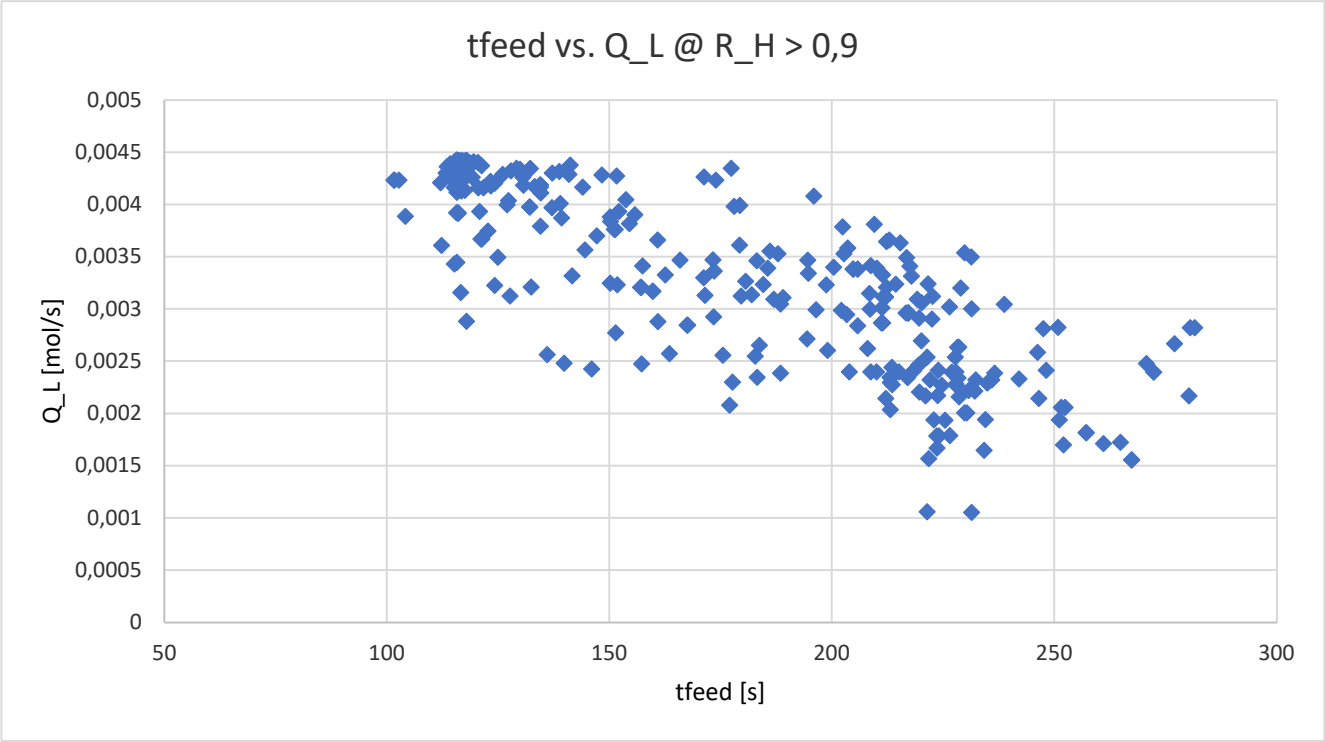

Figure 94: Results with purity > 90% of the heavy product optimization at π = 4

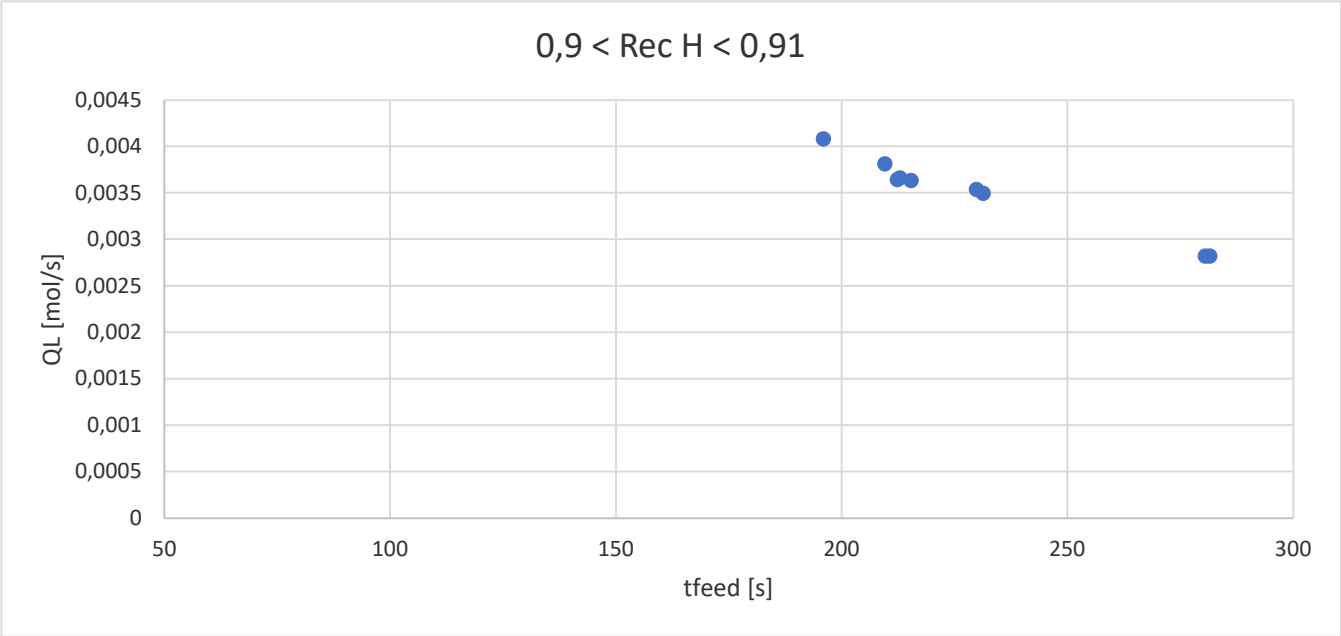

Figure 95: Results with purity between 90 and 91% of the heavy product optimization at π = 4

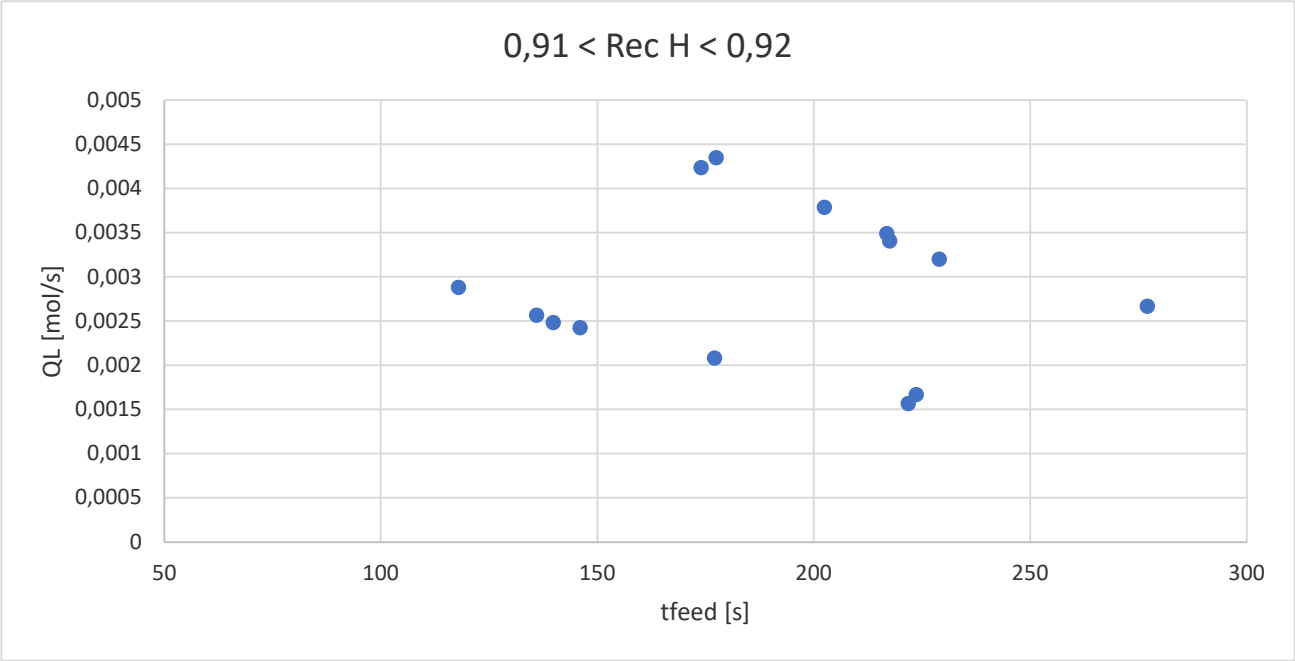

Figure 96: Results with purity between 91 and 92% of the heavy product optimization at π = 4

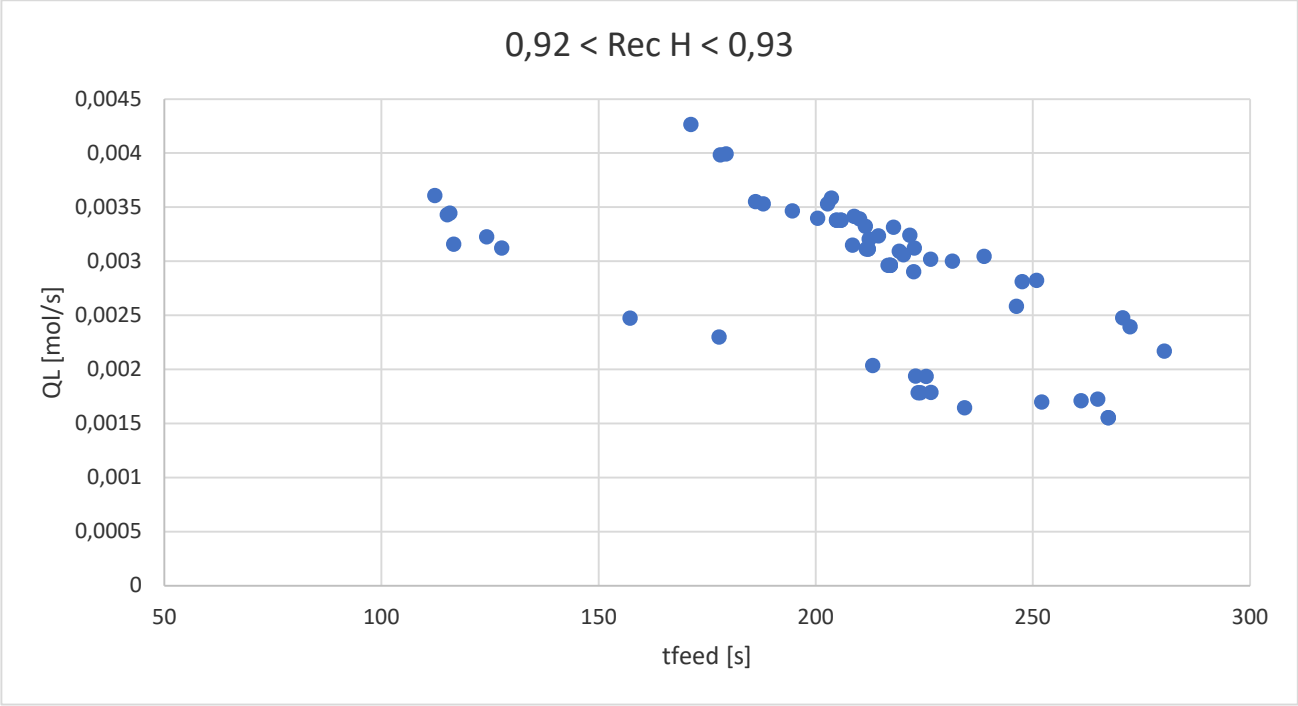

Figure 97: Results with purity between 92 and 93% of the heavy product optimization at π = 4

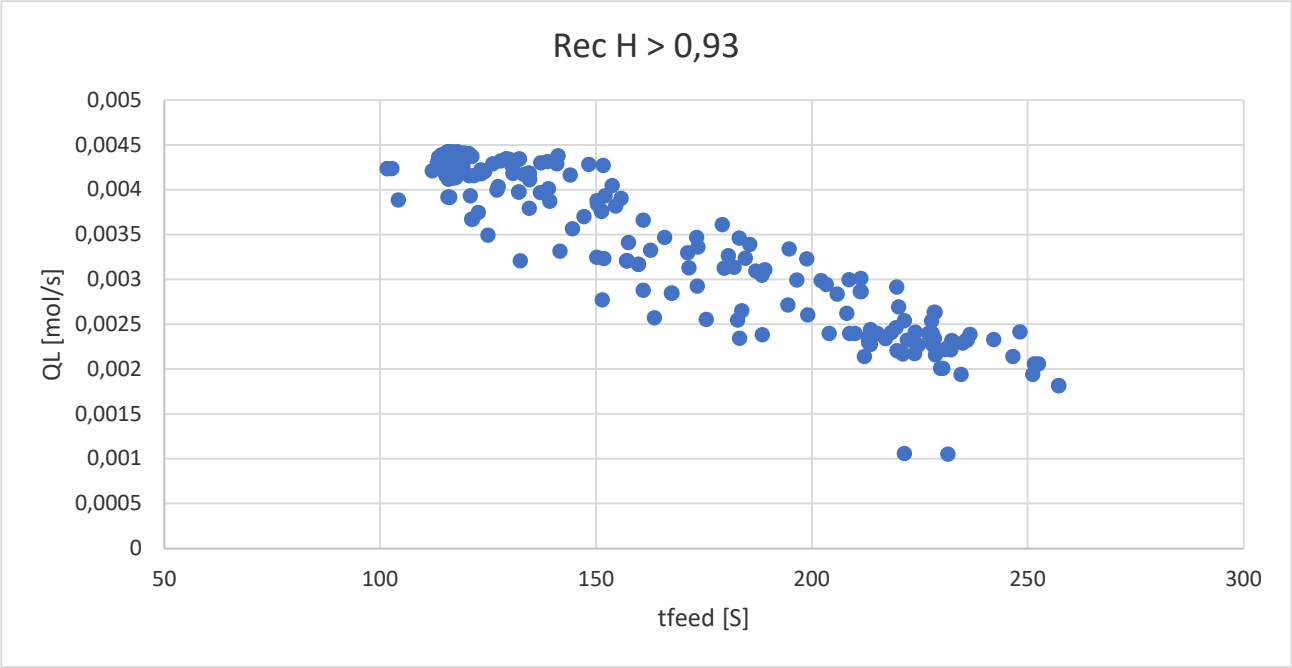

Figure 98: Results with purity > 93% of the heavy product optimization at π = 4

The characteristics of the optimization are shown in Table 32.

Table 3246: Results for the heavy product purity and recovery optimization with variable tFeed and QL for the case at π = 4

	π = 4
Number of points simulated	738
Average number of cycles per point	29
Average error on the BM	0.60%
Average duration for simulation	32.5 min
Recovery and Purity @ CSS conditions	> 93.8

The number of points simulated is larger than the case at π = 2, and this may be a reason for the slight decrease in the average number of cycles per simulation and in the average steady-state error, however the duration of the simulations is tripled.

In order to verify the results obtained from the optimization, some check simulations with higher accuracy were carried out on 5 points, chosen in different areas of the graph in Figure 99, which are highlighted also in Figure 100 and 101.

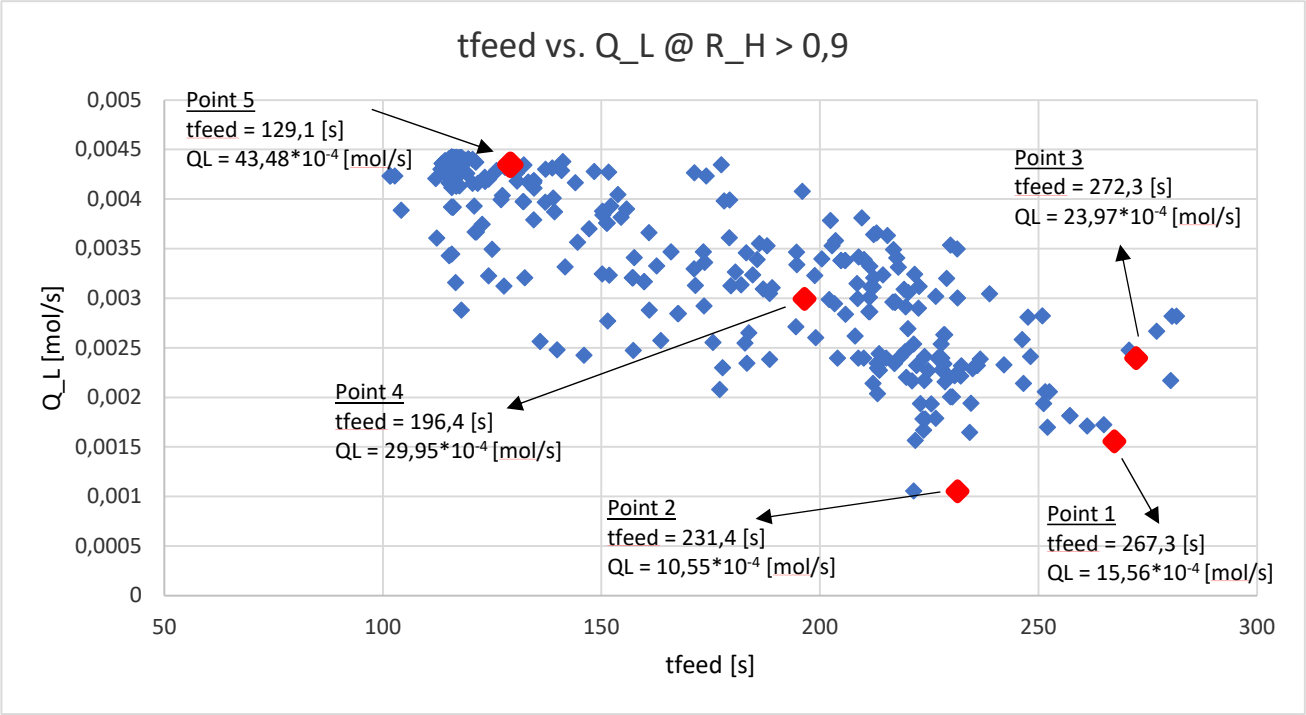

Figure 99: Check simulation points on the tFeed vs. QL plane for the case at π = 4

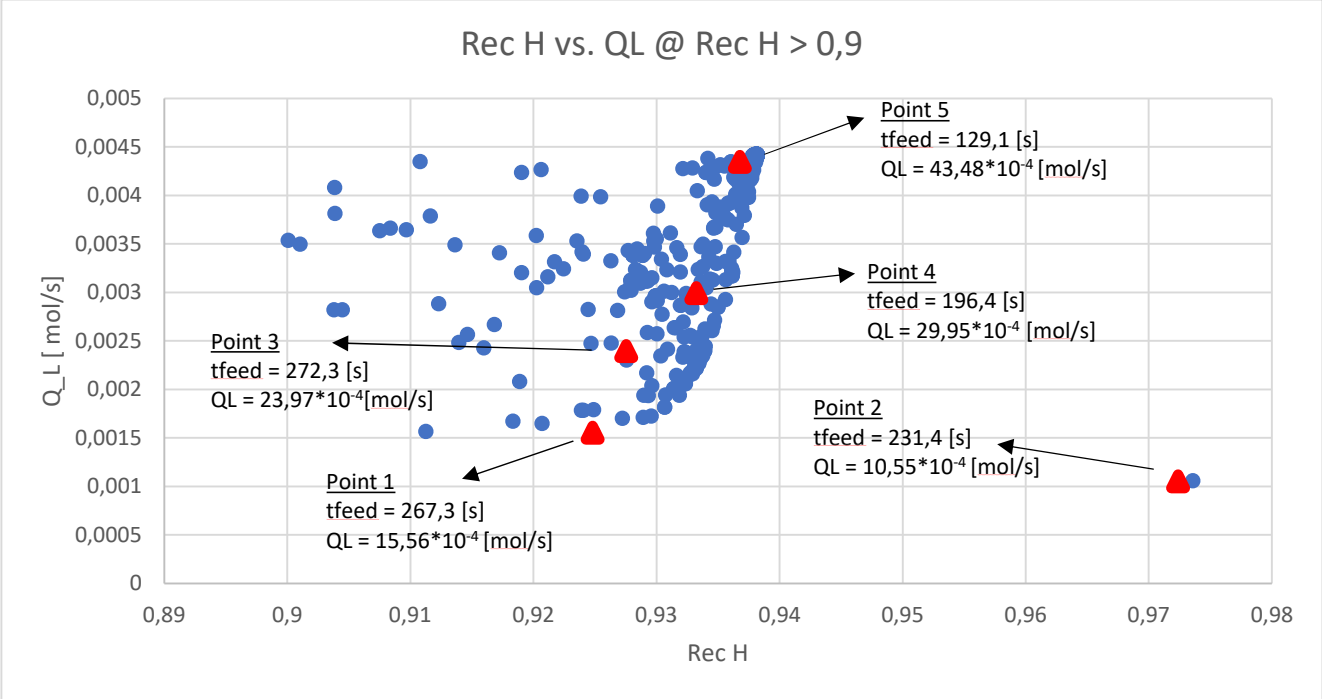

Figure 100: Check simulation points on the heavy product Recovery vs. QL plane for the case at π = 4

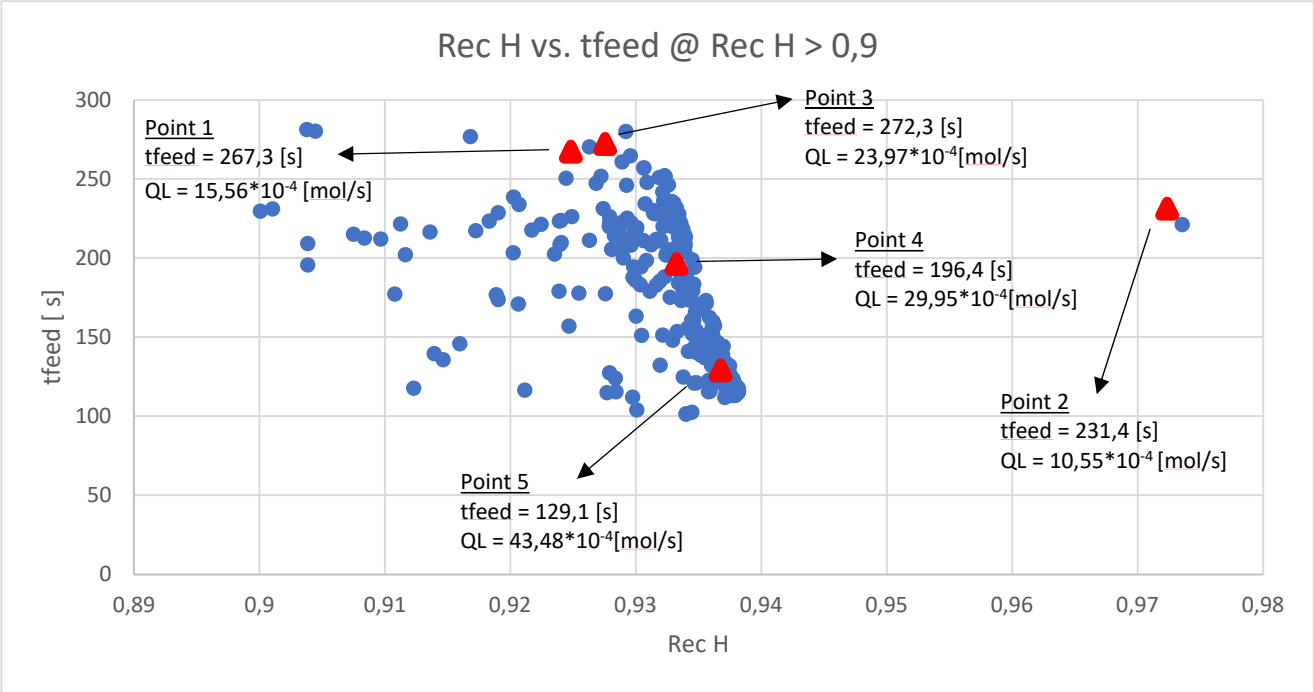

Figure 101: Check simulation points on the heavy product Recovery vs. tfeed plane for the case at π = 4

The simulations were performed with 300 computational points and the input data previously listed for the optimization. The results obtained are reported in Table 33.

Table 33: Check simulations results for the points obtained with the optimization of the case at π = 4

	Point 1	Point 2	Point 3	Point 4	Point 5
$Purity_{HP,A}$ ott	92,48	97,23	92,75	93,32	93,67
$Purity_{HP,A}$ sim	98,33	98,72	94,45	96,02	96,79
$Purity_{LP,B}$ sim	98,65	98,77	94,58	97,00	97,68
tfeed [s]	267,3	231,4	272,3	196,4	129,1
Q_L*10^{-4} [mol/s]	15,56	10,55	23,97	29,95	43,49
$\varepsilon_{rel,A}$	$3,36*10^{-3}$	$5,74*10^{-4}$	$1,65*10^{-3}$	$1,04*10^{-2}$	$9,46*10^{-3}$

The results show high purity and recovery of the heavy compound for some points and for others lower performances compared to the case at π = 2.67, however it must be

remembered that the points selected for the check simulations had purity greater than 90% as a constraint and not 94% as in the previous case.

In Figure from 102 to 107 are reported the profiles resulting for some of the check simulation performed for Point 2 and Point 4.

- Point 2

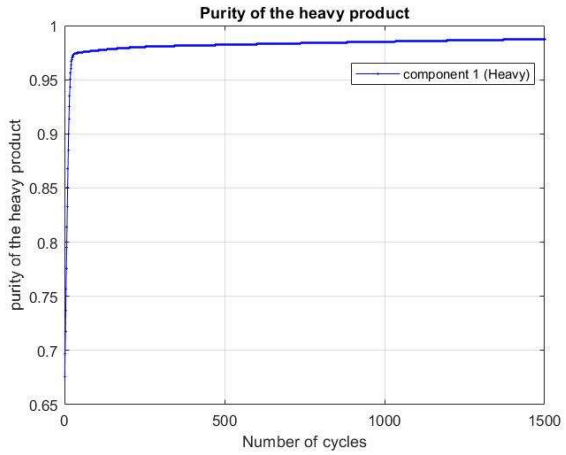

Figure 102: Heavy product purity for the check simulation of Point 2 at π = 4

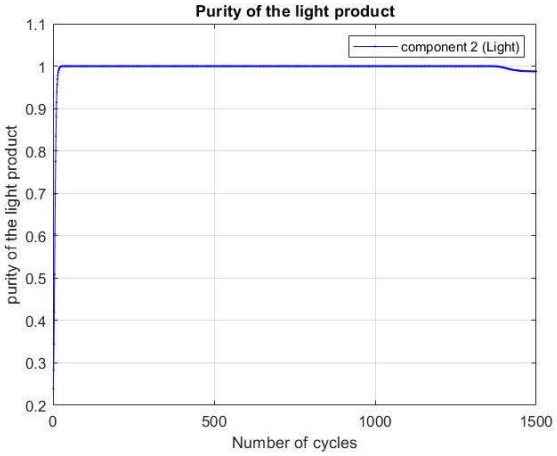

Figure 103: Light product purity for the check simulation of Point 2 at π = 4

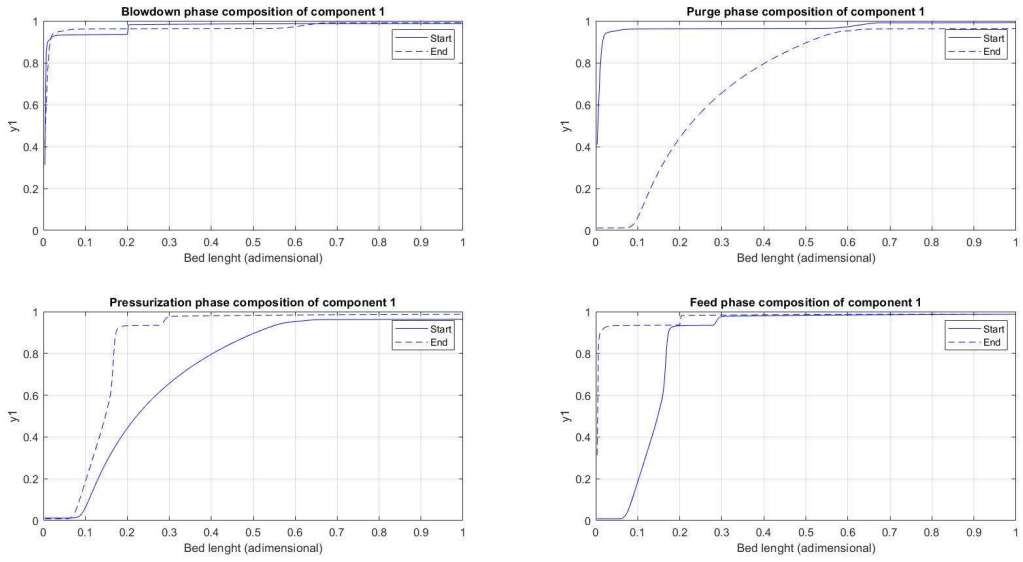

Figure 104: FVM start to end profiles for the check simulation of Point 2 at π = 4

- Point 4

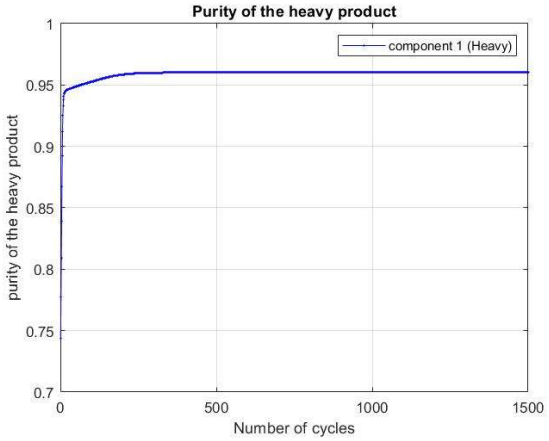

Figure 105: Heavy product purity for the check simulation of Point 4 at π = 4

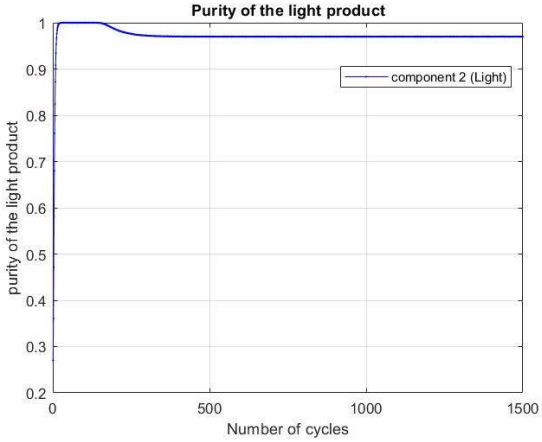

Figure 106: Light product purity for the check simulation of Point 4 at π = 4

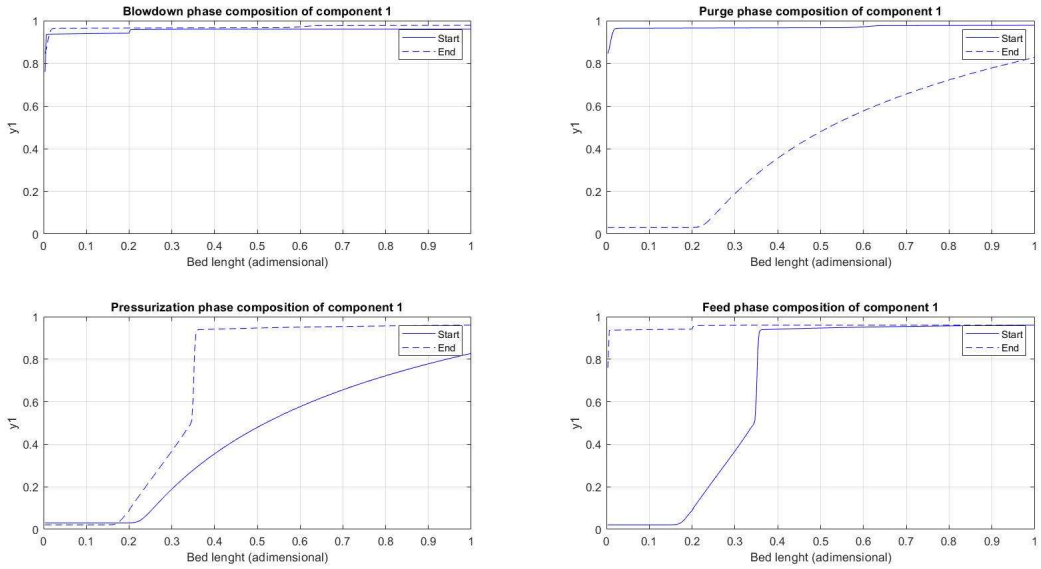

Figure 107: FVM start to end profiles for the check simulation of Point 4 at π = 4

It can be noted in Figure 104 and 107 that very sharp profiles develop in the left end of the column, therefore, small perturbation could lead to very different results.

The study on productivity and work has found results on a wide range as they are directly dependent on t_{Feed} and Q_L, some points have interesting characteristics from an economic point of view.

In Table 34 are reported the results of Productivity and Work, calculated with Eq. 2.23 and 2.24 present in paragraph 8 of chapter 2, which are graphically represented in Figure 108.

Table 34: Productivity and Work results for the simulated points for the case at π = 4

π = 4	Point 1	Point 2	Point 3	Point 4	Point 5
W [J/mol]	74240	56090	103680	134415	198815
Pr [mol/m^3/cycle]	0,054858	0,048475	0,055727	0,041992	0,028743

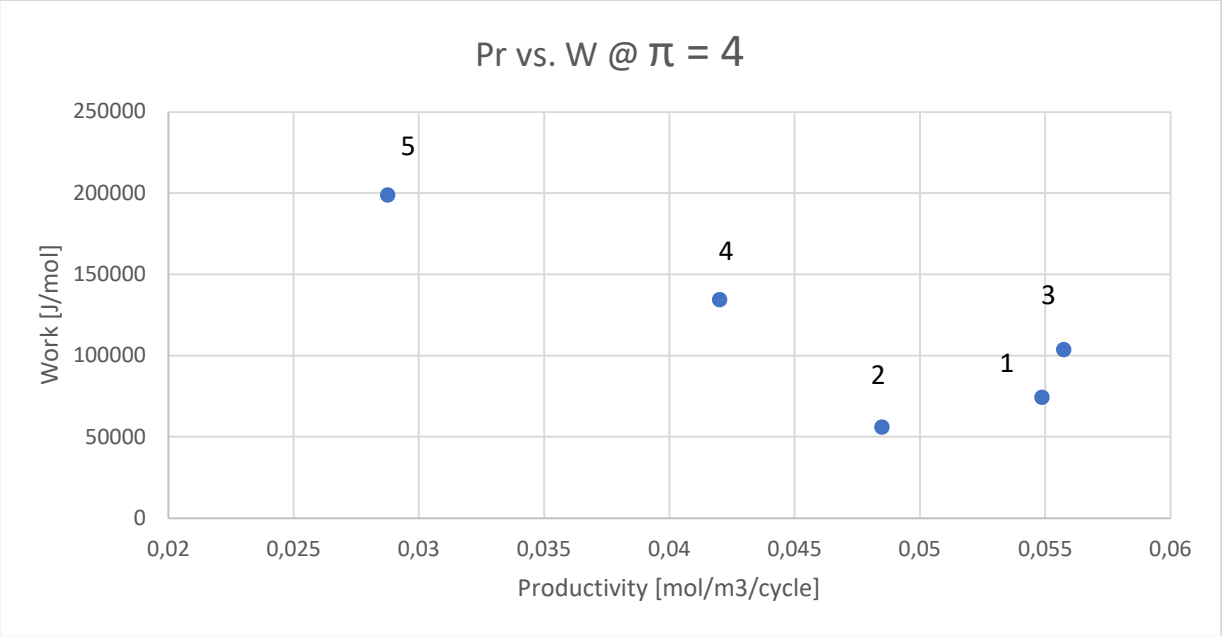

Figure 108: Check simulation Productivity vs. Work for the case at π = 4

As happened for the optimization at π = 2.67, a point was chosen, characterized at the same time by high purity and recovery of the heavy product and by low work required and high productivity, from which we started with the manual optimization by means of the bisection method.

The selected point is 2 because of its low energy requirements and relatively high productivity, associated with high purity even during optimization for which it had exceeded 97%.

The region studied was the one included between point 2 and the upper limits of t_{Feed} and lower limits of Q_L in Figure 109. The simulations were carried out with 300 computational points up to the achievement of the CSS conditions and an error on the BM of the heavy component lower than 1%.

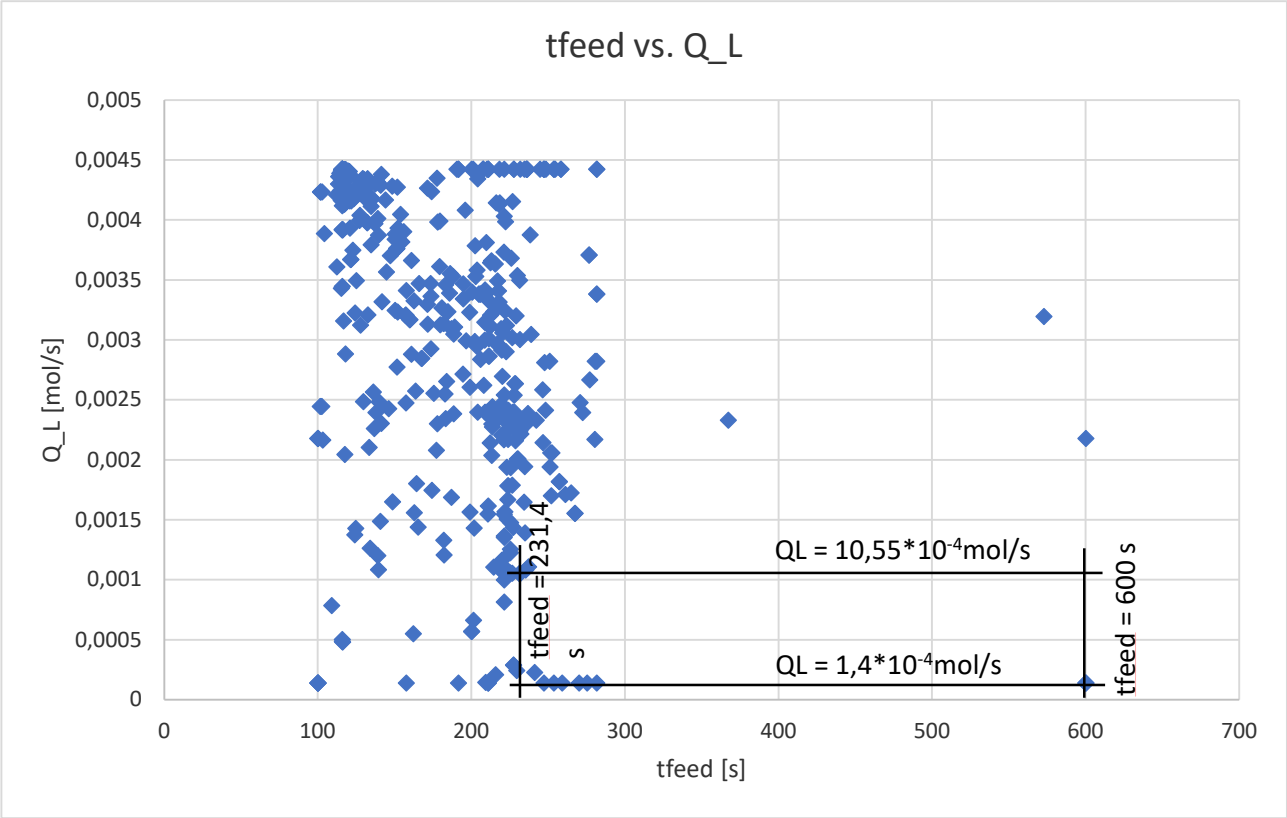

Figure 109: Starting area for the search of the region at high separation for the case at π = 4

The limits of the region at high separation were considered the points beyond which the purity and recovery of the heavy product was lower than 98%, inside it can be considered to obtain almost complete separation.

The Δt_{Feed} and ΔQ_L for the conclusion of the manual optimization work are the same as the previous case:

- Δt_{Feed} = 20 s
- $\Delta Q_L = 2*10^{-4}$ mol/s

The region found is represented in Figure 110 where the points crossed did not reach purity and recovery equal or greater than 98%.

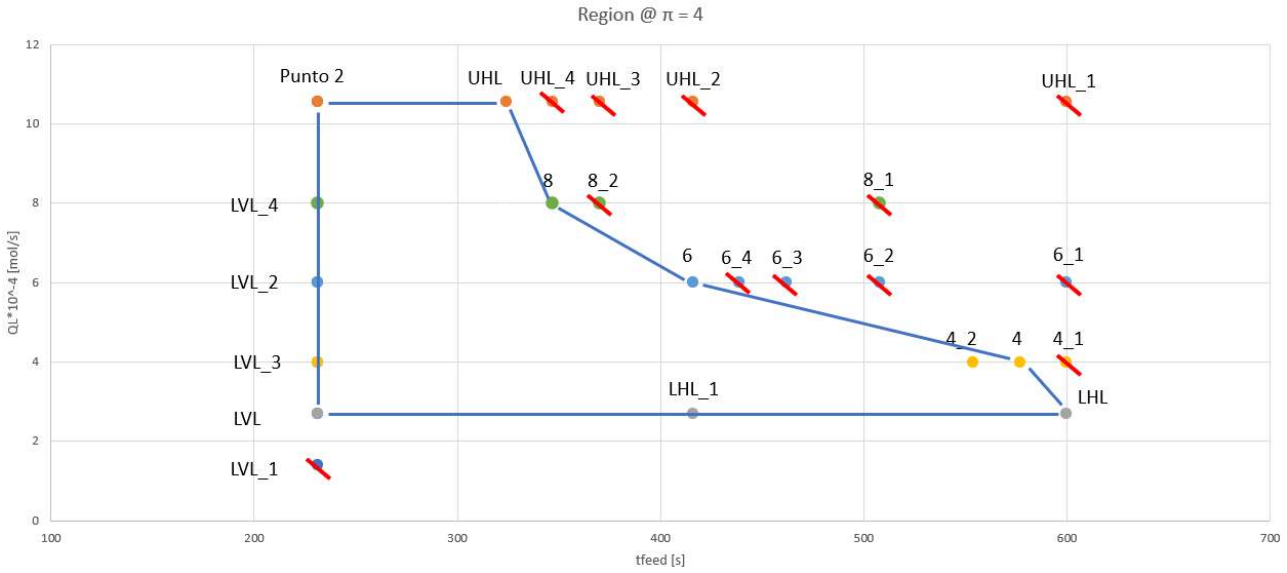

Figure 110: High separation region for the case at π = 4

The results of all the simulation carried out are reported from Table 35 to Table 40.

For the left vertical limit @ t_{Feed} = 231,4 s:

Table 35: Results of the simulations carried out for the vertical limit of the high separation region for the case at π = 2.67

	2	LVL_4	LVL_2	LVL_3	LVL	LVL_1
Q_L*10^{-4}	10,55	8	6	4	2,7	1,4
$Purity_{HP,A}$	98,72	99,04	99,50	99,66	99,66	72,36
$Purity_{LP,B}$	98,77	100	100	100	99,68	72,36
Ncycles	1500	1500	2000	1500	1475	501
$\varepsilon_{rel,A}$	$5,8*10^{-4}$	$9,6*10^{-3}$	$5,0*10^{-3}$	$3,4*10^{-3}$	$1,56*10^{-4}$	$5,8*10^{-4}$

For the upper horizontal limit @ Q_L = 10,55*10^{-4} mol/s:

Table 36: Results of the simulations carried out for the upper limit of the high separation region for the case at π = 4

	2	UHL	UHL_4	UHL_3	UHL_2	UHL_1
tfeed	231,4	324	347	370	416	600
y_H	98,72	97,99	97,70	97,73	97,50	94,16
y_L	98,77	98,01	100	97,75	97,52	94,16
Ncycles	1500	816	723	500	371	222
$\varepsilon_{rel,A}$	5,8*10^{-4}	2,8*10^{-4}	2,6*10^{-4}	2,8*10^{-4}	2,4*10^{-4}	5,0*10^{-6}

For the lower horizontal limit @ QL = 2,7*10^{-4} mol/s:

Table 37: Results of the simulations carried out for the lower limit of the high separation region for the case at π = 4

	LVL	LHL_1	LHL
tfeed [s]	231,4	416	600
$Purity_{HP,A}$	99,66	99,64	99,08
$Purity_{LP,B}$	99,68	99,59	99,08
Ncycles	1475	826	490
$\varepsilon_{rel,A}$	1,56*10^{-4}	5,4*10^{-4}	1,54*10^{-5}

Limit at $Q_L = 4*10^{-4}$ mol/s:

Table 38: Results of the simulations carried out for the limit at QL = $4*10^{-4}$ mol/s of the high separation region for the case at π = 4

	LVL_3	4	4_2	4_1
tfeed [s]	231,4	577	554	600
$Purity_{HP,A}$	99,58	97,99	98,2	97,78
$Purity_{LP,B}$	100	97,99	98,2	97,83
Ncycles	1052	389	500	331
$\varepsilon_{rel,A}$	$3,4*10^{-3}$	$8,2*10^{-5}$	$8,2*10^{-6}$	$3,6*10^{-4}$

Limit at $Q_L = 6*10^{-4}$ mol/s:

Table 39: Results of the simulations carried out for the limit at QL = $6*10^{-4}$ mol/s of the high separation region for the case at π = 4

	LVL_2	6	6_4	6_3	6_2	6_1
tfeed [s]	6	416	439	462	508	600
$Purity_{HP,A}$	99,50	98,03	97,82	97,62	97,26	96,62
$Purity_{LP,B}$	100	98,04	97,83	97,63	97,26	96,63
Ncycles	2000	634	521	534	404	288
$\varepsilon_{rel,A}$	$5,0*10^{-3}$	$8,8*10^{-5}$	$9,0*10^{-5}$	$5,2*10^{-5}$	$8,0*10^{-5}$	$8,6*10^{-5}$

Limit at $Q_L = 8*10^{-4}$ mol/s:

*Table 40: Results of the simulations carried out for the limit at QL = 8*10^{-4} mol/s of the high separation region for the case at π = 4*

	LVL_4	8	8_2	8_1
tfeed [s]	231,4	347	370	508
$Purity_{HP,A}$	99,04	98,05	97,87	97,00
$Purity_{LP,B}$	100	98,07	97,88	97,01
Ncycles	1500	698	658	368
$\varepsilon_{rel,A}$	$9,6*10^{-3}$	$1,66*10^{-4}$	$1,68*10^{-4}$	$1,56*10^{-4}$

In Figure 111 to 115 are reported the profile of the case LHL.

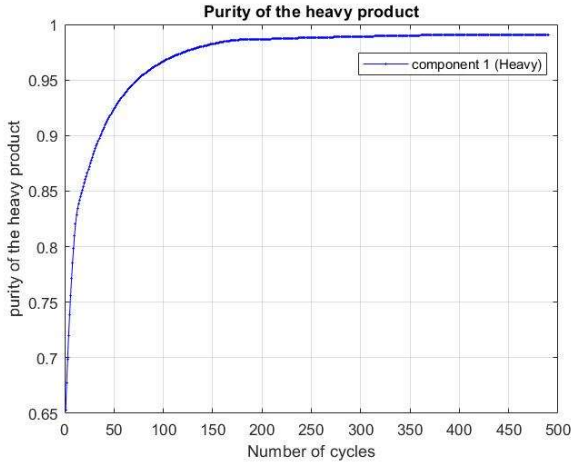

Figure 111: Heavy product purity for the simulation of LHL at π = 4

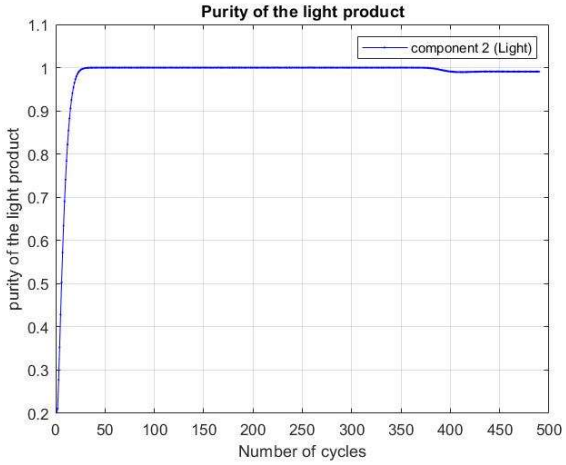

Figure 112: Light product purity for the simulation of LHL at π = 4

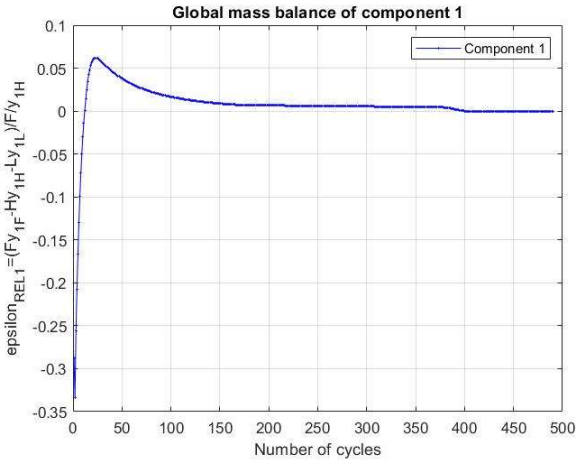

Figure 113: Error on the heavy product BM for the simulation of LHL at π = 4

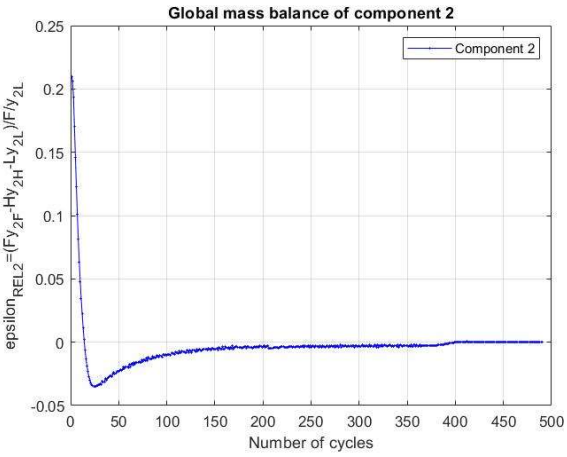

Figure 114: Error on the light product BM for the simulation of LHL at π = 4

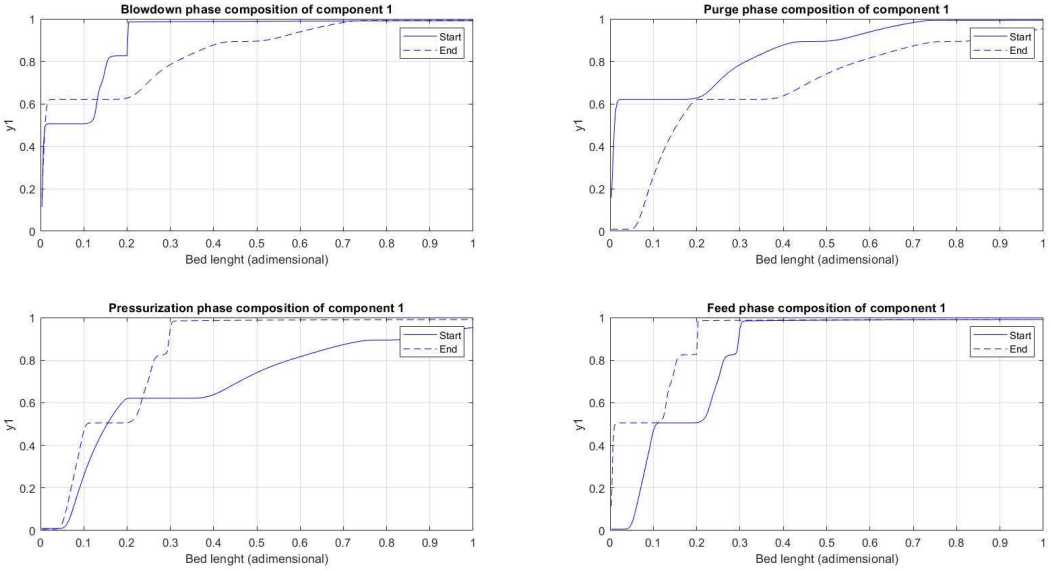

Figure 115: FVM start to end profiles for the simulation of LHL at π = 4

It can be noted in Figure 115 that very sharp profiles develop in the left end of the column, therefore, small perturbation could lead to very different results.

The results in terms of productivity and work for the points constituting the boundaries of the region are reported in Table 41 and Figure 116.

Table 41: Productivity and Work results for the boundaries of the high separation region at π = 4

	tfeed	QL	Pr	W
2	231,4	0,001055	0,048475	56090
UHL	324	0,001055	0,064428	51345
LVL_4	231,4	0,0008	0,048475	46196
LVL_2	231,4	0,0006	0,048475	38342,5
LVL_3	231,4	0,0004	0,048475	30683,5
LVL	231,4	0,00027	0,048475	24986,5
LHL	600	0,00027	0,10363	14976
LHL_1	416	0,00027	0,07875	17836
8	347	0,0008	0,068142	40367,5
6	416	0,0006	0,07875	30615
4	577	0,0004	0,100761	20195,5

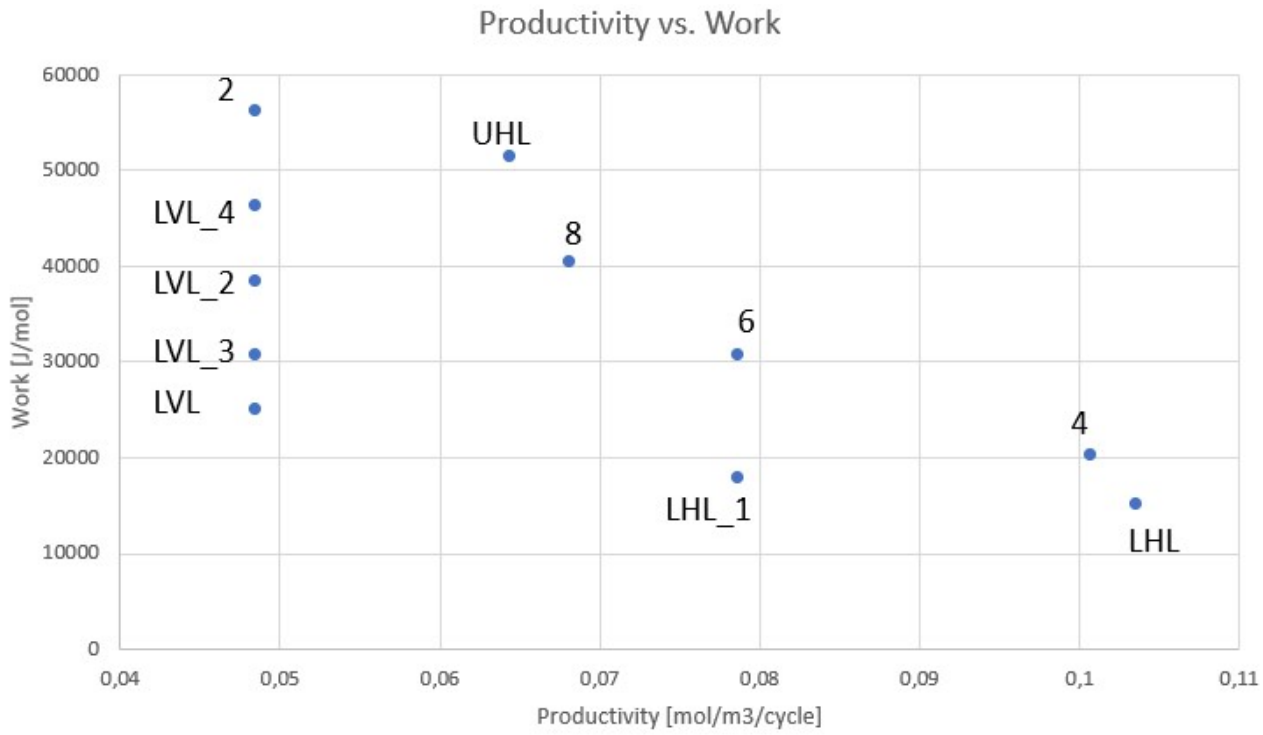

Figure 116: Productivity vs. Work for the high separation region at π = 4

As in the previous case, a further analysis was carried out, moving towards t_{Feed} values beyond the upper boundary and Q_L values up to the upper limit. Several simulations were carried out with 300 computational points, applying the bisection method to find the boundaries of the region with purity and recovery of the heavy product greater than or equal to 98%. Δt_{Feed} and ΔQ_L of the previous cases were maintained.

The new region found is reported in Figure 117.

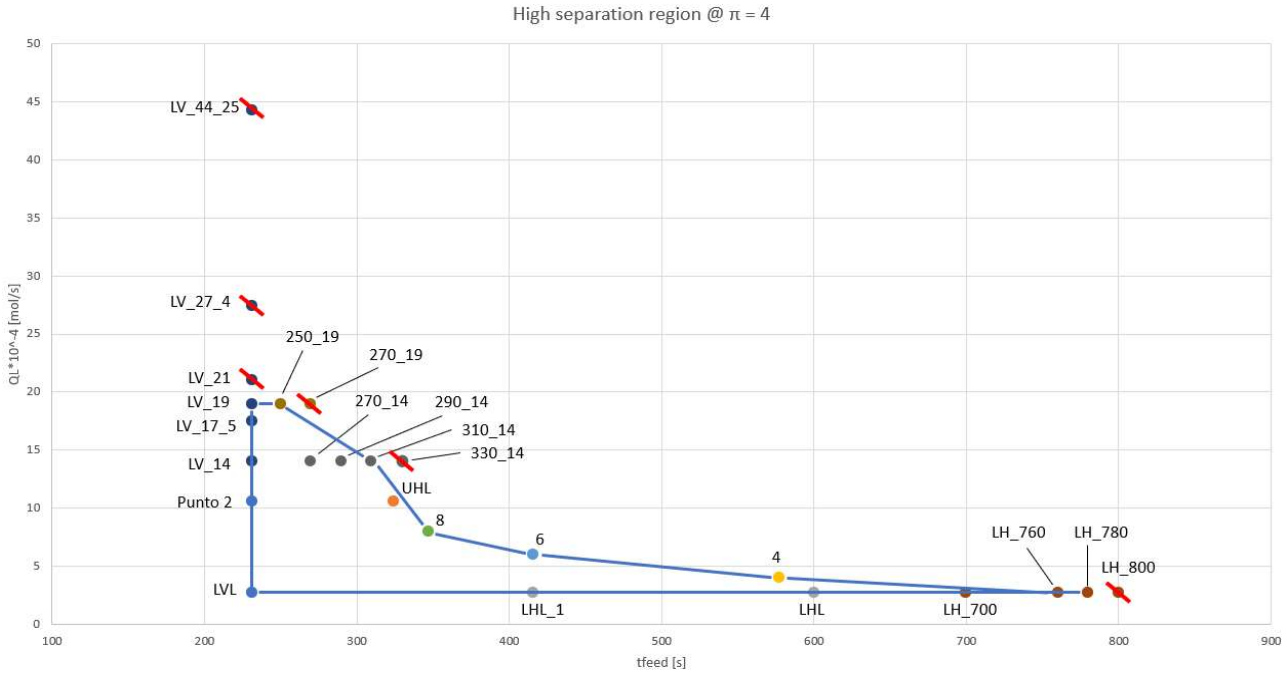

Figure 117: Extended high separation region at π = 4

The numerical results are reported from Table 42 to 44.

Horizontal limit at $Q_L = 2{,}7*10^{-4}$ mol/s:

Table 42: Results of the further simulations performed for the lower limit of the high separation region at π = 4

	LH_700	LH_800	LH_760	LH_780	LHL
tfeed	700	800	760	780	600
$Purity_{HP,A}$	98,51	97,89	98,14	98,02	99,08
$Purity_{LP,B}$	98,51	97,89	98,15	98,02	99,08
$\varepsilon_{rel,A}$	$9{,}6*10^{-6}$	$1{,}8*10^{-5}$	$1{,}06*10^{-5}$	$3{,}8*10^{-6}$	$1{,}54*10^{-5}$
W [J/mol]	14019,5	13276,5	13553,5	13412,5	14976
Ncycles	744	454	382	406	490

Vertical limit at t_{Feed} = 231,4 s:

Table 43: Results of the further simulations performed for the vertical limit of the high separation region at π = 4

	LV_44_25	LV_27_4	LV_14	LV_21	LV_17_5	LV_19	Punto 2
$QL*10^{-4}$	44,25	27,4	14	21	17,5	19	10,55
$Purity_{HP,A}$	85,28	94,99	98,52	97,91	98,53	98,44	98,72
$Purity_{LP,B}$	85,24	95,01	98,56	97,98	98,60	98,51	98,77
$\varepsilon_{rel,A}$	$1,12*10^{-3}$	$5,4*10^{-4}$	$5,4*10^{-4}$	$7,8*10^{-4}$	$7,6*10^{-4}$	$7,6*10^{-4}$	$5,8*10^{-4}$
W [J/mol]	167325	119850	69975	97795	84210	90215	56090
Ncycles	447	350	1500	635	1083	938	1500

Horizontal limit at $Q_L = 14*10^{-4}$ mol/s and $Q_L = 19*10^{-4}$ mol/s:

Table 44: Results of the further simulations performed for the limit at QL = $14*10^{-4}$ mol/s and QL = $19*10^{-4}$ mol/s of the high separation region at π = 4

	270_14	290_14	310_14	330_14	250_19	270_19
tfeed	270	290	310	330	250	270
$Purity_{HP,A}$	98,29	98,19	98,07	97,80	97,99	97,35
$Purity_{LP,B}$	98,33	98,24	98,11	97,82	98,05	97,39
$\varepsilon_{rel,A}$	$5,2*10^{-4}$	$5,2*10^{-4}$	$4,4*10^{-4}$	$3,4*10^{-4}$	$6,6*10^{-4}$	$5,0*10^{-4}$
W [J/mol]	67645	66680	66175	64940	88670	87040
Ncycles	1014	715	832	879	1062	453

The profiles of case LH_780 are reported as example in Figure 118 to 122.

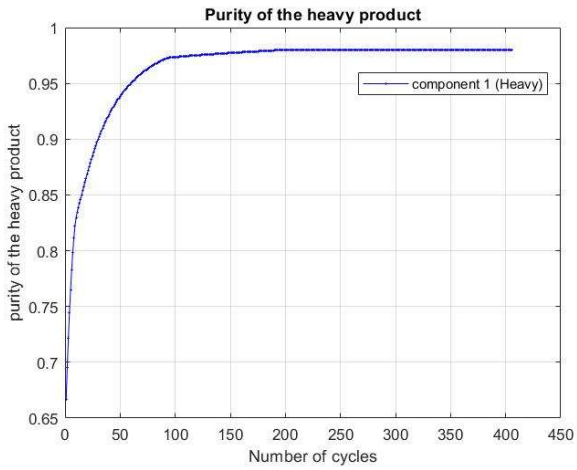

Figure 118: Heavy product purity for the simulation of LH_780 at π = 4

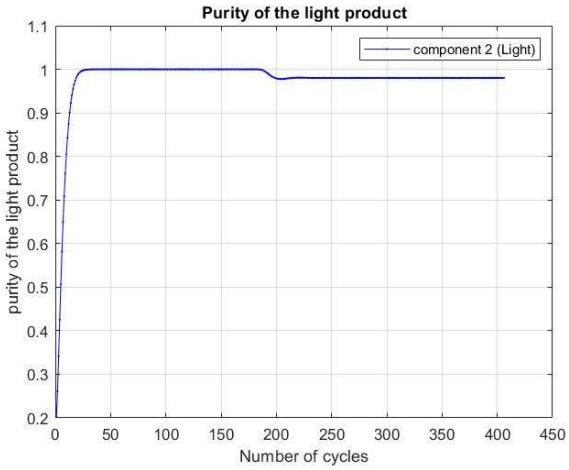

Figure 119: Light product purity for the simulation of LH_780 at π = 4

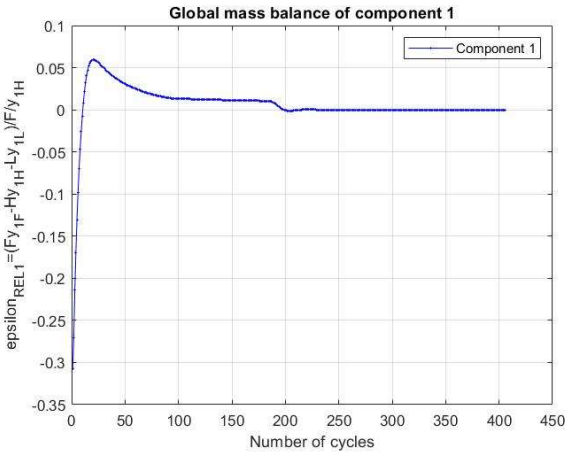

Figure 120: Error on the heavy product BM for the simulation of LH_780 at π = 4

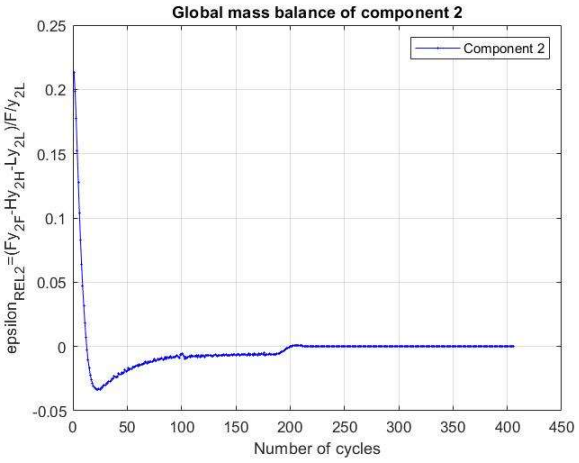

Figure 121: Error on the light product BM for the simulation of LH_780 at π = 4

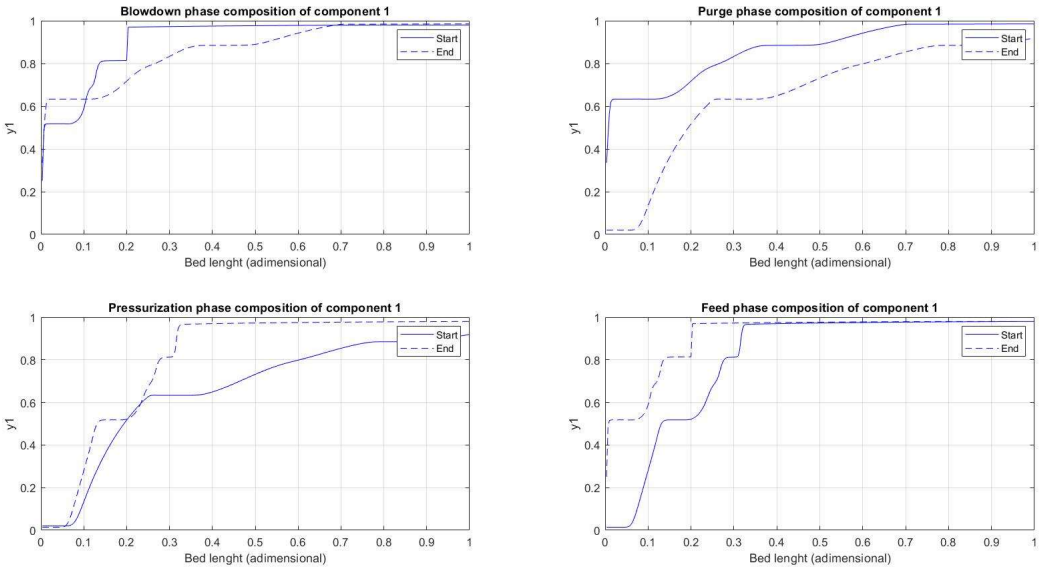

Figure 122: FVM start to end profiles for the simulation of LH_780 at π = 4

The results in terms of productivity and work for the points constituting the boundaries of the region are reported in Table 45 and Figure 123.

Table 45: Productivity and Work results for the boundaries of extended the high separation region at π = 4

π = 4	tfeed	QL	Pr	W
2	231,4	0,001055	0,048475	56090
UHL	324	0,001055	0,064428	51345
LVL	231,4	0,00027	0,048475	24986,5
LHL	600	0,00027	0,10363	14976
LHL_1	416	0,00027	0,07875	17836
8	347	0,0008	0,068142	40367,5
6	416	0,0006	0,07875	30615
4	577	0,0004	0,100761	20195,5
LH_700	700	0,00027	0,115406	14019,5
LH_760	760	0,00027	0,121972	13553,5
LH_780	780	0,00027	0,124083	13412,5
LV_14	231,4	0,0014	0,048475	69975
LV_17_5	231,4	0,00175	0,048475	84210
LV_19	231,4	0,0019	0,048475	90215
250_19	250	0,0019	0,051815	88670
310_14	310	0,0014	0,062121	66175

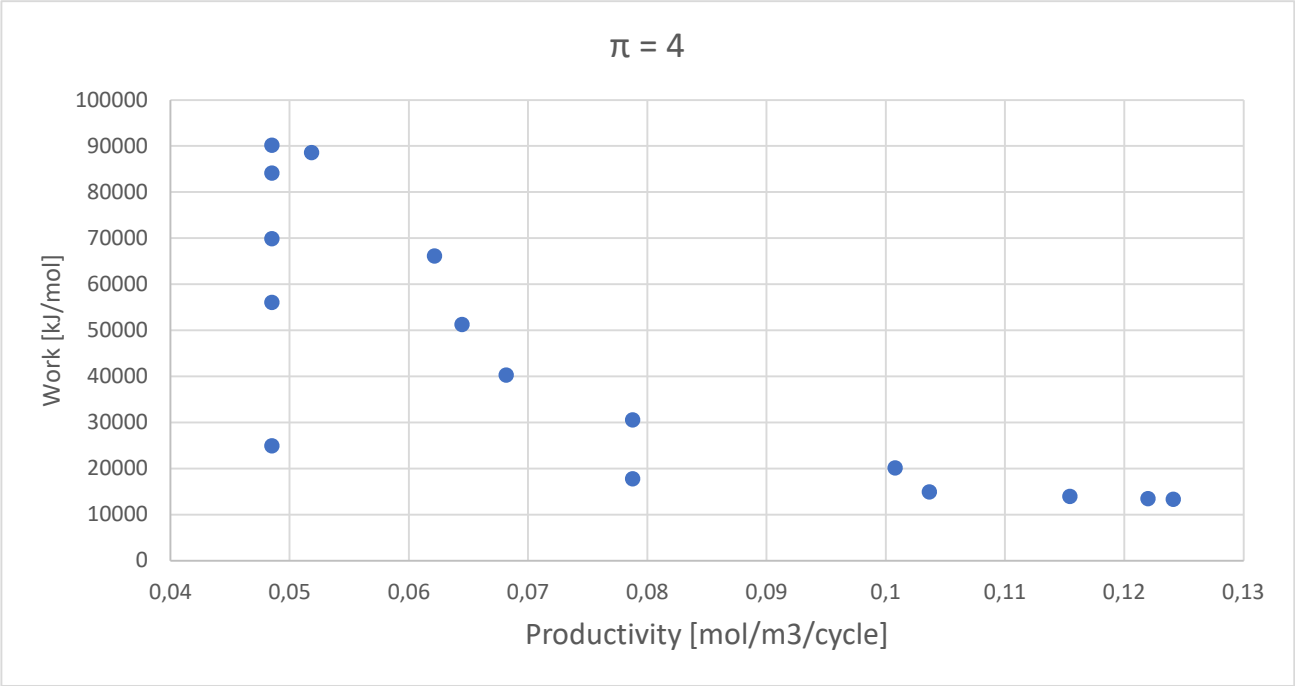

Figure 123: Productivity vs. Work for the extended high separation region at π = 4

The resulting high separation region shows a trend similar to the previous case where the LHL_780 point, characterized by high purity and recovery of the heavy component, is also the point with higher productivity and less work required. Since it is at the right vertex of the region, it cannot be considered robust, in terms of t_{Feed} and especcially Q_L, as with a little variation of the operative conditions the performance of the process falls down, findining a point outside the region where high separation is obtained.

Continuing in this direction, it was decided to carry out a further analysis at π = 6, with the aim of comparing the performance of the process over a wider range of π.

4.3. π = 6

A work similar to the previous cases was carried out by lowering the value of the low pressure P_L at $2*10^5$ Pa, keeping fixed $P_H = 12*10^5$ Pa.

An optimization with 50 computational points was performed with variable t_{Feed} and Q_L inside the boundaries in Table 46 where the upper limit of t_{Feed} was increased in order to favour the search for higher productivity, the Q_L limits remained unchanged compared to the previous optimizations.

Table 46: tFeed and QL boundaries for the optimization of the heavy component purity and recovery for the case at π = 6

	min	max
t_feed [s]	100	700
Q_L [mol/s]	0.8*Q_feed = 0.000142	25*Q_feed = 0.004425

The input data are reported in Table 40 and they are the same as in the previous cases except for the value of P_L.

In Figure 124 are reported the heavy product purity and recovery results, because of the heavy product flowrate set equal to the stoichiometric one, the points are disposed on the diagonal.

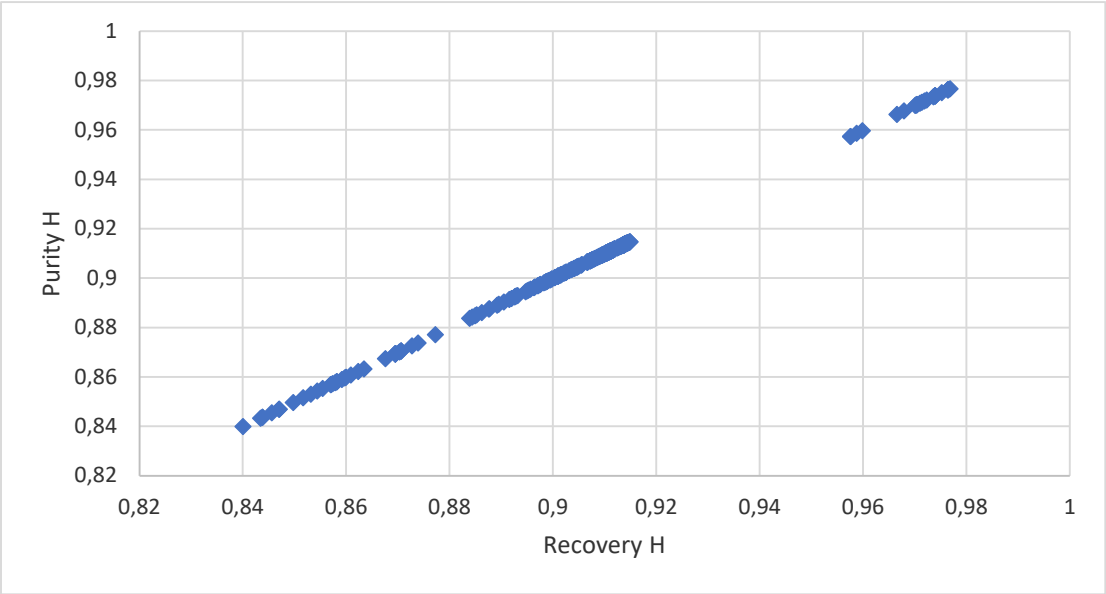

Figure 124: Purity vs. Recovery for the heavy product optimization at π = 6

The results obtained, once stationary conditions are reached, tend to settle at purity and recovery values lower than 92%, although some points were found with purity and recovery of the heavy product between 95 and 98%.

In Figure 121, 122 and 123 all the results obtained by the optimizer are graphically represented, with the recovery as a function of the two manipulated variables t_{Feed} and Q_L and a graph with the duration of the feed phase versus the recycling flowrate of the light component.

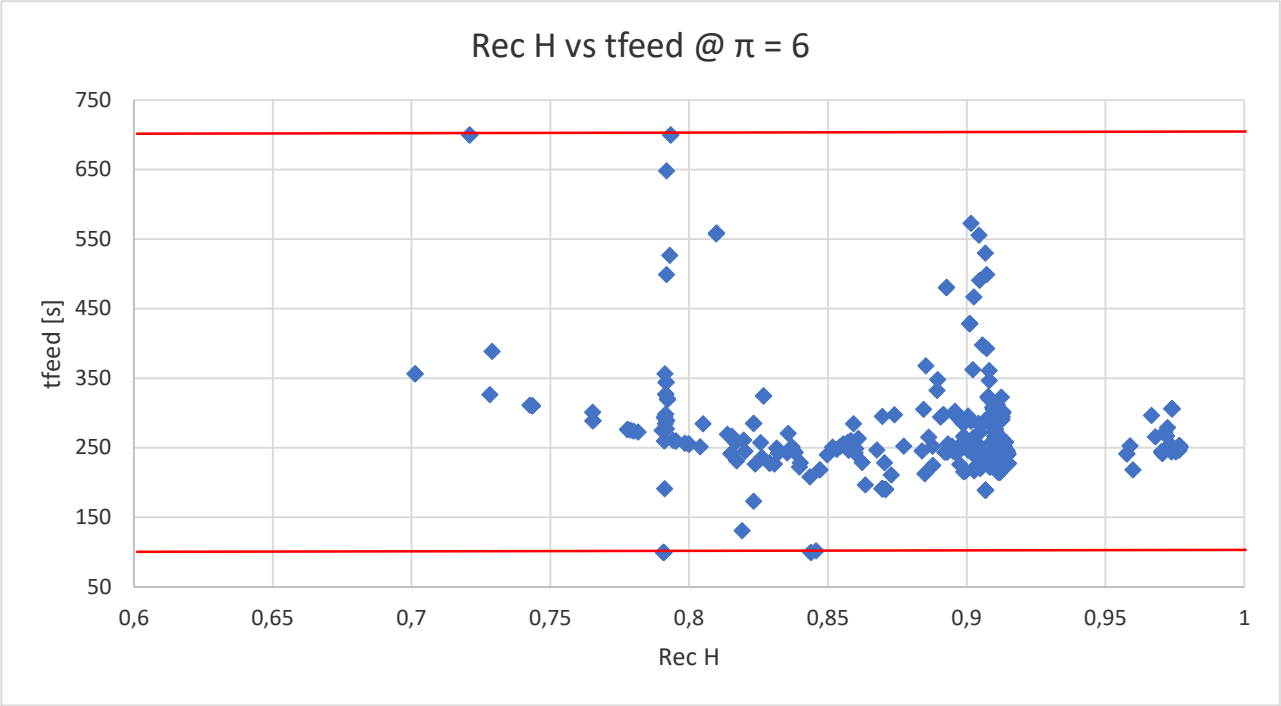

Figure 125: Results on the plane heavy product recovery vs. tFeed for the optimization at π = 6

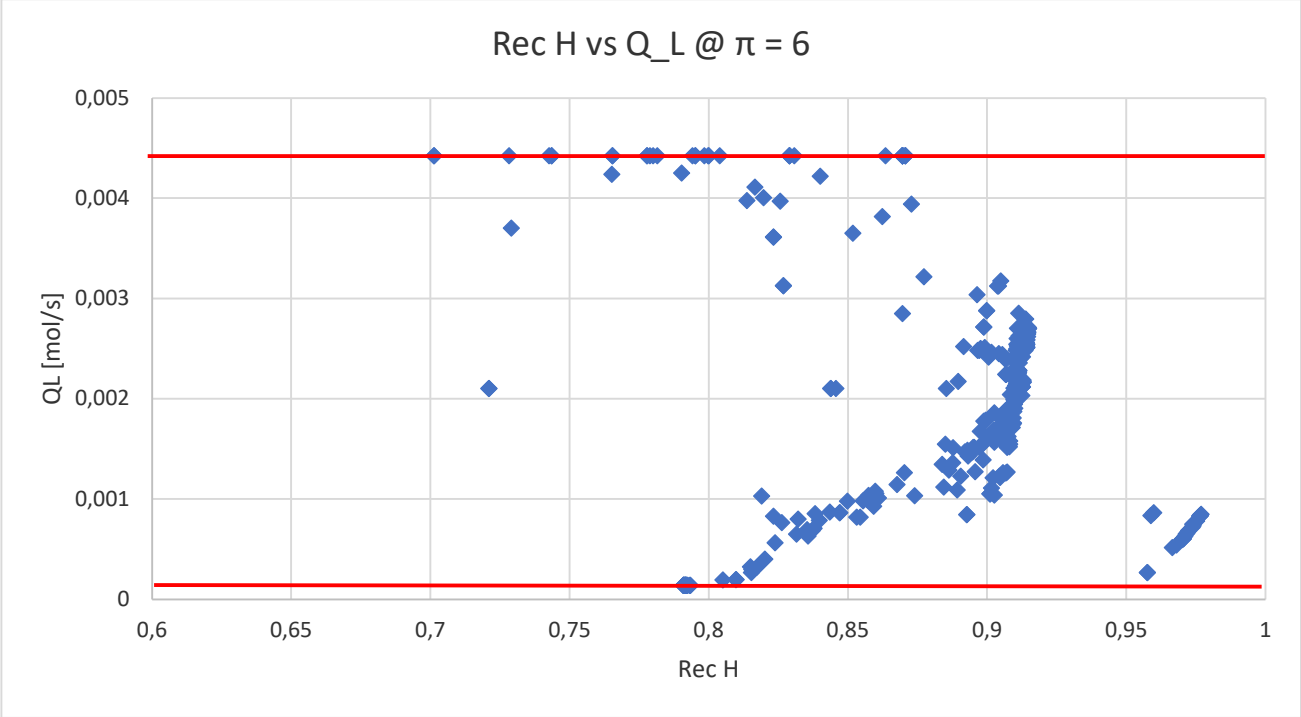

Figure 126: Results on the plane heavy product recovery vs. QL for the optimization at π = 6

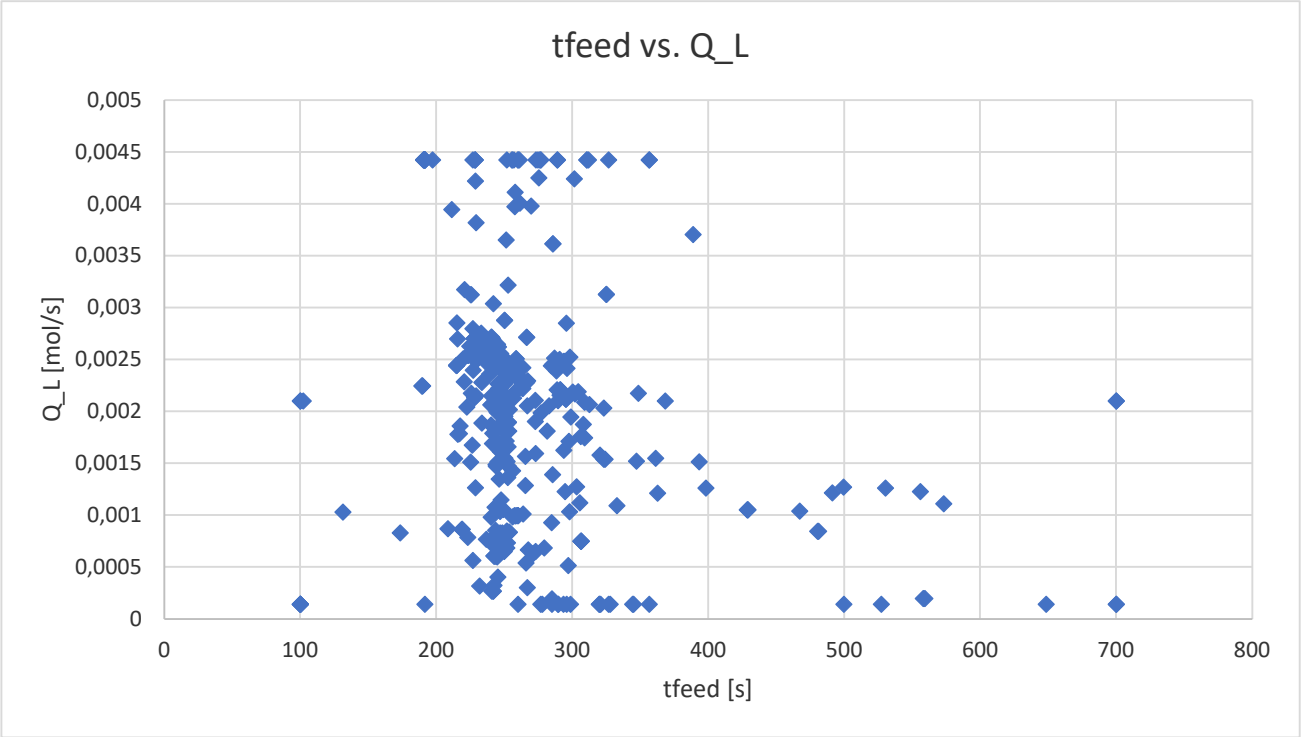

Figure 127: Results on the plane tFeed vs. QL for the optimization at π = 6

Both limits of t_{Feed} and Q_L appear adequate as the points are distributed within them without thickening against.

In Figure 128 to 131 are shows the results on the plane t_{Feed} vs. Q_L at different intervals of purity and recovery of the heavy component.

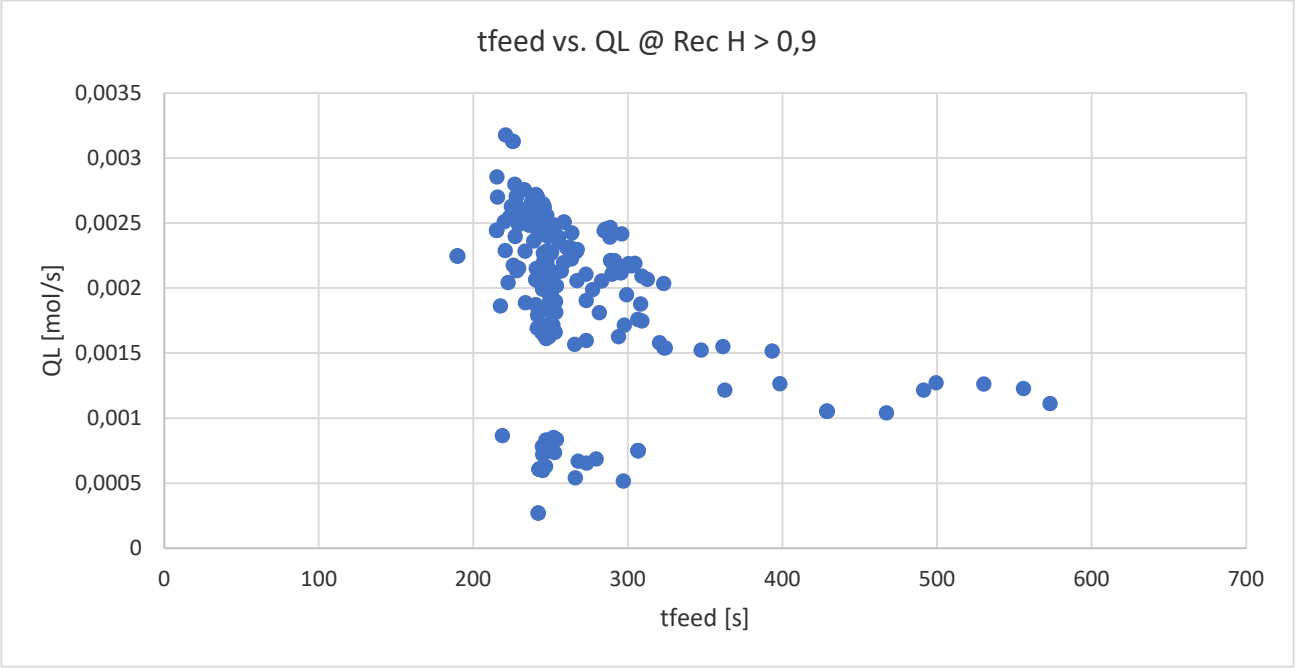

Figure 128: Results with purity > 90% of the heavy product optimization at π = 6

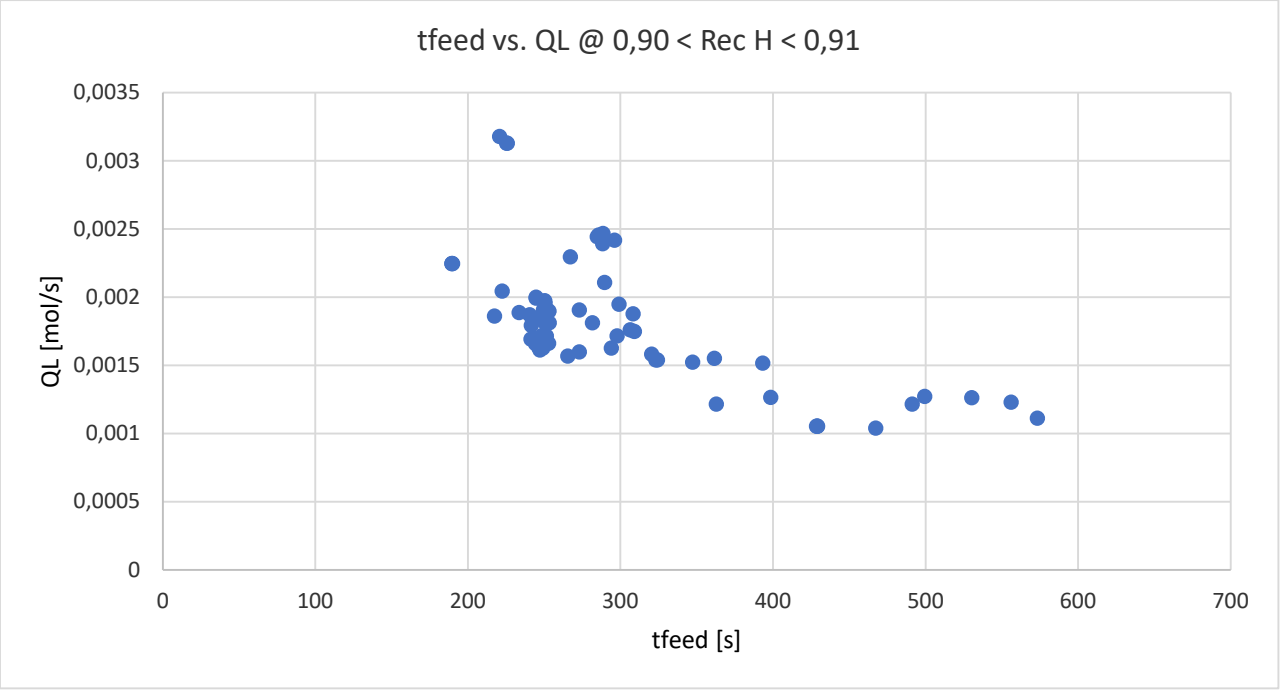

Figure 129: Results with purity between 90 and 91% of the heavy product optimization at π = 6

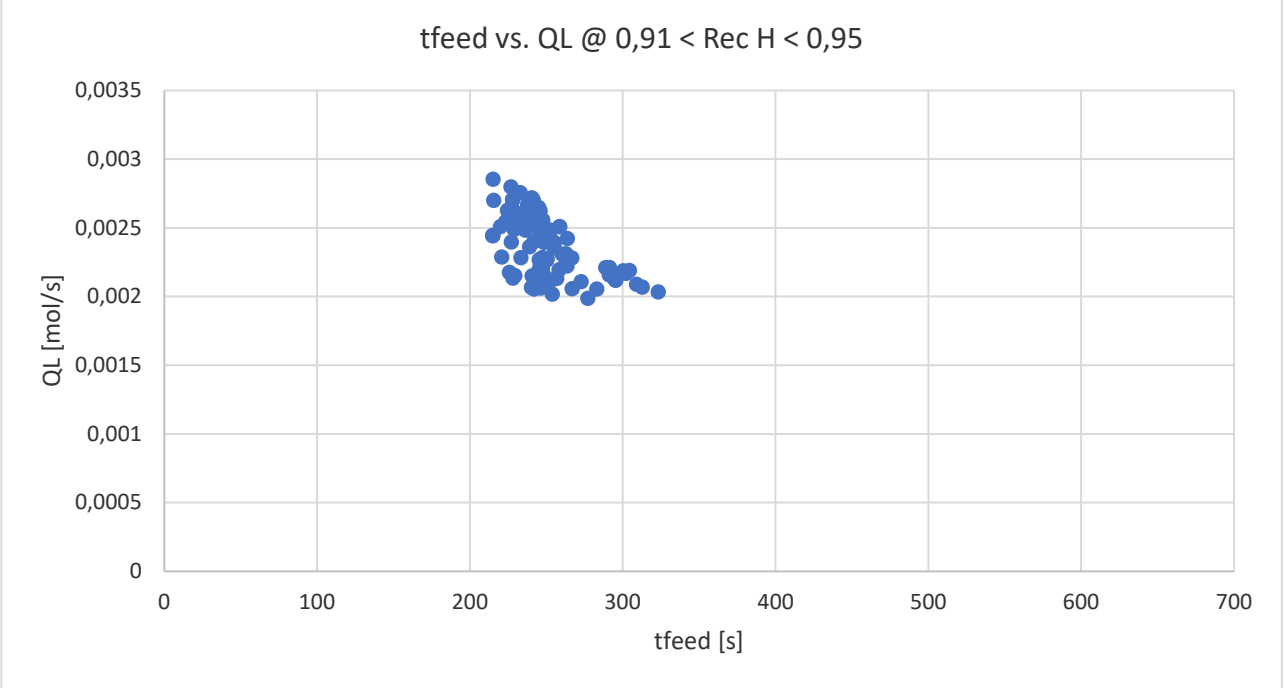

Figure 130: Results with purity between 91 and 95% of the heavy product optimization at π = 6

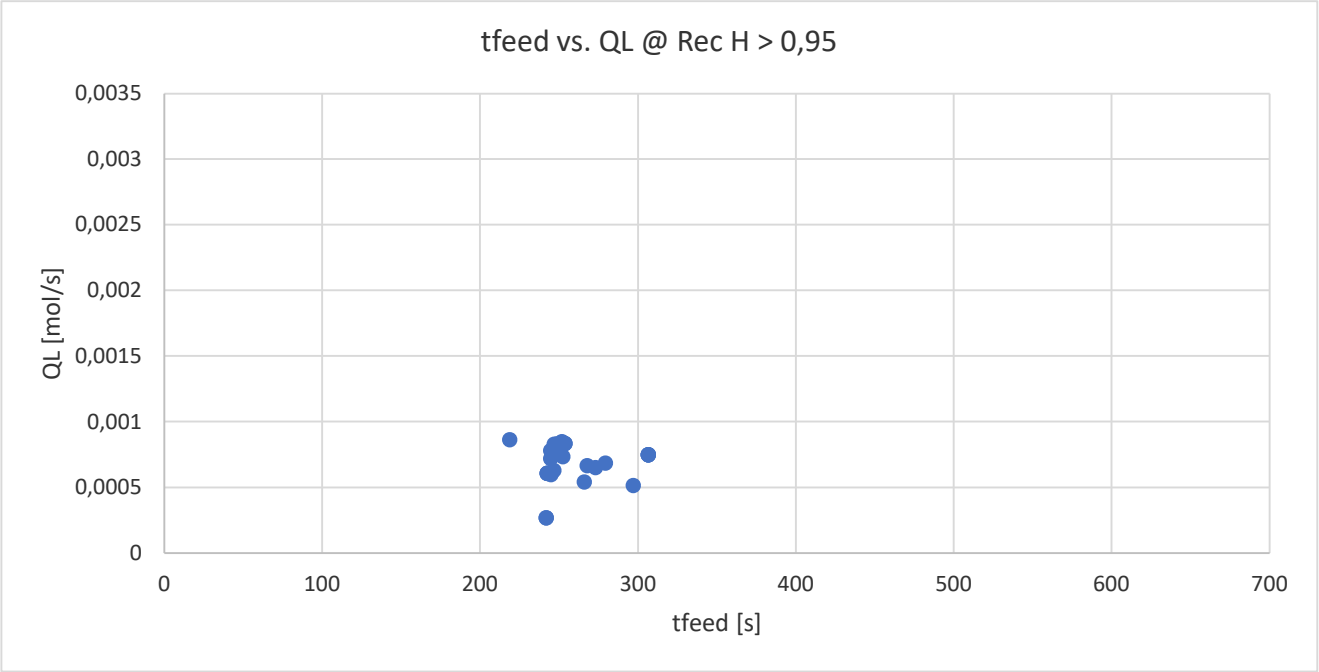

Figure 131: Results with purity > 95% of the heavy product optimization at π = 6

It can be easily seen that there is a relatively small range of Q_L and t_{Feed} in which a group of points is lumped where it is possible to obtain high purity and recovery.

The characteristics of the optimization are shown in Table 47.

Table 47: Results for the heavy product purity and recovery optimization with variable tFeed and QL for the case at π = 6

	π = 6
Number of points simulated	435
Average number of cycles per point	68
Average error on the BM	0.54%
Average duration for simulation	105 min
Recovery and Purity @ CSS conditions	< 92

The average number of cycles is higher because the simulations of the points with high purity and recovery required a greater computational effort, moreover, as π increases also the

duration increases considerably up to 105 minutes per simulation, bringing the total time necessary for this optimization to one month. On the other hand, the average purity obtained in stationary conditions is lower than the one at lower π values.

As performed in the previous cases, the manual optimization work by means of the bisection method was carried out in a region with high productivity and low work required starting from one of the point found. The selected point, named point 1, is among those with the highest purity with:

- t_{Feed} = 253,67 s
- Q_L = 8,35*10^{-4} mol/s

The area under study is shown in Figure 132.

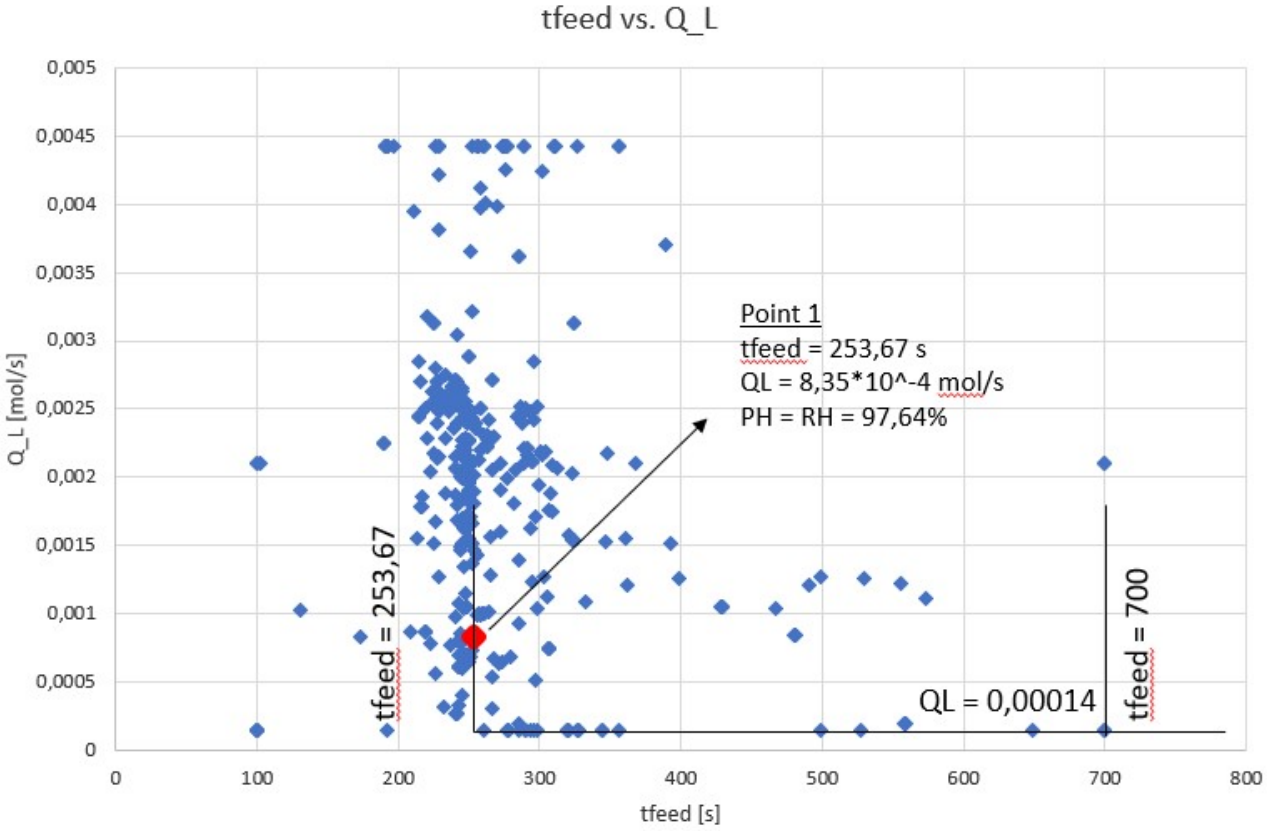

Figure 132: Starting area for the search of the region at high separation for the case at π = 6

The simulations were carried out with 300 computational points up to the achievement of the CSS conditions and an error on the BM of the heavy component lower than 1%. The limits of the high separation region were searched for, an upper limit for Q_L was not initially set for the manual optimization, but we proceeded to look for the value beyond which the purity of the heavy product was less than 98%.

The Δt_{Feed} and ΔQ_L were identified, reached which the manual optimization work could be considered cocluded, as in the previous cases:

- Δt_{Feed} = 20 s

- $\Delta Q_L = 2*10^{-4}$ mol/s

The region found is represented in Figure 133 where the points crossed did not reach purity and recovery equal or greater than 98% which can be obtained in the region between the blue lines.

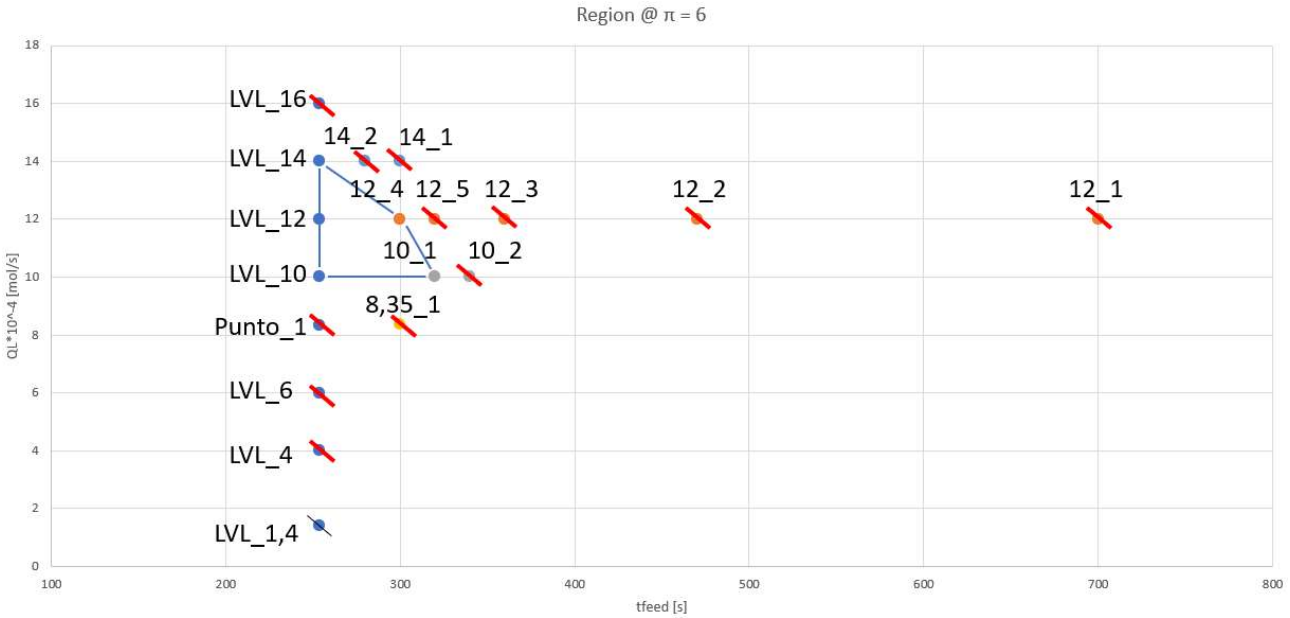

Figure 133: High separation region for the case at π = 6

The results of all the simulation carried out are reported from Table 48 to Table 52.

For the left vertical limit @ t_{Feed} = 253,67 s:

Table 48: Results of the simulations carried out for the vertical limit of the high separation region for the case at π = 6

	1	LVL_1,4	LVL_4	LVL_6	LVL_10	LVL_12	LVL_14	LVL_16
Q_L*10^{-4}	8,35	1,4	4	6	10	12	14	16
$Purity_{HP,A}$	97,77	87,69	96,89	97,24	98,06	98,33	98,21	97,55
$Purity_{LP,B}$	98,22	87,89	97,09	97,57	98,61	99,00	98,98	98,41
Ncycles	1500	600	823	895	489	1196	1014	407
$\varepsilon_{rel,A}$	$4,6*10^{-3}$	$2,2*10^{-3}$	$2,2*10^{-3}$	$3,4*10^{-3}$	$5,6*10^{-3}$	$6,8*10^{-3}$	$7,8*10^{-3}$	$8,8*10^{-3}$

Limit at $Q_L = 12*10^{-4}$ mol/s:

*Table 49: Results of the simulations carried out for the limit at QL = 12*10^{-4} mol/s of the high separation region for the case at π = 6*

	12_1	12_2	12_3	12_4	12_5
tfeed	700	470	360	300	320
$Purity_{HP,A}$	86,83	93,89	96,84	97,98	97,65
$Purity_{LP,B}$	86,82	93,91	96,86	98,02	97,69
Ncycles	194	145	364	557	221
$\varepsilon_{rel,A}$	$5,0*10^{-5}$	$2,8*10^{-4}$	$2,6*10^{-4}$	$4,8*10^{-4}$	$3,8*10^{-4}$

Limit at $Q_L = 10*10^{-4}$ mol/s:

*Table 50: Results of the simulations carried out for the limit at QL = 10*10^{-4} mol/s of the high separation region for the case at π = 6*

	LVL_10	10_1	10_2
tfeed	253,67	320	340
$Purity_{HP,A}$	98,06	97,98	97,89
$Purity_{LP,B}$	98,61	98,02	97,92
Ncycles	489	150	157
$\varepsilon_{rel,A}$	$5,6*10^{-3}$	$4,6*10^{-4}$	$3,4*10^{-4}$

Limit at $Q_L = 8.35*10^{-4}$ mol/s:

*Table 51: Results of the simulations carried out for the limit at QL = 8,35*10^{-4} mol/s of the high separation region for the case at π = 6*

	Punto 1	8,35_1
tfeed	253,67	300
$Purity_{HP,A}$	97,77	97,70
$Purity_{LP,B}$	98,22	97,74
Ncycles	1500	240
$\varepsilon_{rel,A}$	$4,6*10^{-3}$	$3,6*10^{-4}$

Limit at $Q_L = 14*10^{-4}$ mol/s:

*Table 52: Results of the simulations carried out for the limit at QL = 14*10^{-4} mol/s of the high separation region for the case at π = 6*

	LVL_14	14_1	14_2
tfeed	14	300	280
$Purity_{HP,A}$	98,21	97,22	97,71
$Purity_{LP,B}$	98,98	97,23	97,75
Ncycles	1014	153	218
$\varepsilon_{rel,A}$	$7,8*10^{-3}$	$8,6*10^{-5}$	$5,0*10^{-4}$

In Figure 134 to 138 are reported the profiles of the starting point 1.

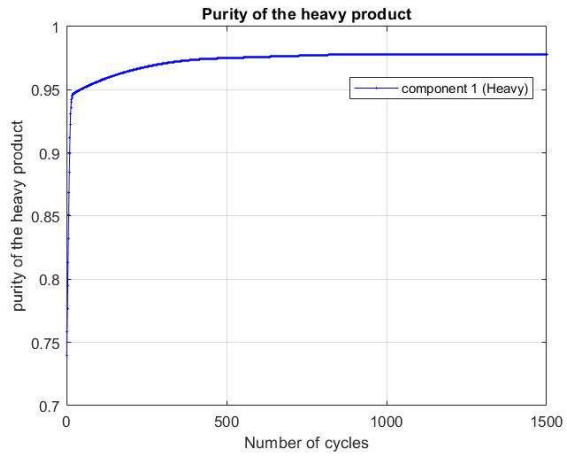

Figure 134: Heavy product purity for the simulation of Point 1 at π = 6

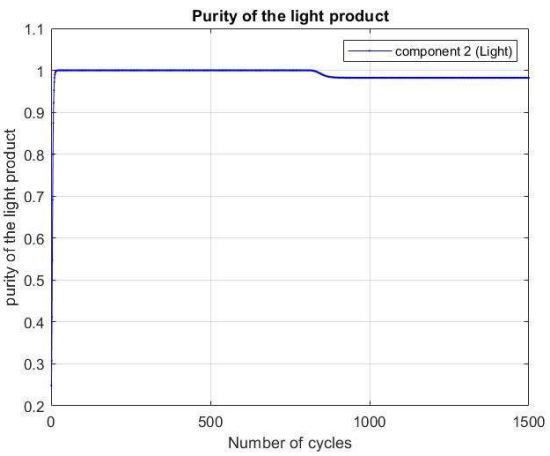

Figure 135: Light product purity for the simulation of Point 1 at π = 6

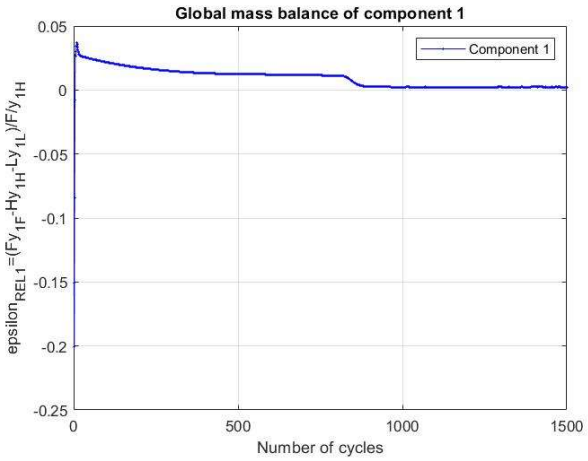

Figure 136: Error on the heavy product BM for the simulation of Point 1 at π = 6

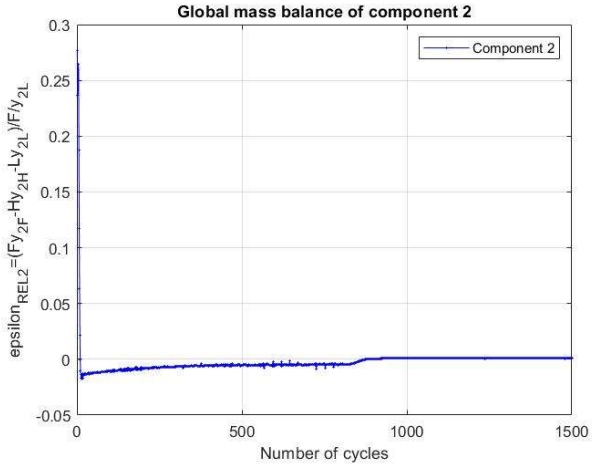

Figure 137: Error on the light product BM for the simulation of Point 1 at π = 6

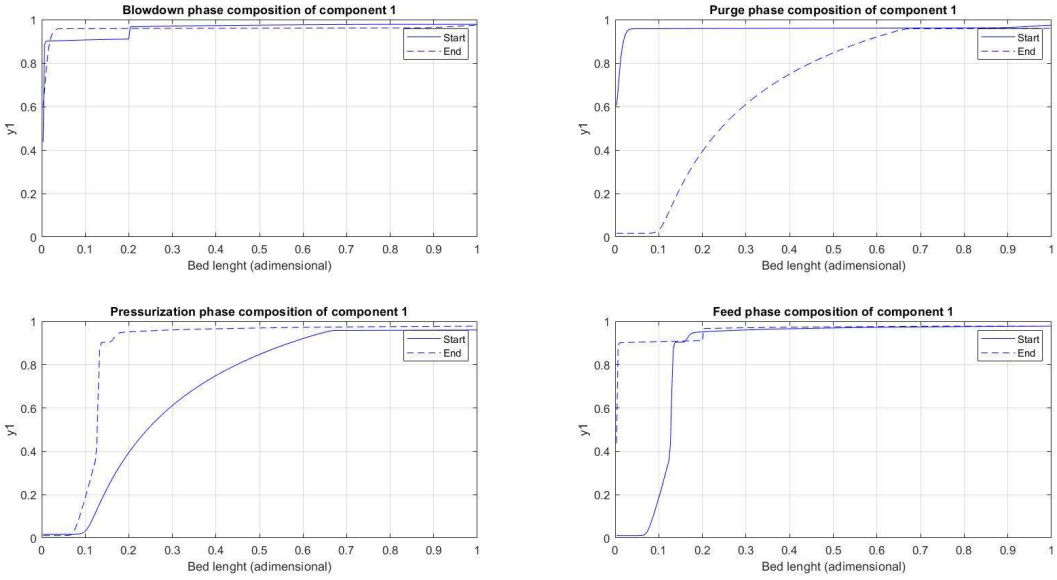

Figure 138: FVM start to end profiles for the simulation of Point 1 at π = 6

It can be noted in Figure 138 that, as in the previous cases, very sharp profiles develop in the left end of the column, therefore, small perturbation could lead to very different results. Moreover, the point 1 did not reach purity and recovery higher than 98%, but a value of 97.77% just above the one obtained during optimization (97.64%), therefore it cannot be considered part of the high separation region.

The results in terms of productivity and work for the points constituting the boundaries of the region are reported in Table 53 and Figure 139.

Table 53: Productivity and Work results for the boundaries of the high separation region at π = 6

	tfeed	QL	Pr	W
LVL_10	253,67	0,001	0,052466	72985
LVL_12	253,67	0,0012	0,052466	84400
LVL_14	253,67	0,0014	0,052466	95510
12_4	300	0,0012	0,060451	80825
10_1	320	0,001	0,063772	68660

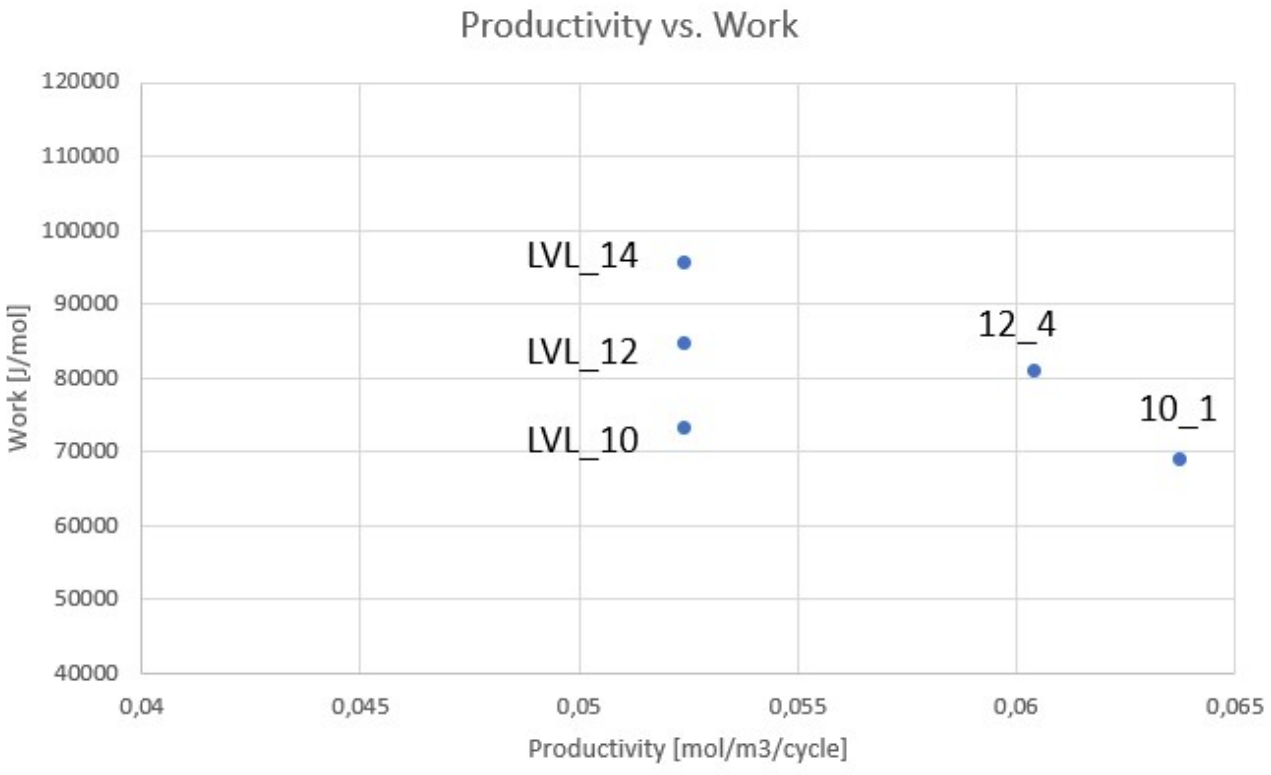

Figure 139: Productivity vs. Work for the high separation region at π = 6

The region obtained at π = 6 is much smaller than those obtained in the cases at lower π, although it has a shape that can be partially traced back to the previous ones with the lower right vertex as the optimal point due to the less work required and higher productivity.

Two other simulations were carried out, with 300 computational points, towards lower t_{Feed} values with the aim of verifying if the region found at π = 6 could have a structure similar to those found in the previous cases, but shifted towards lower t_{Feed} and higher Q_L values.

The points simulated are listed in Table 54.

Table 54: Further points simulated for the analysis of the high separation region at π = 6

	tFeed [s]	QL*10^{-4} [mol/s]
200_10	200	10
200_16	200	16

The results obtained are reported in Table 55 and Figure 140 where the previously defined region has been modified with the new points found.

Table 55: Results of the further simulations performed for the analysis of the high separation region at π = 6

	200_10	200_16
QL*10^{-4}	10	16
tfeed	200	200
$Purity_{HP,A}$	98,12	98,69
$Purity_{LP,B}$	98,18	98,78
Ncycles	357	394
$\varepsilon_{rel,A}$	6,2*10^{-4}	9,6*10^{-4}
Work [J/mol]	78280	

It is noted that, although from a preliminary investigation, the region with complete separation could develop in a similar way to the cases a minor π are shifted to lower t_{Feed} and higher Q_L values on the plane.

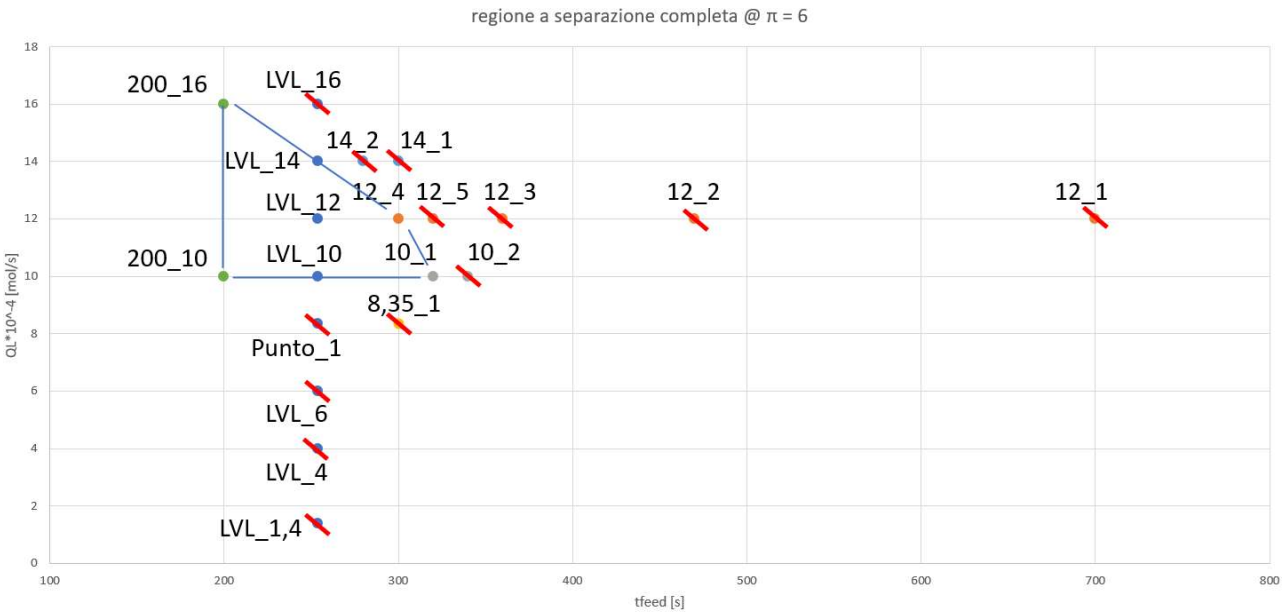

Figure 140: High separation region at π = 6

In Figure 141 a graph where the regions with high separation are compared to each other as π varies is shown and in Figure 142 they are compared with respect to Productivity and Work results.

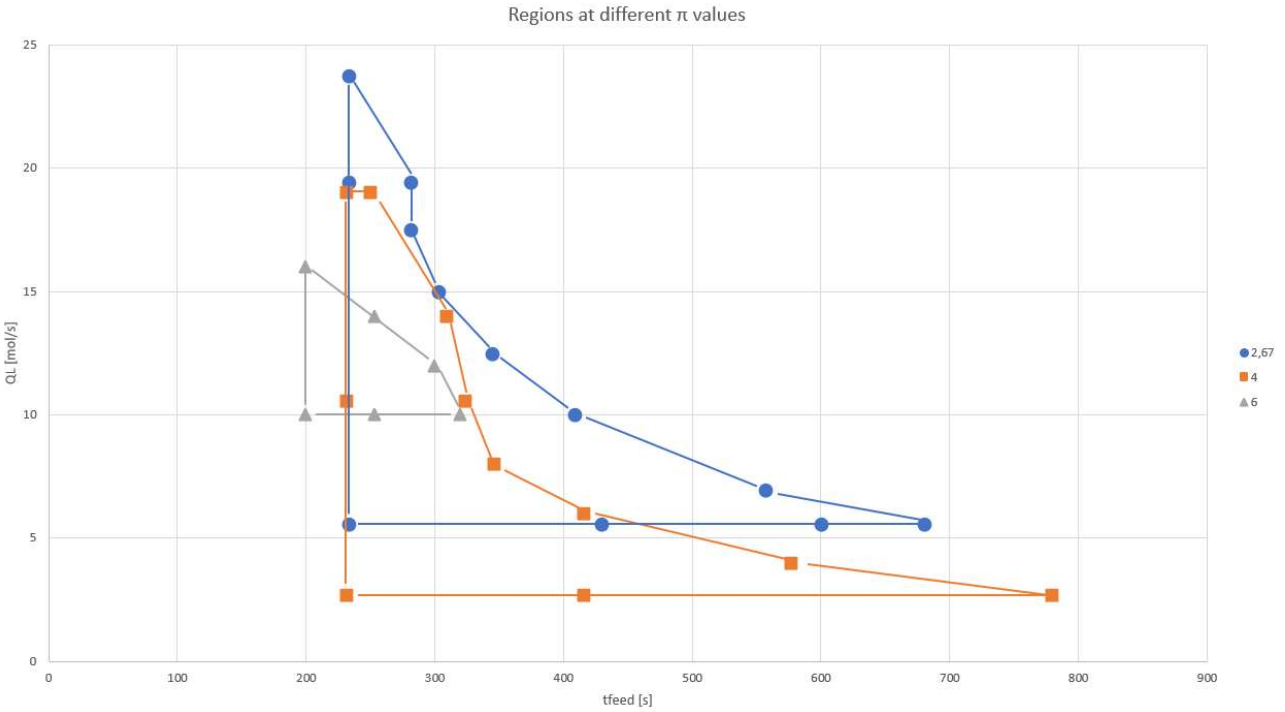

Figure 141: Extended high separation regions at different π values

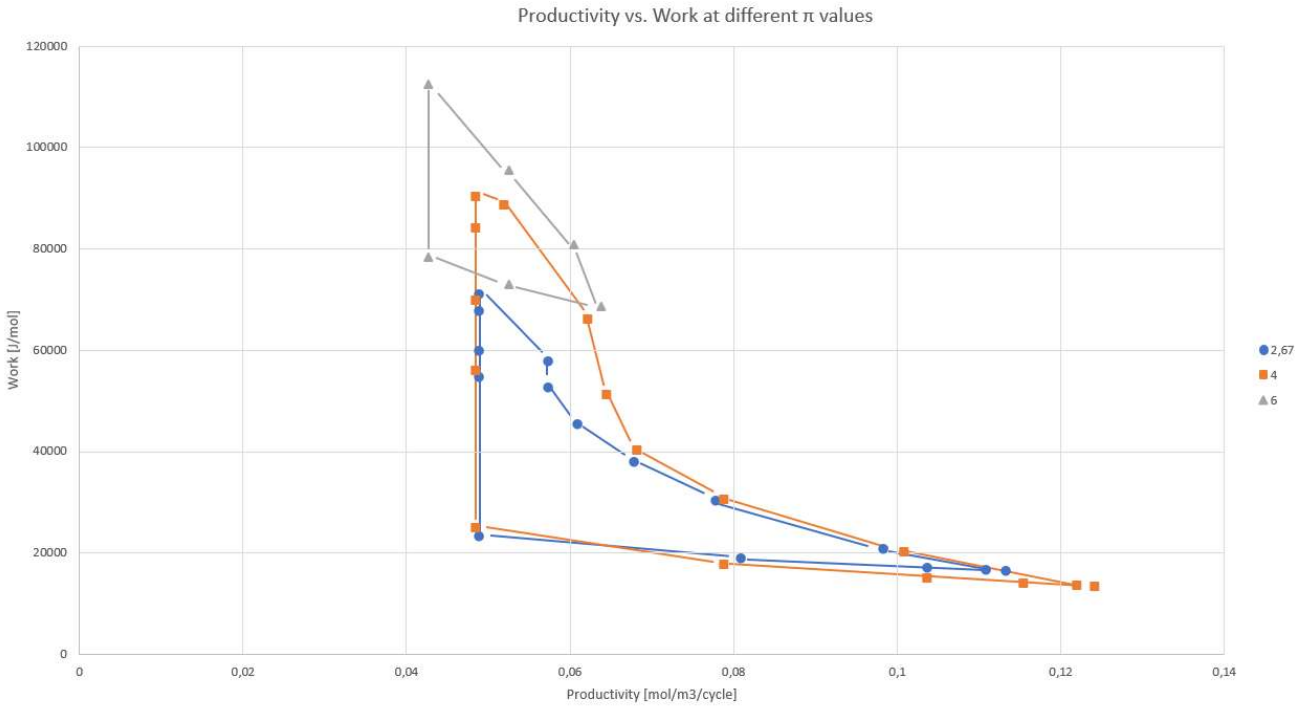

Figure 142: Extended high separation regions Productivity vs Work at different π values

Following the work carried out, it was noted that for different values of π it is possible to obtain a region on the t_{Feed} vs. Q_L plane where high separation > 98% can be achieved. Furthermore, in the cases at π = 2.67 and π = 4, it was possible to obtain high purity and recovery values of the heavy product with parameters that guarantee high productivity and low work.

In particular, the π = 4 configuration guarantees, with the same purity and recovery, higher productivity and lower energy consumption. At π = 6, on the other hand, a much smaller region is obtained, characterized by halved productivity and doubled work required, compared to previous cases.

5. Sensitivity analysis

To conclude the optimization work of the objective functions purity and recovery of the heavy product through the DR - PHA process with variable t_{Feed}, Q_L and π, a sensitivity analysis was carried out on the point identified as optimal for each of case:

- LH_680 (680, $5.565*10^{-4}$) @ π = 2.67
- LH_780 (780, $2.7*10^{-4}$) @ π = 4
- 10_1 (320, $10*10^{-4}$) @ π = 6

The sensitivity coefficient of a function $F(\varphi_j)$, depending on a parameter φ_j, according to the finite difference method, is defined as:

$$S_{F,\varphi_j} = \frac{\varphi_j}{F(\varphi_j)} \cdot \frac{\partial F}{\partial \varphi_j} \sim \frac{\varphi_j}{F(\varphi_j)} \cdot \frac{F(\varphi_j+\Delta\varphi_j)-F(\varphi_j)}{\Delta\varphi_j} \quad (3.6)$$

Where:

- φ_j: value for the variable j of the starting point
- $F(\varphi_j)$: value of the function for the starting point
- $\Delta\varphi_j$: variation of the parameter φ_j
- $F(\varphi_j + \Delta\varphi_j)$: value of the function for the starting point with the increase/decrease

In our case, the function is defined as the purity of the heavy component, while the generic parameter φ_j represents the following variables:

- z_F
- t_{Feed}
- P_L
- y_F
- Q_L
- Q_{HP}
- Q_{Feed}

The variation of the variable was set equal to the 10% of the value corresponding to the starting point. For the case at π = 2.67, an analysis was also carried out for the parameters decreased by 10% of their value, named "2.67 –", while the same π where the 10% was added was named "2.67 +".

For each variable at each π, a high accuracy simulation with 300 computational points was performed, with the other input data set equal to the base case. The purity of the heavy component obtained was then used to calculate the sensitivity coefficient with Equation 3.6.

The results obtained are represented in Figure 143 and reported in Table 56, 58, 60 and 62 for the three π cases, while the results of the simulations performed are reported in Table 57, 59, 61 and 63.

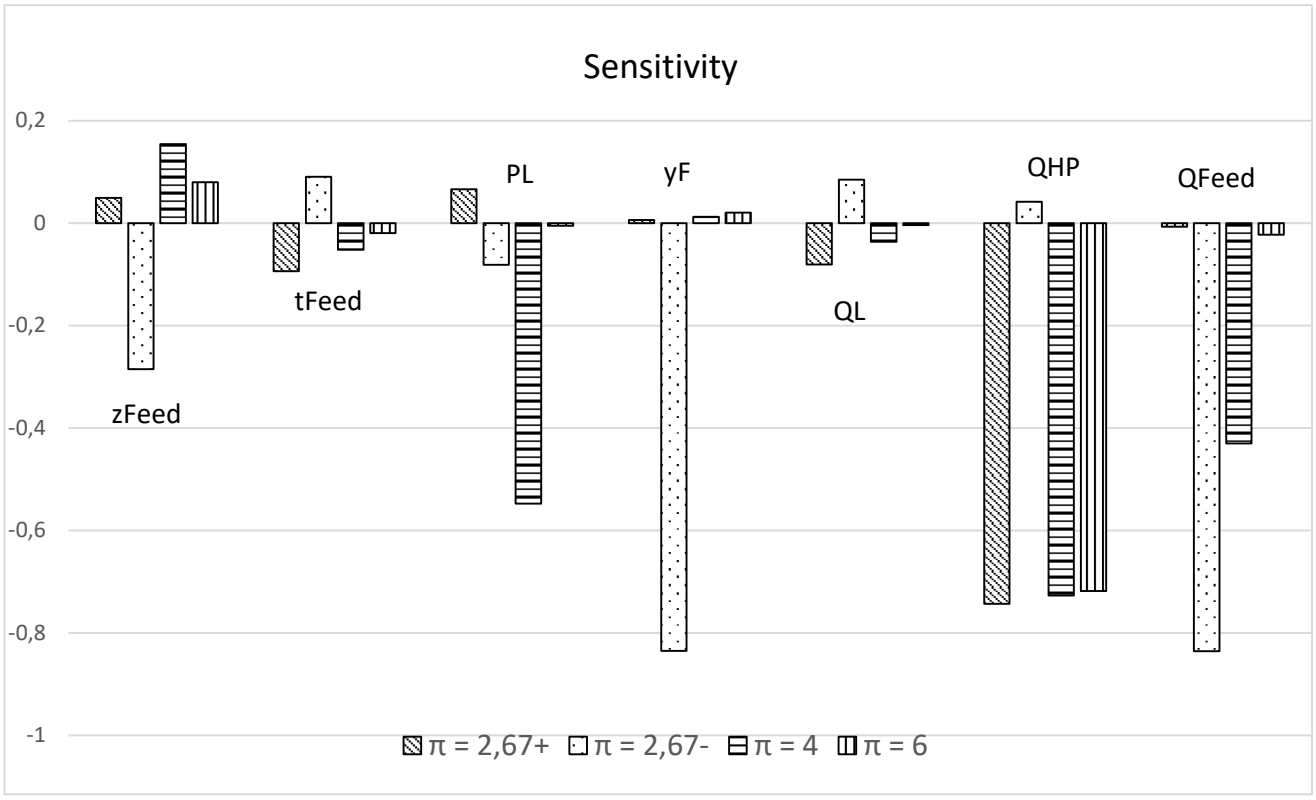

Figure 143: Sensitivity results of the process key parameters at different π values

- π = 2,67 +

Table 56: Sensitivity analysis of point LH_680 increased the 10% for the case at π = 2.67 +

zF	tfeed	PL	yF	QL	QHP	Qfeed	SP_H, ϕ_j
0,88	680	$4,5*10^5$	0,5	$5,595*10^{-4}$	$8,85*10^{-5}$	$1,77*10^{-4}$	0,048875
0,8	748	$4,5*10^5$	0,5	$5,595*10^{-4}$	$8,85*10^{-5}$	$1,77*10^{-4}$	-0,09368
0,8	680	$4,95*10^5$	0,5	$5,595*10^{-4}$	$8,85*10^{-5}$	$1,77*10^{-4}$	0,066185
0,8	680	$4,5*10^5$	0,55	$5,595*10^{-4}$	$8,85*10^{-5}$	$1,77*10^{-4}$	0,006109
0,8	680	$4,5*10^5$	0,5	$6,1215*1010^{-4}$	$8,85*10^{-5}$	$1,77*10^{-4}$	-0,08098
0,8	680	$4,5*10^5$	0,5	$5,595*10^{-4}$	$9,735*10^{-5}$	$1,77*10^{-4}$	-0,74331
0,8	680	$4,5*10^5$	0,5	$5,595*10^{-4}$	$8,85*10^{-5}$	$1,947*10^{-4}$	-0,00713

Table 57: Simulations results of the sensitivity analysis of the point LH_680 increased the 10% for the case at π = 2.67 +

	$Purity_{HP,A}$	$Purity_{LP,B}$	$\varepsilon_{rel,A}$	Work	Ncycles
LHL_680	98,21	98,21	$5,4*10^{-5}$	16512	790
1_zF	98,69	98,7	$1,18*10^{-4}$	16694	625
2_tfeed	97,29	97,29	$4,6*10^{-5}$	16076,5	371
3_PL	98,86	98,86	$5,8*10^{-5}$	14846,5	478
4_yF	98,27	97,9	$5,8,9*10^{-5}$	16355	903
5_QL	97,41	97,41	$6,4*10^{-5}$	17843	493
6_QHP	90,91	100	$1,36*10^{-5}$	15924,5	1500
7_Qfeed	98,14	98,15	$5,0*10^{-5}$	14879	373

- <u>π = 4</u>

Table 58: Sensitivity analysis of the point LH_780 increased the 10% for the case at π = 4

zF	tfeed	PL	yF	QL	QHP	Qfeed	SP_H, ϕ_j
0,88	780	$3*10^5$	0,5	$2,7*10^{-4}$	$8,85*10^{-5}$	$1,77*10^{-4}$	0,15405
0,8	858	$3*10^5$	0,5	$2,7*10^{-4}$	$8,85*10^{-5}$	$1,77*10^{-4}$	-0,05203
0,8	780	$3,3*10^5$	0,5	$2,7*10^{-4}$	$8,85*10^{-5}$	$1,77*10^{-4}$	-0,54785
0,8	780	$3*10^5$	0,55	$2,7*10^{-4}$	$8,85*10^{-5}$	$1,77*10^{-4}$	0,012242
0,8	780	$3*10^5$	0,5	$2,97*10^{-4}$	$8,85*10^{-5}$	$1,77*10^{-4}$	-0,03673
0,8	780	$3*10^5$	0,5	$2,7*10^{-4}$	$9,735*10^{-5}$	$1,77*10^{-4}$	-0,7274
0,8	780	$3*10^5$	0,5	$2,7*10^{-4}$	$8,85*10^{-5}$	$1,947*10^{-4}$	-0,43052

Table 59: Simulations results of the sensitivity analysis of the point LH_780 increased the 10% for the case at π = 4

	$Purity_{HP,A}$	$Purity_{LP,B}$	$\varepsilon_{rel,A}$	Work	Ncycles
LH_780	98,02	98,02	$3,8*10^{-6}$	13412,5	406
1_zF	99,53	99,51	$2*10^{-4}$	13639	414
2_tfeed	97,51	97,5	$1,38*10^{-5}$	12915,5	357
3_PL	92,65	92,67	$2*10^{-4}$	11666	225
4_yF	98,14	97,73	$9,4*10^{-6}$	13178	1194
5_QL	97,66	97,66	$8,4*10^{-6}$	14420,5	358
6_QHP	90,89	100	$1,62*10^{-4}$	12930,5	732
7_Qfeed	93,8	93,8	$5,4*10^{-5}$	11578,5	263

- <u>π = 6</u>

Table 60: Sensitivity analysis of the point 10_1 increased the 10% for the case at π = 6

zF	tfeed	PL	yF	QL	QHP	Qfeed	SP_H, ϕ_j
0,88	320	$2*10^5$	0,5	$10*10^{-4}$	$8,85*10^{-5}$	$1,77*10^{-4}$	0,079608
0,8	352	$2*10^5$	0,5	$10*10^{-4}$	$8,85*10^{-5}$	$1,77*10^{-4}$	-0,01939
0,8	320	$2,2*10^5$	0,5	$10*10^{-4}$	$8,85*10^{-5}$	$1,77*10^{-4}$	-0,0051
0,8	320	$2*10^5$	0,55	$10*10^{-4}$	$8,85*10^{-5}$	$1,77*10^{-4}$	0,020412
0,8	320	$2*10^5$	0,5	$11*10^{-4}$	$8,85*10^{-5}$	$1,77*10^{-4}$	-0,00408
0,8	320	$2*10^5$	0,5	$10*10^{-4}$	$9,735*10^{-5}$	$1,77*10^{-4}$	-0,71851
0,8	320	$2*10^5$	0,5	$10*10^{-4}$	$8,85*10^{-5}$	$1,947*10^{-4}$	0,02245

Table 61: Simulations results of the sensitivity analysis of the point 10_1 increased the 10% for the case at π = 6

	$Purity_{HP,A}$	$Purity_{LP,B}$	$\varepsilon_{rel,A}$	Work	Ncycles
1_zF	98,7	98,8	$3,6*10^{-4}$	69140	660
2_tfeed	97,79	97,82	$3,0*10^{-4}$	67070	138
3_PL	97,93	97,97	$4,2*10^{-4}$	63920	463
4_yF	98,18	97,82	$4,8*10^{-4}$	68395	394
5_QL	97,94	97,98	$3,8*10^{-4}$	74180	172
6_QHP	90,94	100	$3,8*10^{-4}$	74180	1379
7_Qfeed	97,76	89,83	$4,4*10^{-4}$	60505	596

- π = 2,67 -

Table 62: Sensitivity analysis of the point LH_680 decreased the 10% for the case at π = 2.67 -

zF	tfeed	PL	yF	QL	QHP	Qfeed	SP_H, ϕ_j
0,72	680	$4,5*10^{5}$	0,5	$5,595*10^{-4}$	$8,85*10^{-5}$	$1,77*10^{-4}$	-0,2851
0,8	612	$4,5*10^{5}$	0,5	$5,595*10^{-4}$	$8,85*10^{-5}$	$1,77*10^{-4}$	0,090622
0,8	680	$4,05*10^{5}$	0,5	$5,595*10^{-4}$	$8,85*10^{-5}$	$1,77*10^{-4}$	-0,08146
0,8	680	$4,5*10^{5}$	0,45	$5,595*10^{-4}$	$8,85*10^{-5}$	$1,77*10^{-4}$	-0,83495
0,8	680	$4,5*10^{5}$	0,5	$5,0085*10^{-4}$	$8,85*10^{-5}$	$1,77*10^{-4}$	0,013529
0,8	680	$4,5*10^{5}$	0,5	$5,595*10^{-4}$	$7,965*10^{-5}$	$1,77*10^{-4}$	0,041747
0,8	680	$4,5*10^{5}$	0,5	$5,595*10^{-4}$	$8,85*10^{-5}$	$1,593*10^{-4}$	-0,83596

Table 63: Simulations results of the sensitivity analysis of the point LH_680 decreased the 10% for the case at π = 2.67 -

Caso	$Purity_{HP,A}$	$Purity_{LP,B}$	$\varepsilon_{rel,A}$	Work	Ncycles
1_zF	95,41	95,41	$4,6*10^{-5}$	16047	714
2_tfeed	99,10	99,11	$6,6*10^{-5}$	17011	560
3_PL	97,41	97,41	$4,8*10^{-5}$	13612,5	296
4_yF	90,01	100	$5,0*10^{-5}$	15983	851
5_QL	99,05	99,05	$5,6*10^{-5}$	15174,5	514
6_QHP	98,62	89,78	$8,4*10^{-5}$	16148,5	296
7_Qfeed	90,00	100	$1,24*10^{-5}$	16148,5	781

In Figure from 144 to 152 are reported the profiles of 3 cases, one for each π, obtained from the simulations for the sensitivity analysis.

- π = 2,67 – t_{Feed} case

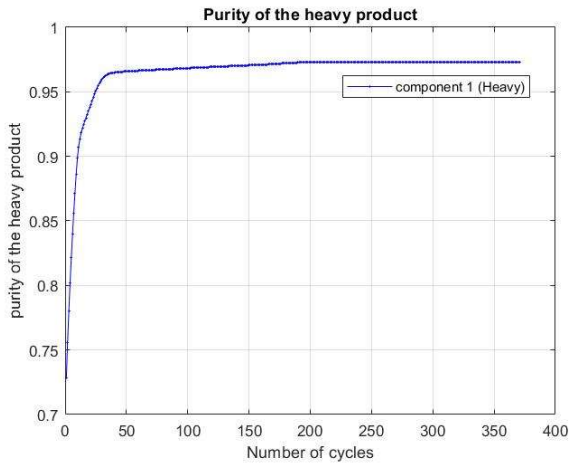

Figure 144: Heavy product purity for the simulation of the tFeed case at π = 2,67

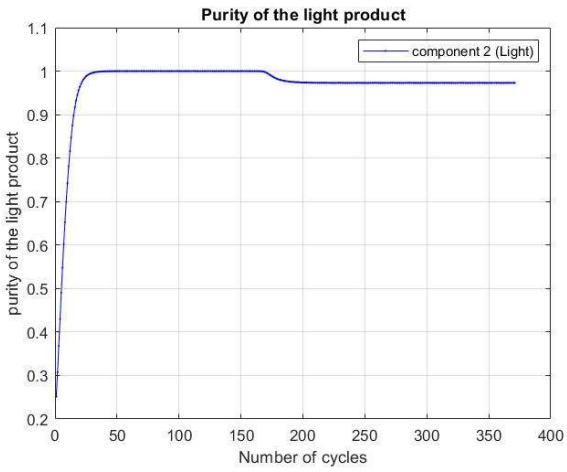

Figure 145: Light product purity for the simulation of the tFeed case at π = 2,67

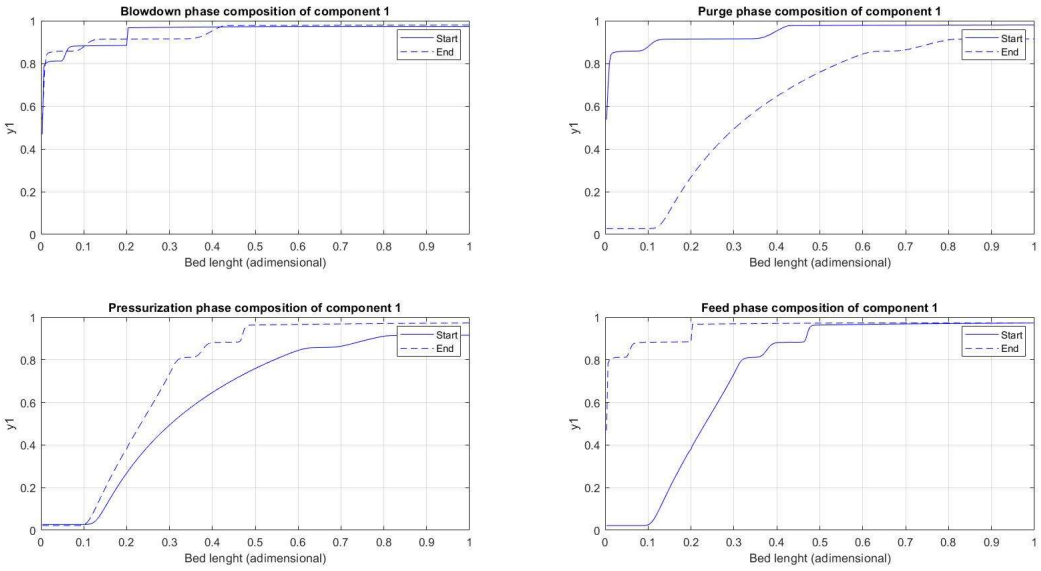

Figure 146: FVM start to end profiles for the simulation of the tFeed case at π = 2,67

In Figure 155, very sharp profiles develop close to the left end of the column, making the system unstable even for small perturbations.

- π = 4 – Q_{HP} case

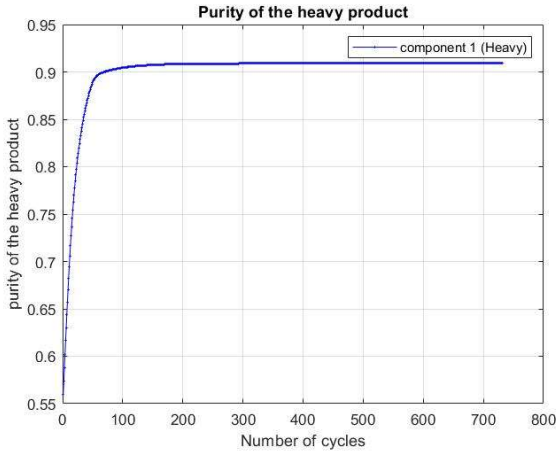

Figure 147: Heavy product purity for the simulation of the QHP case at π = 4

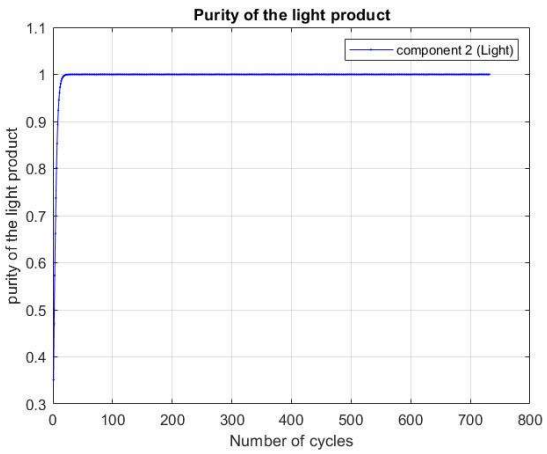

Figure 148: Light product purity for the simulation of the QHP case at π = 4

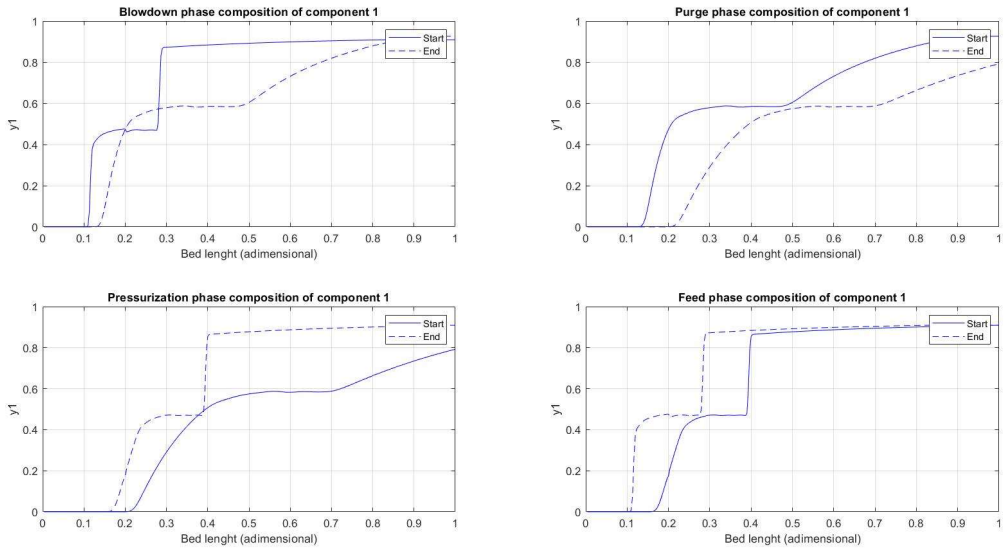

Figure 149: FVM start to end profiles for the simulation of the QHP case at π = 4

- π = 6 – y_F case

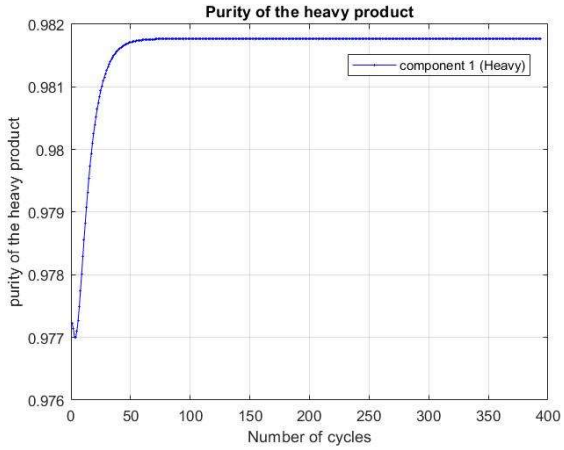

Figure 150: Heavy product purity for the simulation of the yF case at π = 6

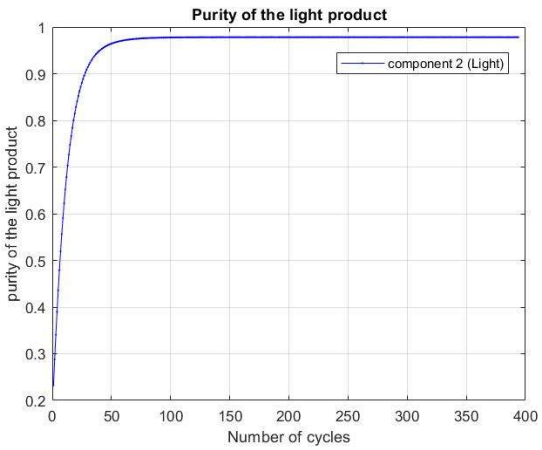

Figure 151: Light product purity for the simulation of the yF case at π = 6

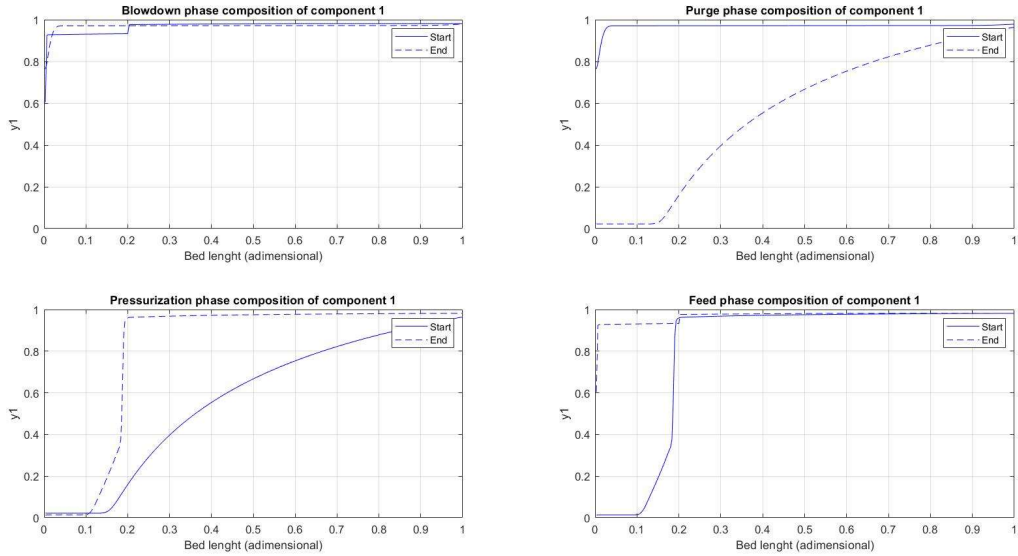

Figure 152: FVM start to end profiles for the simulation of the yF case at π = 6

In Figure 146 and 152 very sharp profiles are developed at the left end of the column, even a small deviation of the operating conditions can lead to different results.

It can be noted that the optimal operating conditions found are characterized by low sensitivity for a 10% increase in the values of t_{Feed}, Q_L and especially y_F, while in the latter case a decrease of 10% causes a large variation in the results.

In the case at π = 4, for a 10% increase in P_L there is a large difference in the results since as can be seen from Figure 141 as P_L increases, therefore as π decreases, the high separation region shifts towards lower t_{Feed} and higher Q_L values and operating conditions will no longer allow to obtain purity > 98%.

z_{Feed} shows an almost homogeneous behavior for all the cases studied with moderate sensitivity values, Q_{Feed} instead is characterized by very low values for an increase of 10% at π = 2.67 and π = 6, while in the remaining cases the sensitivity results considerably higher.

For the heavy product flowrate there are no large variations for a decrease of 10%, however for all π values as Q_{HP} increases the purity values vary greatly. This happens because the heavy product flowrate was set equal to the inlet one, therefore if it increases the purity necessarily drops as part of the light product is extracted together.

Chapter 4

Literature review and code validation for the simulation of the separation process of a stream CO_2/N_2

1. introduction

In Chapter 3, a research methodology for optimal operating conditions was developed in a context where it was not possible to carry out direct optimization, due to the high computational times required and due to the sensitivity of the code that in some cases leads to the failure of the process. The procedure was developed on a fictitious system, with the aim of being applied following real cases.

For this purpose, the separation of a $CO_2 + N_2$ stream was chosen, since it is a system already studied in literature, but for which the presence of optimal operating conditions has not yet been verified. A literature review was carried out to analyse the performance obtained in terms of purity vs. recovery and work vs. productivity with PSA and DRPSA processes.

Among the cases studied, a DRPSA process, different from the 4 standard configurations, was chosen, for which a preliminary work for the optimization process was carried out, starting from the validation of the code for the system simulation.

2. Literature review

A literature research has been carried out, initially in the PSA field and after also in the DRPSA, for the CO_2 separation from a flue gas stream. Performances in terms of purity and recovery of CO_2 have been collected, together with more economic aspects like power consumption and productivity, in order to identify the studies with the best performances, and specifications on the process studied and the solid adsorbent used. Productivity and Work are two important aspects of the process since they represent respectively the fixed costs (column dimension) and operating costs (power required by the compressor and recycle streams).

From the results collected in the literature review, it is possible to notice that the DRPSA configuration, and its modified versions, are more competitive in purity and recovery of CO_2 for the CO_2 + N_2 gas streams than the standard PSA processes as it can be seen in Figure 153 and its zoom Figure 154.

All the data collected are shown in the table in the appendix.

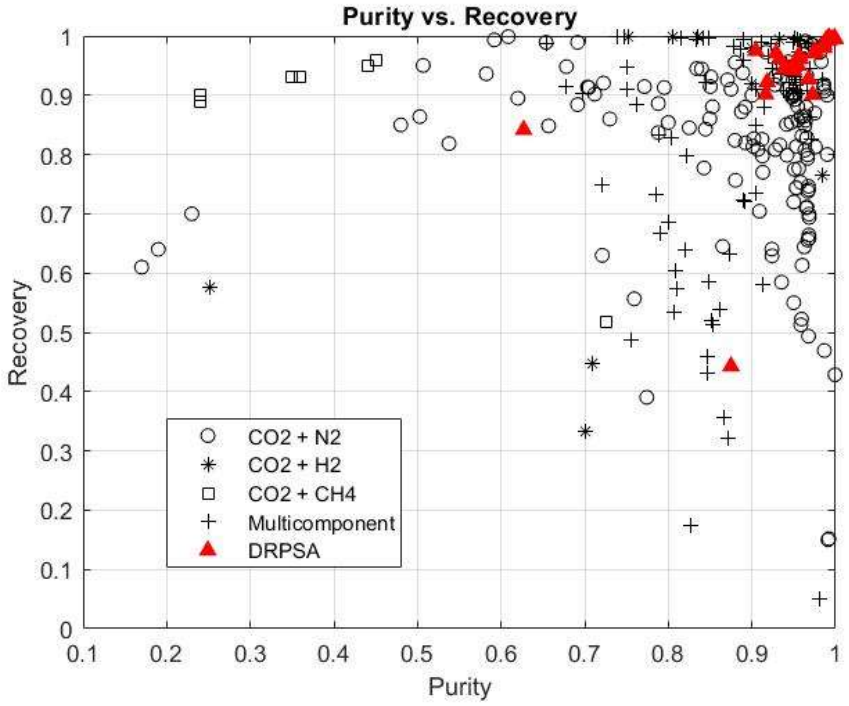

Figure 153: Literature review of Purity vs. Recovery for CO2 separation

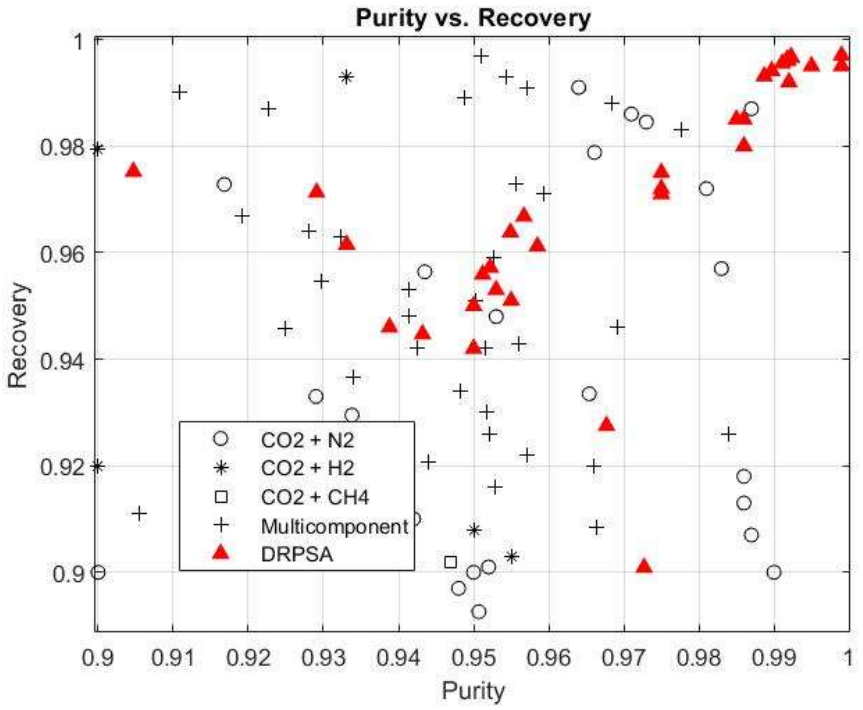

Figure 154: Literature review of Purity vs. Recovery for CO2 separation, zoom of Figure 153

Figure 155 and 156 show the results found in the literature review for Work and Productivity, as it can be seen these are less than the Purity/Recovery ones and strongly dependent on the type of the mixture:

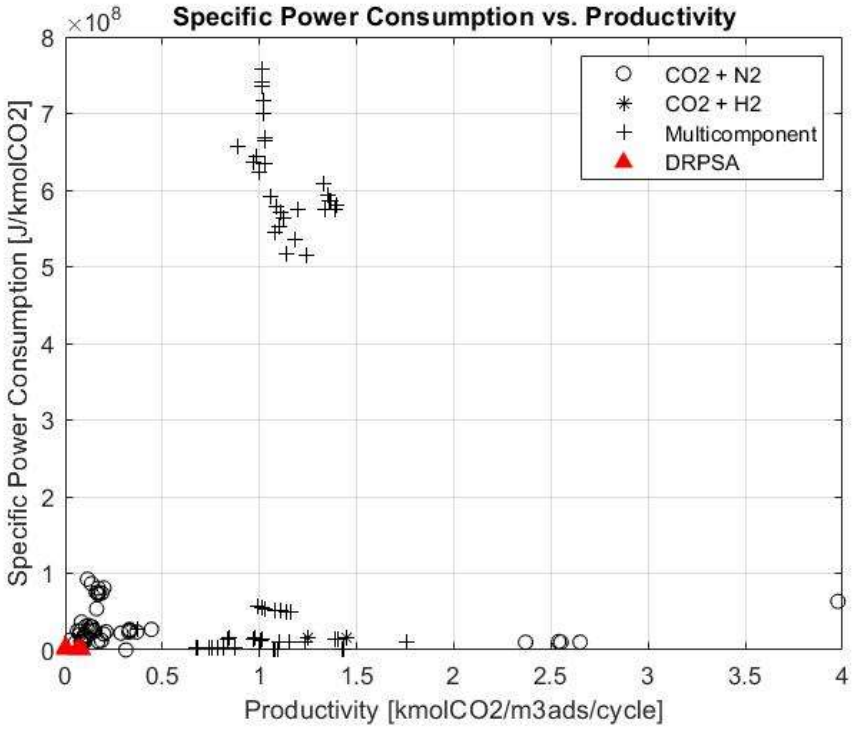

Figure 155: Literature review of Productivity vs. Specific Power Consumption for CO2 separation

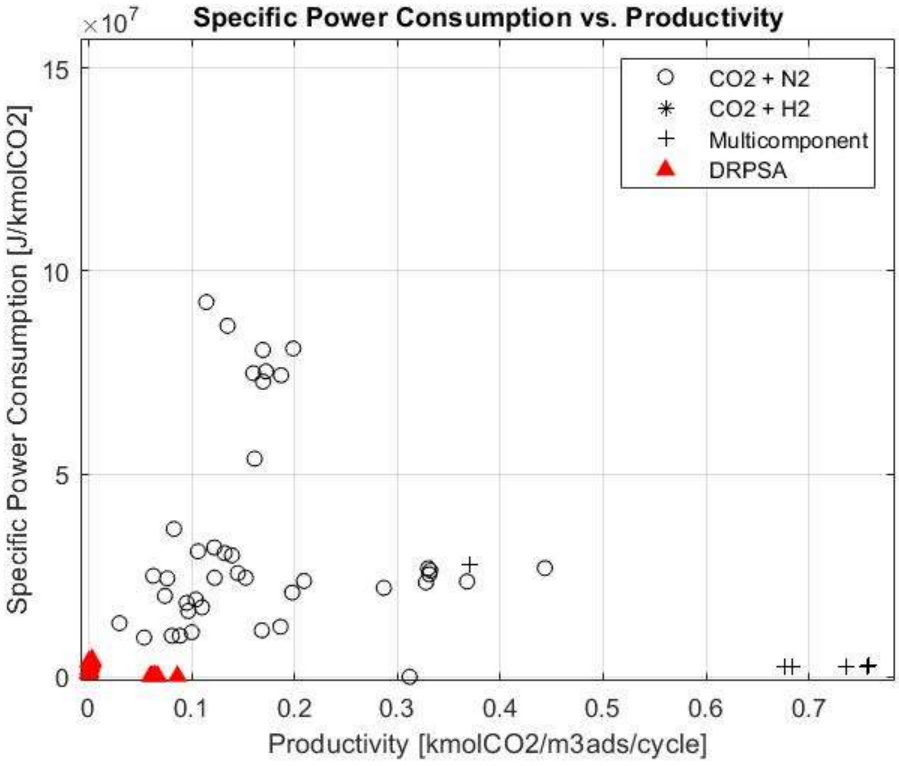

Figure 156: Literature review of Productivity vs. Specific Power Consumption for CO2 separation, zoom of Figure 155

3. 6-step DRPSA process by Shen et al.

Among the DRPSA studies found in literature, we have chosen one recent work of particular interest because of the sharp separation results achieved with its modified configuration, Shen et al. 2017 in which a mixture of 15% CO_2 and 85% N_2 is separated on silica gel adsorbent. A dedicated code has been implemented to validate the results reported in the article through several simulations.

The process is a 6 step DR – PSA where a typical cycle consists in:

- High pressure feed step
- Depressurization equalization step
- Blowdown depressurization step
- Light product reflux step
- Repressurization equalization step
- Heavy product reflux step

A half cycle is represented in Figure 157.

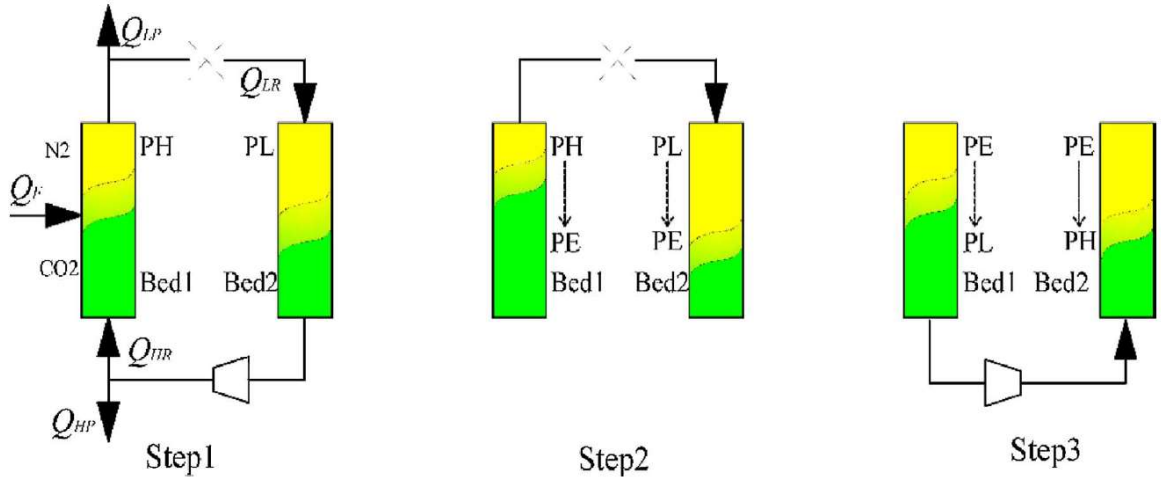

Figure 157: Shen et al. 6 step-DRPSA process, half cycle representation

In the standard DRPSA process, the pressure swing is performed from the top or from the bottom of the columns, respectively with light or heavy component in the case of complete separation, otherwise a mix of the two components. The Shen et al. configuration is characterized by a hybrid process where the equalization step is performed from the top of the columns, while the repressurization takes place by means of a compressor from the bottom of the beds. The important implication of this top to bottom switch during the pressure swing phase is the change in the pressure profiles inside the columns from the standard DRPSA configuration.

The previously discussed model has been extended to the simulation of this different cycle. As in the standard cases, during the implementation of the code it was necessary to take

into account that, to ensure proper operation, two additional tanks have to be added as shown in Figure 158. Since the process never reaches steady state conditions, before reaching CSS conditions, to comply with the material balances some additional amount can be required with respect to that recovered by the columns. Moreover, due to the non-linear shape of the adsorption isotherms, the amount of gas desorbed in the BD step can be different from that required in the PR step. Therefore, the tanks were placed at the top and at the bottom of the columns as shown in the following scheme:

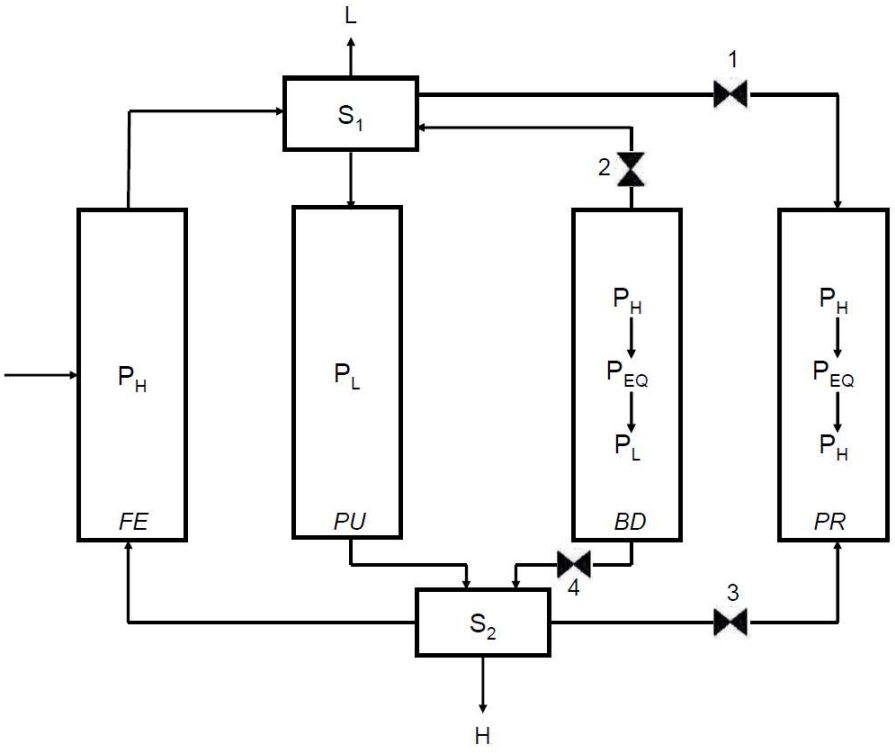

Figure 158: Process layout implemented in the code for the validation simulations

The system simulated undergoes the steps in Table 64 where the indicators represent the verse in which the movement along the column occurs.

Table 64: Steps of the Shen et al. process

FE	PU	BD1	BD2	PR1	PR2
z ↑	z ↓	z ↑	z ↓	z ↓	z ↑
Phase 1	Phase 2	Phase 3	Phase 4	Phase 5	Phase 6

The four valves in the layout of Figure 172 follow the scheme in Table 65.

Table 65: Scheme of the valves for the Shen et al. process configuration

Valve 1	Open	P < PEQ
	Close	P > PEQ

Valve 2	Open	P < PEQ
	Close	P > PEQ

Valve 3	Open	P > PEQ
	Close	P < PEQ

Valve 4	Open	P > PEQ
	Close	P < PEQ

The data used for the validation of the developed code were collected from the paper of Shen et al., (2017) and in the supplementary information attached, except for the k_{LDF} which was estimated. The values of the simulation parameters are reported in Table 66.

Table 66: Input data of the simulations for the Shen et al. code validation

Variable	Values	Units	Meaning
ε_p	0.1429	-	particle void fraction
ε_b	0.3125	-	bed void fraction
P_H	$2*10^5$	Pa	high pressure
P_L	$0.2*10^5$	Pa	low pressure
$y_{F,A}$	0.15	-	feed composition
T	298	K	temperature
ρ_s	963.67	kg/m3	solid density
$d_{particles}$	$3*10^{-3}$	m	particle diameter of the solid adsorbent
μ_{mix}	$1.5*10^{-5}$	Pa*s	mixture viscosity
L_{column}	1	m	length of the column
D_{column}	0.06	m	diameter of the column
$k_{LDF,1}$	0.4043	1/s	mass transfer constant of the heavy component
$k_{LDF,2}$	13.92	1/s	mass transfer constant of the light component
$Langmuir_{1,A}$	$2.1384*10^{-5}$	mol/kg/Pa	Langmuir parameter a of the heavy component

$Langmuir_{2,A}$	$4.6502*10^{-6}$	1/Pa	Langmuir parameter a of the light component
$Langmuir_{1,B}$	$6.214*10^{-7}$	mol/kg/Pa	Langmuir parameter b of the heavy component
$Langmuir_{2,B}$	$1.845*10^{-7}$	1/Pa	Langmuir parameter b of the light component
t_{Feed}	160	s	feed/purge time
t_{Press1}	1500	s	equalization time
t_{Press2}	300	s	blowdown time

The values of z_{Feed}, Q_{Feed}, Q_L and Q_{HP} for the simulations carried out are reported in Table 73.

The expression of the Langmuir isotherm was the classical one:

$$q_i^* = \frac{a_i P y_i}{1+b_i P y_i} \tag{4.1}$$

with a_i in $\frac{mol}{kg*Pa}$ and b_i in $\frac{1}{Pa}$, while the expression reported by Shen et al., (2017) is:

$$q^* = \frac{IP_{1i}*e^{\frac{IP_{2i}}{T}}*Py_i}{1+\sum_i IP_{3i}*e^{\frac{IP_{4i}}{T}}*Py_i} \tag{4.2}$$

which is temperature dependent. However, it can be shown that a temperature difference of about 30 degrees does not significantly affect the adsorption process, therefore, in this study, an average temperature of 298 K was chosen.

Figure 159 shows the trend of CO_2 and N_2 Langmuir's isotherms.

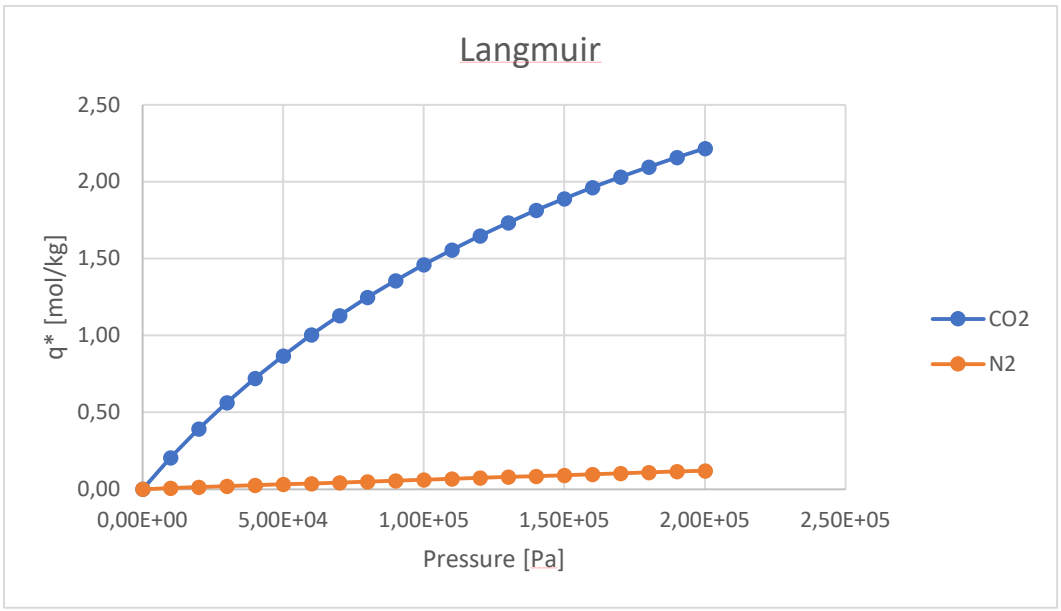

Figure 159: Langmuir's isotherms for CO2 and N2

It is possible to notice that the heavy component is CO_2, since its adsorption is favoured respect to N_2.

The values reported in the supplementary information of Shen et al. for the parameters of the Langmuir's isotherms are reported in Table 67.

Table 67: Langmuir's parameters reported in Shen et al.

Parameters	CO_2	N_2
$IP_1(mol \cdot kg^{-1} \cdot bar^{-1})$	6.07×10^{-4}	6.77×10^{-5}
$IP_2(K)$	2435	2034
$IP_3(bar^{-1})$	1.32×10^{-4}	2.01×10^{-5}
$IP_4(K)$	2435	2034

While the values used in this work are reported in Table 66.

Since in the paper by Shen et al. (2017) there are no indication regarding the mass transfer coefficients of the components (k_{LDF}), therefore it was necessary to compute them as follow:

$$k_{LDF,i} = 15 \cdot \frac{D_p \cdot \epsilon_p}{R_p^2} \left(\frac{1}{k_i}\right) \tag{4.3}$$

With:

- D_p: macropore diffusivity
- ϵ_p: adsorbent porosity
- R_p : macroparticle radius
- k_i: ratio between q (adsorbed amount) and c_0 (concentration)

The complete equation used for the calculation of the k_{LDF} is the one reported in the paper «*A review of mathematical modeling of fixed-bed columns for carbon dioxide adsorption*» by Mohammad Saleh Shafeeyan, Wan Mohd Ashri Wan Daud∗, Ahmad Shamiri of 2014:

$$\frac{1}{k_{LDF,i}} = \frac{R_p q_0}{3 k_{fi} c_0} + \frac{R_p^2 q_0}{15 \ {}_p D_{pi} c_0} + \frac{R_c^2}{15 D_{\mu i}} \tag{4.4}$$

Where the first and the third term are not considered because the diffusivity in the external film and the diffusivity in the micropores are negligible, thus leading to Equation 4.3.

For the estimate of the k_{LDF} we had to obtain the Henry's constant because it was necessary to have a fixed value of the ratio between amount adsorbed and concentration. Since in the present case the adsorption isotherm was nonlinear of the Langmuir type, in order to obtain Henry's constants, a linear interpolation of the adsorption curves was carried out using the

Curve Fitting Toolbox on Matlab dividing the pressure range (P_H to P_L, 2 bar to 0,2 bar) into 101 points and imposing the passage at the origin. The graphical results for the Henry's constant are reported in Figure 160 and 161.

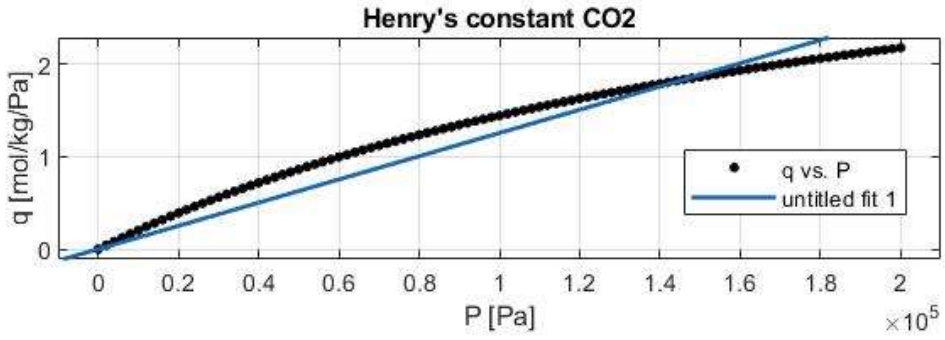

Figure 160: Henry's constant estimation for CO2

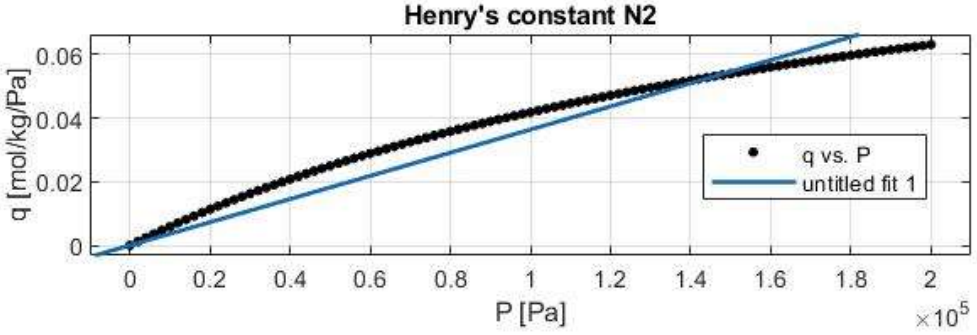

Figure 161: Henry's constant estimation for N2

We obtain:

- $k_{LDF,1}$ = 0,4043 1/s
- $k_{LDF,2}$ = 13,92 1/s

from the graphical representations in Figure 162 and 163.

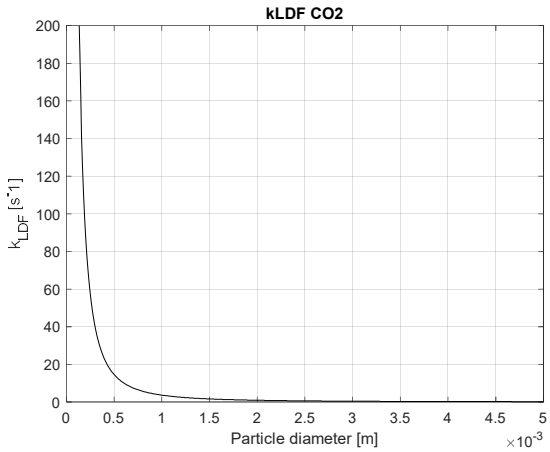

Figure 162: kLDF estimation for CO2

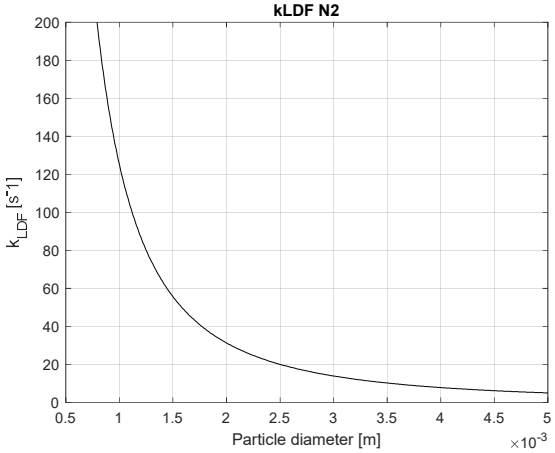

Figure 163: kLDF estimation for N2

A crucial step during the simulations carried out, was the setting of the initial conditions for the PU and PR phases, through four parameters:

- y_{L0}^{CO} for the PU phase
- y_{H0}^{CO2} for the PR phase
- $y_{L0}^{N2} = 1 - y_{L0}^{CO}$
- $y_{H0}^{N2} = 1 - y_{H0}^{CO2}$

They are critical values because, before reaching stationary conditions, it starts with:

1. BD1: left column of step 2 in Shen et al. configuration – Figure 171
2. BD2: left column of step 3
3. PU: right column of step 1
4. PR1: right column of step 2
5. PR2: right column of step 3
6. FE: left column of step 1

During PU there is a recycle to FE that has not yet been simulated, therefore it is necessary to assign an arbitrary IC y_{L0}^{CO} . If the value does not agree with the profile inside the column, it results a negative gradient, which in physical terms, would represent that the compound exits instead of entering the bed.

At the first few cycles, the results are still affected by the arbitrary value chosen, after that they become independent.

4. Validation of the code

Among the thirteen cases reported in the paper, four have been carried out for the validation of the code, respectively case 1, 2, 9 and 10. The parameters that have been varied in the paper to study their influence on the performance of purity and recovery are:

- z_{Feed}: feed injection axial dimensionless coordinate
- Q_{HP}: heavy product flowrate
- Q_L: light product reflux flowrate

In the Table 68 are reported the input data for the cases reproduced:

Table 68: Variable for the case simulated for the validation of the code

Case	zfeed	QF [slpm]	QHP [slpm]	QL [slpm]
1	0.5	4.006	0.603	0.204
2	0.5	4.010	0.604	0.102
9	0.5	4.006	0.645	0.203
10	0.2	4.013	0.606	0.204

- Case 1

This is considered the "Base case" by Shen et al., (2017), from which the influence of z_{Feed}, Q_{HP} and Q_L on the performances of the process have been evaluated.

Three simulations were performed for this case at different numbers of computational points. The results are shown in Table 69.

Table 69: Results for the simulations performed for the base case

	y_{CO2}	y_{N2}	Err rel BM_{CO2}	Err rel BM_{N2}	Ncycles
Sim w 25 points	93.07	98.82	$8*10^{-4}$	$2.5*10^{-4}$	300
Sim w 50 points	96.97	99.52	$4.6*10^{-4}$	$2.9*10^{-4}$	1300
Sim w 100 points	98.53	99.8	$2.5*10^{-4}$	$3.6*10^{-3}$	1300
Shen et al. (sim)	95.12	99.28	0.23	$6.5*10^{-3}$	
Shen et al. (exp)	95.05	99.36	0.23	$5*10^{-3}$	

In Figure from 164 to 168 are reported the profiles obtained from the simulation of the base case with 50 computational points.

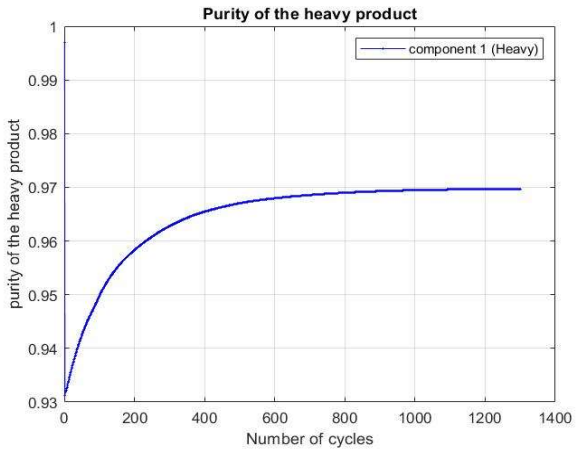

Figure 164: Heavy product purity for the simulation of base case with 50 computational points

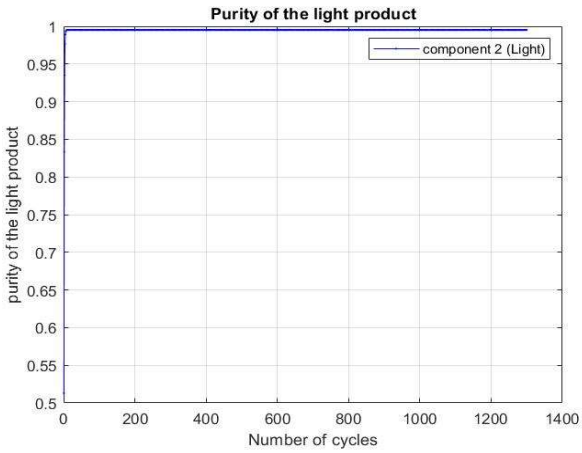

Figure 165: Light product purity for the simulation of base case with 50 computational points

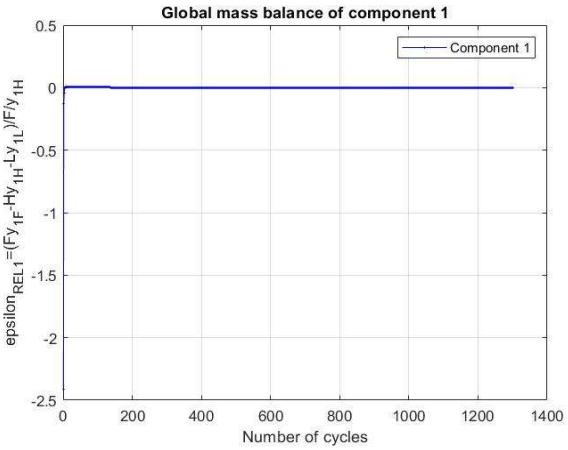

Figure 166: Error on the heavy product BM for the simulation of base case with 50 computational points

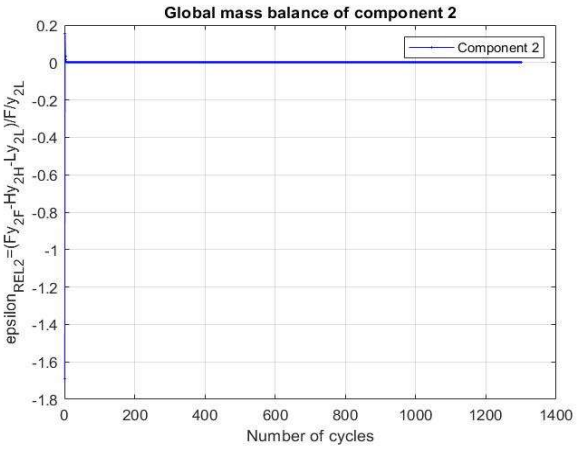

Figure 167: Error on the light product BM for the simulation of base case with 50 computational points

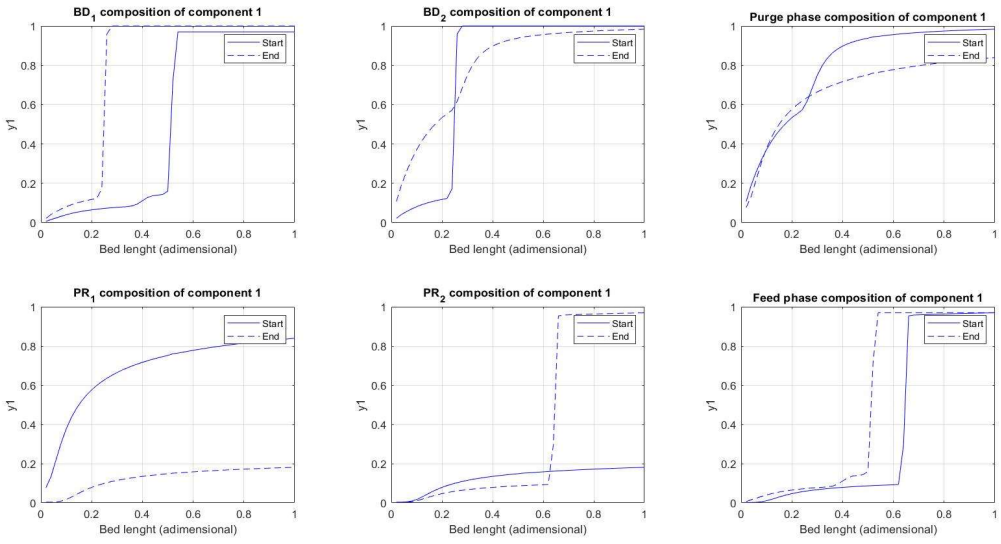

Figure 168: FVM start to end profiles for the simulation of base case with 50 computational points

It can be seen how the purity of CO_2 increases with the accuracy of the simulation, reaching, a higher value than those obtained in the article for the simulation and experimental results.

- Case 2

With respect to the "Base case", the light recycle flowrate was halved, the other data remained almost the same. Only one simulation was carried out for this case, with 50 computational points and 800 cycles, the results of which are reported in Table 70 and the profiles represented from Figure 169 to 173.

Table 70: Results of the simulation performed for the case 2

	y_{CO2}	y_{N2}	Err rel BM_{CO2}	Err rel BM_{N2}	Ncycles
Sim 50 points	94.51	99.09	$3.1*10^{-4}$	$1.7*10^{-4}$	800
Sim 100 points	96.84	100	$3.8*10^{-4}$	$1.9*10^{-4}$	1500
Shen et al. (sim)	93.88	99.07	0.29	$8.3*10^{-3}$	
Shen et al. (exp)	93.70	99.14	0.3	$6.6*10^{-3}$	

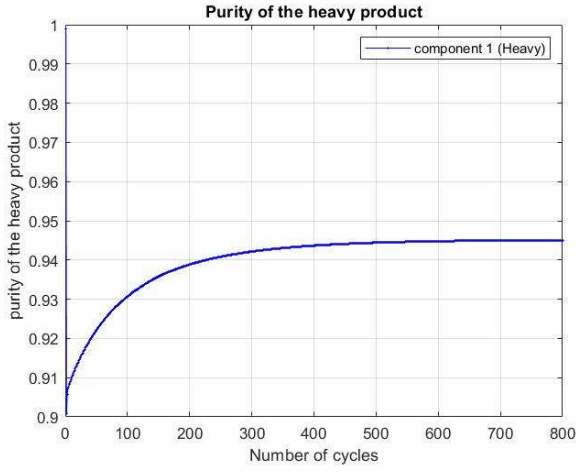

Figure 169: Heavy product purity for the simulation of case 2 with 50 computational points

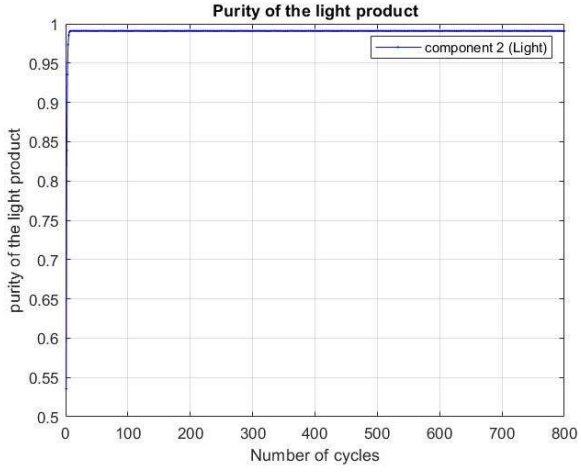

Figure 170: Light product purity for the simulation of case 2 with 50 computational points

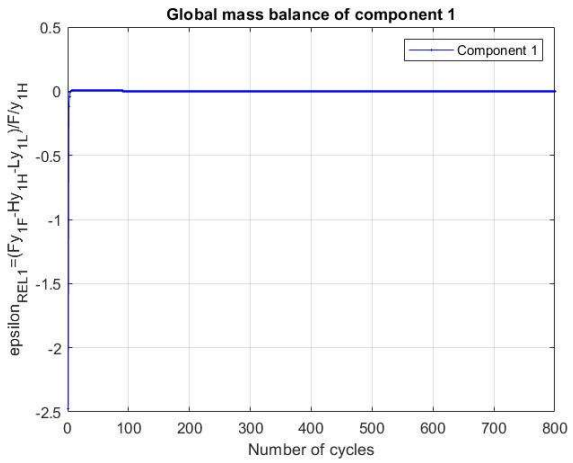

Figure 171: Error on the heavy product BM for the simulation of case 2 with 50 computational points

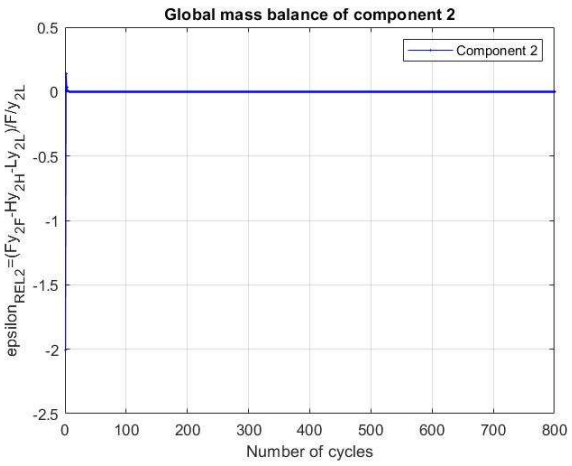

Figure 172: Error on the light product BM for the simulation of case 2 with 50 computational points

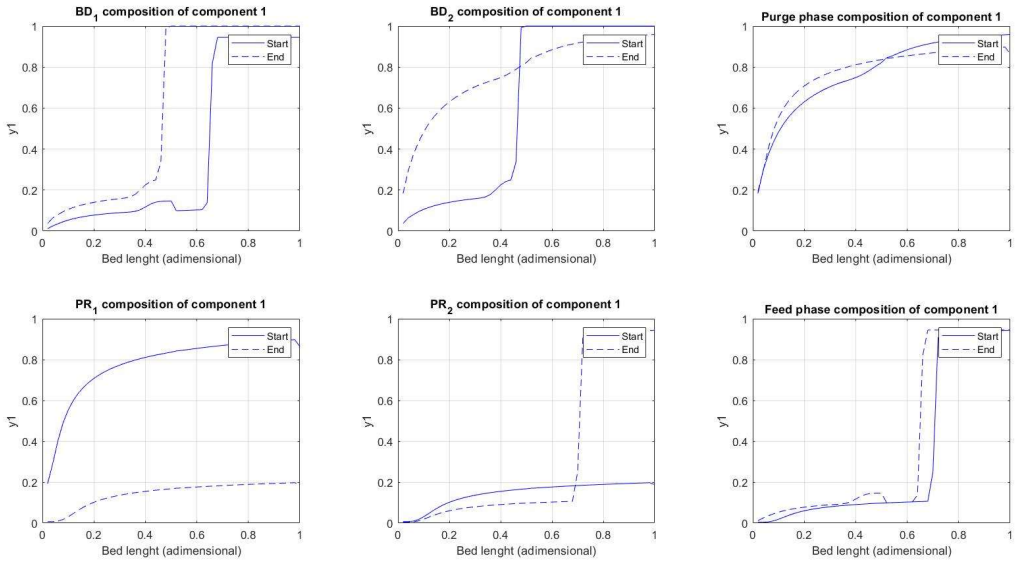

Figure 173: FVM start to end profiles for the simulation of case 2 with 50 computational points

Good results were obtained for case 2 with 50 points, as the difference with respect to those reported in the article is small.

- Case 9

With respect to the “Base case”, the heavy product flowrate has been increased from 0.603 SLPM to 0.645 SLPM, while the other data can be considered unchanged. Two simulations were performed with 50 and 100 computational points and 300 and 600 cycles respectively.

The numerical results obtained are reported in Table 71, while the profiles of the simulation with 100 computational points are shown from Figure 174 to 178.

Table 71: Results of the simulations performed for the Case 9

	y_{CO2}	y_{N2}	Err rel BM_{CO2}	Err rel BM_{N2}	Ncycles
Sim w 50 points	90.65	99.52	$1.3*10^{-4}$	$2.2*10^{-4}$	300
Sim w 100 points	92.13	99.8	$4.6*10^{-5}$	$2.4*10^{-4}$	600
Shen et al. (sim)	90.47	99.58	0.5	$1.6*10^{-2}$	
Shen et al. (exp)	90.16	99.85	0.52	$1.2*10^{-2}$	

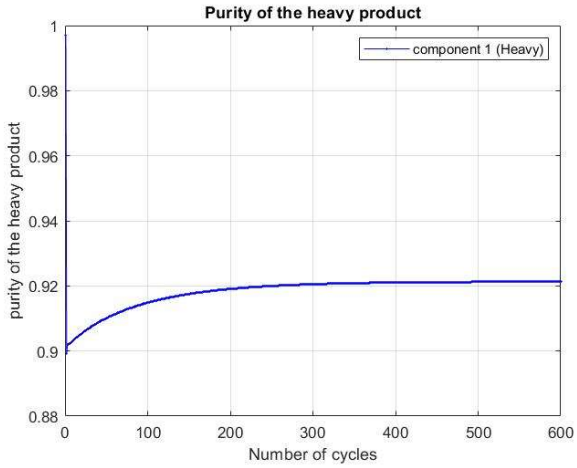

Figure 174: Heavy product purity for the simulation of case 9 with 100 computational points

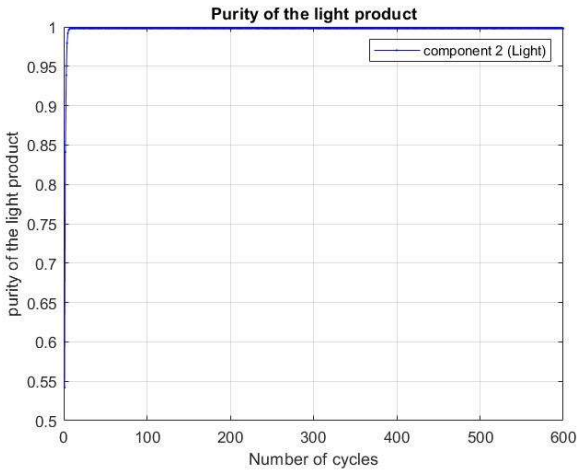

Figure 175: Light product purity for the simulation of case 9 with 100 computational points

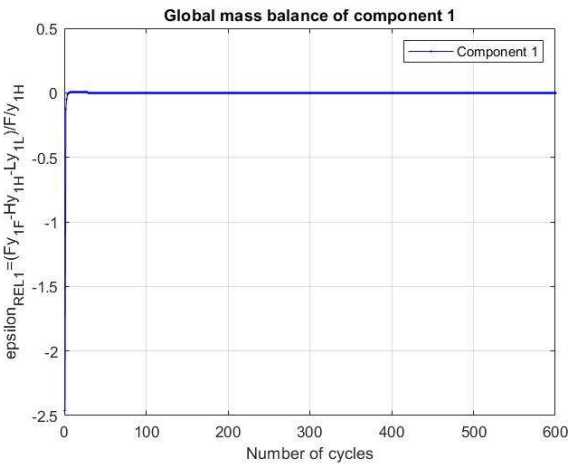

Figure 176: Error on the heavy product BM for the simulation of case 9 with 100 computational points

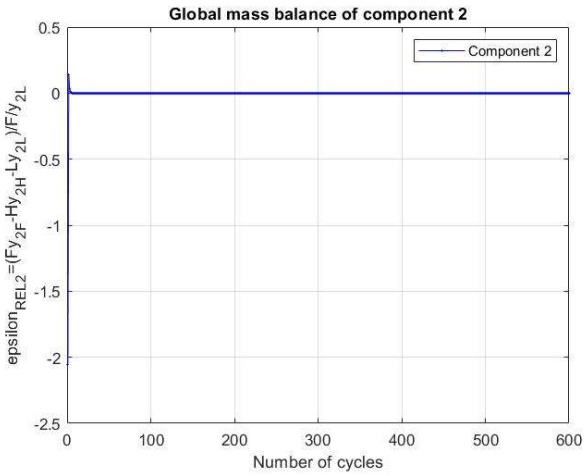

Figure 177: Error on the light product BM for the simulation of case 9 with 100 computational points

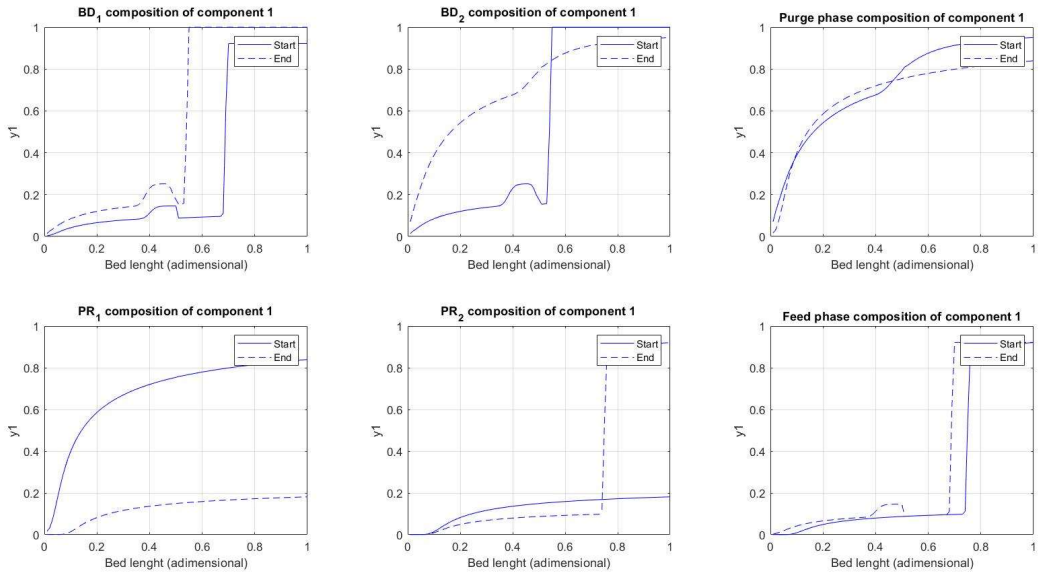

Figure 178: FVM start to end profiles for the simulation of case 9 with 100 computational points

Also for case 9 there is a tendency to obtain higher CO_2 purity as the number of points increases, however in this case with 50 points results almost equal to those obtained by Shen et al., (2017).

- Case 10

The feed inlet position z_{Feed} has been modified with respect to the base case from 0.5 to 0.2. Only one simulation was carried out for this case, with 50 computational points and 800 cycles, the results of which are reported in Table 72 and the profiles represented in Figure 179 to 183.

Table 72: Results of the simulation performed for the case 10

	y_{CO2}	y_{N2}	Err rel BM_{CO2}	Err rel BM_{N2}	Ncycles
Sim w 50 points	96.56	99.51	$3.8*10^{-4}$	$3.1*10^{-4}$	800
Shen et al. (sim)	93.31	99.38	0.3	$6.3*10^{-3}$	
Shen et al. (exp)	93.13	99.51	0.3	$4.5*10^{-3}$	

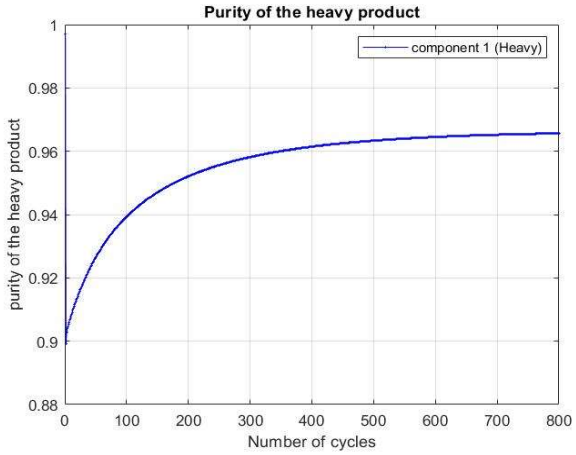

Figure 179: Heavy product purity for the simulation of case 10 with 50 computational points

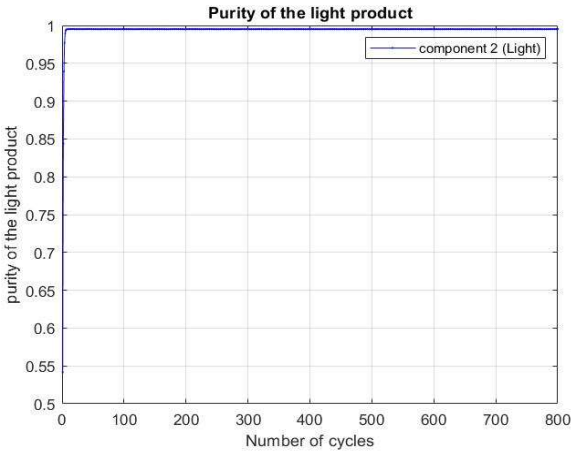

Figure 180: Light product purity for the simulation of case 10 with 50 computational points

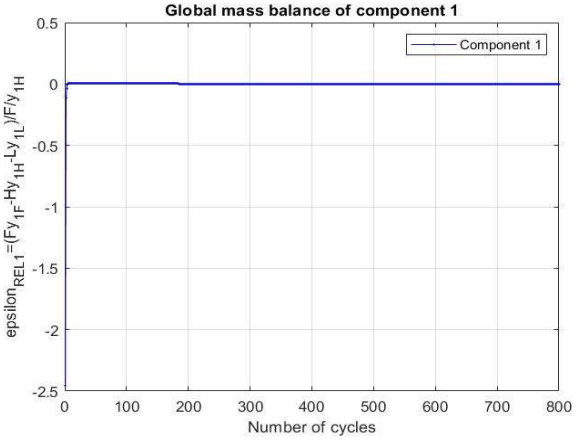

Figure 181: Error on the heavy product BM for the simulation of case 10 with 50 computational points

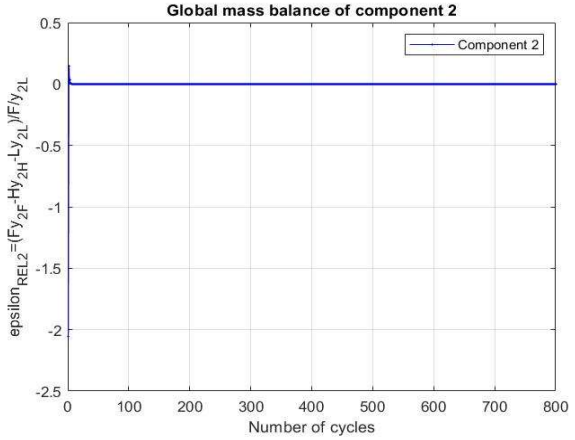

Figure 182: Error on the light product BM for the simulation of case 10 with 50 computational points

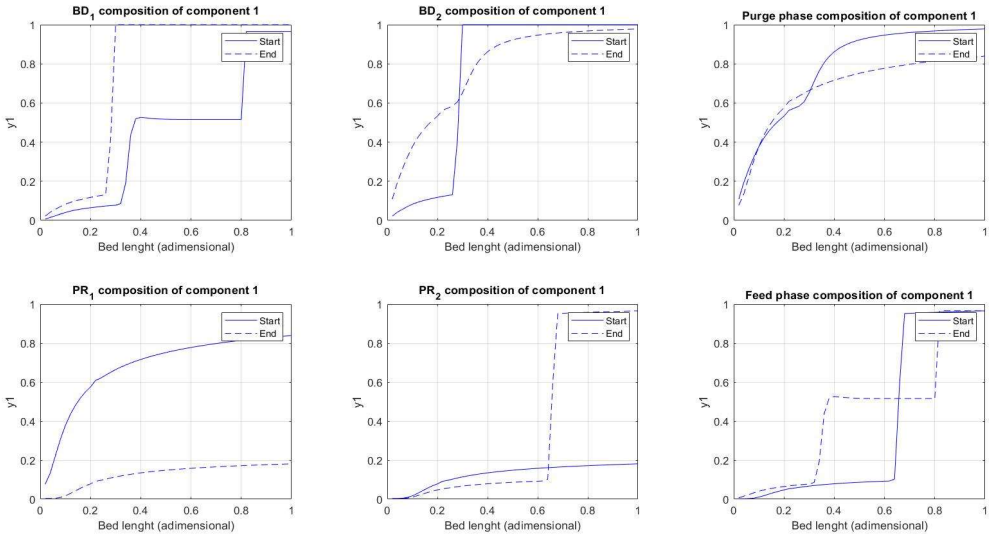

Figure 183: FVM start to end profiles for the simulation of case 10 with 50 computational points

In this case it can be noted that the CO_2 purity obtained is higher than that reported by Shen et al.

It can be concluded that for some cases, with the code and the model that have been developed, it was possible to obtain results consistent with those found in literature, however there is a trend towards higher CO_2 purity values than those reported by Shen et al., especially as the number of computational points increases.

Moreover, the results obtained in this thesis show greater accuracy since the relative errors on the BM are lower than the ones obtained in the study reported by Shen et al. (2017).

The aim of this preliminary code validation work is to lay the foundations to be able to implement a code in the optimizer to allow an optimization work similar to that proposed in chapter 3 for cases present in the literature with different gas mixtures.

Chapter 5

Conclusions

In this thesis work, a study of gas separation processes, based on adsorption and pressure variation, has been carried out with focus on a particular process based on the PSA, known as DR-PSA. Among the possible configurations, which differ in the pressure of the feed column and in the component of the mixture that is used to perform the pressure swing, in this work the DRPHA has been mainly studied.

In Chapter 2, the model, the equations and the key parameters considered in this work have been presented.

In Chapter 3, after a preliminary study to tuning the process, an optimization of the purity and recovery of A was carried out with variable t_{Feed} and Q_L at $\pi = 2.67$. The results of the check simulations showed high separation at high productivity and low work required, therefore, a region characterized by high t_{Feed} and low Q_L was explored by manual optimization with the bisection method, which resulted in a high separation region with purity of A > 98%.

A similar work was performed again for the cases at $\pi = 4$ and $\pi = 6$, first carrying out the optimization of purity and recovery of A and subsequently studying the region with high productivity and low work by means of the bisection method.

The results show that at $\pi = 2,67$ and $\pi = 4$ wide high separation regions can be found towards very high productivity and low work required, while in the case at $\pi = 6$ the region found is smaller and shifted towards lower t_{Feed} and higher Q_L. Moreover, the shape of the regions can be considered similar.

To conclude the optimization study, a sensitivity analysis was carried out on the three points characterized by the highest productivity and the least work for each case of π, with the variation of 7 parameters: z_{Feed}, t_{Feed}, P_L, y_F, Q_L, Q_{HP} and Q_{Feed}.

Since the DRPSA process is too complicated to find optimal operating conditions with rule of thumb, it is necessary to carry out detailed simulations. Two approaches are possible: trial and error to simulate different operating conditions, however without the possibility to verify if they represent an optimum; or coupling the simulation program with an optimizer.

However, since the DRPSA optimization process is expensive in terms of computational time and characterized by a possible lack of robustness when operating conditions vary, a high accuracy optimization would require both long computational and setting times.

In this thesis it was shown that it is possible to perform optimizations with lower accuracy, without compromising the results reliability, and then carrying out a manual optimization in the region of interest near the optimal operating conditions found.

The feasibility of this approach was verified with a fictious system with the aim of implement its applicability on real cases.

For this purpose, in Chapter 4, a literature review was carried out for the separation of CO_2 from flue gas, where different studies have been reported in terms of purity vs. recovery and productivity vs. work. Among the works collected, one has been chosen where interesting results were obtained with a different DRPSA configuration. A simulation code was developed for this case to be subsequently implemented in the optimization process.

References

Bhatt, T.S., Storti, G., Rota, R., (2013). *Optimal design of dual-reflux pressure swing adsorption units via equilibrium theory*.
Chem. Eng. Sci. 102, 42–55. https://doi.org/10.1016/j.ces.2013.07.040

Bhatt, T.S., Storti, G., Denayer, J.F.M., Rota, R., (2017). *Optimal design of dual-reflux pressure swing adsorption units via equilibrium theory: process configurations employing heavy gas for pressure swing*.
Chem. Eng. J. 311, 385–406 (2017). https://doi.org/10.1016/j.cej.2016.11.111

Bhatt, T.S., Storti, G., Denayer, J.F., Rota, R. (2019). *Equilibrium theory-based assessment of dual-reflux pressure swing adsorption cycles that utilize light gas for pressure swing*.
Ind. Eng. Chem. Res.
58(1), 350–365 (2019). https://doi.org/10.1021/acs.iecr.8b04415

Capra, F., Gazzani, M., Joss, L., Mazzotti, M., Martelli, E., (2018). *MO-MCS, a Derivative-Free Algorithm for the Multiobjective Optimization of Adsorption Processes*.
Industrial and Engineering Chemistry Research, 57 (30), pp. 9977-9993.
https://doi.org/10.1021/acs.iecr.8b00207

Deb, Kalyanmoy, (1999). *Introduction to genetic algorithms*.
Sadhana - Academy Proceedings in Engineering Sciences, 24 (4), pp. 293-315.
https://doi.org/10.1007/BF02823145

D. Diagne, M. Goto, T. Hirose, (1994). *New PSA Process with Intermediate Feed Inlet Position Operated with Dual Refluxes: application to Carbon Dioxide Removal and Enrichment*.
Chem. Eng. Jpn. 27 (1994) 85–89. https://doi.org/10.1252/jcej.27.85

Diagne, D., Goto, M., Hirosi, T., (1995a). *Experimental study of simultaneous removal and concentration of CO2 by an improved pressure swing adsorption process*.
Energy Conversion and Management 36, 431–434. https://doi.org/10.1016/0196-8904(95)00037-E

Diagne, D., Goto, M., Hirosi, T., (1995b). *Parametric studies on CO2 separation and recovery by a dual reflux PSA process consisting of both rectifying and stripping sections*.
Industrial and Engineering Chemistry Research 34, 3083–3089. https://doi.org/10.1021/ie00048a020

Ebner, A.D., Ritter, J.A., (2002). *Equilibrium theory analysis of rectifying PSA for heavy component production*.
AIChEJournal48(8), 1679–1691. https://doi.org/10.1002/aic.690480810

Farooq, S., Ruthven, D., Boniface, H., (1989). *Numerical simulation of a pressure swing adsorption oxygen unit*.
Chem. Eng. Sci. 44 (12), 2809–2816. https://doi.org/10.1016/0009-2509(89)85090-0

Fiandaca G., Fraga E. S., Brandani S., (2009). *A multi-objective genetic algorithm for the design of pressure swing adsorption*.
https://doi.org/10.1080/03052150903074189

D.T. Kearns, P.A. Webley, (2006). *Modelling and evaluation of dual-reflux pressure swing adsorption cycles: Part I. Mathematical models*.
Chem. Eng. Sci. 61 (2006) 7223–7233. https://doi.org/10.1016/j.ces.2006.07.040

S. Krishnamurthy, R. Haghpanah, A. Rajendran, S. Farooq (2014). *Simulation and optimization of a dual-adsorbent, two-bed vacuum swing adsorption process for CO_2 capture from wet flue gas.*
Ind. Eng. Chem. Res., 53 (2014), pp. 14462-14473. https://doi.org/10.1021/ie5024723

Leavitt, F.W., (1992). *Duplex Adsorption Process*. US Patent 5,085,674.

Li, D.D., Zhou, Y., Shen, Y.H., Sun, W.N., Fu, Q., Yan, H.Y., Zhang, D.H., (2016). *Experiment and simulation for separating CO2/N2 by dual-reflux pressure swing adsorption process*.
Chem. Eng. J. 297, 315–324. https://doi.org/10.1016/j.cej.2016.03.075

May, E. F., Zhang, Y., Saleman, T. L. H., Xiao, G., Li, G. Kevin, & Young, B. R. (2017). *Demonstration and optimisation of the four Dual-Reflux Pressure Swing Adsorption configuration*s.
Separation and Purification Technology, 177, 161–175. https://doi.org/10.1016/j.seppur.2016.12.007

Mc Intyre, J. A., Holland, C. E., & Ritter, J. A. (2002). *High Enrichment and Recovery of Dilute Hydrocarbons by Dual-Reflux Pressure-Swing Adsorption*.
Industrial & Engineering Chemistry Research, *41*(14), 3499–3504. https://doi.org/10.1021/ie020139d

McIntyre, J. A., Ebner, A. D., & Ritter, J. A. (2010). *Experimental Study of a Dual Reflux Enriching Pressure Swing Adsorption Process for Concentrating Dilute Feed Streams*.
Industrial & Engineering Chemistry Research, *49*(4), 1848–1858. https://doi.org/10.1021/ie901266y

Perez L.E., Sarkar P., Rajendran A., (2019). *Experimental validation of multi-objective optimization techniques for design of vacuum swing adsorption processes*.
Sep. Purif. Technol., 224 (2019), pp. 553-563

E. Rossi, M. Paloni, G. Storti, R. Rota (2019). *Modeling dual reflux-pressure swing adsorption processes: numerical solution based on the finite volume method*.
Chem. Eng. Sci., 203 (2019), pp. 173-185. https://doi.org/10.1016/j.cej.2019.123753

Rossi, E., Storti, G., Rota, R., (2020). *Influence of the main operating parameters on the DRPSA process design based on the equilibrium theory*.
Adsorption 27(1), pp. 27-39.

Ruthven, D.M., Farooq, S., Knaebel, K.S., (1994). *Pressure Swing Adsorption*.
VCH Publishers, New York, NY.

Shen, Y., Zhou, Y., Li, D., Fu, Q., Zhang, D., Na, P., (2017). *Dual-reflux pressure swing adsorption process for carbon dioxide capture from dry flue gas*.
Int. J. Greenhouse Gas Control **65**, 55–64 (2017). https://doi.org/10.1016/j.ijggc.2017.08.020

Sholl, D.S., Lively, R.P., (2016). *Seven chemical separations to change the world*.
Nature 532 (7600), 435–437. https://doi.org/10.1038/532435a

S.V. Sivakumar, D.P. Rao, Modified duplex PSA. 1 (2011). *Sharp separation and process intensification for CO2-N2-13X zeolite system*.
Ind. Eng. Chem. Res. 50 (2011) 3426–3436. https://doi.org/10.1021/ie101177x

S.V. Sivakumar, D.P. Rao, Modified duplex PSA. 2 (2011). *Sharp separation and process intensification for N2-O2-5A zeolite system.*
Ind. Eng. Chem. Res. 50 (2011) 3437–3445. https://doi.org/10.1021/ie200175h

Subramanian, D. ,Ritter, J.A., (1997). *Equilibrium theory for solvent vapor recovery by pressure swing adsorption: analytical solution for process performance*.
Chemical EngineeringScience52(18),3147–3160. https://doi.org/10.1016/S0009-2509(97)00121-8

Subraveti, S.G., Pai, K.N., Rajagopalan, A.K., Wilkins, N.S., Rajendran, A., Jayaraman, A., Alptekin, G., (2019). *Cycle design and optimization of pressure swing adsorption cycles for pre-combustion CO_2 capture.*
Applied Energy, 254, art. no. 113624. https://doi.org/10.1016/j.apenergy.2019.113624

Thakur, R.S., Kaistha, N., Rao, D.P., (2011). *Process intensification in duplex pressure swing adsorption*.
Computers and Chemical Engineering 35, 973–983. https://doi.org/10.1016/j.compchemeng.2011.01.024

Tian, C., Fu, Q., Ding, Z., Han, Z., Zhang, D., 2017. *Experiment and simulation study of a dual-reflux pressure swing adsorption process for separating N2/O2*.
Sep. Purif. Technol. 189, 54–65. https://doi.org/10.1016/j.seppur.2017.06.041

Wawrzyńczak, D., Majchrzak-Kucęba, I., Srokosz, K., Kozak, M., Nowak, W., Zdeb, J., Smółka, W., Zajchowski, A., (2019). *The pilot dualreflux vacuum pressure swing adsorption unit for CO2 capture from flue gas*.
Sep. Purif. Technol. 209, 560–570 (2019). https://doi.org/10.1016/j.seppur.2018.07.079

M. Yoshida, J.A. Ritter, A. Kodama, M. Goto, T. Hirose, (2003). *Enriching reflux and parallel equalization PSA process for concentrating trace components in air*.
Ind. Eng. Chem. Res. 42 (2003) 1795–1803. https://doi.org/10.1021/ie010114z

Zhang, Y., Saleman, T.L.H., Li, G.K., Xiao, G., Young, B.R., May, E.F., (2016). *Non-isothermal numerical simulations of dual reflux pressure swing adsorption cycles for separating N2 + CH4*.
Chem. Eng. J. 292, 366–381. https://doi.org/10.1016/j.cej.2016.02.018

Appendix

- $CO_2 + N_2$

AUTHORS	TITLE	COMPOSITION	PURITY	RECOVERY	PRODUCTIVITY [kmolCO2/m3ads/cycle]	WORK [J/kmolCO2]	SOLID	PROCESS
Chou, Hsu, Shen, Lee, Yang	Experimental Study of High Purity CO2 Concentration from Syngas by a Dual-bed Six-step Pressure Swing Adsorption Process	0,95 CO2 + 0,05 N2	99,94%	42,84%	0,311853367	13379,04	UOP 13X	Dual bed 6-step PSA
Zhao, Wu, Men, Webly, Grande	CO2 capture using a novel hybrid monolith (H-ZSM5/activated carbon) as adsorbent by combined vacuum and electric swing adsorption (VESA)	0,15 CO2 + 0,85 N2	17,00%	61,00%			hybrid monolith	VSA
			19,00%	64,00%				
			23,00%	70,00%				
Webley, Qader, Ntiamoah, Xiao, Zhai	A New Multi-bed Vacuum Swing Adsorption Cycle for CO2 Capture from Flue Gas Streams	0,15 CO2 + 0,85 N2	88,04%	75,65%		15403500	13X zeolite	VSA
			90,90%	70,44%		14963400		
			92,38%	64,05%		14523300		
			93,54%	58,47%		14523300		
			95,85%	51,27%		13643100		
			89,20%	88,01%		14523300		
			91,20%	82,57%		13643100		
			92,80%	80,83%		14523300		
			95,83%	75,32%		14523300		
			96,68%	73,77%		14083200		

Kim, Lee	Adsorptive cyclic purification process for CO2 mixtures captured from coal power plants	0,9 CO2 + 0,1 N2	95,00%	55,00%			activated carbon	PVSA
			98,70%	90,70%				
			96,68%	65,56%				
			96,83%	65,90%				
			96,84%	69,39%				
			96,78%	74,10%				
			96,65%	79,35%				
			96,31%	84,85%				
			95,47%	88,13%				
			93,38%	92,95%				
			96,81%	66,41%				
			96,82%	69,93%				
			96,77%	74,64%				
			96,66%	79,95%				
			96,42%	85,75%				
			95,07%	89,26%				
			92,78%	91,76%				

Yan, Fu, Zhou, Li, Zhang	CO2 capture from dry flue gas by pressure vacuum swing adsorption: A systematic simulation and optimization	0,15 CO2 + 0,85 N2	87,96%	82,40%			silica gel	VSA
			89,22%	81,96%				
			90,12%	81,39%				
			90,72%	80,86%				
			91,25%	79,74%				

Qasem, Ben-Mansour	Energy and productivity efficient vacuum pressure swing adsorption process to separate CO2 from CO2/N2 mixture using Mg-MOF-74: A CFD simulation	0,15 CO2 + 0,85 N2	95,30%	94,80%	2,539408657	10886137,56	Mg-MOF-74	PSA/VPSA
			94,20%	91,00%	2,368822427	10036920,6		
			99,00%	80,00%				
			95,00%	72,00%				
			95,90%	86,40%	3,976369007	63215964		
			97,30%	98,45%				
			97,10%	98,60%				
			98,10%	97,20%	2,649514315	10171591,2		
			98,30%	95,70%	2,55065184	10122476,04		
			96,40%	99,10%				
			95,60%	77,65%	0,135034509	86479650		
			95,30%	74,40%	0,122124233	31845636		
			99,00%	80,00%				

Ntiamoah, Ling, Xiao, Webley, Zhai	CO2 capture by vacuum swing adsorption: role of multiple pressure equalization steps	0,15 CO2 + 0,85 N2	92,40%	62,90%	0,186474791	12322800	13X zeolite	VSA
			91,30%	77,00%	0,168383953	11442600		
			82,50%	84,50%	0,088714686	10122300		
			79,50%	91,30%	0,08088692	10122300		
			86,50%	64,50%	0,10019541	11002500		
			78,80%	83,70%	0,053924613	9682200		
			70,50%	91,30%	0,029919463	13203000		

Haghpanah, Nilam, Karimi, Majumder, Amanullah	Multiobjective optimization of a four-step adsorption process for postcombustion CO2 capture via finite volume simulation	CO2 + N2	90,00%	90,00%	0,2093231	23606964	13X zeolite	4-step PVSA

Krishnamurthy, Haghpanah, Rajendran, Farooq	Simulation and optimization of a dual-Adsorbent, two-bed vacuum swing adsorption process for CO2 capture from wet flue gas	0,15 CO2 + 0,82 N2 + 0,03 moisture	95,20%	90,10%	0,144995456	25539883,2	13X zeolite	VSA
			78,80%	88,60%	0,139356743	29912716,8		
			80,00%	85,40%	0,132106971	30483086,4		
			95,00%	90,00%	0,106330001	30910863,6		
			95,00%	90,00%	0,082969622	36440280		
			95,00%	90,00%	0,122440607	24399144		

Chou, Huang, Cheng, Yang, Yang	Adsorption processes for CO2 capture from flue gas using polyaniline solid sorbent	CO2 + N2	62,00%	89,50%			polyaniline	single bed 2-step PSA
			73,00%	86,00%				single bed 2-step PSA
			96,50%	88,00%				single bed 3-step PSA
			97,50%	87,00%				single bed 3-step PSA
			88,00%	95,53%				Dual bed 6-step PSA
			88,90%	93,78%				Dual bed 6-step PSA

Krishnamurthy, Rao, Guntuka, Karimi, Farooq	CO2 capture from dry flue gas by vacuum swing adsorption: A pilot plant study	CO2 + N2	94,70%	85,40%	0,19881845	80881578	13X zeolite	VSA
			85,10%	93,10%	0,114399505	92320657,2		
			95,50%	85,80%	0,161369049	53741491,2		
			83,40%	94,50%	0,169574255	72722124		
			95,90%	86,40%	0,160001515	74813479,2		
			92,90%	93,30%	0,187036616	74306484		
			94,80%	89,70%	0,172309324	75257100		
			96,30%	86,50%	0,169363865	80533018,8		

Haghpanah, Nilam, Rajendran, Farooq, Karimi	Cycle synthesis and optimization of a VSA process for postcombustion CO2 capture	CO2 + N2	90,00%	90,00%	0,1978299	20755116	13X zeolite	VSA
			95,00%	90,00%	0,1527108	24399144		

Liu, Grande, Li, Yu, Rodrigues	Multi-bed vacuum pressure swing adsorption for carbon dioxide capture from flue gas	0,15 CO2 + 0,85 N2	53,77%	81,85%	0,104244338	19038726	5A zeolite	VPSA
			50,67%	95,04%	0,096824813	16217685		
			50,27%	86,39%	0,110179959	17097885		
			58,23%	93,62%	0,095313084	18206937		
			71,19%	90,20%	0,076374744	24258312		
			69,15%	98,92%	0,074195259	19927728		
			77,14%	91,46%	0,062843384	24874452		

Wang, Liu, Li, Wang, Yu	CO2 capture from flue gas by two successive VPSA units using 13XAPG	CO2 + N2	69,15%	88,42%		16343553,6	13X zeolite	VPSA
			75,92%	55,66%		20091445,2		
			77,42%	39,04%		25212888,9		
			65,38%	98,92%		15918417		
			67,81%	94,83%		17159939,1		
			70,33%	91,40%		18416424,6		
			60,85%	99,89%		17243118		
			65,68%	84,84%		15566777,1		
			72,24%	92,06%		16049566,8		
			59,19%	99,35%		16024041		
			84,26%	77,73%				
			84,44%	84,27%				
			85,02%	91,47%				
			87,07%	92,60%				
			95,31%	81,38%				
			94,18%	79,89%				
			96,54%	93,35%	0,327809725	23254443,9		2 successive VPSA
			94,35%	95,64%	0,330961742	25259099,4		
			91,68%	97,28%	0,329911069	26738275,5		
			97,59%	81,28%	0,367735268	23466132		
			98,66%	46,93%	0,443383667	26782725,6		
			96,61%	97,88%	0,332012414	26142380,1		
			95,98%	83,14%	0,286833509	21920060,7		

Liu, Shen, Lopes, Grande, Rodrigues	Zeolite Apgiia for Adsorption Based Carbon Dioxide Capture	CO2 + N2	72,10%	63,00%		17177103	13X zeolite	VSA

Agarwal, Biegler, Zitney	A superstructure-based optimal synthesis of PSA cycles for post-combustion CO2 capture	CO2 + N2	95,07%	77,51%			13X zeolite	PSA
			90,22%	82,68%				

Shen, Liu, Li, Yu	Two-stage VPSA process for CO 2 capture from flue gas using activated carbon beads	CO2 + N2	84,96%	86,04%			activated carbon	VPSA
			88,75%	87,22%				
			94,14%	85,08%				
			87,50%	91,03%				
			83,98%	94,44%				
			85,28%	88,07%		36986884,2		
			95,29%	74,36%		31843875,6		
			96,26%	64,42%		31963142,7		
			96,77%	49,36%		33411951,9		
			96,34%	80,72%		36496612,8		
			96,56%	82,86%		39715064,1		
			95,93%	52,23%		29528949,6		
			96,00%	61,32%		30555262,8		
			93,33%	81,62%		32991656,4		

Reynolds, Mehrotra, Ebner, Ritter	Heavy reflux PSA cycles for CO2 recovery from flue gas: Part I. Performance evaluation	CO2 + N2	98,70%	98,70%			K-promoted HTlc	5-bed 5-step PSA
			98,60%	91,30%				6-bed 6-step PSA
			98,60%	91,80%				5-bed 5-step PSA
			96,60%	71,10%				5-bed 5-step PSA
			96,50%	71,10%				4-bed 4-step PSA
			96,50%	71,00%				5-bed 5-step PSA
			99,20%	15,20%				4-bed 4-step PSA
			99,10%	15,00%				5-bed 5-step PSA
			99,20%	15,20%				4-bed 4-step PSA

Ho, Allinson, Wiley	Reducing the cost of CO2 capture from flue gases using pressure swing adsorption	CO2 + N2	48%	85%			13X zeolite	PSA
			99,00%	90,00%				

- $CO_2 + CH_4$

AUTHORS	TITLE	COMPOSITION	PURITY	RECOVERY	PRODUCTIVITY [kmolCO2/m3ads/cycle]	WORK [J/kmolCO2]	SOLID	PROCESS
Abdullah, Shamsudin, Othman	Methane enrichment from high carbon dioxide content natural gas by pressure swing adsorption	0,7 CO2 + 0,3 CH4	94,70%	90,20%			Activated carbon	PSA
			72,50%	51,80%			UiO-66	
Danaci, Singh, Xiao, Webley	Assessment of ZIF materials for CO2 capture from high pressure natural gas streams	CO2 + CH4	24,00%	90,00%			ZIF-8	PSA
			35,00%	93,00%			ZIF-8	
			44,00%	95,00%			ZIF-8	
			24,00%	89,00%			ZIF-71	
			36,00%	93,00%			ZIF-71	
			45,00%	96,00%			ZIF-71	

- $CO_2 + H_2$

AUTHORS	TITLE	COMPOSITION	PURITY	RECOVERY	PRODUCTIVITY [kmolCO2/m3ads/cycle]	WORK [J/kmolCO2]	SOLID	PROCESS
Subraveti, Pai, Rajagopalan, Jayaraman, Alptekin	Cycle design and optimization of pressure swing adsorption cycles for pre-combustion CO2 capture	0,4 CO2 + 0,6 H2	70,10%	33,30%			activated carbon	4-step PSA
			70,90%	44,70%				4-step PSA
			75,20%	99,90%				6-step PSA
			93,30%	99,30%				6-step PSA
			80,50%	99,90%				6-step PSA
			83,50%	99,90%				6-step PSA
			95,00%	90,80%	1,25136	15162325,2		6-step PSA
			95,50%	90,30%	1,45005	16699154,4		6-step PSA
Idris, Abdullah, Shamsudin, Othman	Optimizing purity and recovery of hydrogen from syngas by equalized pressure swing adsorption using palm kernel shell activated carbon adsorbent	0,15 CO2 + 0,85 H2	25,17%	57,68%				
Park, Kang, Lee	Efficient pressure swing adsorption for improving H2 recovery in precombustion CO2 capture	0,5 CO2 + 0,5 H2	98,40%	76,60%				PSA
Agarwal, Biegler, Zitney	Superstructure-based optimal synthesis of pressure swing adsorption cycles for precombustion CO2 capture	CO2 + H2 + impurities	90%	92%			Activated carbon	PSA
			90,00%	97,95%				

- Multicomponent mixtures

AUTHORS	TITLE	COMPOSITION	PURITY	RECOVERY	PRODUCTIVITY [kmolCO2/m3ads/cycle]	WORK [J/kmolCO2]	SOLID	PROCESS
Capocelli, Luberti, Inno, Di Natale, Lancia	Post-combustion CO2 capture by RVPSA in a large-scale steam reforming plant	0,173 CO2 + 0,646 N2 + 0,017 O2 + 0,009 Ar + 0,155 H2O	65,40%	98,70%			13X zeolite	RVPSA
			96,60%	92,00%				RVPSA
			96,64%	90,84%	0,3696456	27679209,3		2-stages RVPSA
Reynolds, Ebner, Ritter	Carbon dioxide capture from flue gas by pressure swing adsorption at high temperature using a K-promoted HTlc: Effects of mass transfer on the process performance	0,15 CO2 + 0,75 N2 + 0,1 H2O	75,50%	48,80%			K-promoted HTlc	5-bed PSA
			84,50%	92,10%				
			89,20%	72,00%				
			90,50%	85,00%				
			88,90%	72,30%				
			91,50%	88,00%				
			98,10%	5,00%				
			82,70%	17,40%				
Ribeiro, Santos, Rodrigues	PSA design for stoichiometric adjustment of bio-syngas for methanol production and co-capture of carbon dioxide	0,2 CO2+ 0,4 H2 + 0,35 CO + 0,02 CH4 + 0,03 N2	95,10%	99,70%			activated carbon	4-bed PSA

Golmakani, Fatemi, mnanloo	CO2 Capture from the Tail Gas of Hydrogen Purification Unit by Vacuum Swing Adsorption Process, Using SAPO-34	0,55 CO2 + 0,25 H2 + 0,17 CH4 + 0,1 CO + 0,2 N2	75,10%	94,70%	1,150920245	10386360	SAPO-34	4-bed 7-step VSA
			75,00%	91,10%	1,4310384	1144260		
			67,80%	91,40%	1,236173597	10958490		
			76,20%	88,50%	1,077845944	1760400		
			82,10%	79,90%	1,759872756	10430370		
			80,70%	53,50%	1,096114519	1584360		
			69,80%	90,40%	1,102204045	10826460		
			78,80%	83,40%	1,424948875	1188270		
			78,60%	73,20%	1,072974324	1496340		
			80,30%	82,80%	1,004771643	11926710		
			85,20%	52,00%	0,815996364	1980450		
			72,10%	74,80%	1,010861168	13379040		
			80,80%	60,30%	0,736832538	2552580		
			87,30%	63,30%	1,400590775	13158990		
			86,60%	35,70%	0,785548739	2376540		
			80,10%	68,50%	0,83426494	14259240		
			84,80%	58,60%	0,998682118	1672380		
			84,60%	46,00%	0,675937287	2332530		
			90,50%	73,46%	0,969756873	13425690,6		
			85,31%	51,18%	0,870142392	2012137,2		
			79,06%	66,73%	0,976551769	15010930,8		
			81,06%	57,37%	0,757333939	2691211,5		
			91,27%	58,08%	1,388005756	14354741,7		
			87,21%	32,08%	0,756146482	2577665,7		
			82,09%	63,82%	0,842501022	15326482,5		
			86,19%	53,95%	0,998057941	1822894,2		
			84,72%	43,01%	0,683249792	2513411,1		

Ribeiro, Santos, Rodrigues, Rifflart	Syngas Stoichiometric Adjustment for Methanol Production and Co-Capture of Carbon Dioxide by Pressure Swing Adsorption	0,39 CO2 + 0,55 H2 + 0,03 CO + 0,022 CH4 + 0,008 N2	95,15%	94,20%	1,338514815	574857009,5	activated carbon	4-bed PSA
			73,95%	99,80%	1,024522222	668025146,3		
			74,66%	99,80%	1,024522222	664663409,4		
			81,52%	99,70%	1,024522222	634888025,5		
			88,94%	95,80%	0,98325	644492988		
			96,88%	86,30%	0,886138889	657459687,5		
			84,87%	99,60%	1,023308333	700201770,9		
			89,01%	99,50%	1,022094444	716049959,1		
			97,77%	98,30%	1,009955556	735740132,4		
			96,84%	98,80%	1,014811111	740542613,7		
			84,24%	99,70%	1,193859722	575337257,6		
			95,43%	99,30%	1,359555556	585902716,4		
			95,71%	99,10%	1,369266667	586382964,5		
			92,26%	98,70%	1,349844444	593586686,5		
			91,08%	99,00%	1,016025	758792042,6		
			95,93%	97,10%	1,328803704	608474378,4		
			95,56%	97,30%	1,398642778	581100235,1		
			95,15%	94,20%	1,388446111	574857009,5		
			90,54%	91,10%	0,996602778	622881822,3		
			94,25%	94,20%	0,967469444	636809018		
			91,92%	96,70%	1,057863704	591665693,9		
			92,81%	96,40%	1,121228704	562850806,2		
			94,13%	95,30%	1,108847037	571495272,6		
			94,82%	93,40%	1,086835185	578698994,5		
			93,23%	96,30%	1,185726667	535956911,1		
			94,14%	94,80%	1,101968333	553245843,7		
			95,18%	93,00%	1,081332222	545561873,6		
			95,72%	92,20%	1,1362	516266737,8		
			95,29%	91,60%	1,24108	515306241,6		

Shi, Yang, Shen, Zhang, Fu	Two-stage PSA/VSA to produce H2 with CO2 capture via steam methane reforming (SMR)	0,2 CO2 + 0,035 CH4 + 0,005 CO + 0,76 H2	94,40%	92,08%			5A zeolite	3-bed VSA
			93,40%	93,66%				
			92,50%	94,57%				
			97,13%	82,64%				
			88,59%	97,85%				
			93,84%	90,67%				
			92,98%	95,45%				
			87,83%	98,32%				
			83,30%	99,41%				

Ribeiro, Santos, Rodrigues, Rifflart	Pressure swing adsorption process in coal to Fischer-Tropsch fuels with CO 2 capture	0,3011 CO2 + 0,4707 H2 + 0,0003 CH4 + 0,2226 CO + 0,0053 N2	98,39%	92,60%	0,992151852	56308154,4	activated carbon	4-bed PSA
			96,91%	94,60%	1,014811111	54913917,6		
			95,26%	95,90%	1,027759259	53836552,8		
			95,03%	95,10%	1,075748333	51871946,4		
			95,60%	94,30%	1,110951111	50604458,4		
			95,21%	92,60%	1,14097463	49336970,4		
			94,87%	98,90%	1,157564444	48655695,6		

- DRPSA

AUTHORS	TITLE	COMPOSITION	PURITY	RECOVERY	PRODUCTIVITY [kmolCO2/m3ads/cycle]	WORK [J/kmolCO2]	SOLID	PROCESS
Shen et al.	Dual-reflux pressure swing adsorption process for carbon dioxide capture from dry flue gas	0,15 C02 + 0,15 N2	95,12%	95,59%	0,0629937	98667	silica gel	6-step DRPSA modified
			93,88%	94,60%	0,0636174	87284		
			95,49%	96,38%	0,0642411	107842		
			95,67%	96,68%	0,064449	110576		
			95,85%	96,12%	0,0640332	125515		
			97,27%	90,09%	0,0600831	126166		
			96,77%	92,75%	0,0617463	118860		
			92,91%	97,13%	0,0646569	85290		
			90,47%	97,52%	0,0650727	73324		
			93,31%	96,15%	0,0642411	89733		
			95,22%	95,72%	0,0638253	96505		
			94,32%	94,47%	0,0629937	94243		
			91,64%	90,18%	0,0600831	107644		

Wawrzyńczak et al.	The pilot dual-reflux vacuum pressure swing adsorption unit for CO2 capture from flue gas	0,135 CO2 + 0,865 N2	62,70%	84,20%	0,086344013	154950,408	270 kg AC1, 270 kg AC2, 130 kg AC-P	9-step DRVPSA
			87,50%	44,30%	0,067257441	84604,824		

Thakur et al.	Process intensification in duplex pressure swing adsorption	0,2 CO2 + 0,8 N2	99,20%	99,20%	0,003346123	4260000	Zeolite 13X	4-step DRPSA
			99,50%	99,50%	0,000334612	3740000		
			99,90%	99,50%	0,001383064	3500000		6-step DRPSA modified
			99,90%	99,70%	0,000345766	1220000		
			98,50%	98,50%	0,003346123	3720000		
			98,50%	98,50%	0,000334612	1920000		4-step DRPSA
			98,60%	98,50%	0,001204604	2280000		6-step DRPSA modified
			98,60%	98,00%	0,000345766	1160000		
			97,50%	97,50%	0,003346123	3460000		4-step DRPSA
			97,50%	97,50%	0,000334612	1260000		
			97,50%	97,10%	0,001226912	2260000		6-step DRPSA modified
			97,50%	97,20%	0,000345766	1020000		
			95,00%	95,00%	0,002119211	2780000		
			95,30%	95,30%	0,000334612	720000		4-step DRPSA
			95,00%	94,20%	0,001561524	1260000		6-step DRPSA modified
			95,50%	95,10%	0,00035692	980000		

Li et al.	Experiment and simulation for separating CO2/N2 by dual-reflux pressure swing adsorption process	0,15 CO2 + 0,85 N2	99,23%	99,67%			silica gel	6-step DRPSA
			91,83%	92,24%				
			98,97%	99,41%				
			98,87%	99,31%				
			99,11%	99,55%				
			99,23%	99,67%				
			99,22%	99,66%				
			99,17%	99,60%				
			99,17%	99,61%				
			99,18%	99,62%				